Metal-Composite Joining Using Hybrid Penetrative Reinforcement

Parkes, Philip

Award date:
2015

Awarding institution:
University of Bath

METAL-COMPOSITE JOINING USING HYBRID PENETRATIVE REINFORCEMENT

Philip Nicholas Parkes

A thesis submitted for the degree of Doctor of Philosophy

Department of Mechanical Engineering
University of Bath

2015

COPYRIGHT

Philip Nicholas Parkes

Signed on behalf of the Faculty of Engineering and Design

Abstract

Hybrid Penetrative Reinforcement (HYPER) is a unique joining technology that can significantly improve the integration of metal-composite structures. Small pins are built on to a metallic substrate/component using additive manufacturing, embedded into an uncured laminate and then co-bonded. The pins provide a mechanical interlock and the epoxy matrix provides adhesion. Unlike mechanical fasteners, pre-drilling is not required and the pins only penetrate partway through the laminate so there is no aerodynamic penalty. This doctoral research project explored the design, analysis methods, manufacture processes, inspection procedures and performance of HYPER joints. Firstly, a range of non-destructive inspection methods were evaluated based on ability to detect HYPER joint defects. An ultrasonic technique was developed and used to characterise failure modes during subsequent mechanical testing. The influence of design variables, such as pin geometry and surface treatments, on the ultimate strength and fatigue life of HYPER joints was identified. HYPER pins were shown to delay the initiation of failure, slow the propagation of damage and increase the ultimate strength by up to 6.5 times compared to an unpinned reference joint. The maximum elongation, energy absorption and fatigue life were also increased substantially. In addition, a previously unreported failure mode was identified during fatigue testing. Despite impressive performance, the joint design was still thought to be sub-optimal. Thus, prior to the optimisation of the pin/joint design for improved mechanical performance, a new finite-element modelling strategy was conceived. This was used to evaluate the interaction between the pins and carbon-fibre. It was found that "conventional" modelling approaches lacked adequate accuracy for this application and that design rules for mechanical fasteners could not be applied. The work within this thesis has led to the increased maturity of HYPER joining technology and, in part, progression to a new Technology Readiness Level.

Acknowledgements

Firstly, I wish to thank my supervisors, Professor Richard Butler and Professor Darryl Almond, for their guidance and support throughout the project. I thoroughly enjoyed my time at the University of Bath and I have learnt a great deal thanks to their knowledge and expertise.

Secondly, I would like to thank my supervisor and collaborators at Airbus Group Innovations, Jonathan Meyer and André de Oliveria, as well as the other external project partners. Their technical input, enthusiasm and practical assistance has been very much appreciated. I would also like to thank my colleagues at the University of Bath: Dr Andrew Rhead, Dr Simon Pickering and Mr Nick Gathercole for their help during experimental work and Dr Tim Dodwell and Dr David Betts, for their insight and camaraderie.

I would have never been in a position to begin this doctorate without the upbringing from my parents, Janet and Dennis. This enabled me to commence my undergraduate degree and, thus, the opportunity to begin a career in research.

I also wish to thank my wife, Joyce, for her endless support and encouragement during the last few years. She has undoubtedly witnessed this process most closely and shared all the highs and lows with me.

Contents

List of Acronyms

AM	Additive manufacture/manufacturing
ASTM	American Society for Testing and Materials
BNC	Bayonet Neill-Concelman [connector]
BST	Back-face strain technique
CAD	Computer aided design
CAE	Computer aided engineering
CFRP	Carbon fibre reinforced plastic(s)
CMT	Cold metal transfer
CSV	Comma-separated values [file format]
CT	Computerised tomography
DIC	Digital image correlation
DMLS	Direct metal laser sintering
EBM	Electron beam melting
EOS	Electro Optical Systems [GmbH]
GUI	Graphical user interface
HIP	Hot iso-static pressing
HSS	High speed steel
HYPER	Hybrid penetrative reinforcement
MPI	Magnetic particle inspection
NDT	Non-destructive testing
RP	Reference point
RVE	Representative volume element
SLS	Single-lap shear [specimen/coupon]
STL	Stereolithography [file format]
TIG	Tungsten inert gas [welding]
TRL	Technology readiness level
UTS	Ultimate tensile strength

List of Figures

List of Tables

Chapter 1

Introduction

1.1 Context and Motivation

With an ever growing demand for increased performance in the aerospace industry, engineers are continually required to push the boundaries of structural design, materials science and manufacturing technologies. Customer specifications and industrial strategic aims require aircraft not only to go further and faster, but also to have lower through-life cost and impose less environmental impact. Forecasts suggest that the number of aircraft in service will almost double by 2030 compared to the size of the fleet in 2010 (45,300 and 23,800 respectively [4]). However, significant reductions in carbon dioxide emissions are targeted for the same period. The Air Transport Action Group (ATAG) has committed the aviation industry to an improvement in fuel efficiency of 1.5% per annum until 2020 and, beyond 2020, net emmisions should be capped. ATAG has also proposed that a 50% reduction should be achieved by 2050 compared to 2005 levels [4]. These goals are inline with the responsibilities of the International Civil Aviation Organisation, as stated in Article 2.2 of the United Nations' Kyoto Protocol [91]. Compliance with environmental legislation will consequently lead to increased fuel efficiency which will also provide significant economic benefits for airlines. Between 2005 and 2011, airline operational expenditure, resulting from the purchase of fuel, has increased from 5 to 30%. This is partly due to an increase in air-miles per capita but also due to the average price of jet fuel more than doubling in the last decade to more than US$100 per barrel [5]. A trend that is likely to continue as reserves become ever more depleted. The rising cost of fuel and increasing levels of legislation have also impacted other industries and modes of transport and has played a part in shaping research trends; this is particulary noticable in the automotive sector. As shown in Figure 1.1, it is proposed that research and development of new technologies will play a major role in achieving the objectives set out by ATAG (in addition to operational and infrastructure changes). The Advisory Council for Aeronautics Research in Europe (ACARE) was established to "develop and maintain a strategic research agenda" that would help realise this vision [2]. The Clean Sky Joint Technology Initiative is an example of a successful public-private partnership between the European Commission and the aviation industry that is co-ordinating technology development at a national level [32].

"Clean Sky will speed up technological breakthrough developments and shorten the time to market for new and cleaner solutions tested on full scale demonstrators, thus contributing significantly to reducing the environmental footprint of aviation" [32].

In the longer term (towards 2050), these goals will only be achieved with the introduction of radically new airframe configurations, propulsion systems and/or fuel types. For example, a next generation aircraft may have a highly integrated (blended) fuselage/wings with embedded engines running on bio-fuel [6]. In the shorter term (up to 2030), incremental changes can be achieved with advances in materials science, manufacturing technologies and topology optimisation of parts. However, it is likely that significant gains will only be achieved with a hybrid or multi-disciplinary approach that combines advances in each these individual areas.

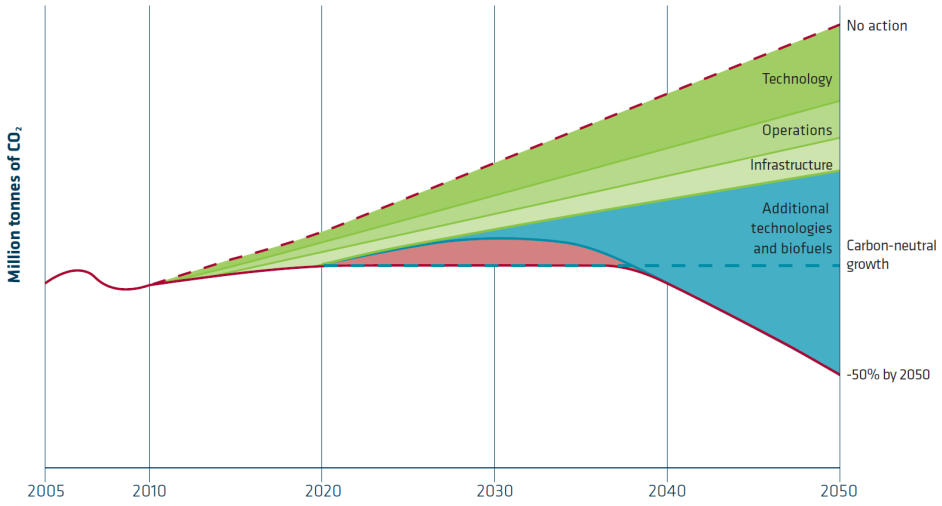

Figure 1.1: Illustrative forecast of aviation emissions until 2050. The emissions reductions that could potentially be achieved from different sectors of the industry are also shown compared to a scenario where no action is taken [4, 5].

Novel hybrid materials and manufacturing methods can provide large reductions in weight which is a significant factor governing the fuel efficiency of an aircraft. A lighter aircraft requires less lift and thus, more slender wings. Smaller wings result in less skin drag and therefore less thrust is required. Reduction in weight also means that the aircraft can accelerate more easily on take-off. Improved integration of sub-assemblies can not only save weight but could potentially reduce pressure drag by minimising surface discontinuities and maintaining laminar flow over aerodynamic surfaces.

Over the last 40 years, development of fibre reinforced plastics has provided new opportunities for weight minimisation due to their high specific strength; see Figure 1.2. During the 1970's, in-service evaluation was conducted of fibre reinforced plastics for secondary aerospace structures such as fairing panels. In 1985, the Airbus A310-300 was first production aircraft to have primary structures manufactured from glass and carbon fibre reinforced plastics (CFRP) [62].

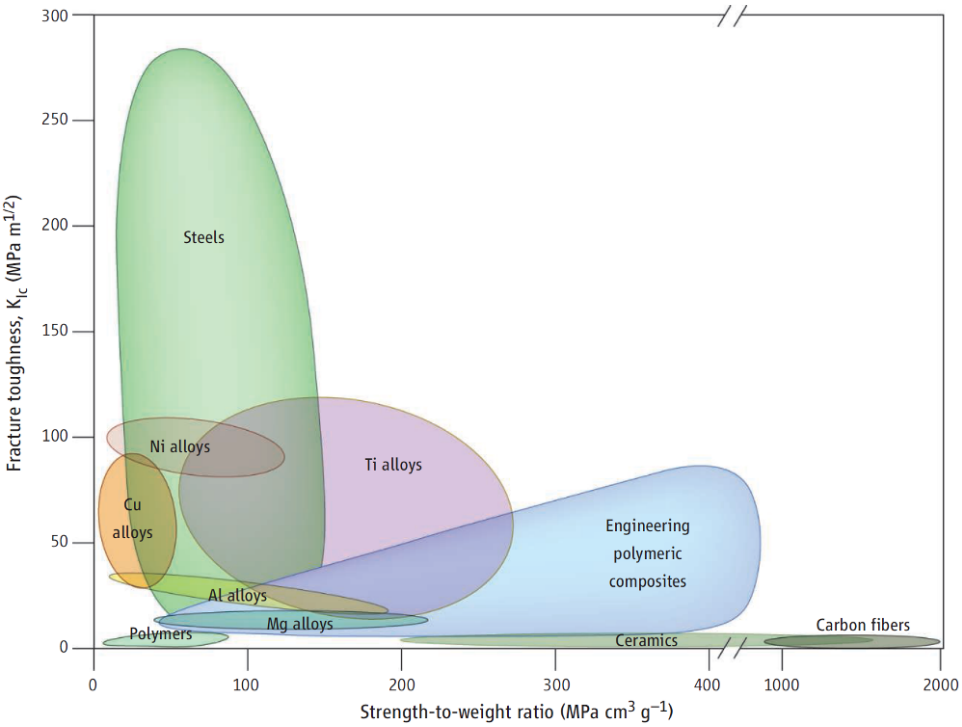

Figure 1.2: Specific strength and fracture toughness for a range of common engineering materials [56].

The use of CFRP for primary structures then became more widespread with the introduction of aircraft such as the Airbus A380 and A400M and continued investment in composites research has subsequently led to the development of a whole new generation aircraft. The Boeing 787, Airbus A350XWB and Bombardier C-Series each have around 50% of their primary structure manufactured from CFRP [49]; see Figure 1.3. Yet, despite these advances, there are (and will continue to be) a significant proportion of metallic components used in aerospace structures. Complex multi-axis loadings are more suited to isotropic metallic components because CFRP is inherently weak through-thickness [67] and has a low fracture toughness; see Figure 1.2. In addition, CFRP is unsuited to high temperature applications due to the poor heat resistance of the resin matrix and low hardness makes CFRP inappropriate for bearing surfaces and many mechanisms. As a result, use of both metallic and composite elements within modern aerospace structures will ultimately require them to be joined. Again, the increased use of CFRP and associated challenges (such as joining) are not unique to the aerospace sector and are also common within the automotive, astronautic, maritime and leisure industries.

Traditionally, joining metal and CFRP components is achieved with bolting or riveting but these techniques are fundamentally flawed as drilling through high aspect ratio, reinforcing fibres reduces the load carrying capability of the material and creates stress concentrations. To minimise these disadvantageous effects, overlap areas are increased to accommodate larger bolt arrays and/or laminates are locally thickened to reduce bearing and net-section stresses. However, these conservative strategies result in additional weight.

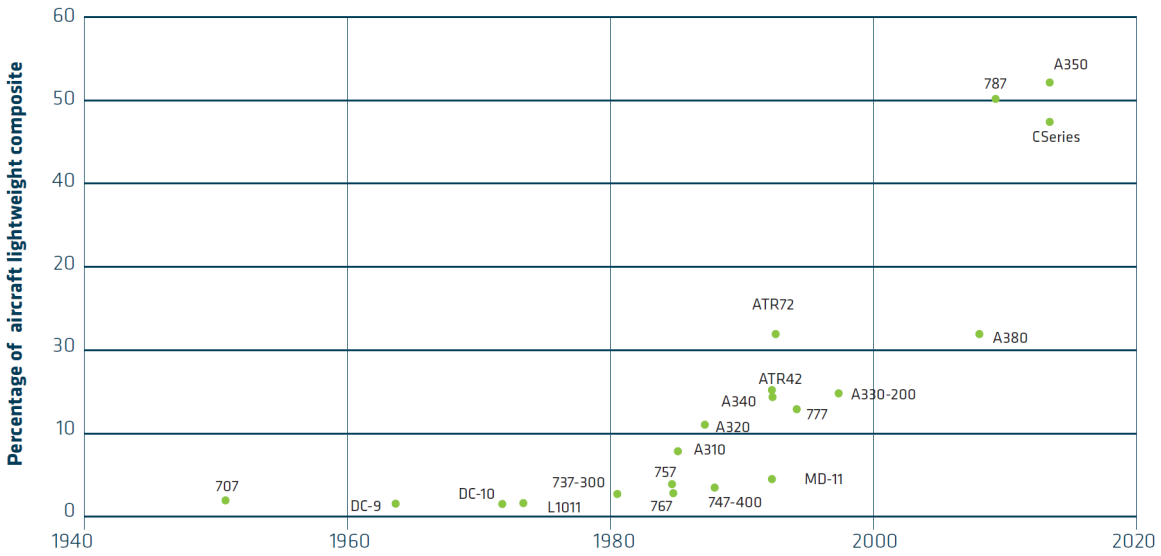

Figure 1.3: Increased use of fibre reinforced composite materials in civil aircraft from 1940 to the present day; adapted from [3].

Adhesive bonding presents a potential alternative, with negligible increase in weight, but careful surface preparation is required and, following the initiation of failure, joints typically have little residual strength and adherend separation can be catastrophic. This said, following several decades of research, mechanical fastening and adhesive bonding are well understood and design practices are mature [1, 42, 60, 67, 77]. Bonded-bolted approaches can offer some compromise between weight minimisation and increased structural redundancy [17, 43, 48]. However, a step change in joining technology is required in order to improve the integration of hybrid structural assemblies and maximise weight saving. One proposed solution to this challenge is the use of Hybrid Penetrative Reinforcement (HYPER).

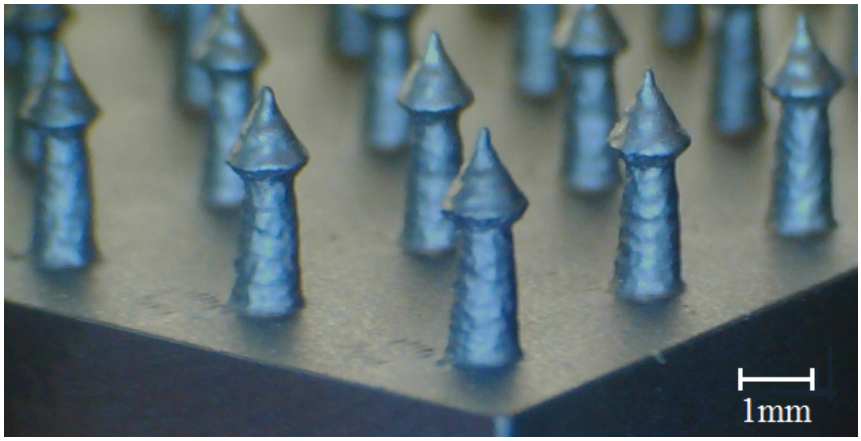

Figure 1.4: HYPER pin array on a titanium substrate.

Additive manufacturing (AM) enables arrays of small arrow-headed pins (approximately 1mm in diameter) to be built onto the surface of a metallic component; Figure 1.4. These are embedded into a composite laminate and the two pieces are co-bonded to form both a mechanical interlock *and* adhesive bond. By exploiting the latest manufacturing processes and the inherent properties of each material, it is hoped that HYPER can provide strong, efficient and damage tolerant joints.

At the beginning of the project, HYPER joining technology was at a fairly low state of maturity. The concept was first conceived by Airbus Group Innovations[†] circa 2007. Initial development work and manufacturing trials were conducted within the Airbus project "Integrated Wing" (2007-2009). During this time, a number of patents were filed to protect the company's intellectual property [61]. The HYPER programme subsequently became part of the HILOMECS (Highly Loaded Metallic Composite Structures) project (2009-2013) and more recently (2013-) the "ALFET" project which have been (partially) funded by the Clean Sky Technology Initiative [32] and the Technology Strategy Board (Innovate UK). The research herein was begun at the start of the 2010-2011 academic year in support of these broader Airbus Group development programmes. The manner in which the work packages were delegated is outlined in the project scope (overleaf).

[†]At the beginning of the research collaboration (with the University of Bath), Airbus Group was known as European Air Defense and Space (EADS) and "Innovations" known as "Innovation Works". Throughout this thesis, the industrial partner will be named as Airbus Group (Innovations) regardless of whether the context refers to a period before or after corporate re-branding.

1.2 Project Scope

Due to HYPER being at a low Technology Readiness Level (TRL), parts of the the development programme were, and remain, commercially sensitive. Prior to the research collaboration between Airbus Group and the University of Bath, except for the initial patents, no literature had been published in the public domain by Airbus Group. In addition, only a small volume of work had been written internally, notably by de Oliveira [27]. The primary focus had been the development of the manufacturing processes and undertaking pilot studies to investigate mechanical performance and sizing methods. Collaborators, at the University of Manchester, were focusing on the additive manufacturing processes from a materials perspective rather than mechanical performance in an applied context. Thus, the work herein can be segregated from that of other researchers as follows:

J. Meyer Research Team Leader at Airbus Group Innovations. Manages a diverse range of metallic technology and surface engineering projects. Completed early conceptual design/trials and filed patents for HYPER. Has overseen the development of HYPER technology and provided industrial supervision for academic partners; chairing quarterly reviews, etc.

R.J. Olukele Postgraduate Researcher at the University of Manchester; supervised by Professor P. Prangnell. Micro-structural analysis of HYPER pins produced by powder-bed additive manufacturing and percussion welding. Refinement of manufacturing parameters and assessment of mechanical and physical properties of *individual unembedded* pins. Investigations did not considered assembled HYPER joints and focused solely on the pins.

A. de Oliveira Former Research Engineer at Airbus Group Innovations. Conducted initial process development with Meyer et al. Completed preliminary mechanical testing of HYPER joints using, primarily, ARCAN coupons [10]. Thus, considered a range a load cases such as pull-off, combined tension-shear, etc. During the doctoral work of Parkes et al., was responsible for stress analysis methods with an emphasis on failure modelling using explicit finite element methods. Furthermore, assisted with the acquisition of materials and manufacture of test specimens for academic collaborators.

P.N. Parkes A multi-disciplinary investigation of *assembled* HYPER joints, with a focus on single lap shear coupons, rather than ARCAN specimens. Tasked with evaluation of inspection methodologies for HYPER joints that could be used both during manufacture for quality assurance and in-service for the detection of damage. Subsequently, utilised these methods to determine the influence of manufacturing defects and damage on the mechanical performance of HYPER joints. Thus, identify potential designs/configurations that could increase the mechanical performance of HYPER joints. In addition, conceive/develop new modelling capability/methods that will simulate the influence of potential defects in production parts.

1.3 Thesis Objectives

Given the scope for this specific part of the overal project, the following aims were identified for this doctoral thesis:

- Review existing literature, topics should include: comparable technologies, manufacturing processes, methods of non-destructive evaluation, experimental procedures/results and modelling techniques. This should include internal reports by Airbus Group as well as material in the public domain.
- Identify and categorise potential manufacturing defects and in-service damage that could be found in HYPER joints. This could be through investigation of the manufacturing methodology as this could also (subsequently) enable refinements to be made to the fabrication techniques. If possible, co-ordinate the manufacture of HYPER joint coupons at the University of Bath in order to the observe/undertake these processes first-hand.
- In parallel to characterisation of potential defects, evaluate methods of non-destructive testing (NDT) in order to determine effective means of HYPER joint inspection. Assessment should to be made based on ability to detect defects/damage as well as suitability for use in-service, if the technology was industrialised. This capability would allow Airbus Group to provide quality assurance on both the "shop floor" and in the field.
- Once work has been undertaken to identify suitable NDT methods, establish a test matrix for an experimental campaign to investigate the mechanical performance of HYPER joints and the influence of defects and damage. This could include different pin and/or array designs and metallic surface treatments. Some coupons could have seeded defects such as disbonds and fractured pins.
- Ideally, the experimental programme should include both quasi-static and fatigue testing. Identify performance factors such as compliance, limit load, ultimate strength, fatigue life and failure modes. The NDT techniques investigated in the preliminary stages of the project could be utilised.
- In addition to any experimental investigations, explore the influence of manufacturing defects and in-service damage on the mechanical performance of HYPER joints with numerical or analytical modelling. Adaptation of existing Airbus stress analysis and finite element methods could be considered for simulation of defects/damage. Alternatively, develop new capability/methods to account for manufacturing variability and damage.

1.4 Executive Summary

Following the introductory matter set out in this chapter, **Chapter 2** provides relevant background information and a review of associated literature. This covers traditional joining and reinforcement techniques as well as novel hybrid technologies (comparable to HYPER) under development by third parties. Additional information is provided on the advances in additive manufacturing, the different methodologies available and the challenges of using these techniques. The procedures used for the fabrication and integration of HYPER pins are subsequently detailed.

The first practical work is reported in **Chapter 3**. Non-destructive testing methods are evaluated for HYPER joint inspection. A bespoke ultrasonic technique was developed and, with the equipment available, inspection was found to be favorable through the metallic side of the joint. However, analytical modelling revealed that a smaller ultrasonic transducer may be able to improve evaluation through the CFRP substrate.

The influence of design variables such as pin geometry and surface treatments on performance were next investigated with mechanical tests. The compliance, limit load and ultimate strength were determined in **Chapter 4**. Non-destructive inspection techniques were used to monitor growth of damage and characterise failure modes. This was followed by assessment of fatigue life in **Chapter 5**. Points of damage initiation, rates of damage growth and failure mechanics were again identified. A previously unreported failure mode was observed in the high cycle regime. Mechanical performance of HYPER joints was found to be impressive yet it was believed that the joint design was still sub-optimal. Thus, in an effort to achieve higher strength and prolonged endurance, in the second part of this thesis, analysis of the pin geometry is presented.

Due to forcibly embedding the pins in to the laminate, it is possible to distort fibres in reinforced areas. Therefore, as a precursor to (the future) optimisation of the pin geometry, for increased mechanical performance, this manufacturing effect was investigated in **Chapter 6**. A detailed finite-element strategy was developed and this model was compared to a conventional modelling approach. It was found that a traditional model (homogenising individual plies and retaining the nominal volume fraction throughout) was unrepresentative as increasing the pin diameter induced a softening response. Conversely, the detailed model resulted in a stiffening response with increased pin diameter. Consequently, it was established that design rules for mechanically fastened joints would be invalid for HYPER joints. Without a refined modelling strategy, pin and laminate stresses would be incorrectly located/quantified and the compliance of HYPER joined structures would also be inaccurately simulated.

Finally, **Chapter 7** discusses the underlying challenges that remain within powder-bed additive manufacturing and the fabrication of HYPER joints. A case study is presented to highlight these points and future manufacturing strategies suggested. The conclusions from all of the preceding experimental and analytical work are also summarised. Design and operational recommendations are made and areas that require additional investigation identified.

1.5 Prizes

The American Society for Composites Award for Best Student Paper in Composite Materials at the 54th AIAA/ASME/ASCE/AHS/ASC Structures, Structural Dynamics and Materials Conference. Boston, Massachusetts, USA, 8-11th April 2013.

1.6 Publications and Presentations

P.N. Parkes, R. Butler, J. Meyer, A. de Oliveira, *Static Strength of Metal-Composite Joints with Penetrative Reinforcement*, Composite Structures, 118, pp.250-256, December 2014.

The following papers were all orally presented by the author.

P.N. Parkes, R. Butler, *Interaction Between Metallic Micro-Fasteners and Carbon-Fibre Composite Laminates*, 19th International Conference on Composite Materials. Montreal, Canada, 28th July - 2nd August 2013.

P.N. Parkes, R.Butler, D.P. Almond, *Fatigue of Metal-Composite Joints with Penetrative Reinforcement*, 54th AIAA/ASME/ASCE/AHS/ASC Structures, Structural Dynamics and Materials Conference. Boston, Massachusetts, USA, 8-11th April 2013.

P.N. Parkes, R. Butler, D.P. Almond, *Growth of Damage in Additively Manufactured Metal-Composite Joints*, 15th European Conference on Composite Materials. Venice, Italy, 24-28th June 2012.

In addition to the conferences papers above, the author has also presented at the following:

Oral Presentation, *Detailed Modelling of HYPER Joints*, Airbus Group Seminar on Additive Manufacturing. Filton, Bristol, 26th March 2014.

Oral Presentation, *Hybrid Joining Technologies for Aerospace Applications*, International Postgraduate Summer School on Aeronautics and Astronautics. Beihang University, Beijing, China, 10-17th July 2012.

Poster Presentation, *Mechanical Performance and Non-Destructive Evaluation of HYPER*, Airbus Group Technology Showcase. Filton, Bristol, 28-29th May 2012.

Poster Presentation, *The Impact of Additive Manufacturing*, Images of Research (Competition Finalist). The Octogan, Bath, 12-13th May 2012.

Oral Presentation, *Non-Destructive Inspection Techniques for HYPER Joining*, Airbus Group Seminar on Additive Layer Manufacturing. Filton, Bristol, 5th October 2011.

Chapter 2

Background

2.1 Joining and Reinforcement Techniques

A modern aircraft is an assembly of a huge number of individual structural elements and sub-assemblies. This is due to manufacturing limitations such as dimensional constraints, geometric requirements (form, shape) and functional necessity (mechanisms, reparability). This creates an fundamental need to join materials. This has traditionally been achieved using either mechanical fasteners (rivets or bolts) or adhesive bonding [60].

2.1.1 Conventional Methods

Mechanical fastening is a mature, established approach as fastener failure modes are well understood being (typically) metallic components and having been traditionally used on metallic structures. Bolts are favourable compared to rivets as clamping pressure can be both higher and more precisely controlled, leading to a stronger joint. Even if a nut loosens in service, considerable load carrying capacity is retained. They also offer the ability to disassemble the joint for inspection/repair and require minimal surface preparation, pre- and post-drilling. Mechanically fastened composite joints exhibit more complex behaviour. Whilst metals can yield locally to equalise loads and account for any misalignment of fit, composites are comparatively brittle and have very little capacity to redistribute loads. Typical load distributions are shown in Figure 2.1. This results in a parabolic stress distribution with high bearing stresses concentrated around the outer-most holes which will subsequently be prone to initiate failure [67]. This could be: a bearing failure (i.e. localised crushing of the laminate ahead of the bolt), net-section due to a high bypass load around the bolt (fracture perpendicular to the load) or shear-out (fracture parallel to the load).

Adhesive bonding can often be a better way to permanently join composite materials. A lighter joint is created without fasteners and there is also no requirement for drilling which can result in fewer stress concentrations and risk of damage during manufacture (machining of potentially high-value components). However, surface preparation is critical and adhesives are susceptible to hot and wet environmental conditions. Furthermore, regardless of adherend

material (metallic and/or composite), the adhesive will be subjected to a parabolic shear stress distribution that peaks at the edges of the overlap; a widely studied phenomenon since the seminal papers of Goland and Reissner [37] and, later, Hart-Smith [42]. Comprehensive reviews are provided by da Silva et al. [22, 23]. These stress concentrations, at the perimeter of the overlap, commonly lead to cracking of the adhesive and the onset of a disbond. Initiation and propagation of disbonding can be accelerated due to the weakness of bonded joints to peeling stresses, which also maximise at the overlap edges [1, 67, 80]. Pinto et al. [73] compared peel stress distributions for similar and dissimilar adherends; albeit with a ductile adhesive. Aerospace adhesives are typically expoxide based and comparatively brittle, with a tensile modulus (E) of around 3-5 GPa and failure strain (ϵ_f) of 3-5% [47]. Thus, assuming there is no redundancy (pins, stitches, etc.), failure is rapid and catastrophic.

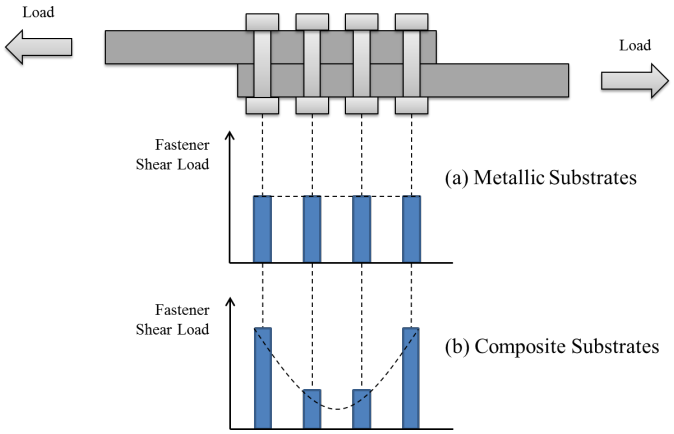

Figure 2.1: Generalised bolt shear load distributions for two single-lap joints, each with four bolts. (a) Two metallic substrates and (b) two CFRP substrates. Illustrative only, not to scale.

Bonded-bolted joints are a hybrid solution, combining an adhesive bond with mechanical fasteners to increase redundancy. Federal Aviation Authority (FAA) regulation states that there must be no adhesive cracking up to design load and that fasteners must provide the capacity to withstand ultimate design load alone in the event of complete disbond [46]. Bonding and bolting is, however, a structurally inefficient design when both load paths are intact as bolts offer little relief from peel stresses at the joint edges. Furthermore, in a typical bonded-bolted aerospace joint with an epoxide adhesive, 98-99% of the load is transferred through the adhesive [43, 48, 46]. It was shown by Paroissien that the bolt load share is inversely proportional to the square of the adhesive modulus [72]. The proportion of an applied load transmitted by bolts can be increased by up to 35% but only by using a very ductile adhesive such as a polyurethane type; $E = 0.6$ GPa and $\epsilon_f = 60\%$ [47]. It is proposed that HYPER joints are comparable to bonded-bolted joints given the combination of adhesive bond and metallic through-thickness reinforcement. Preliminary, finite element analysis by de Oliveira [27] has shown that, as expected in a composite joint, the pins adopt a parabolic load share with the outermost rows most highly loaded. However, although HYPER laminates are constructed using an epoxide resin (Hexcel M21 [44]), unlike a bonded-bolted joint, this modelling has shown that HYPER pins may share a larger proportion of applied loads. This would be a significant advantage as adhesive stresses at the adherend interface would be reduced and the

onset of adhesive cracking could be delayed. Furthermore, the rate of damage propagation could be reduced whilst the ultimate load and/or elongation to failure may be increased [17, 38, 48].

Z-pinning is another method for providing through-thickness reinforcement to CFRP laminates and retardation of damage growth [63]. Although composite laminates exhibit high in-plane strength, they are comparably weak through thickness which is why they are prone to delamination [54]. Fibrous Z-pins or thin metallic rods are created by extrusion and compiled into an array within a foam preform; which is used to retain a consistent orientation. They would typically have a high aspect ratio with a diameter on the sub-millimetre scale (0.28-0.5mm) and a pin density of 0.5-4.0% by area [74]. The pins are forced into the laminate, normal to the plies, using an ultrasonic horn. Although increasing Z-pin density will create a local reduction in laminate fibre volume fraction due to dilution, it is reported that 91-98% of in-plane tensile strength can be retained [54]. Insertion also creates resin rich pockets around the pins and in-plane wavines due to separation of fibres, yet, it has been shown that Z-pinning can provide a 6 to 25-fold increase in Mode I fracture toughness for a pin density of 1-2% [54]. As a result, pins can increase damage tolerance and it has been shown that delamination due to impact can be reduced [38]. However, the benefits (and failiure modes) are not only dependent on the pin density but also the pin diameter [16].

2.1.2 Novel Hybrid Concepts

Surfi-Sculpt is a patented surface treatment technology for metals developed by The Welding Institute, UK [80]. The process utilises electron beam melting to create textured surfaces or small features. A pool of molten material is created on the surface of a component and by translation of the beam parallel to the surface, the melt pool is then displaced forming a raised mound with an adjacent depression. Through repetition and orthogonal translation, the height of the material above the original surface can be increased to create structures such as ridges or pins. The difference between additive manufacturing techniques and Surfi-Sculpt is that AM is used to build features onto a base component using additional feedstock whereas Surfi-Sculpt creates features by the displacement of material from the original substrate. Novel metal-composite (Comeld) joints can be created with Sulfi-Sculpt by creating pin arrays on a metallic substrate; see Figure 4.1. This part is then embedded into a pre-impregnated carbon fibre laminate and then co-bonded to form a integrated part. This is conducted in a comparable manner to the manufacturing methods for HYPER joints (detailed in Section 2.3).

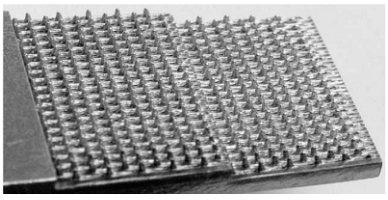

Figure 2.2: Comeld pins on a two-step double-lap joint [88]. It can be seen that the pin density is very high; they cover approximately 45% of the overlap area.

A weakness of the Surfi-Sculpt approach is that it is (believed to be) comparatively expensive and also incapable of creating a bulbous head on the Comeld pins. Firstly, HYPER is cheaper as the whole part *and* pins can be made with AM. Secondly, the head feature is a distinct advantage as it increases the resistance to a pull out failure [76] and, hence, joints would be much stronger if exposed to peeling forces (Mode I). As a result, it is unsurprising that literature published on Comeld reveals experimental results for joints in a double lap configuration [80]. These pins have a low aspect ratio and high density so the layer penetrated by the pins has a much higher (equivalent) modulus compared to other hybrid schemes. This influences the load transfer and changes the failure modes. The pin geometry is outlined in Table 2.1 and failure modes detailed in Chapter 4.

Cold Metal Transfer (CMT) has been developed by Fronius GmbH and the Vienna University of Technology, Austria. Essentially an arc-welding process, pre-fabricated metallic pins can be fused perpendicularly onto a metallic part [76, 82]. Computer numerically controlled (CNC) manufacturing equipment allows arrays of pins to be created with ease. Pre-fabrication of the pins also enables the use of different pin profiles. As with Comeld, published literature [90] shows experimental results, again, with a double-sided lap joint. The authors report that the layup and embedding processes are hindered by this configuration of joint and that there is significant eccentricity following co-curing. Again, an unpinned bonded lap joint is used as a control with the "pre-preg" resin acting as an adhesive. In addition, the reported CMT experimental work trials two different pin designs, a straight cylinder as well as a ball-headed design. Although not stated by the authors, it is envisaged that these pins are pressed from a wire feedstock using a simple die. These are shown in Figure 2.3, with the approximate dimensions detailed in Table 2.1 (alongside those of three other penetrative technologies). The mechanical performance of CMT is discussed further in Chapters 4 and 5.

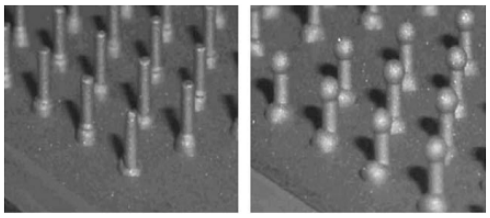

Figure 2.3: Two pin designs reportedly used for testing of the Cold Metal Transfer method [90].

Type	Diameter (mm)	Penetration	Pin Density	d/w
Z-pins	0.3-0.5	100%	1-6%	0.11-0.28
CMT (ball-head)	0.8-1.5	75%	8%	0.32
HYPER	0.9-1.8	72%	4-13%	0.23-0.41
Comeld	0.8	50%	≈45%	0.76

Table 2.1: Geometry of four penetrative reinforcement technologies. Pin density is the total pin area relative to the overlap size. The ratio d/w compares the average pin diameter (d) to the pitch/width (w) between pin centres; see Figure 2.4.

2.1.3 Geometric Comparison

Figure 2.4 shows the six dimensions chosen to fully define a "standard" HYPER pin; consisting of two frusta and a conical top. These variables will be stated throughout the project in an array, as given in Equation 2.1. The pin dimensions stated below form the Airbus baseline geometry. Additional factors such as pin pitch, or unit cell width (w), were considered array/joint level parameters so were specified separately; as these were application specific. However, the specimens, used herein, typically had a pitch of 4.233mm (i.e. six per inch) in both the X and Y axes (forming uniform squarely-spaced grids/arrays). The majority of the author's experimental work was conducted using single-lap specimens with a square overlap of 25.4×25.4mm and thus contained a total of 36 pins; see Figure 2.4.

$$[D_b, D_n, D_h, \theta_1, \theta_2, Z] = [1.20\text{mm}, 0.90\text{mm}, 1.50\text{mm}, 90.0^\circ, 60.0^\circ, 3.60\text{mm}] \tag{2.1}$$

It would have been possible to define a pin using additional heights (to key vertices) rather than angles but these two angles have more of a tangible influence on manufacturing and mechanical performance. For example, increasing θ_1 would increase the surface area of the central frustum and (it is believed) the resistance to a "pull out" failure. However, this would be likely to increase the stress concentration at the neck and induce fracture at this location. If θ_2 is decreased and the point becomes sharper, it is believed that the force required to insert a pin array into the CFRP would also be decreased. This may also have influenced the extent of fibre misalignment and resin redistribution during manufacture. Varying either of these two angles would also have changed the height of neck and length of the lower frustum which would have altered the axial stiffness of the pin. Unlike CMT, AM provides the capability to easily tailor the pin design for a given position within an array. This emphasises that selection of HYPER pin geometry was challenging as all the design variables were highly coupled.

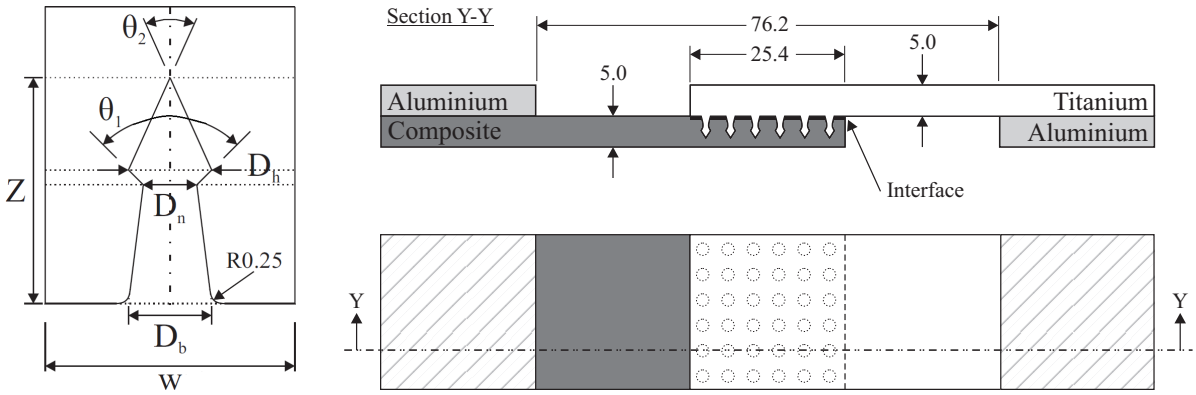

Figure 2.4: Definition of HYPER pin geometry using three diameters, two angles and the total height. Other variables required included pin pitch (or cell width, w), overlap area, adherend thickness, etc. Typical HYPER joint test coupon also shown (right).

Table 2.1 compares HYPER to three other "pinning" technologies although, given the variation in diameter with pin height described above, it only provides a generalised overview. Column three lists the percentage height/penetration of the pins compared to the thickness of the laminates used. The pin density is calculated as a percentage of the cumulative base area of all

pins compared to the total overlap area. The ratio of pin diameter to the pin pitch is defined as d/w as this is analogous to bolt diameter (d) compared to joint width (w). It can be seen that the geometry of the HYPER pins is similar to the CMT design.

It is unsurprising that the CMT and HYPER baseline designs had a d/w ratio of approximately one third as it was known that, in this region of the performance envelope, the greatest joint strength can be achieved for bolted/riveted joints; see Figure 2.5. Achieving a maximum on this design curve could result in an unpredictable failure mode though and it may vary from test to test or generate a combination of both modes. This may be undesirable as repair of the joint may be more difficult. Bolted or riveted joints with a diameter less than the "optimum" ratio of one third results in a bearing failure due to the high stress concentration induced. This is due to the reduction in pin surface area and increased contact pressure. If the edge distance (e) is not also maintained, such that the ratio e/w decreases, through-thickness shear would become worse and the chance of shear-out increased. As the diameter of the fastener is increased, the stress concentration factor reduces significantly and the substrate will fail due to net-section fracture. The net-section or membrane stress in the laminate/substrate will increase due to the reduction in cross sectional area by drilling of a larger hole and removing material to accommodate the bigger fastener.

If the number of fastener rows (in the direction of the load) is increased so does the load which bypasses individual fasteners. Therefore, with the load shared across additional fasteners, the load required to generate a bearing failure is increased; potentially even beyond that of a net-section failure and, thus, the former may not be seen at all. Whether these design rules holds true for novel joining schemes is explored later in this thesis (Chapter 6). It should be noted that the hybrid methodologies, outlined in this section, do not require pre-drilling and insertion of the pins displaces material rather than removing it. Again, additional detail on the specific manufacturing processes is provided in Section 2.3.

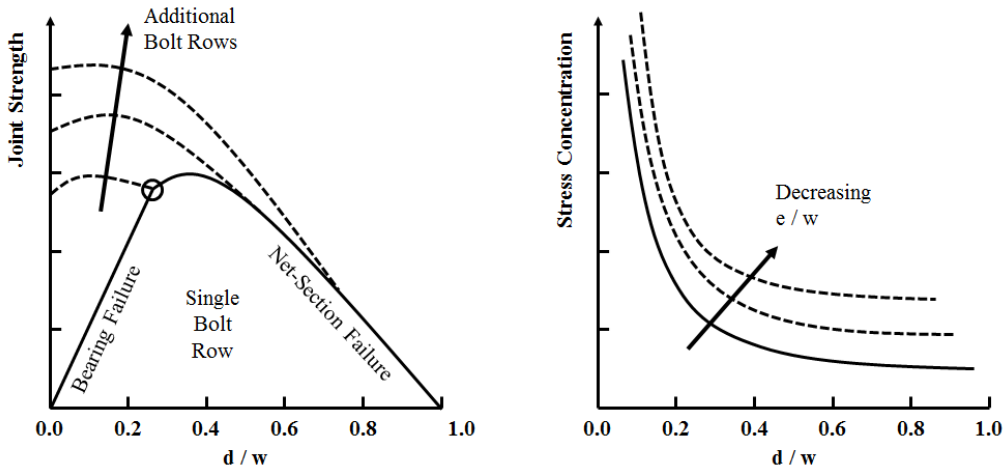

Figure 2.5: Influence of bolt diameter on failure mode and associated stress concentration factors. Increased fastener diameter and additional rows of fasteners can switch the failure mode resulting in net-section fracture of the substrate. Decreasing edge distance (e) exacerbates stress concentrations and can lead to shear-out failure. Both plots adapted from [62].

2.2 Additive Manufacturing

2.2.1 Technology Overview

Additive layer manufacturing or, simply, additive manufacturing (AM) is the enabling technology, fundamental, to the fabrication of HYPER joints. Unlike traditional machining processes, based on subtraction of waste material from a solid piece of feedstock, AM builds components progressively from "the ground up" in consecutive slices. In principle, this approach uses only the material required; analogous to a sculptor using clay rather than stone.

There are many advantages to additive manufacturing but, primarily, complex structures can be manufactured with comparative ease (giving engineers new design flexibility). For example, open-cellular reticulted meshes and stochastic foam-like structures with a low bulk density. These complex parts can be functionally-graded at both the micro- and macro-scale. These features/designs would be almost impossible to produce by conventional monolithic fabrication [65].

By not being constrained to design methodologies established for conventional manufacturing processes (e.g. tool paths, access for secondary operations, etc.) the available design space has been increased substantially. In combination with topology optimisation, AM solutions can offer vast weight reductions. Some cases studies have revealed that the mass of typical aircraft parts could be reduced by 50-60% [64]. A 100kg reduction in the gross weight of a single aircraft would save around US$300,000 in fuel per annum and many millions during its total service life [85]. This would also help to reduce the environmental impact of aviation, as described in Chapter 1.

AM is particularly advantageous for components manufactured from hard materials (such as nickel and cobalt-based superalloys) due to very high tool wear generated by mechanical cutting [33]. In addition, AM has the potential for significant reductions in production costs; from both a material usage and operational perspective. AM generates 85-90% less waste because (although swarf can be recycled) it is possible to reuse surplus AM feedstock with minimal or even no post-processing. It may also be possible to reduce the number of manufacturing operations on certain parts because features such as holes, threads and splines can be built additively. The process is, however, is not likely to be a replacement for current mass production manufacturing solutions. AM is (at present) most profitable for low volume production of complex, high value parts. These may not necessarily be "flying components" and fabrication of custom tooling is one area of the aerospace industry currently utilising the process.

In some regards, AM technologies are currently more suited to other sectors of engineering. For example, the integrated design and manufacturing capability of additive methods can allow medical patients to receive bespoke orthopaedic implants with high "biological compatibility" [65]. The motorsport industry is also exploiting AM for lightweight, high performance components such as intricate hydraulic manifolds.

However, the productivity of commercially available systems increased almost 50-fold in only 8 years and, if the status quo is maintained, productivity will continue to increase and both overhead and operating costs reduced. Scanning speed of commercial machines had increased from 1.5m/min in the "DTM 2000" in 1996 [55] to 72m/min in the "EOSINT M270" by 2004 [65, 78]. Further advances will subsequently lead to it being financially viable for alternative types of parts to be produced by AM *and* in greater quantities.

2.2.2 Additive Manufacturing Techniques

AM was firstly developed in the late 1980's and the earliest systems were used for production of polymer prototypes; mostly commonly by stereolithography. Resin feedstock is applied in liquid form and solidified by photo-polymerisation [52]. Continued process development now allows production quality *metallic* parts to be fabricated in a number of ways. For example, this can be achieved with the layer-wise deposition of solid feedstock (most commonly powder) that is subsequently melted or direct application of molten material; in a similar manner to stereolithography.

Fused metal deposition or wire-based additive manufacturing is analogous to tungsten inert gas (TIG) welding. Raw material (wire) is melted within a feed nozzle by a TIG torch or alternatively with a laser beam [12]. Layers are formed by the subsequent solidification of the feedstock. By mounting the feed head on a multi-axis robot, complex sections and profiles can be built. Stress alleviation methods, such as inter-pass rolling, allow large near net-shape components with almost homogeneous and isotropic micro-structure to be fabricated with this method [18].

The use of wire as a raw material is advantageous compared to powdered feedstock because of a lower surface to weight ratio, thus, there is less risk of contamination. Fabrication of wire is also a mature process and cheaper than the manufacture of powders which are usually produced by gas or plasma atomisation. Processes that can introduce gas porosity to the particles which can also vary in size/sphericity. However, if any porosity is remaining in the finished part, this can be almost entirely removed with hot iso-static pressing (HIP). Controlled storage of powders is also paramount to prevent moisture absorption and because of the risk of explosion. The quasi-spherical powder may vary from 5-60 μm in diameter, with a nominal size of around 30-40 μm [65, 86]. In general, wire-based AM is preferential for larger and more simplistic geometries such as prismatic or shell-like structures (due to higher deposition rates compared to powder systems). Thus, given that a primary strength of AM is the fabrication of geometrically complex parts rather than speed of manufacture, it is unsurprising that there is significant use of powder based systems.

There are two primary methods of powder deposition: (1) Selective injection of powder onto a locally melted substrate, known as laser cladding. (2) Selective sintering/melting of a bed of powder that has been spread across the entire substrate, using a laser or electron beam. The latter is the more common method and the sole method used within this work; see Figure 2.6.

Translation of the heat source in the xy-plane and continued fusing/melting of the raw feedstock creates an individual layer. Solidification of the molten material is rapid due to its high thermal conductivity. The build platform/substrate is then lowered in the z-axis by the thickness of the layer; typically 30-60 μm. Additional powder is spread across the work bed by a deposition system/re-coater arm and the process is repeated until the full height of the part is built.

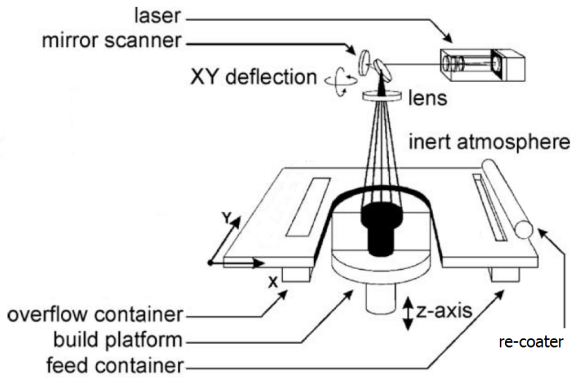

Figure 2.6: Configuration of powder bed additive manufacturing system, adapted from [86].

There is still some ambiguity regarding the classification of even the most common additive processes using powdered feedstock. In part, this is due to developers wanting to differentiate their products/processes from competitors but, in practice, there are often few differences between them. Even with the increasing maturity of metallic AM technologies, it is believed that there is still a lack of consensus in the literature. Shellabear and Nyrhilä [78] sought to clarify some these uncertainties, from a commercial perspective. Despite sintering generally being considered the fusing of powders *below* their melting temperature, sintering and melting are often used interchangeably. It is proposed that these discrepancies may have arisen due to the nature of metallic AM development. Prior to the realisation of a one stage "direct metal laser sintering" method (DMLS), it was common to mix the primary (metallic) powder with a polymer binder and use a two step process. After selective melting of the binder, the component was removed and heated in an oven to purge the binder and sinter the metal; comparable to investment casting. Alternatively, the binder can be purged by the infiltration of a second metal to create a metal matrix composite. These superannuated methods are documented in the older reviews of Kruth et al. [52] and Levy et al. [55].

More recently (2012), Murr et al. [65] reported a comparison of "laser and electron beam melting technologies" yet used an EOSINT M270 which the manufacturer describes as a sintering machine [78]. It is proposed that this results from the EOSINT and other similar machines not being material specific and parameters, such as intensity of the heat source, are controlled by the end user. Thus, sintering and melting could potentially both be undertaken within a single build. Local part temperatures and the size of the heat affected zone are also geometry specific and dependent on the build strategy. All these factors influence the micro-structure of the material and, because the process parameters are highly coupled, maintaining consistent build conditions can be problematic.

2.2.3 Challenges of Additive Manufacturing

Although early HYPER joint trials were conducted with stainless steel (17-4), throughout this body of work, all HYPER pins were manufactured from titanium. Titanium is a widely used aerospace material as it offers a good compromise between specific strength and fracture toughness; as shown in Figure 1.2. It can be used at elevated operating temperatures (around 600°C) and also has excellent corrosion resistance [29]. One of the most commonly used alloys is Ti-6Al-4V which comprises of 6% aluminium and 4% vanadium (by weight). Ti-6Al-4V is an alloy with a mixed α-β structure, where the α phase has hexagonal close packed atoms and the β phase has a body-centered cubic arrangement. The inclusion of aluminium acts as an α stabiliser and the vanadium as a β stabiliser. The latter promotes β formation at lower temperatures, as shown in Figure 2.7.

Alpha or near-alpha alloys are the most weldable and offer the best corrosion resistance. Beta or near-beta alloys are "intrinsically" stronger and provide an increase in formability. Alpha-beta alloys can generate the most advantageous combination of strength and ductility. Mixed structure alloys can also be effectively heat treated (unlike alpha dominant materials), providing capability for manipulation of the grain configuration [29]. Although the melting point is alloy dependent, it would typically be in excess of 1660°C. In an idealised case, a component would be furnace cooled and material would be gradually reduced in temperature at a very low rate. As the material solidifies, a plate-like β structure is formed. Once the β-transus temperature is reached (995°C for Ti-6Al-4V, 12% higher than pure titanium [65]), the beta phase begins to precipitate an acicular alpha phase. Continued cooling promotes growth of the α phase in parallel sets, forming a classical Widmanstätten structure.

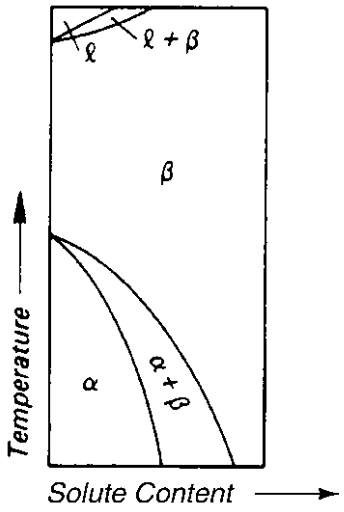

Figure 2.7: Generalised pseudo-phase diagram for a non-eutectoid (isomorpheus) β-stabilised titanium alloy. Increased temperature, decomposes the primary α phase creating a mixed α+β structure. Further heating creates a pure β phase and then a mixed liquid-solid state (ℓ+β) before the material becomes fully molten (ℓ). Increased solute content (e.g. vanadium) promotes β phase content at reduced temperatures. Adapted from [29].

However, AM processes generally present a significantly different thermal history. Irradiation is intense and the base plate of the machine acts as a large heat sink so thermal gradients can be extremely high; in in excess of 1000°C/mm [50, 65]. The primary factors controlling the micro-structure evolution of the material during AM are the intensity and duration of irradiation as these influence cooling rate of the material [50].

Hence, additively manufactured parts tend to have an inhomogeneous, segregated micro-structure because of the high thermal gradients induced and repeated melting/solidification of material. These characteristics are challenging to control because there is a high degree of coupling between individual process parameters; e.g. scan speed, scan pattern, laser power, etc. This can result in local variability in strength, stiffness, dimensional accuracy and surface finish. Different parameters are also required for different part geometries.

If solidification is very fast it is comparable to quenching and this can result in decomposition of the β phase into an almost entirely martensitic (α') phase. Heat dissipation can vary with position in the build chamber due to relative proximity to other (potentially dissimilar) parts. Conductivity is also influenced by the inclusion of any sacrificial supporting material (see Section 2.3). All these factors must be considered in order to avoid variation in mechanical properties between parts/builds.

Murr et al. have shown that cooling rate, and thus micro-structure, is also very dependent on technique used [65]. The DMLS process maintains the substrate at a temperature of around 90°C whereas the electron beam melting (EBM) process preheats the substrate to approximately 80% of the melting temperature. This leads to more rapid cooling in DMLS and martensitic alpha prime compared to a preferencial, mixed α-β structure with EBM. It is, however, possible to alleviate some of these undesirable characteristics in DMLS parts with heat treatment in order to reform some of the β grains [29].

2.3 HYPER Joint Construction

2.3.1 Fabrication of Metallic Substrate

The earliest coupon trials were manufactured from 17-4 stainless steel [27]. Initially, both metallic substrate and HYPER pin array were manufactured as a single part which was both costly and time consuming. Process development has subsequently allowed titanium pins (Ti-6Al-4V) to be built directly onto a piece of stock material or the surface of an existing component (as a retro-fit), as long as the build surface was flat. For the purposes of coupon-type laboratory tests, by only building the pins additively, the volume of material built by AM was vastly decreased and, subsequently, process cost was reduced and throughput increased.

Ultimately, if this approach was used for future applications, fabrication of HYPER pins would still induce an additional manufacturing operation which would make the technology less desirable as an alternative solution to bolting. The long-term strategy would be for parts to be re-designed to take full advantage of the capabilities of additive manufacturing and build both the part and the HYPER pins in a single operation. Not only could this then achieve a competitive cost and time compared to a bolted joint but a more significant weight saving as well if combined with topology optimisation [64].

Airbus Group Innovations used an Electro Optical Systems (EOS) EOSINT M270 direct metal laser sintering machine for fabrication of HYPER joints. The build volume of this machine was 250×250×215 mm [30] which, allowed pin arrays be built on up to fourteen standard single lap shear (SLS) specimens (100×25×5 mm) or 45 ARCAN coupons (25×25×100 mm) simultaneously [10].

The stock pieces of titanium would be secured onto either a universal baseplate (SLS) or custom fixture (ARCAN); as shown in Figure 2.8. The assembly was then placed into the build chamber and bolted to the bed of the machine. The re-coater arm was then moved over the substrates and a dial gauge attached. This was moved back and forth to ensure that the specimens/baseplate were flat and, if not, leveled accordingly. This was achieved using the integrated actuation system of the EOS machine. This step was crucial to ensure that an even layer of powder would be deposited across all specimens (30 μm per layer).

Choice of re-coater blades was another key factor for HYPER specimens, given their size. A rubber blade, although more compliant to variations in the surface heights of the substrates, would tend to flex and could "flick" powder away creating regions lacking adequate powder. Insertion of a rubber re-coater blade into the fixture on the re-coater arm could also created an uneven tension which would exacerbate an inconsistent distribution of powder across the bed of the machine. A high speed steel (HSS) blade was less forgiving to any unevenness in a substrate or created during previous layers (due to thermal distortion) and it was not uncommon for parts to be broken off the base plate by a HSS blade. A stiff blade did, however, create a far more level layer of powder providing the substrates were sufficiently flat.

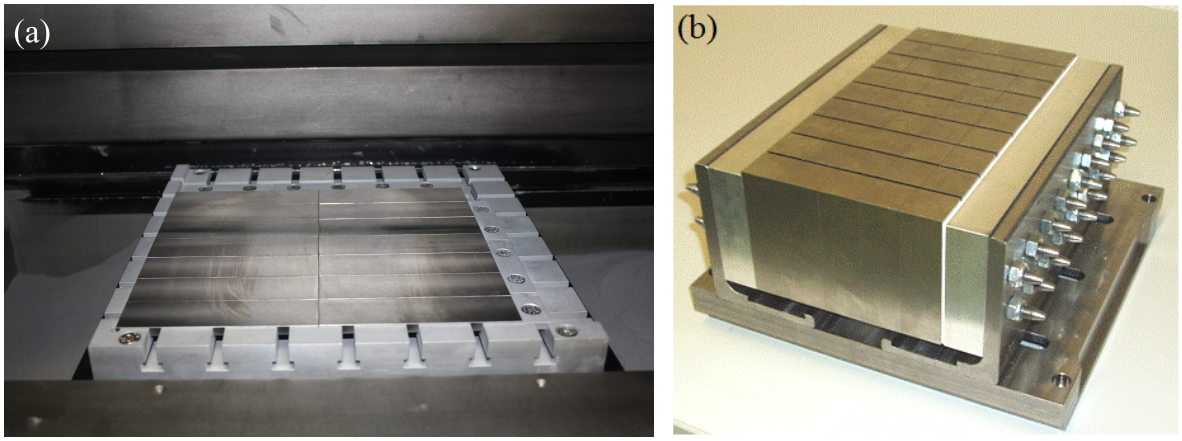

Figure 2.8: (a) Build chamber of EOSINT M270 with 14 substrates secured to a universal baseplate. (b) A custom fixture was used for ARCAN specimens; 45 could be built simultaneously.

Once the powder was sieved into the machine, agitated to remove any air pockets and the substrates loaded and leveled, the electronic data needed for the build could be uploaded to the machine. This was prepared away from the manufacturing facility and transfered using physical storage device. The first stage in the creation of these files was to generate a model of the part using a CAD package and export it in the STL file format. This task was completed using the Dassault Systèmes program, CATIA (Version 5, Build 21). The STL file was then imported into software specifically for additive manufacturing for additional processing; Magics by Materialise (Version 18). This program allowed relative positioning of multiple parts within a single "scene", that formed a digital representation of the build chamber.

This allows parts to be nested/tessellated, where possible, to maximise machine usage and reduce the cost of individual components. The relative positioning and orientation of parts on the build plate is an important factor that as it can influence the success of the build. Ideally, parts should not be situated in a row parallel to the direction traveled by the re-coater to ensure even powder coverage; right to left, as per the orientation shown in Figure 2.6. This is due to shrinkage of the part normal to the layer (z-axis) and additional powder retention in these depressions. One strategy to alleviate these coverage effects is to increase the powder "dosing". For example, additional powder (20% or more) could be dispensed and re-coated to ensure that there is a consistent layer thickness over the full width of the build plate. This conservative approach is, however, less efficient due to the increased volume of material transfered to the overflow hopper.

In addition to positioning of individual parts within Magics, a second key task of this software is the inclusion of supporting material. Although this was not a requirement for pins built directly onto a flat substrate, were pins to be integrated into a fully additively manufactured component, supports would almost certainly be required.

Typically, an AM part would be built directly onto the baseplate. In this case, additional material would be included on the bottom of the final design to allow it to be cut from the base plate without damage to the part. The plate would subsequently be machined back in a secondary operation so that it could be re-used. In addition to supporting the first layer of the part, any down facing surfaces that were orientated at an angle of 45 degrees or less (relative to the build plate) may not be self-supporting and collapse without a temporary sacrificial structure. Hence, there is often an optimal orientation for the part in order to minimise the amount of supporting material required. Airbus Group is currently developing guidelines and automated design tools to assist with this process but, at present, the orientation of the part, location of supports and, ultimately, the success of the build is largely down to experience. Additive manufacturing can be perceived to be a shortcut to achieving a physical, near-net shape part from a digital model with negligible lead time and minimal user intervention. This is not necessarily the case and (currently) dependent on the individual part and the experience of the engineer.

With any necessary modifications made to the digital part(s), the model was exported as a "slice" file (*.sli) which was the native form required by the EOSINT machines. This could be achieved directly within Magics or, alternatively, in SliView; part of EOS' RP-Tools (Version 5.06). This process essentially discretised the part and associated supports into individual layers of a specified thickness (typically 30 μm, normal to the build direction). It was from these planar sections that the manufacturing machine would calculate the paths required by the laser to realise the build.

With the electronic data uploaded, the build chamber was purged with argon to inert the atmosphere. The EOSINT M270 was not specifically designed for additively manufacturing new parts onto existing components. Hence, accurate in-plane positioning of pins on the substrates was not straightforward. With the chamber purged, a single layer had to be exposed (irritated without powder) on to one of the substrates in order to create a reference and check the position of the array relative to the edges of the substrate; see Figure 2.9. Once any necessary translations adjustments were made to the baseplate, a single layer was exposed onto another substrate and the alignment rechecked.

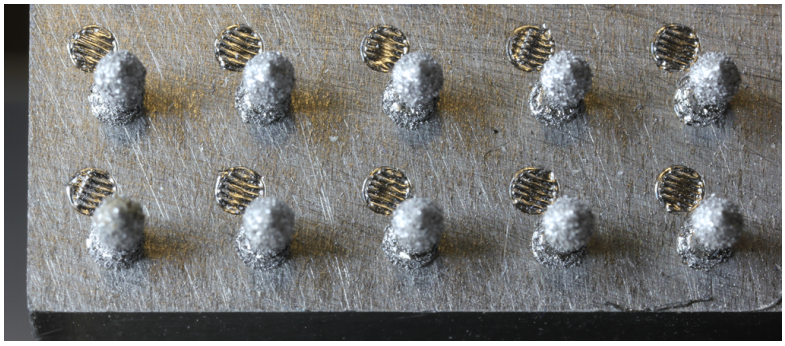

Figure 2.9: Alignment of substrates within the build chamber can require an initial layer to be irradiated in order to create a reference. The contour and the hatched infill path of the laser in the primary layer are also visible in this plan view.

The remainder of the build could then be started. Going forward, it was hoped that a bespoke metrology system or alternative build strategy could be used to exclude this manual intervention. This was partially realised during the course of the project and an alternative methodologies are discussed in Chapter 7.

With the lateral position of the baseplate corrected. The full build could now be started. Building fourteen coupons, each with 36 baseline pins (3.6 mm tall), took approximately two hours. Once the build was complete, the excess powder around the parts was recovered with a vacuum system and the baseplate removed from the build chamber. The specimens were then grit-blasted to remove any loose powder and partially sintered particles from the outer surfaces of the pins. Each pin array (25 mm square) would require a duration of approximately two minutes. A Guyson Euroblast 2 suction fed cabinet was used with a cyclonic media separator. The blast media was Guyson Honite Grade 13 (soda-lime glass beads, 0.1-0.2 mm particles, Mohs Hardness 5). This made a significant difference to the visual appearance of the pins, as can be seen in Figure 2.10. Any blast media remaining on the parts was removed with compressed air. The last step in the preparation of the metallic part, prior to integration, was for the bonding surfaces to be cleaned and de-greased with acetone.

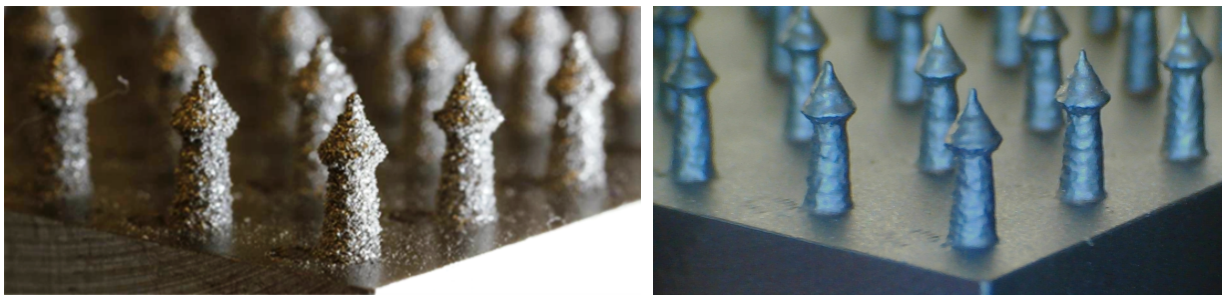

Figure 2.10: Surface finish of pins; as-made and after grit-blasting (left and right respectively). It can be seen that this process removes any partially sintered powder remaining on the surface of the pins.

2.3.2 Integration with Composite Substrate

Once the metallic half of the joint had been fabricated, the composite substrate could be prepared. The laminates were produced from sheets of uni-directional carbon fibre, pre-impregnated with an epoxy matrix. All the manufacturing trials and mechanical tests reported herein used Hexcel M21-268-T800S [44] with the following stacking sequence: $[\pm 45/0/90/\pm 45/0/90/\pm 45]_S$. This 20-ply layup, dominated by 45 degree plies (60%), exhibits high strength under shear and bearing loads. It is a common stacking sequence that abides by standard design rules and would be found in many aerospace components. This layup was used throughout as variation of the stacking sequence was beyond the scope of the project. Furthermore, it would be unlikely that the stacking sequence would be a free variable at the time that a HYPER jointed fixture would be sized. For example, potential aerospace applications, such as wing covers, spars and ribs, would be constrained at a comparably early stage in an aircraft design programme based on global loadings such as fuselage size, engine masses and aerodynamic pressures.

At the time of writing, only coupon-sized specimens had ever been fabricated. However, even for these small parts, a large CFRP panel would be laid-up so that multiple HYPER joints could be integrated concurrently using a single tool (described below). This panel was assembled and cold de-bulked in a conventional manner [20]. With the entire thickness of the laminate assembled onto a PTFE covered tool plate, a layer of peel ply and release film were applied to the upper surface. Both these pieces of material had a square cutout for each coupon, approximately 5mm larger than the dimensions of the overlap. An examples is shown in Figure 2.11. The peel ply provides a good surface finish for the secondary bonding of "tabs"; these spacers were required for mechanical testing (see Chapter 4). The release film prevents the tooling from adhering to the CFRP panel. The cutouts ensure that the release film does not interfere with the co-bond between CFRP and titanium substrates. The two halves of the joint could now be integrated. Two insertion techniques had been trialled prior to the project; the original method was developed as an out-of-autoclave process (for SLS coupons) but a second, more "automated", method was also successfully trialled (for ARCAN coupons).

The original technique was commenced by heating the the upper surface of the laminate with a hot air gun to around 60-80°C to reduce the viscosity of the resin [31]. The metallic part was then manually pressed into the laminate using an ultrasonic horn as per the insertion of Z-pins. Embedding the pins with ultrasound provided mechanical stimulation as well as some additional heating and allowed the pins to penetrate the fibres more easily. Insertion of the pins in this manner did induce some localised fibre distortion. Consequently, during the cure cycle, it was also possible for rich rich zones to form around the pins. Furthermore, by embedding by hand, the metallic part could "see-saw" into the laminate rather than inserting which may have increased the extent of fibre misalignment and magnitude of any resin rich zones. These manufacturing characteristics are explored in more detail in the following chapters. Going forward, development of better tooling (for the SLS coupons as well as the ARCAN coupons) would ensure that metallic substrates are always pressed into the laminate perpendicularly and with a consistent pressure.

With the metallic substrates inserted into the laminate, a rubber tool was placed over them with each tool covering multiple coupons, shown in Figure 2.11. Without this part, the vacuum bag would form a fillet radius around the metallic substrate and there would be regions of reduced consolidation pressure on the CFRP. Consequently, localised wrinkles would form through the thickness of the laminate, see Figure 2.13. A second layer of release film was placed over the tooling, followed by a breather layer and then a vacuum bag. The entire bagging sequence is shown in Figure 2.14. It was found that it was very difficult to remove the breather from the tooling without this additional layer of release film. The assembly was now ready to be baked within an autoclave.

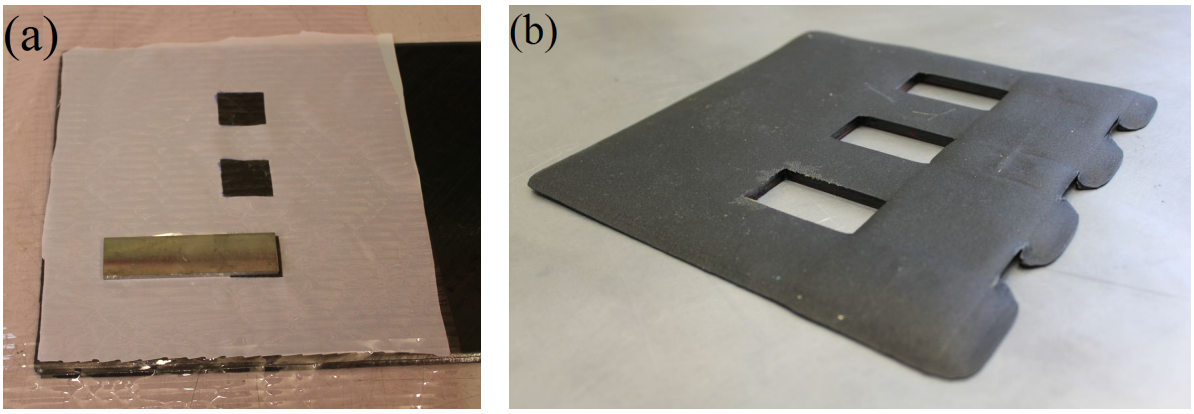

Figure 2.11: (a) Single SLS substrate embedded into the composite laminate through holes in peel ply and release film. (b) Rubber tooling for three SLS substrates.

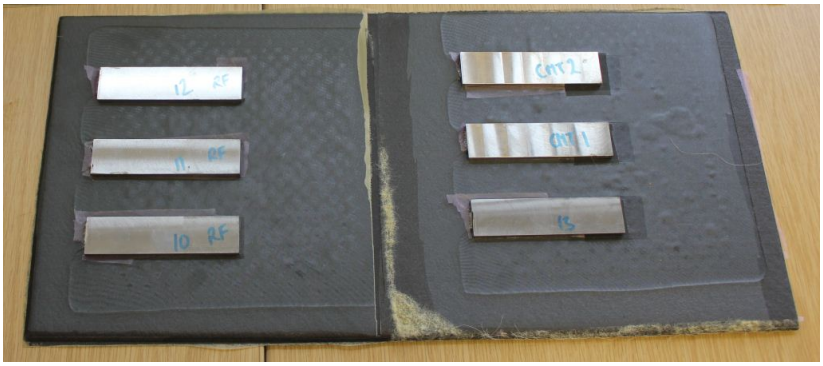

Figure 2.12: An integrated and cured panel prior to machining.

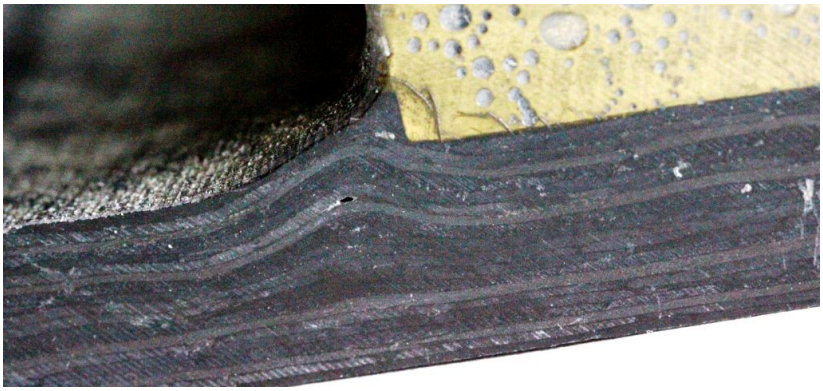

Figure 2.13: Wrinkle formation at edge of metallic substrate without tooling.

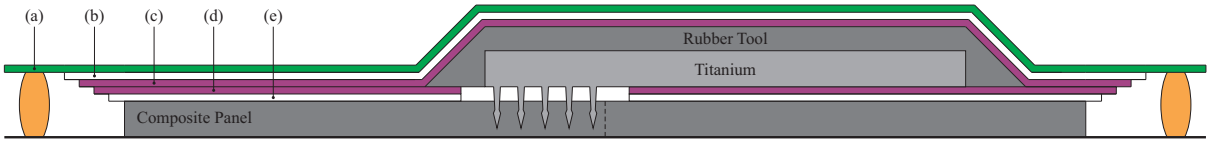

Figure 2.14: Complete tooling assembly within vacuum bag. (a) Vacuum bag adhered to tool surface. (b) Breather layer. (c) Release film over tooling. (d) Release film under tooling and titanium, with cutout. (e) Peel-ply with cutout. Composite panel to right of dashed line cut away after cure. Not to scale.

Initially, the ARCAN specimens were also manufactured with a rubber tool; using the SLS methodology previously described. However, due to the aspect ratio of the metallic part, the rubber tools trialled did not offer enough support to retain adequate perpendicularity with the CFRP. Hence, at the time, it was more pressing to develop an alternative method for these coupons rather than for the SLS coupons.

Due to the requirement for greater angular accuracy during insertion/cure a stiffer tool was required so an aluminium part was manufactured. A split tool was needed because of the square cross-section of the ARCAN configuration; see Figure 2.15. With this fixture placed onto the laminate and aligned rotationally (about the laminate normal) the metallic substrate was coated with release agent (Henkel Frekote) and placed inside. It was observed that rather than applying the insertion force manually, with the addition of a cap over the substrate, it would be possible to use the vacuum bag to integrate the two parts within the autoclave during the cure. This combination would also accurately control the depth to which the metallic part/pins were inserted into the composite. Going forward, this technique could be a more accurate, less user-intensive technique which would allow insertion of a large number of independent HYPER joined fixtures on a large composite component. Thus, the vacuum bag was laid over the metallic parts and this assembly was now also ready to be placed into the autoclave.

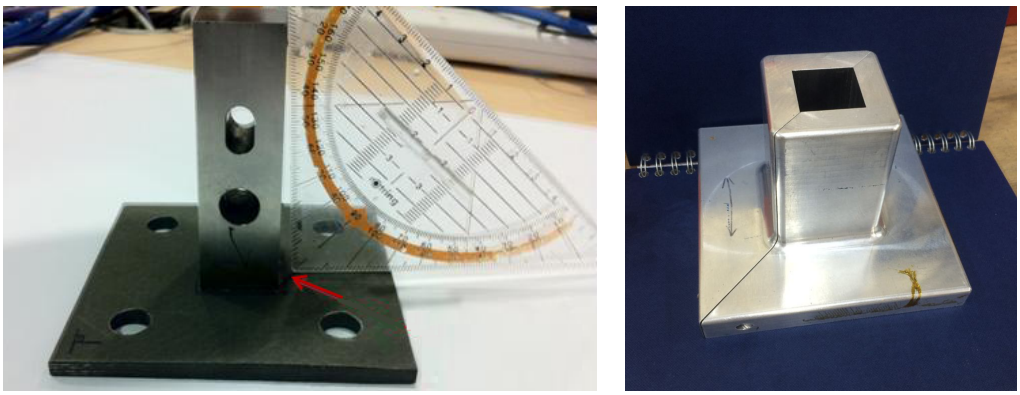

Figure 2.15: Distortion in ARCAN specimen fabricated using rubber tooling and a second generation, split metallic tool for in-autoclave insertion of ARCAN substrates (left and right respectively).

Regardless of the tooling methodology, the manufacturing process was identical from this point forward. The vacuum bag was sealed to the tool plate with double sided tape and two vacuum ports were inserted. A vacuum test was conducted and the specimens were placed inside the autoclave. The cure cycle ramped to 180°C and 7 bar pressure at a rate of 1-3°C/minute and was then held for 120 minutes. Upon completion of this dwell period, the autoclave was then cooled at 2-5°C/minute. Once at room temperature, the specimens were removed and separated from the vacuum bag/tooling. The coupons were now cut from the CFRP panel. This was initially completed by milling however results were poor and this method was found to induce delaminations. Water jet cutting was found to be more effective as the surface finish of the cut edges was far superior and less damage was observed at the joint interface (between substrates, see Chapter 3).

Chapter 3

Non-Destructive Inspection

3.1 Overview of Research

The design and manufacture of HYPER joints makes them inherently challenging to inspect. The pins are small, conically headed and have an uneven surface due to additive manufacturing. Furthermore, they only penetrate partway through the CFRP laminate; which is also thick and opaque. In order to increase the maturity of HYPER joint technology, a methodology for HYPER joint inspection was required for quality assurance following manufacture (identification of defects) and in-service for the detection of damage. This would also help future mechanical testing programmes (Chapters 4 and 5). It was anticipated that manufacturing HYPER joints may induce fibre misalignment (waviness/wrinkling), resin rich zones and potentially voiding/porosity within the AM metallic part/pins. The goal of this chapter was to identify if/when these defects were generated and how they could be detected. No work had been completed by Airbus Group in this area. Following a review of the literature and assessment of available equipment, three inspection methods were selected for further investigation: thermography, radiography and ultrasound. Each of these techniques were evaluated for application to HYPER joints, through either numerical modelling, experimentation or a combination of both. These preliminary trials found that thermography lacked adequate resolution, given the relative size of the pins/overlap and the magnitude of defects that needed to be observed. This was despite the implementation of a novel inspection strategy. Radiography and ultrasound were the most effective but this research has shown that each would have application specific limitations/restrictions if implemented in an industrial context. For example, it was found that specimens needed to be inspected through the metallic substrate (rather than the carbon side) to generate the best results with ultrasound. Delaminations at the interface and internal pin damage could be observed in this way. X-ray computerised tomography could generate excellent visual results (fibre misalignment, porosity and damage) but not without precise inspection conditions and extensive post-processing of the data. Both these stages would incur a significant time penalty and labour cost to the business; in addition to vastly greater capital expenditure. To emphasise the relative capabilities of these two methods, a pair of case studies were also completed and these validated the initial findings.

3.2 Context

Apart from using visual inspection methods (sectioning, optical microscopy, etc.), none of the other comparable technologies, found in the literature, have specifically reported NDT research as being part of their development programmes [68, 82, 76, 87, 90]. For example, Graham et al. [38] used transparent glass fibre substrates for their test joints so damage growth could be observed through the laminate without destructive inspection. In this work, opaque CFRP laminates were used so an alternative method of inspection was required. It was believed that this type of composite laminate would be more representative of future applications. Given that there was little specific guidance written by other authors, inspection methods for standalone metallic and composite applications are described below. Methods of non-destructive testing and evaluation for composite materials were developed from established techniques used for inspection of metallic parts. Within the latter, there were five well established methods used for assessment of components: ultrasound, radiography, eddy current testing, magnetic particle inspection and visual examination [15].

Visual inspection techniques are aided with optical lenses and dye penetrants. It has been found that although dyes are a good method of detecting surface breaking cracks in composites, due to the inherent structure of laminated composites, it is more typical for damage to occur in-plane [15]. Furthermore, removal of all dye from a crack is troublesome and hence hampers in service repair of the damaged area. Thus, it is more suited to aid crack detection in laboratory experiments [46] rather than used in-service where a repair would be required. Eddy current testing has been found to only have limited use for inspection of composite materials. An alternating current is applied to a test coil and it is moved over the specimen. Eddy currents are induced in the surface of the coupon which, in turn, modify the field in the test coil. The magnitude of these fluctuations is measured and provides an insight into variations in the coupon surface but interpretation can be difficult [40]. Although the location, and *potentially* the magnitude, of the defect may be known, it would be almost impossible to correlate these fluctuations with the exact nature of the damage unless only (very) limited number of defect types could occur. This would not be the case for a complex, multi-material joint such as HYPER. Magnetic particle inspection (MPI) is only usable for ferrous metallic components. MPI uses a coil to magnetise a ferrous specimen prior to the distribution of magnetic particles onto the inspection surface. Any near surface or surface-breaking cracks would distort the magnetic field and the resultant flux leakage would attract the particles; the location of the defect could then be visually detected. Although, early HYPER joint trials were manufactured from steel [8], titanium is the only material used within this work and thus, this method would not be suitable.

Hence, of the five listed above, only radiography and ultrasound have found to be particularly applicable for fibre reinforced composites [41]. However, there are also some other less widely used techniques that are of practical use for inspection of certain CFRP applications; most notably, thermography. Assessment of these three techniques will be made in this chapter. They will be evaluated with respect to their effectiveness for detecting defects/damage in HYPER joints and their suitability for industrial implementation.

3.3 Radiography

Radiography was evaluated prior to the other techniques as it was believed that this method would yield the highest resolution. If this was found to be the case, the results could then serve as a benchmark for comparison with the other methods that were subsequently assessed; thermography in Section 3.4 and ultrasonic inspection in Section 3.5.

3.3.1 Background

Electromagnetic radiation is emitted by naturally occurring sources but can also be artificially produced. X-rays are a band of electromagnetic radiation with a wavelength of 0.1 to 10 nanometres. They can be produced from a metal anode (typically tungsten) when bombarded by beam of electrons from an electrified filament (cathode). Longer wavelengths (soft X-rays) will only penetrate short distances in soft materials whereas the shorter, higher energy waves (hard X-rays) can penetrate up to 500mm of steel. The electron beam can be focused and accelerated to increase the energy of the emitted X-ray beam. Variation in material absorption can be used for the purpose of non-destructive inspection by placing a specimen between an X-ray source and a recording media. Conventionally, a picture would have been created on a photographic type film but film-less detection using an electronic array allows the incoming signal to be digitised for manipulation on a computer. Changes in material characteristics affect the absorption of the beam. For example, thinner or voided regions would have a lower absorption of the incident beam so the resulting image would be more intense. With respect to CFRP, in-plane damage such as a delamination, which if normal to the beam, given it would have negligible thickness, would cause almost no difference to the absorption level and would be challenging to detect on a conventional radiographic image.

Computerised Tomography (CT) was developed in the early 1980's for medical use but quickly adapted for industrial applications. By rotating a source and detector array on a common frame, around a patient, a series of cross-sectional images can be taken. Alternatively, a specimen can be rotated and the source/detector fixed, as is the case for industrial inspection systems. This configuration is shown in Figure 3.1. With either system, the subsequent use of reconstruction algorithms allows these sectional images to be processed into three dimensional visualisations [34].

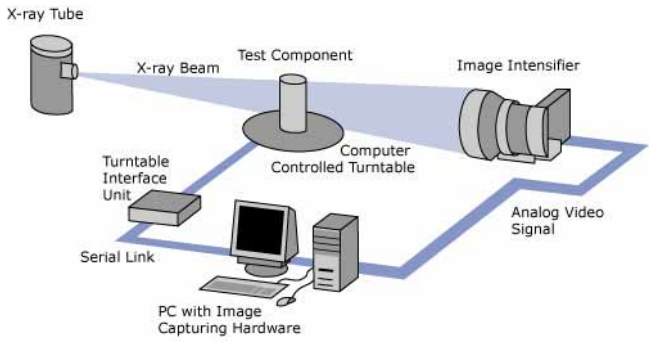

Figure 3.1: Basic configuration of X-ray CT scanner.

3.3.2 CT Scanning - Methodology

The experimental work reported in this section was conducted at the University of Bath using a Nikon X-Tek H-Series industrial X-ray CT scanner (Model 225 ST). This machine had a 225kV X-ray source, a 2000×2000 pixel Perkin panel detector, 5-axis actuation stage and a cylindrical working volume of 350×450×750mm [66].

The test specimens used for these inspection trials were single lap-shear coupons constructed from titanium and CFRP (Ti-6Al-4V and Hexel M21-T800S respectively). Each substrate was 101.6mm long, 25.4mm wide and 5mm thick. The overlap was 25.4mm square and contained an array of 36 additively manufactured pins. The pins were almost all built using the baseline geometry specified in Equation 2.1 (1.2mm base diameter, 3.6mm high). Each coupon was mounted vertically on the rotary table of the scanner using blocks of aluminium. With the X-ray source activated, the specimen was rotated through a full rotation to check the alignment and ensure that the specimen was not offset from the axis of rotation. Reference features, such as the edges of the coupon and tips of the pins, were used to ensure that there was no lateral or vertical translation of the part with rotation. Otherwise, the edges of features in the reconstructed images would not be sharply defined.

Once the physical setup of the machine had been completed, the scan parameters could then be chosen. It was found, through an iterative process, that for specimens of this size/material, the beam voltage should be set at around 170kV and the current at 300mA. As the scan resolution was paramount, and inspection was being conducted in-house (so usage costs were not prohibitive), long scan durations were implemented. A rotational step of 0.1 degrees was made between projections (3600 projections per scan) and four images taken in each projection position. The specimen was not translated vertically. The exposure time of each image was around one second and thus, accounting for additional time necessary for data transfer, processing (of the four images taken per projection) and storage, scans took approximately six to eight hours.

With the two-dimensional slice images transfered to a high performance workstation, reconstruction was conducted with Nikon's proprietary CT Pro 3D software; using a method based on Feldkamp's cone-beam algorithm [34]. The volume file (*.vol) was then transfered to a second workstation for post-processing; which was realised using Avizo Fire 7 by FEI Visualization Sciences Group (*sic*). The first step required, prior to conducting analysis of defects/damage, was to ensured that sectioning planes were normal to the surfaces of the substrates. Despite making every effort to align the coupon with the axes of the scanner's actuation system, a small amount of rotational adjustment was commonly required within Avizo. If this was not completed, sectional views would cut through multiple CFRP plies simultaneously so it was difficult to identify in-plane characteristics such as fibre waviness/wrinkling. After loading the volume file, a "volume rendering" was created and the grey-scale limits manipulated so that the scan data could be seen. The global co-ordinate system axes and grid were overlaid to create a reference for rotation of the part volume. The "transform module" could then be entered (within Avizo) and the part volume manually rotated in each of the principle axes.

Coarse adjustments were typically in the order of 0.1 degrees and subsequent fine adjustments of around 0.025 degrees were found to be suitable; a schematic is show in Figure 3.2. The volume then had to be "re-sampled" in order to create a new copy of the raw data with the global and local axes aligned and the volume rendering transfered to the new (resampled) data set in the Avizo "process tree".

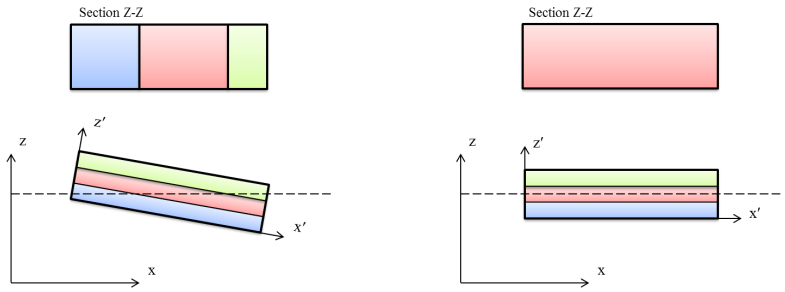

Figure 3.2: Rotation of data volume to align global and local axes. Example shows original volume (left) and modified data (right). This allows individual plies to be seen within sectional slices rather than cutting through several simultaneously. Illustrative only, not to scale.

The visualisation could now be *effectively* used for analysis of the specimen and creation of slice planes allowed individual plies seen. Completion of these steps also meant that any out-of-plane wrinkling could be differentiated from model misalignment. Although, additional processing was not required to observed defects (examples are shown in the following section), "image segregation" was found to be a very effective tool for damage identification *and* quantification. This technique enabled different materials and/or regions to be grouped into colour sets rather than being assigned a gray-scale tone based on material density/absorption. In this manner, geometric features could be isolated to emphasise their size and position relative to other features.

To achieve this type of enhanced rendering, a "label field" had to be created within the image segregation module. This was essentially a storage location so that an integer could be assigned to each voxel (rather than a decimal value defining the voxel density/grey-scale). In turn, these values associated the voxels to user defined groups; e.g. 1-Titanium, 2-CFRP, 3-Damage, etc. With the label field generated, Avizo provided the user with a range of tools to assign regions of interest (voxel sets) to these groups. Use of the "magic wand" ("propagating front") tool was found to be the most effective for this procedure. However, in order to achieve a suitably representative result, a lot of user intervention was required and a high proportion of slices had to be (manually) examined. For example, iterative threshold adjustment was required to capture as much damage as possible from the selection of a single point without encroaching into undesired areas.

Once the user was satisfied that defects/damage were adequately selected and all voxels were grouped into material sets, a surface mesh could be generated to encompass any given set from the label field. It was essential to smooth the mesh and reduce the total number of elements to prevent prohibitively slow computation and visualisation times (even on a high performance workstation). All damage was selected as a single group rather than manually creating groups based on depth within the CFRP. This was faster as the automated tools within Avizo could be used more extensively and any user influence was also reduced.

With the surface displayed, an "analytical scalar field" was created. This was based on original data volume and stored positional data, such as the through-thickness location (z), of each voxel. A user-defined colour map could then be used to render the voxels of any given set (surface mesh) based on position through-thickness. This process and the coupling of different data types is depicted in Figure 3.3. By customising the colour map to match the output of other inspection systems/methods, such as an ultrasonic time of flight C-Scan, this allowed direct comparison of results. This technique was implemented in Section 3.7.

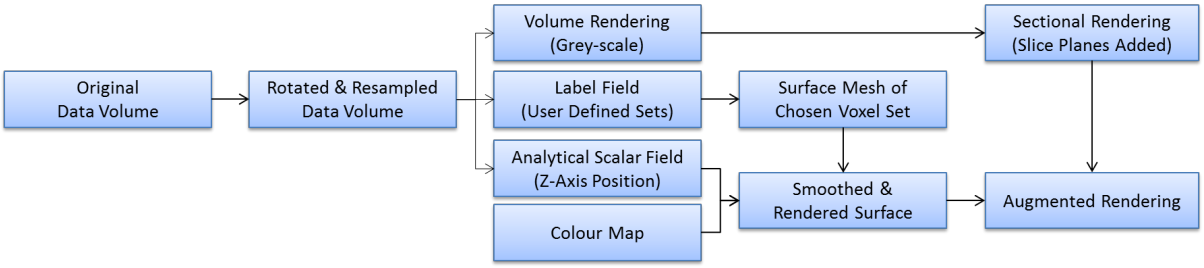

Figure 3.3: Workflow and data manipulation/interdependency within Avizo Fire in order to generate a sectioned rendering with damaged extracted.

3.3.3 Results and Discussion

Figures 3.4 to 3.7 show a selection of CT images that have been generated by the author during the project. These were primarily single lap-shear coupons (as described in the previous section) but some compression-after-impact panels were also used; the design/specification of these is defined in Section 3.7. Later in the project, the lap-shear coupons were used for mechanical testing; the results of these tests are reported in Chapters 4 and 5.

Firstly, in-plane and through-thickness sectional views are presented to illustrate that fibre waviness/wrinkling and resin rich zones that were found to be generated within the composite substrate during insertion of the pins. It can be observed that CT scanning provides images of the embedded pins with excellent resolution. Due to the difference in X-ray absorption between the titanium and CFRP, there is a significant difference between grey-scale threshold required to visualise the composite part of the joint and the pins. Hence, in Figures 3.4 to 3.6, in order to observe the plies of the laminate, the pins appear over-exposed. As a result, the outer profile of the pin can be observed but internal detail is hidden.

Figure 3.5 shows delaminations within the laminate (primarily at the tips of the pins) as a result of a 30J impact. The panel was subjected to a strike at the centre of the array but the image shows one of the outer rows. Although, the objective of this chapter was to evaluate methods of non-destructive inspection, impacting a set of CFRP panels was an effective means of creating damage representative of real applications. A thorough assessment of damage tolerance and mechanical performance after impact was beyond the scope of the project, however, an initial assessment is made as part of the case study; presented in Section 3.7.

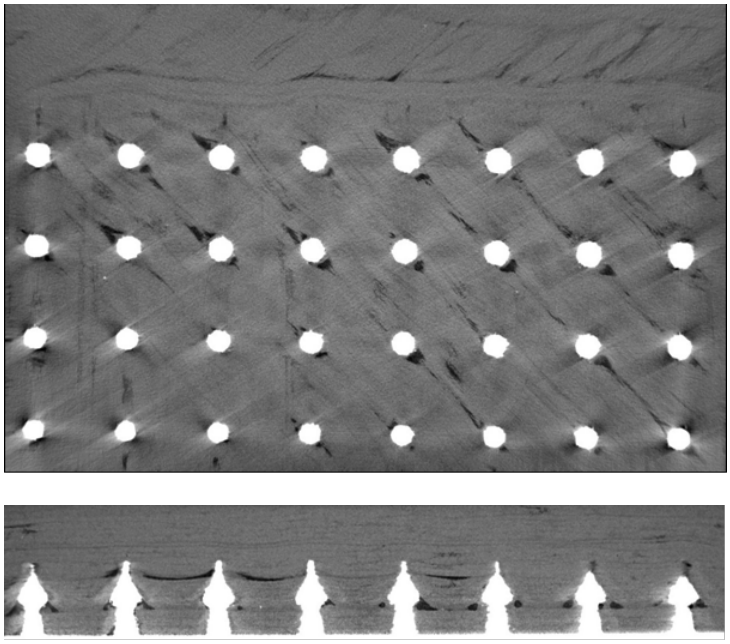

Figure 3.4: In-plane and through-thickness sections from a CT scan showing typical fibre misalignment in proximity to the pins.

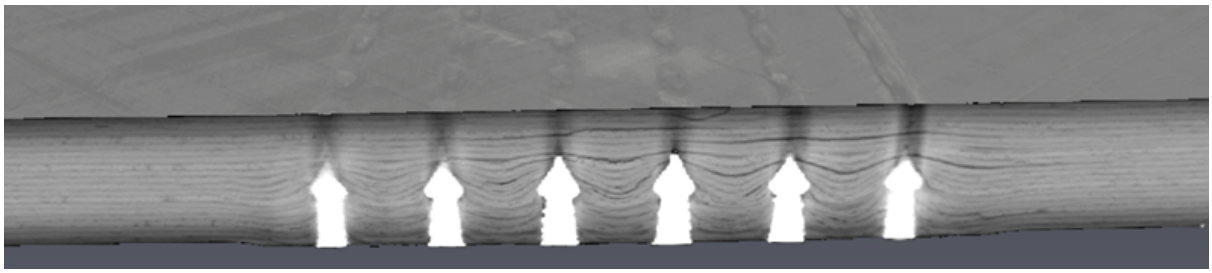

Figure 3.5: Delaminations within a HYPER panel that had been subjected to a 30J impact. Damage is primarily above the tips of the pins, in the upper quarter of the laminate.

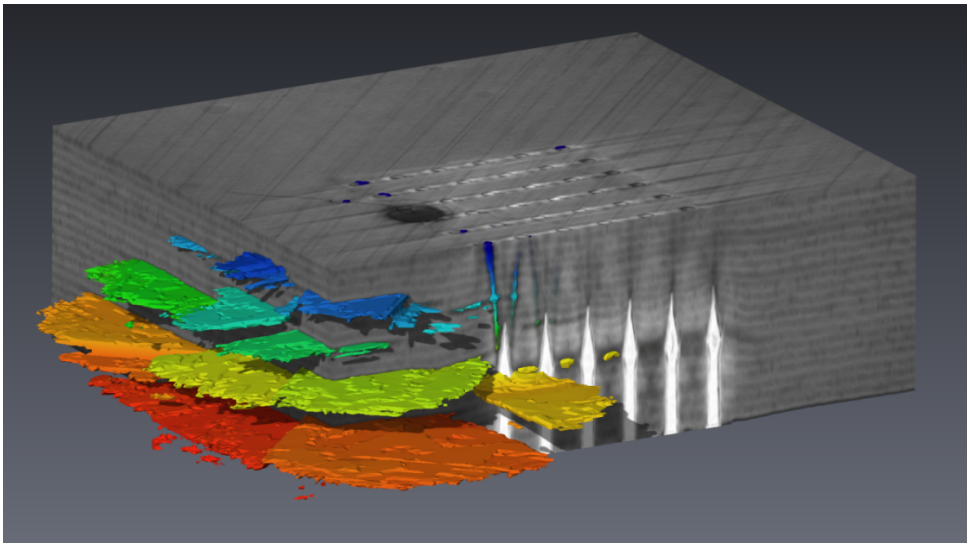

Figure 3.6: Grey-scale cutaway of the scan volume with damage extracted and rendered. Specimen was subjected to a 30J impact at the side of the array. For clarity, the volume has been stretched through-thickness to separate the delaminations.

Use of the "impact" panels also served to highlight a disadvantage of using X-ray CT inspection. It is desirable for parts to have an aspect ratio of around one and, ideally, be circular. This is so that there is a minimal variation in absorption as a result of the exterior geometry. The region of interest in Figure 3.4 of the lap-shear coupon was 25.4×12.7×10.0mm (the overlap). In contrast, the impact panels were 100×150×5mm in order to conform to the Airbus test standard [7]. This can result in a variation of the image intensity through-thickness, as seen in Figure 3.5. This made it harder to identify near surface delaminations/damage due to contrast variation. Regardless of the dimensions of the composite substrate, Figures 3.4, 3.5 and 3.6 all show that artefacts were generated by the pins (artificial tonal variation such as streaking).

Figure 3.6 shows an example of what can be achieved using X-ray CT and the advanced post-processing capabilities of Aviso Fire. The panel shown in the figure had been subjected to a 30J impact at the edge of the pin array. The laminate was cut back to reveal the pin array and delaminations within the laminate. Individual delaminations and their relative depth can be easily differentiated given the (automatic) colour scaling which was applied. Although an impressive capability for comparison with other specimens and methodologies (ultrasonic C-Scans), generation of this rendering took approximately two to three times as long as that in Figure 3.5. Therefore, this would not be practical solution for large numbers of coupons and/or use outside of a research environment. However, for small numbers of samples, it was found to be extremely effective and a comparative study (between ultrasonic evaluation and this refined radiographic method) is reported in Section 3.7.

The previous three figures have all shown the resolution that is possible if the user wishes to encompass an entire pin array (circa 25×25mm) and also include a substantial proportion of the surrounding material. Figure 3.7 shows the maximum possible resolution that could be achieved with the available hardware/specimens. The pins shown in this figure *were* embedded within CFRP when they were scanned yet it is possible to view the pins (and not the composite) without conducting the extensive image segregation; described above. This is because of the large difference in material density and, consequently, absorption of the incident X-rays. The less dense material has been excluded simply by setting the grey-scale threshold (minimum visible tone) to a sufficiently high level.

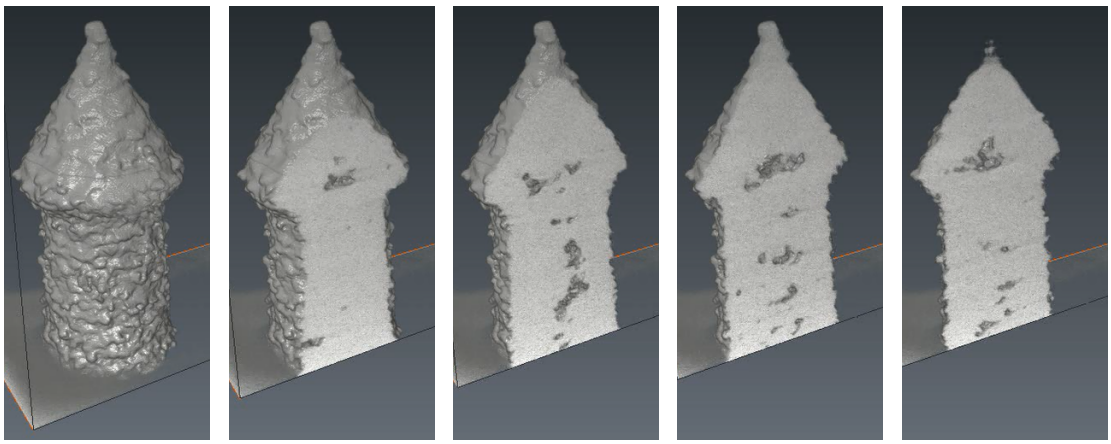

Figure 3.7: Series of sectional views through a pin showing significant porosity. The pin was embedded within a CFRP substrate during scanning.

Figure 3.7 shows a series of sections through a single pin. It is clear to see that a high degree of porosity was present in this example. Individual voids are up to 0.5 mm in size and total voiding was approximately 2% of the pin volume. These defects are thought to have resulted from incomplete sintering and a subsequent lack of fusion; generated as a result of the laser not having been calibrated correctly. This level of porosity was thought to be a "one-off" and not representative of manufacturing capability in general. All coupons from the same build were identified and excluded from the main testing programme. However, some were tested in a separate trial so that the knockdown in performance with this level of porosity could be quantified. The results from these specific (defective) coupons are discussed further in Section 5.6.3. It should be noted that these were the only specimens tested that were known to contain significant porosity.

Although CT imaging allowed detailed evaluation of defects within HYPER joints (pin porosity, fibre misalignment, resin rich zones, etc.) it would not be a practical option for batch inspection of large numbers of coupons. Producing CT images is a costly, time consuming and complex process. Thus, an alternative approach was still required. The quality of the CT images could, however, be used as a benchmark for other NDT methods that were subsequently evaluated.

3.4 Thermography

The second NDT technique assessed was thermographic inspection, a method based on the principle of observing the heat distribution on the surface of a specimen. The uniformity of the flux provides an indication of the homogeneity of the sample and anomalies can reveal the presence of defects. The manner in which heat is generated categorises methods into two distinct groups; active and passive. A review of the literature is presented, highlighting the advantages and disadvantages of each method. The suitability of these techniques for the evaluation of defects within HYPER joints is then discussed. As part of this assessment, a numerical model was developed to analyse heat flow within a multi-material pinned joint and a series of experimental trials were also conducted.

3.4.1 Background

An example of active heating is ultrasonic thermography. Externally induced mechanical vibration will be converted to thermal energy at locations of flaws due to frictional contact. Most significant advantage compared to passive methods is that flaws such as closed cracks can be detected. It is unlikely that these would be visible without dynamic stimulation as there would be negligible difference in the conductive heat path. For example, Tenek and Henneke [84] used specific excitation frequencies (13.5-15.0 kHz) to achieve resonance in a 3-ply sheet (280×130 mm) and achieved a 5 degree temperature rise from a 7 mm square delamination. However, such a significant temperature rise would not be possible on thicker specimens unless the energy input or delamination size was also larger (twenty-ply laminates were used for HYPER joints). A thermal field could also be generated with the application of lower frequency cyclic loading

for a prolonged duration; e.g. during a fatigue test. A temperature rise would be created around flaws due to stress concentrations. However, temperature variation would also be created at geometric features (with stress concentrations) which could produce misleading results. Regardless of accuracy and method of stimulation, dynamic excitation of a component for the purposes of inspection would only be a suitable strategy for small specimens and/or in research environment for parts at a low technology readiness level; i.e. coupon-scale tests.

Passive thermography is the application of thermal energy to the surface of a component from an external source; rather than generating heat from within the part. Heat input can be pulsed for a short, transient response from a photographic flash tube or for a longer duration using a modulated input source (locked-in thermography). In either case, the surface temperature of the structure is typically monitored with an infra-red camera. Alternatively, thermally-sensitive liquid crystals could be sprayed onto the surface.

In a similar manner to ultrasonic inspection, either the reflected or transmitted radiation can be observed; from the exposed face or rear face respectively. Thermography differs from other electromagnetic techniques as the propagation of the applied energy is not instantaneous. The rate of propagation is dependant on thermal diffusivity and observation time is a critical factor. Thermal NDT is most effective for detection of voids, inclusions, cracks and delaminations. This is due to the presence of air which has significantly different diffusivity compared to metals and CFRP. However, this method is only truly quantitative technique for isotropic materials, such as metals. With an anisotropic material such as CFRP, conductivity in the laminate plane is much higher than through the thickness, differences in contrast due to flaws are more difficult to detect as the heat propagates away in-plane and does not penetrate deep into the part. The thermal diffusivity parallel to the fibres is approximately 3.7×10^{-6} m^2s^{-1} whereas perpendicular (through-thickness) it is considerably lower; 0.42×10^{-6} m^2s^{-1} [58]. Metals are an order of magnitude higher (10-100$\times 10^{-6}$ m^2s^{-1}), so would require very short observation times to capture the response. As a result, pulsed thermography is unlikely produce a sufficiently high contrast ratio to successfully detect deeply buried flaws. In general, flaws must be twice as large as they are below the heated surface to produce an adequate thermal contrast. Therefore, this technique is most sensitive to defects close to the surface and, for example, only those less than 2 mm deep in strongly anisotropic CFRP. However, thermography can offer a ten-fold reduction in inspection time as it is an area inspection technique rather than a point based method. Experimentation reported in the literature shows that accuracy of detection can be comparable with ultrasound for particular applications [35].

Pulsed phase thermography with thermographic signal reconstruction is a signal processing technique that helps reduce the influence of the variations seen in traditional time domain analysis and contrast based passive thermography. A sinusoidal heating of known magnitude and phase is applied to a specimen and a (sinusoidal) response measured. The phase image of the response is of most use as it is reported to be independent of optical or surface features. The phase image can effectively penetrate approximately twice the thickness of the magnitude image [58].

Based on the literature found and, primarily, the large reduction in resolution with increased defect depth, it was concluded that thermography would not be suitable for inspection of HYPER joints. It is believed that potentially critical defects (porosity within the pins and surrounding material) could be less than a millimetre in size and generated at a depth of several millimetres (≈3-5 mm) within the joint. This assumption was based on the evidence gathered from CT imaging, reported in Section 3.3. However, although thermography may not offer the type of detailed inspection that is desired in a laboratory environment, an area inspection method would offer a significant speed advantage for in-service evaluation. Therefore, efforts were made to consider novel ways in which a thermal technique could be applied to HYPER components. It was thought that the high thermal conductivity of the metallic HYPER pins could be exploited to enhance the capability of thermographic methods. Thus, a numerical heat transfer model was created to simulate conduction by metallic pins embedded within a CFRP laminate.

3.4.2 Modelling of Heat Transfer

The objective of this study was to determine if the unique construction of HYPER joints could be utilised to increase the effectiveness of thermal inspection. It was hypothesised that by applying heat through the metallic substrate, it would be possible to observe the location (and potentially the integrity) of the pins, due to their higher conductivity, if the thermal response was observed from the carbon half of the joint. A configuration analogous to a through-transmission ultrasonic inspection [41]. It was hoped that local "hot-spots" would be induced on the surface of the composite above pins as the surrounding material (CFRP) would have a lower thermal diffusivity through-thickness. If a pin was defective (e.g. contained internal porosity), the thermal path would be less conductive and, hence, a less significant hot-spot may be produced.

Figure 3.8 shows the configuration of the model. The pin shape was simplified and each represented by rectangular sections. The dashed lines show the true pin geometry and the boundaries of the model are also highlighted. The model was prismatic and of unit depth. Two half pins were used as the pin pitch was also a free variable. The centrelines represent planes of symmetry and, hence, were suitable places to section the model. Finally, the design space was discretised using a square mesh of cells. The constituent equations were formed using a resistance network analogy and solved iteratively by explicit forward differences. This approach was based on the work of Blomberg [13] and realised using the MATLAB visual development environment [59].

There were three discrete stages to the program:
1. Automated population of matrices with cell properties (diffusivity, etc.) and stability check.
2. Iterative loop to generate results; temperatures written to matrix, T.
3. Output and visualisation of results.

This approach allows changes to be made to an individual part of the programme (output method/format) without necessarily being required to run the iteration process.

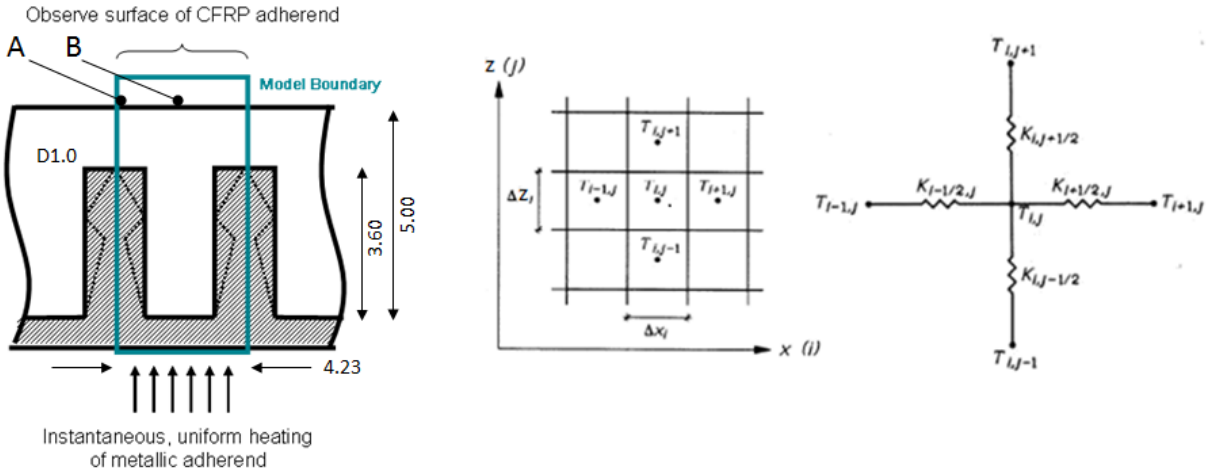

Figure 3.8: Boundary of the thermal model showing application of heat through metallic substrate and observation from the carbon side (at A and B). Centre: Modelling space was discretised into cells of temperature $T(i,j)$, width Δx and height Δz. Right: Resistance network was then applied between adjacent cells [13].

It was assumed that the entire model was at room temperature (20 degrees Centigrade) and then the rear of the metallic substrate was instantaneously heated by 30°C. The temperatures at locations A and B (above the center of a pin and mid-point between pins respectively) were captured at multiple time points. Only a single pin design and spacing were trialled due to time constraints.

A fixed Dirichlet boundary condition $T_{1\rightarrow m,1} = 50°\text{C}$ was used for the bottom face to simulate constant uniform heating of the metallic adherend. Throughout the rest of the model, the initial condition stated that the coupon was at room temperature $T_{1\rightarrow m,2\rightarrow n} = 20°\text{C}$ and thus represented an instantaneous 30°C rise at the lower edge. Heating by conduction through the thickness of the metal adherend was not considered as it was assumed that it would be generated uniformly. Neumann boundary conditions were used to create symmetrical boundaries on the left and right edges (pin centrelines) and an insulated boundary on the top edge. The top edge (external carbon face) would have actually lost heat by radiation. Heat loss by thermal radiation at the surface would have reduced any temperature differential across the surface as heat loss would be proportional to temperature. Therefore, by assuming an insulated boundary, this formed a non-conservative approach.

It was assumed that thermal conductivity was constant with temperature variation for the range of temperatures considered (20-50°C). Therefore, the conductance between cells was also constant with temperature variation and, thus, not time dependent. By making all these calculations prior to the main loop of the programme, run times were reduced by 50%. Full account was made for the stacking sequence; $\delta x = \delta z = 50\mu$m therefore each ply was 5 cells thick given the nominal thickness of 0.25 mm [44]. The maximum timestep is found using Eftring's criterion, outlined by Blomberg [13]. Although i and j were used for cell notation in the x and z axes respectively, matrix convention is maintained within MATLAB so matrix $T_{i,j}$ had to be transposed to output the results in the expected Cartesian orientation.

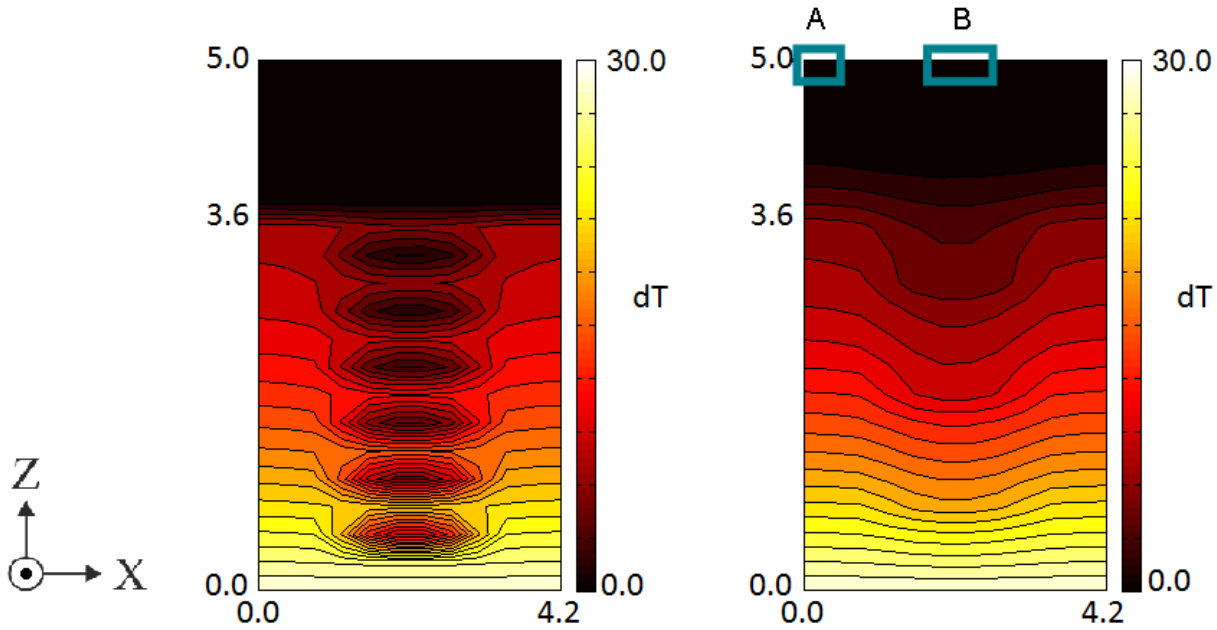

Figure 3.9: Thermal profile at t=1s for $[(0/90)_{10}]$ layup (left) and quasi-isotropic layup (right).

Firstly, a "worst-case" stacking sequence was used to emphasise the influence of anisotropy; $[(0/90)_{10}]$. Contours plot are shown in Figure 3.9. The zero degree plies were parallel to the x-axis and the nineties with the y-axis. It is shown that the heat has propagated up the length of the pin and has then propagated laterally along the highly conductive zero degree plies to form distinct bands. Once the model was modified to represent a quasi-isotropic stacking sequence $[\pm45/0/90/\pm45/0/90/\pm45]_S$, it was observed that the thermal distribution was significantly more uniform throughout the composite; also shown in Figure 3.9. This uniformity would have reduced the effectiveness of this approach as the surface contrast between a pin (A) and mid-point between pins (B) would be minimised. The observation time (from the start of the simulation) is another key factor that would influence the success of this method. It was found that, although observation time was proportional to temperature difference $(T_A - T_B)$, it was inversely proportional to contrast which would further reduce the effectiveness of the approach.

$$\text{Contrast} = \frac{T_A - T_B}{T_A} \tag{3.1}$$

In conclusion, the rate of heat of flow through the pin was not significantly faster than lateral (radial) flow from the pin into the laminate. This was because the higher conductivity of the zero and forty-five degree plies and their dominance in a quasi-isotropic layup. The result is inter-laminar conduction and near uniform heating through the laminate making the pins undetectable due to inadequate contrast ratio at the surface. This was found to be the case regardless of observation time. If pristine pins could not be clearly observed by this method, then it is highly unlikely that any variation due to damage would be detectable. Therefore, thermography is not thought to be a suitable inspection technique for detection of *internal* HYPER joint defects; even in a laboratory environment. However, thermography still had potential for the identification of *surface* breaking flaws. An experimental investigation into this capability is presented in the following section.

3.4.3 Experimentation

Although, thermography may not be able to detect potentially critical flaws within the pins or deep within the composite, it was still possible that near-surface or surface breaking defects could still be a successful identified. If this was possible, this could still be an effective tool for detection of, for example, cracking around the edge of the joint. If HYPER joints behave in a similar manner to adhesive joints, based on evidence in the literature [46], edge cracking would be the first failure mode. Thus, it was thought that if this could be detected, a more detailed inspection could then only be applied when necessary.

Ultrasonic thermography was selected as the most promising candidate given this technique's success at detecting fine cracks in turbine blades. Three single lap-shear coupons were subjected to this method. These were provided by Airbus Group and had not been tested during initial joint characterisation trials (prior to this project) as it was believed they contained manufacturing flaws. A 35 kHz ultrasonic welding horn was used to excite each specimen for one second. A pre-load of 50 N was applied and a PTFE sheet used to aid coupling of the horn and coupon. An infra-red camera system used to capture the thermal response. This was observed within two seconds so the camera was set to record at 60 fps. The first frame was used as a reference image and subtracted from all subsequent frames; which were gated using logarithmic spacing.

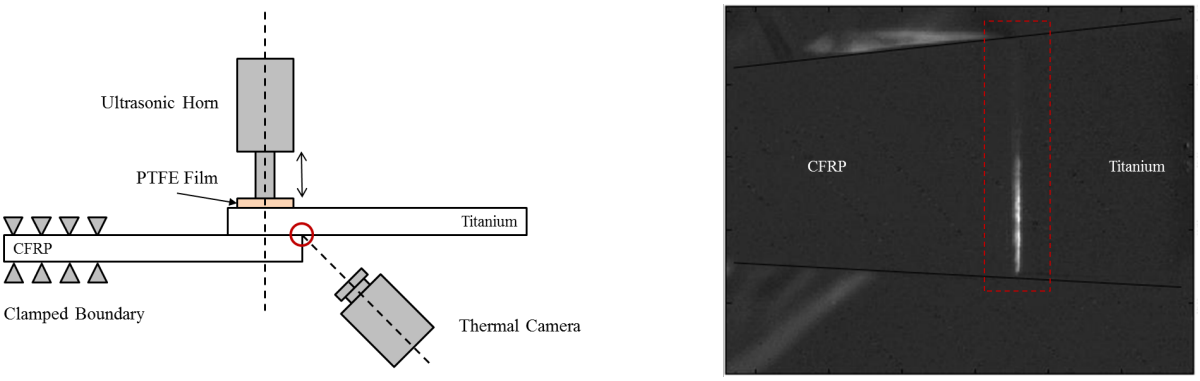

Figure 3.10: Plan view of the test setup and thermal image of coupon following excitation. Coupon geometry as per Figure 2.4.

The configuration of the test is shown in Figure 3.10 along with an image generated by the thermal camera. This image was captured at approximately 0.5 seconds after excitation. For clarity, the intersection highlighted in the schematic is shown on the thermal image with a dashed line. The white line within this box demonstrates an area of increased temperature due to the presence of a crack; which has propagated approximately 50% of the joint width. Results from the other two coupons were also promising, clearly showing edge cracks at the joint interface. These all correlated well with defects that were found during subsequent ultrasonic inspection (presented in the following section). However, ultrasound provided quantatative data on the magnitude of crack penetration and, therefore, ultrasonic thermography could only be used for an initial assessment of joint integrity. A second method would also be required to provide more comprehensive information.

3.5 Ultrasound

3.5.1 Background

Ultrasound is the propagation of mechanical vibration in a medium at frequencies in excess of 20kHz (above the audible range). Reciprocation of a piezo-electric transducer creates an ultrasonic pulse, formed from a synthesis of different frequency sinusoidal waves. A wave front then travels through the specimen at the corresponding speed of sound (c) which, being a form of mechanical excitation, is a property of the elastic modulus. In solid materials, this not only applies to primary compression waves as it is also possible to generate shear waves that oscillate perpendicular to the wave's direction of travel. The shear wave speed is generally considered to be half of the compressive wave speed in an isotropic material [41]. Propagation of the wave front will be disrupted at any internal discontinuity or at an interface between media. A proportion of the wave will be reflected and the remainder transmitted across the interface. By receiving this response (echo), it is possible to deduce information about the geometry/structure of the material or test specimen.

The strength of reflected wave is dependent on the energy of the incident wave and the specific acoustic impedance (Z) of each material; itself a property of the material density (ρ). The greater the impedance mismatch, the greater the energy reflected (E_r), as shown in Equation 3.3. This equation is valid for both compression and shear waves. It is also assumed that the sum of the reflected and transmitted energy equals unity and that there are no losses. The impedance mismatch at an interface between a solid and a gas is very large and results in almost complete reflection of the incident wave and, thus, in order to transmit a wave from a transducer into a test specimen, it is necessary to couple the two. This is typically achieved by immersion in, or application of, water or a gel.

$$Z = \rho \cdot c \tag{3.2}$$

$$E_r = \left(\frac{Z_1 - Z_2}{Z_1 + Z_2} \right)^2 \tag{3.3}$$

Snell's law states that the transmitted signal will also refract for non-zero incidence angles (θ_1) because of the change in the speed of sound; see Equation 3.4. It is also possible for both reflected and transmitted waves to undergo mode conversion from compressive to shear (or vise versa) when $\theta_1 > 0$. Therefore, it is essential to ensure that the transmitter is perpendicular to the test specimen which can be challenging when the material/specimen is not flat.

$$\frac{\sin \theta_1}{\sin \theta_2} = \frac{c_1}{c_2} \tag{3.4}$$

The transmitter and receiver can be positioned in a range of configurations but the most commonly used is a "pulse-echo" system. This allows the incident signal to be generated and any reflections detected by the same probe. This allows inspection without access to both sides of the part which can be a practical solution for in-service applications.

3.5.2 Methodology

A series of pilot studies were conducted to determine the effectiveness of ultrasonic inspection for evaluation of HYPER joint defects and damage. This was conducted using single lap shear coupons, the dimensions of which are shown in Figure 3.11. The overlap is one inch square and contains a 6×6 array of uniformly distributed pins. The substrates are titanium (Ti-6Al-4V) and Hexcel M21-T800S CFRP; both were nominally 5mm thick.

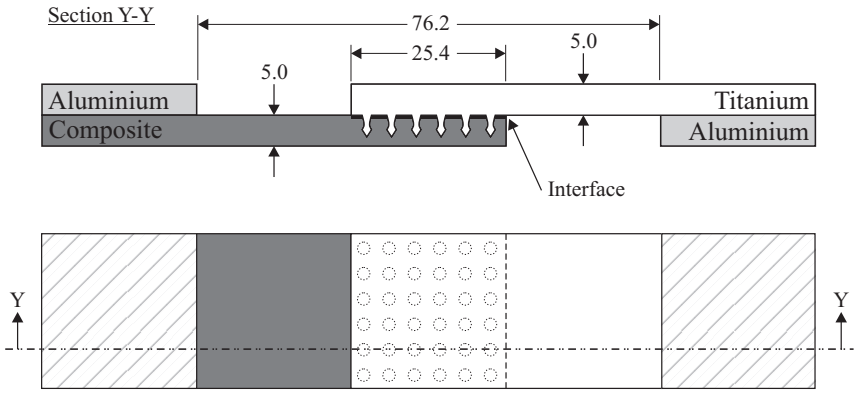

Figure 3.11: Standardised single lap shear HYPER joint test specimen.

The system used to conduct the inspection was an Ultrasonic Sciences Limited, USL immersion system with an Olympus Panametrics 35 MHz PVDF spherically focused probe. The probe diameter was 0.25 inches (6.35 mm) and the focal length 1.5 inches (38.1 mm). This polymer transducer was chosen as it offered an optimal impedance match to water and the high frequency provided excellent spatial resolution [69]. Coupons were firstly submerged in the water tank and both the inspection surface and backface wiped to ensure that no air bubbles were attached. The probe was then lowered into the water and positioned over the coupon. The underside of the probe was also wiped to ensure no air was trapped beneath it. This was particularly necessary when using a probe with a short (spherical) focal length as the lens was deeply concaved. The probe height, and thus the distance to the test specimen (water path), was initially set by eye. This ensures an echo was transmitted from the front face of the coupon so that the interface "gate" could be set on the A-Scan (a plot of received signal strength with respect to time received). This gate was the "trigger" that commenced data acquisition and/or captured data. Gates are "fired" when a signal of adequate magnitude was received within specified time limits. Hence, by appropriately setting the gate threshold (and range), weaker signals could be selectively excluded. Additional gates could also be positioned *relative* to the interface gate so that any geometric fluctuations in the front surface of the material did not alter the time/depth at which the latter (deeper) gates were located.

By selection of key signals from the A-Scan with gates, and cross-referencing these with the corresponding xy-position of the probe, a "map" (or C-Scan) can be constructed to show regions of interest/damage. These regions can be coloured based on signal intensity or time received (relative to transmission of the signal). The later (known as time of flight), can be used to differentiate between signals that were received from different depths.

With the interface gate positioned on the A-Scan, the water path was displayed within the software (as long as the material speed of sound had been input) so the desired offset could be accurately achieved using the motion control interface (±0.1mm). The theoretical offset for a focused probe is governed by Equation 3.5.

$$\mathrm{WP} = \mathrm{FL} - \mathrm{MP} \cdot \frac{c_m}{c_w} \tag{3.5}$$

WP, FL and MP are water path, focal length and material path respectively. The speed of sound is denoted c and subscripts m and w are the test material and water respectively [69]. The speed of sound for the materials used are listed in Table 3.1.

Given that the focal length of the 35 MHz probe was nominally 1.5 inches (38.1 mm), to focus the probe on the interface between substrates, the offset was 28.1 mm if the carbon substrate was uppermost and 17.8 mm if the incident signal first passed through the titanium. The advantages/ disadvantages of each approach is discussed below. It should be noted that the water path was commonly adjusted with manual iterations (of up to 2mm) to ensure that echoes were indeed maximal. Once the probe height (z-axis position) had been set, the coordinates governing the scan area in the xy-plane were input. Specimens were then raster scanned with a scanning speed of 10mm/s in the x-axis and a transverse step of 0.1mm in the y-axis. The scanning window (region of interest) was typically 35mm square. This was centered on the overlap region and hence produces a boundary on each side of around 5mm.

It was clear that when multiple coupons were to be inspected, or a single coupon repeatedly scanned, an efficient setup procedure would provide the user with a significant time saving as well as increased accuracy. A jig was manufactured so that the probe position could be indexed relative to the coupon and aid the setup procedure. The probe was maneuvered into the jig and then the co-ordinate system of the machine reset. Knowing the dimensions of the jig, any desired scan area and position could be entered quantitatively.

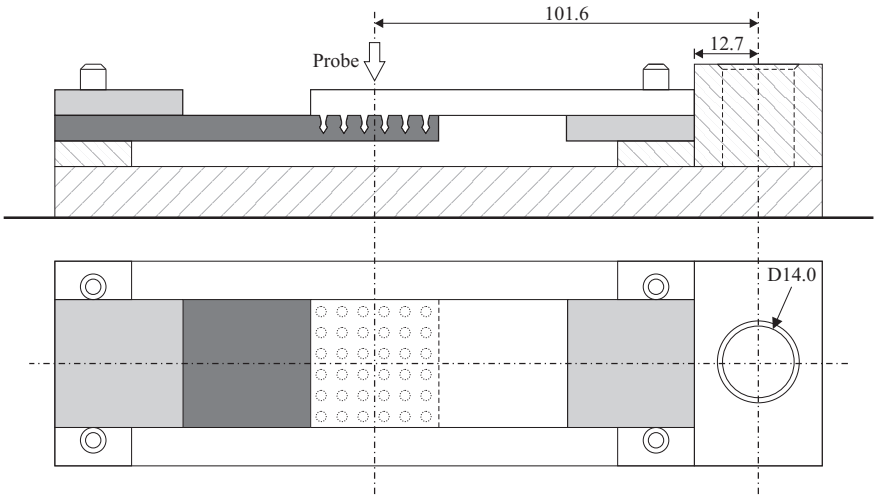

Figure 3.12: Jig used for calibration of probe orientation and alignment of test specimens. The coupon can be positioned with either substrate uppermost and inspection conducted through either the metallic or composite side of the joint.

The head of the machine also had two rotational degrees of freedom. Two adjustment wheels allowed control but (again) this was a manual, iterative adjustment to set the probe normal to the coupon and ensure that echoes were maximal. Modification was made to the head and the wheels removed so that the probe was free to move and could be manipulated. Two lock-nuts were added so that the head could subsequently fixed a desired orientation. In this manner, the probe could be set into the alignment block of the jig for calibration and then secured. This ensured that it was perpendicular to the test piece and that there was no refraction of the wavefront as it was transmitted into the test specimen (Equation 3.4).

3.5.3 Results and Discussion

3.5.3.1 Inspection Through Carbon Substrate

Pulse-echo ultrasound was firstly undertaken through the carbon face and then the metal face to determine if either orientation was advantageous. It is theoretically possible to achieve a better image of an interface disbond by scanning from the carbon side rather than the metallic side. At the water-coupon interface, 73% of the incident signal energy is transmitted into the carbon whereas only 19% is transmitted into into titanium. Reflection of the signal at a disbond would effectively the same in either orientation as a carbon-air interface has the same impedance mismatch as metal-air (≈100%). Furthermore, the contrast ratio (difference between a good bond and bad bond) is the same in either orientation as carbon-metal is the same as metal-carbon due to the calculation of impedance mismatch being absolute and not direction specific. Upon returning to the carbon-water interface more energy is again transmitted in comparison to a metal-water interface and thus a stronger signal could be received by the probe.

Material	Density (kg/m^3)	Speed of Sound (m/s)	Impedance (kg/m^2s)	Energy Reflected (%)
Titanium (Ti-6Al-4V)	4420	6100	26.962×10^6	N/A
CFRP (M21-T800S)	1580	3070	4.851×10^6	49.1
Water	998	1480	1.477×10^6	80.1
Air	1.2	343	412	99.9

Table 3.1: Material properties at 20°C [29, 69]. Impedance calculated using Equation 3.3. Values of reflected signal energy are for interfaces between titanium and other materials listed, i.e. $Z_1 = 26.962 \times 10^6$ kg/m^2s.

In practice, the irregularity of the laminated structure produces a significant amount of signal disruption and, as a result, it is actually disadvantageous to inspect in this orientation. Despite trialling a range of different frequency probes, it has not been possible to distinguish the HYPER pins using pulse-echo ultrasound via the carbon side of the joint. Lower frequency probes (5, 10 and 15 MHz) were also trialled in order to gain greater depth penetration. To ensure that the system was calibrated correctly and had adequate resolution, a series of blind, flat bottomed holes of varying diameters and depths were back-drilled into a CFRP substrate. These were all visible when scanned. It is believed that the pins were not visible with the coupon in this

orientation because the incident wave front is scattered by the angle and surface irregularity of the head feature. Furthermore, the probes used were either 6.4 and 9.5 mm in diameter and it was believed that the dimensions of the probe relative to the pins (1.5 mm maximum diameter) also influenced the success of the tests.

To validate this hypothesis, the theoretical reduction in signal strength in proximity to a pin was modelled. By considering a single unembedded pin, undesirable noise from the CFRP laminate and signals reflected from adjacent pins were excluded (an idealised test case with no interaction from other pins). As an unfocused ultrasonic probe passed over the pin it was assumed that no signal was reflected back to the probe from any overlapping areas; calculated by trigonometry. Subsequently, the magnitude of the signal received from the surface of the metallic part/joint interface decreased proportionally. Thus, the signal reduced until the probe completely covered the pin and then returned to a nominal value as the probe moved beyond the pin. The cross-sectional area of the probe relative to the pin determined the duration and severity of signal loss. It was assumed that the effect would be similar for both focused and unfocused probes; an unfocused probe was assumed to exaggerate the effect. Thus, beam convergence/divergence and probe height did not need to be considered.

Figure 3.13 shows three configurations of the model; where r_1 and r_2 were probe and pin radii respectively and λ was the offset between centres. The problem was one dimensional as the Cartesian positions of the probe and pin were converted to Polar coordinates and the results were independent of angle. Thus, if $\lambda < r_1 + r_2$ where $\lambda = \sqrt{\Delta x^2 + \Delta y^2}$, the probe partially overlapped the pin. However, if $\lambda \leq |r_1 - r_2|$ the probe completely overlapped the pin.

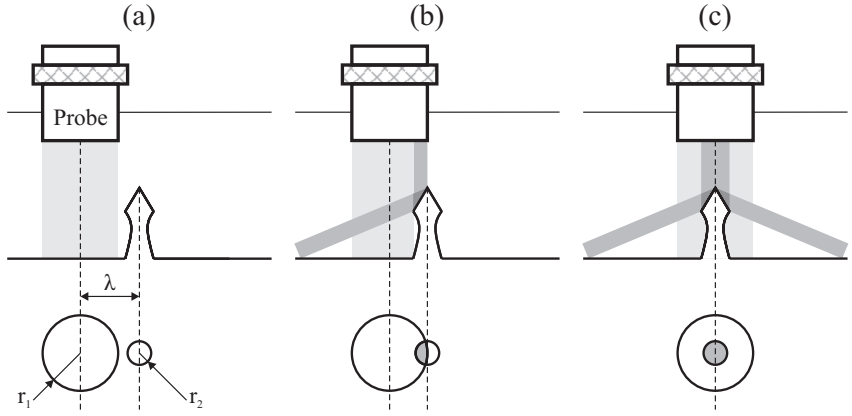

Figure 3.13: Idealised signal scattering for three probe positions.

Figure 3.14 shows the normalised signal strength for a range of probe offsets (λ), relative to a single pin at the origin ($r_2 = 0.75$mm). It can be seen that as the probe radius was reduced, signal loss became more significant and discrete and thus, it would have been easier to observe the pins experimentally. In an ideal case, the probe would be considerably smaller than the pin ($r_1 \ll r_2$) and there was an almost instant and total loss of signal. The smallest probe used experimentally was approximately four times the size of the pin ($r_1 = 3.175$mm). As a result, reduction in signal from pin overlap and scattering of the incident wavefront would have been no more than 6% making observation diffucult, particularly in the presence of the CFRP.

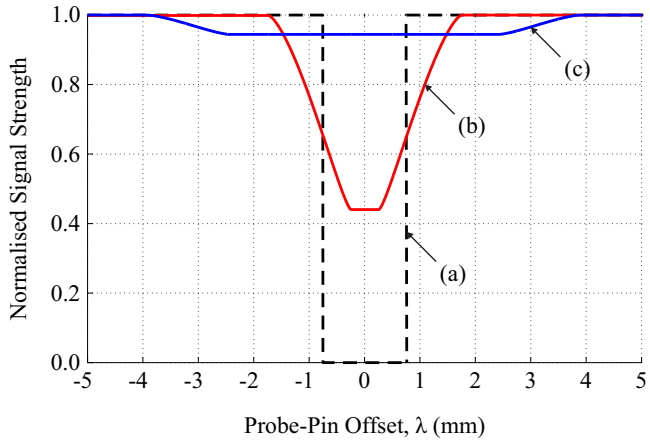

Figure 3.14: Normalised signal strength for ultrasonic probe at a range of distances from a single pin. Generated using the analytical model with a pin located at the origin ($r_2 = 0.75$mm). Results shown for three probe radii: (a) Infinitesimally small probe, $r_1 \ll r_2$, (b) $r_1 = 1.0$mm, (c) $r_1 = 3.175$mm. As the probe diameter was decreased, signal loss increased and became more discrete.

Immersion probes with a diameter as small as 2mm are available commercially (1.33 times the current pin diameter) so a reduction of around 55% could be achieved. This would vastly improve the quality of HYPER joint inspection through the carbon substrate.

This analytical method was adapted to model translation of a probe in two axes and relative to an array of several pins. This generated an idealised "C-Scan" as shown in the three examples in Figure 3.15 (each for a different probe radius). Intensity of white is proportional to normalised signal strength. An array of 4×4 pins was modelled rather than the 6×6 array of the standard coupon. It could be considered that the outer rows were excluded or that the 16 pins were within an infinitely large array as the effect of focus loss at the edge of the coupon was not included. The pin pitch was 4.2 mm and all pins had a radius of 0.75 mm. Again, an artificial case ($r_1 \ll r_2$) shows the pins as sharp discrete features. Using a probe with a radius of 1.0 mm (best case), signal loss over the pins could still be observed and, crucially, the signal returns to the nominal value between pins. Thus, any variation in signal as a result of interface disbonding could be differentiated from areas of good bonding and the influence of the pins. However, the probes used experimentally (smallest $r_1 = 3.175$ mm) were adequately large to overlap multiple pins simultaneously and this resulted in a significantly different response. Figure 3.16 shows the normalised signal strength for a diagonal path across an idealised 16 pin C-Scan; corner to corner. Results are again shown for three probe radii: $r_1 \ll r_2$, $r_1 = 1.0$ mm and $r_1 = 3.175$ mm. For small probe diameters the signal minimises over the pins whereas, for a larger probe, the signal minimises *between* the pins, inverting the response. Hence, the result is somewhat counter-intuitive as the strongest signal is returned from the pin.

In practice, the difference between maximum and minimum signals for large probes may be less. It is believed that a focused probe could retain some convergence of the beam between the pins. Therefore, it is recommended that inspection should be conducted with a probe less than 6 mm in diameter and, consequently, further experimental trials should be completed for comparison with the simulated results.

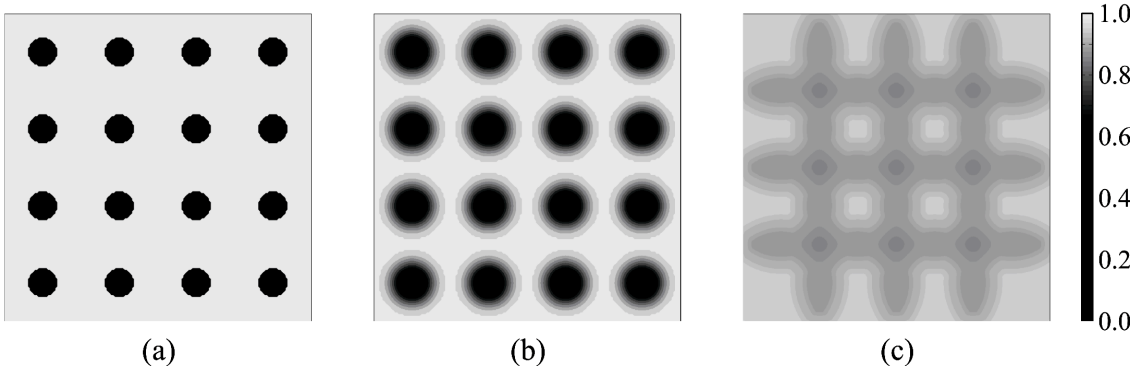

Figure 3.15: Idealised "C-Scans" generated using the analytical method. Intensity of white is proportional to normalised signal strength. (a) An artificial case (infinitesimally small probe, $r_1 \ll r_2$) shows the pins as sharp discrete features. (b) Using a probe with R1.0mm, signal loss over the pins can still be observed and the signal returns to the nominal value between pins. (c) If $r_1 = 3.175$mm, it is possible for the probe to overlap multiple pins simultaneously. Pin radius (r_2) = 0.75mm and pin pitch = 4.2mm for all three plots.

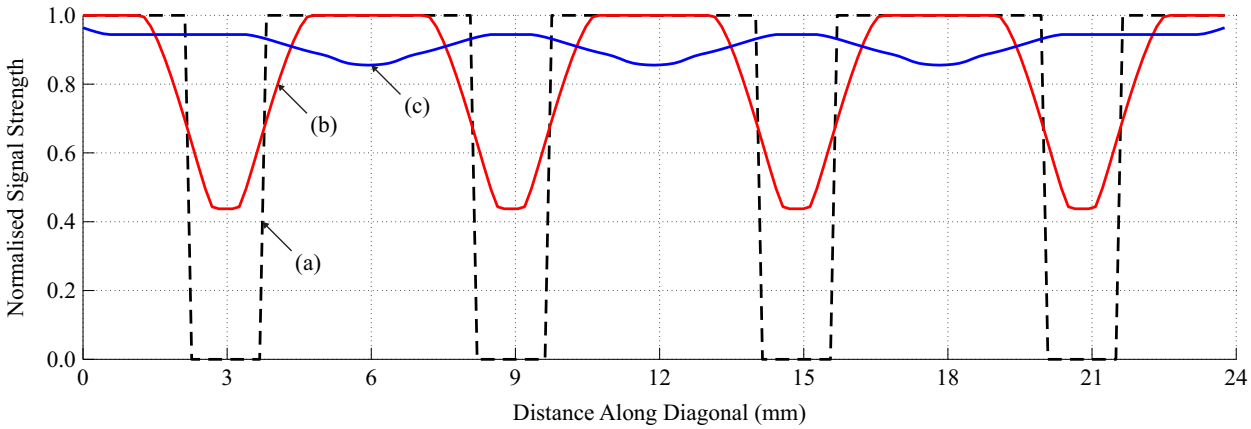

Figure 3.16: Normalised signal strength for a diagonal path across an idealised 16 pin C-Scan; corner to corner. Results shown for three probe radii: (a) $r_1 \ll r_2$, (b) $r_1 = 1.0$mm, (c) $r_1 = 3.175$mm. For small probe diameters the signal minimises over the pins whereas, for a large probe, the signal minimises *between* the pins.

3.5.3.2 Inspection Through Metal Substrate

Coupons were next inspected from the metal side, which provided some advantageous qualities. Due to the homogeneous nature of the material, it exhibits a very clean acoustic signature which makes interpretation of the A-Scan and calibration of the system simple. An idealised depiction of the wave paths and A-Scans for this coupon orientation can be seen in Figures 3.17 and 3.18. The position and width of the "gate" is user-defined and data is recorded when a signal exceeds the gate threshold within the left and right bounds; as described in Section 3.5.2. Firstly, at probe position (a), there is a prominent signal reflection (echo) from the front face. There are then a series of clear internal reflections, each transmitting an ever reduced signal back to the receiver at regular intervals. The wave that is transmitted into the CFRP and undergoes a degree of scattering, due to the laminated structure, which results in noise on the A-Scan. The rear face of the CFRP then displays an observable echo but its magnitude is significantly reduced (compared to those from the metal) due to the energy loss from scattering and the increased depth. If the interface echo is gated, the bond quality and the pin integrity can be observed. When the probe is in position (b), the wave front travels into the pin as they are integral to the substrate and there should be no discontinuities.

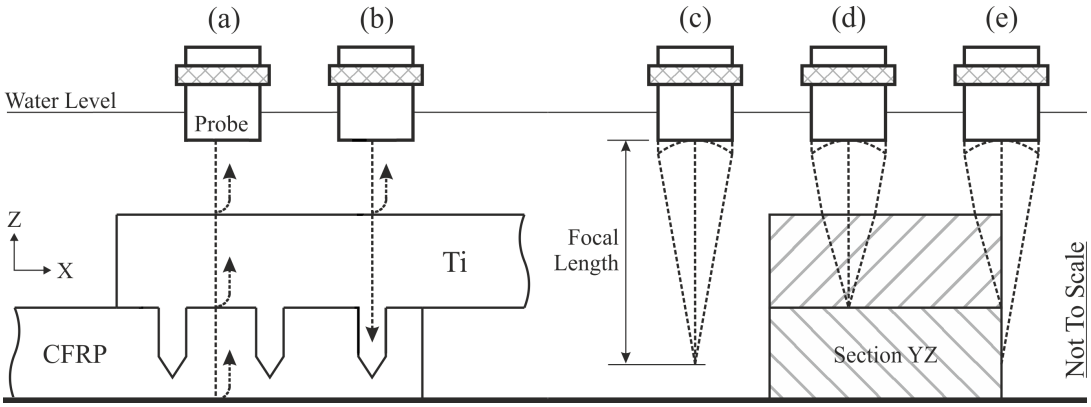

Figure 3.17: Pulse-echo ultrasonic inspection of the interface from the metallic side. (a) within the overlap but away from the pins signal is reflected from interface, (b) interface signal is lost over pins, (c) focal length of probe in water, (d) refraction reduces focal length, (e) coupon edge results in partial loss in focus and slight decrease in signal strength.

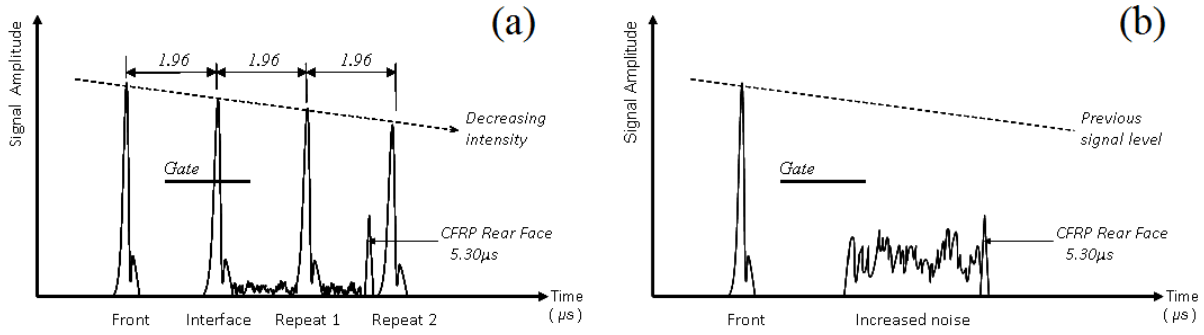

Figure 3.18: Idealised wave paths and A-Scans for two probe positions: (a) Between pins, (b) above a pin, corresponding with the locations shown in Figure 3.17. Illustration by author.

It is assumed that AM produces pins that are integral to the metallic adherend. As a result, there is no interface echo (or repeats) and the pins are visible as areas of no signal; see Figures 3.17 and 3.19. If a pin had fractured at the base, there would be a discontinuity and an echo would be returned. Thus, the condition of the pins could be monitored. By adjusting the image threshold different features can be observed. A metal-air interface reflects almost 100% of the incident wave energy whereas metal-carbon interface nominally reflects only 49%. By increasing the signal threshold, the weaker signals from areas of good bonding (metal-carbon) can be removed to show only areas of damage/disbonding; see Figure 3.20. It should be noted that there is a small reduction in signal strength around three edges of the specimens due to the probe losing focus, as shown in Figure 3.17.

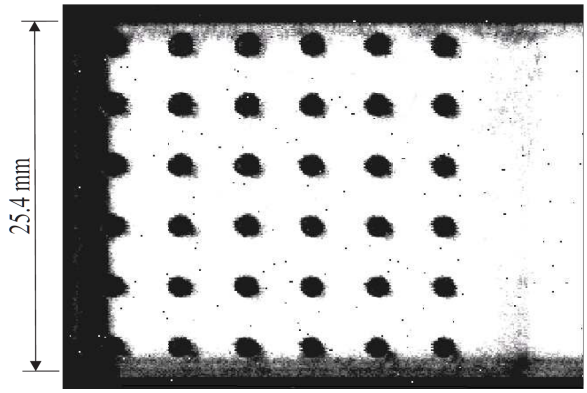

Figure 3.19: C-Scan of adherend interface showing pin locations. Intensity of white proportional to reflected signal strength. Threshold is low so no distinction can be made between good bonding and damage.

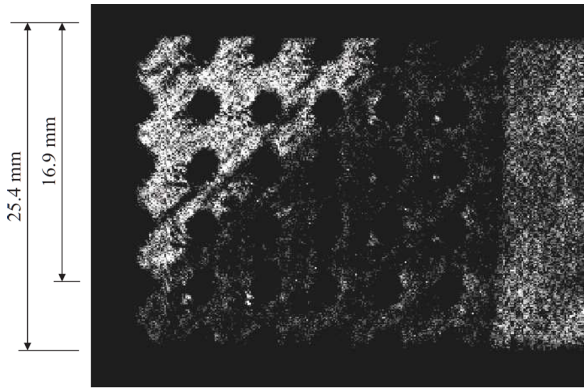

Figure 3.20: C-Scan with increased signal threshold to remove weaker signals from areas of good bonding. This reveals the titanium-water interface (beyond the right edge of the overlap) and a disbond in the upper left corner; which covered 35% of the overlap ($\approx$220 mm^2). Example shows coupon SLS-01-01.

In addition, the composite substrate could still be inspected for damage (between the pins) with the joint in this configuration. However, due to repetition of echoes generated in the metallic part, it is possible for delaminations at certain depths of the composite to be masked. The first repeat of the interface echo (see Figure 3.18) would return to the probe at the same time as a signal resulting from any damage at the mid-plane of the composite. It is proposed that

it would still be possible to differentiate signals from damage at this depth but an alternate process would be required. Due to superposition of these two waves (repeat and damage), the resulting signal magnitude would be increased. Thus, by using an additional gate to monitor this correct point of the A-Scan, and subtraction of the nominal signal strength, damage could potentially still be identified.

Given the results presented above, although it has not yet been shown, it is proposed that the equipment and techniques employed have achieved adequate accuracy/resolution to capture fracture of the pins at their root. However, to determine if it would be possible to observe pins that were fractured at the neck, a test was conducted with pin array that had not been embedded within a laminate. Damage was artificially generated by mechanical removal of the six pin heads with pliers (one outer row). This method was deliberately chosen as it left an angled fracture surface on the frustum of the pin. Three of the pins were subsequently filed to flatten the tops of the frustums and create a more uniform surface. These three pins were considered to be an idealised test case and were likely to return a more prominent echo from the incident signal. Both sets of pins (angled and flat) are shown in Figure 3.21.

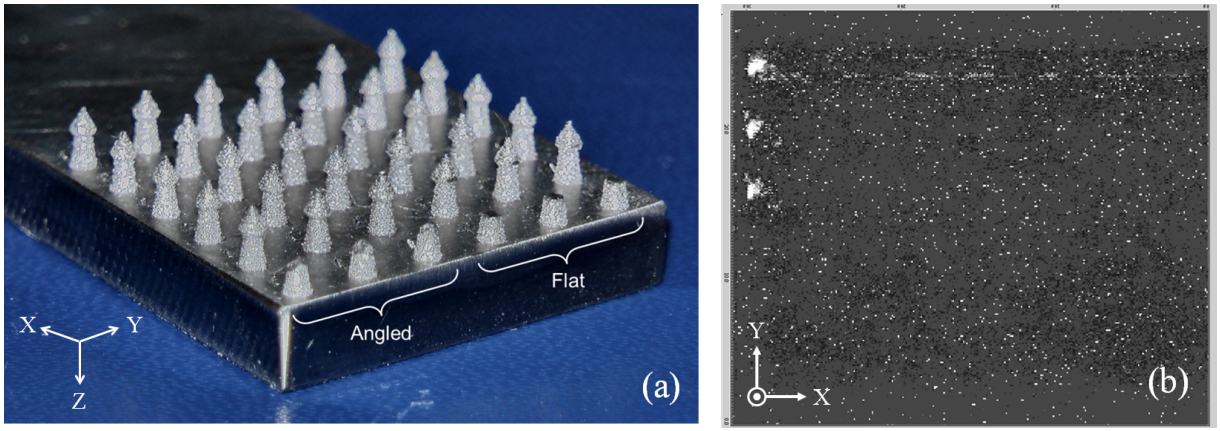

Figure 3.21: (a) An unembedded titanium substrate with exposed HYPER pins. The pin heads were removed from the outer row of the array. (b) C-Scan of artificial neck fractures. Only the pins with flat tops were detectable.

The A-Scan gate setting differed from the procedure previously described in order to specifically tailor the test for observation of damage at the pin neck. A single gate was positioned 0.66 μs beyond the backface echo of the titanium (equivalent to the metal-composite interface within an integrated joint). By allowing a 4.0 mm return path at a speed of 6100 m/s, this time difference would capture signals 2.0 mm further from the probe; see Table 3.1. If the array had been embedded within CFRP, this gate would also have captured noise and any defects 1.0 mm inside the laminate (less deep due to the reduced speed of sound). Hence, by inspecting solely the metallic part, signals generated from the "fracture surfaces" were isolated. The position of the gate deliberately excluded echoes from the back face of the titanium substrate (and hence the other pins). If successful, it was known that echoes returned from the pin neck would be much weaker than those from the interface. Excluding the backface signals subsequently improved the image contrast. Hence, an additional gate would be required to concurrently inspect the interface and segregate these responses into two separate images for analysis.

Figure 3.21 also shows a C-Scan generated by the "neck break" test. It can be seen that only three of the six pins inspected were visible. As expected, these were the three pins with the idealised "fracture" surface; flattened normal to direction of the incident wave. It is believed that the three pins with the irregular angled surface did not reflect a signal as the wavefront was scattered, just as when the head is still intact. Hence, observation of HYPER pin neck breaks would be dependent on the geometry of the fracture surface. However, if the pin and/or head of the pin were to break off within the CFRP, the resulting void/discontinuity would create a more significant impedance mismatch than in this artificial test. The signal reflected from a titanium-water interface is approximately 20% lower in strength. Therefore, validation of the ultrasonic method for pin fracture could only be completed with an integrated array and thus damage would have to be generated by mechancial loading (see Chapters 4 and 5).

Other hardware configurations could also yield successful means of evaluation; see Figure 3.22. Given that the speed of sound in metal is twice that in carbon, through-transmission could prove advantageous. It would be simple to distinguish the signal passing through a pin compared to that which has passed through the carbon due to the delay. This is similar to the way in which Z-pinned composites are inspected as the speed of sound in the fibre axis is much greater than in the transverse direction [54]. However, this method would require access to both sides of the joint which may not be practical. It is thought that some future applications may have access restrictions and only one side of the joint could be used. For example, in service, it would more practical to inspect parts of an aircraft's wing, such as leading/trailing edge brackets or spar/skin bonds, through the external (composite) surface.

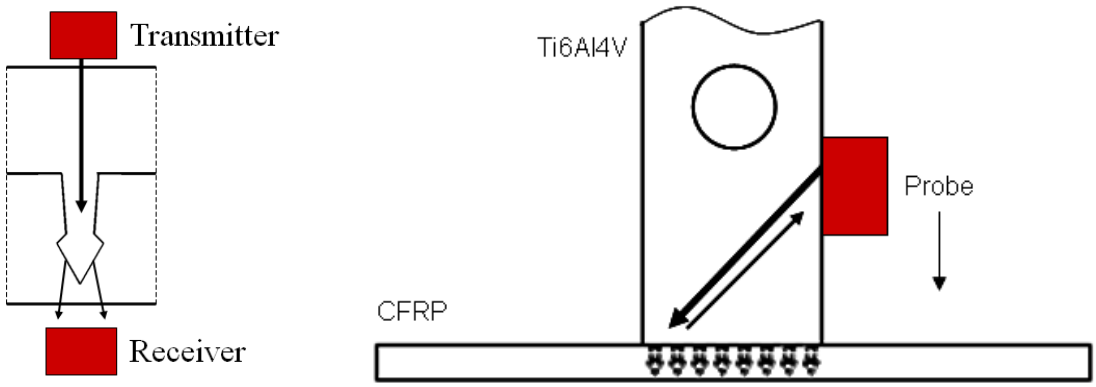

Figure 3.22: Alternative inspection configurations. (a) Through-transmission. (b) Use of a shear probe to bypass geometric complexity such as transverse holes.

Scanning from the metallic side may also be challenging regardless of access restrictions. If the metallic adherend has any complex geometry such as cutouts or holes these could block a direct path from probe to joint interface. In the case of the ARCAN coupons, it may be possible to avoid the transverse holes with the use of a shear probe; as shown in Figure 3.22. D-scanning utilises shear waves for inspection of butt welds to ensure full root penetration. This technique can observe features that would have practically no cross-sectional area on a C-Scan but are significantly larger when viewed orthogonally [41]. Alternatively, inspection constraints could be incorporated at the design stage to aid in-service evaluation. For example, leaving adequate clearance around arrays for probe access.

3.5.4 Augmented Method

In an effort to improve the visualisation of the interface/pins through the carbon substrate, an enhanced post-processing tool was created. It was believed that by positioning a series of narrow gates throughout the thickness of the coupon, additional spatial resolution could be attained and defects surrounding the pins identified. Configuring this setup manually with the OEM default software was time consuming and lacked repeatability. However, by extracting the raw scan data volume, an automated processing operation was created with MATLAB.

The raw scan data, contained within a volume file (*.vol), was firstly extracted and a three dimensional matrix constructed, $\mathbf{M} = [x(i), y(j), t(k)]$. A script was then written to convert this matrix into a series of bespoke two dimensional displays for analysis. The matrix $[x(i), y(j)]$ corresponds to the size of the scan area, each cell is a physical point in space at which an A-Scan was generated. The value of that cell was an integer value of the signal strength returned at a given point in time. Variation in the third dimension (t) presented a new matrix $[x(i), y(j)]'$. This was a data set for a later point in time, i.e. an in-plane section at a greater depth through the thickness of the laminate. The size of dimension t was dependent on the region of the A-Scan captured and the sampling rate of the system (100 MHz). A "sectioning" C-Scan is created by moving consecutively from one timestep to the next. The gate is effectively one sample point wide which allows a high level of detail to be seen; such as the fibre orientation. The configuration of the graphical output is shown in Figure 3.23.

Selection of a location on the C-Scan automatically updated the A-Scan for that position. If the gate position is moved on the A-Scan, the C-Scan and depth indication are updated. The depth is shown relative to the HYPER pin geometry so comparison can be made with any feature of interest on the C-Scan. Depth is calculated based on the speed of sound in the material and the time difference between the first and current time steps. A graphical overlay could also be added to the C-Scan to aid quantification of damage, e.g. markers to indicate the position of the pins.

Unfortunately, this refined method of visualisation did not yield the anticipated benefits and aid detection of flaws. For example, it is possible for echoes from a planar discontinuity not to be shown within a single C-Scan because a very narrow gate was used. The volume file is captured between two user-defined limits on the A-Scan which, critically, are set relative to the front face echo. This time of flight correction can be advantageous if the coupon is not completely flat with respect to the plane of the probe actuation. However, due to the sensitivity of this analysis, any minor fluctuations (such as texture) on the front surface of the laminate will create a (non-constant) time offset from a planar discontinuity. Figure 3.24 shows two detailed A-Scans, each for a different position (several pixels apart) on the same coupon scan. The gate position shows the frame used for the C-Scan, the abscissa is the time in microseconds from the front face echo and the amplitude is the percentage signal strength compared to the front face echo. At location (145,201) the gate captures the echo whereas at location (145,187) it does not. The time difference between the signal peak and the gate at (145,187) is around 55ns which equate to a distance of 0.17mm. This resulted in "C-Scan" not showing a coherent/representative picture of these signals.

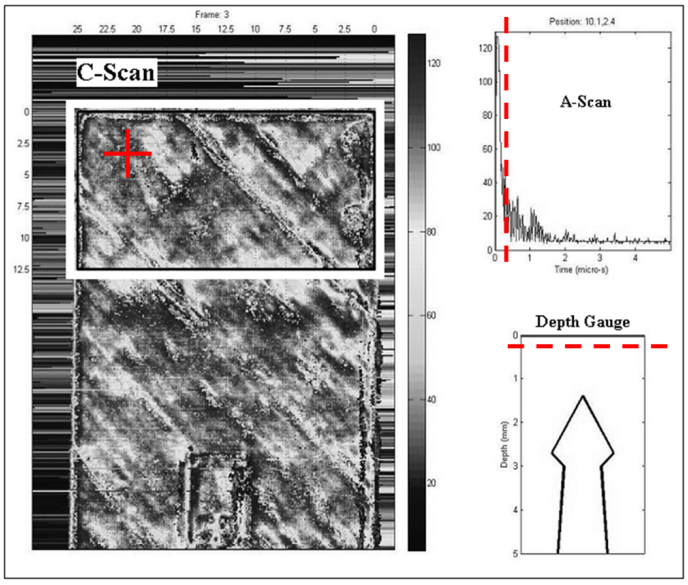

Figure 3.23: Ultrasound scan of coupon visualised using bespoke MATLAB interface. A-Scan corresponds to cross-hair position on C-Scan. The C-Scan is associated with the time shown on the A-Scan (vertical dashed line). The depth within the CFRP, relating to the selected time, is also shown relative to the pin profile (horizontal dashed line). The cross-hair and two lines can all be moved independently; all displays automatically update following a move.

It is also possible that these particular signals were not generated at the same depth, however, refinements would still be required to reduce the sensitivity of the C-Scan extraction. This could be achieved with a series of logic operations. If a gate was set between t_1 and t_2, the highest signal received between these limits for each position $[x(i), y(j)]$ could be found, prior to construction of the C-Scan. A suitable gate for the example in Figure 3.24 would be 3.25-3.50μs in order to capture the echo at both positions. At the time of writing, this step had not been implemented but it is proposed that this should be undertaken as part of a future work package.

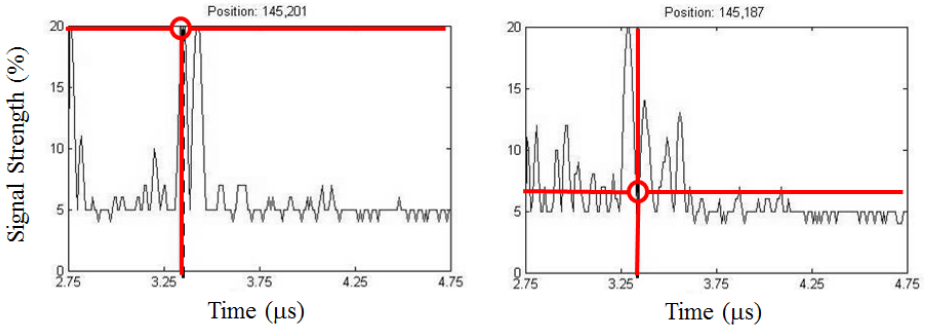

Figure 3.24: A-Scan comparison for two xy-positions on the C-Scan (3.35μs gate for both).

Continued development of this bespoke NDT interface would be essential for evaluation outside of a research environment. If an in-service application were to be inspected through the metallic side of the joint, multiple gates/displays could be integrated and each tailored to identify specific types of damage (delaminations, interface disbonding and pin fracture). For example, the complexity of segregating delaminations from repeat echoes at the mid-plane of the laminate (by reverse-superposition) was detailed in Section 3.5.3. Secondly, gate positioning for detection of pin root fractures differs from that for pin neck fractures. These gate positions would also differ from application to application with the use of different pin/array geometries.

3.6 Case Study A: Interface Quality

The aim of this investigation was to evaluate the manufacturing quality of the composite substrate and joint interface following the integration of the HYPER pins. This was conducted using the ultrasonic methodology described in the Section 3.5.3.2 and OEM software; rather than the MATLAB method described in Section 3.5.4 as this was still under development. At this stage of the project, process control during HYPER pin manufacture was becoming increasingly mature and therefore it was assumed that the metallic part was made to tolerance and of high quality. For example, any defects (such as gas porosity) were microscopic and below the detectable threshold of an ultrasonic technique. A batch of thirteen single lap shear (SLS) specimens were manufactured by Airbus Group for testing at the University of Bath. These coupons were the first set manufactured specifically for the author so were identified as Batch 1 or SLS-01-XX, where XX was the coupon number (01-13). These coupons were subsequently used for the quasi-static and fatigue testing programmes documented in Chapters 4 and 5. Coupon usage and test results are shown in Sections 4.6.5 and 5.6.4.

Figure 3.25 shows interface C-scans from a selection of coupons in Batch 1; specimen numbers 02 to 08 and also 13. A C-scan of coupon number one (SLS-01-01) has already been presented in Figure 3.20. It can be seen that the quality of bonding at the interface was mixed. There was almost complete interface disbonding in several examples (in particular coupons 03 and 05). However, it was possible to achieve good adhesion between titanium and CFRP as shown in coupons 04, 08 and 13. In addition, there was no detectable pin damage and no significant flaws were found within the thickness of the laminate. The variability in the bondline was thought to be due to inadequate surface preparation prior to co-bonding. Fortunately, it was found to be possible to enhance this aspect of the manufacturing process during the project (see Chapter 4). However, the reduction in interface adhesion in these resulted in some conservative results during mechanical testing; an influence described in more depth in the Chapter 4.

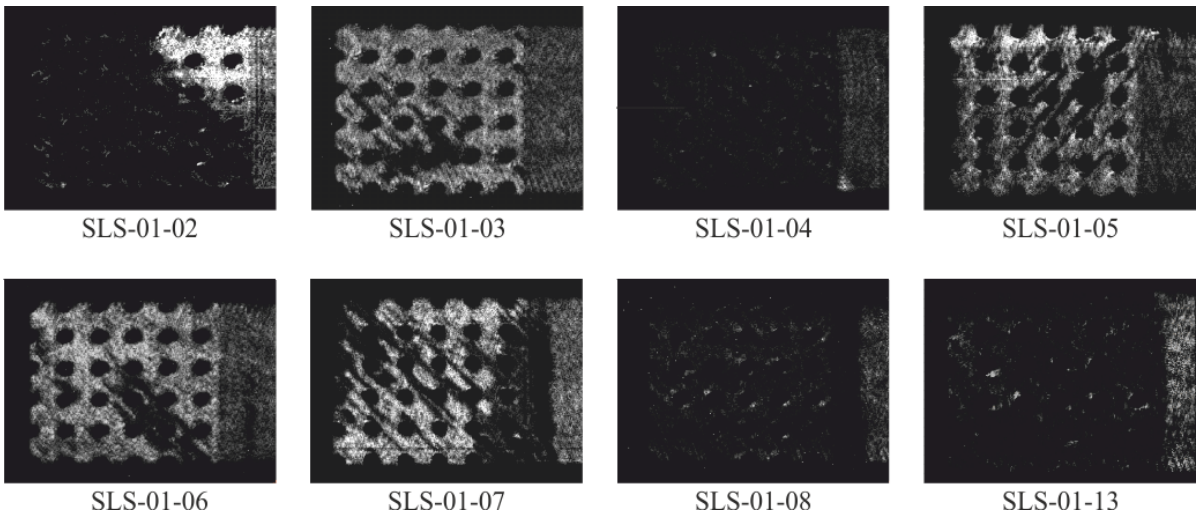

Figure 3.25: C-Scans showing the joint interface of eight coupons from Batch 1. Intensity of white proportional to reflected signal strength. All images have the same threshold as Figure 3.20. Manufacturing quality was varied and large disbonds can be seen in a number of the specimens.

3.7 Case Study B: Impact Damage

3.7.1 Methodology

The purpose of this study was to compare ultrasonic and radiographic techniques for evaluation of HYPER CFRP panels. Specimens were subjected to impact damage to create damage within the composite, rather than at the interface between substrates; as already observed in the previous study. It was proposed that these coupons would subsequently be used as part of a compression after impact (CAI) investigation but this second experimental phase was not completed during the project.

In total, three panels were impacted and inspected. The dimensions of the specimens were 100×150 mm and conformed to the Airbus Compression Test Standard [7]. They were 5mm thick and used a 20-ply quasi-isotropic layup; $[\pm 45/0/90/\pm 45/0/90/\pm 45]_S$. Two panels were reinforced with HYPER pins and one (benchmark) was not. The reinforced regions contained a 6×6 array of pins with a pitch of 4.223mm, the centre of which was aligned with the centre of the panel; as shown in Figure 3.26. The pins were 3.6mm tall so penetrated 72% of the laminate. These were built onto a metallic substrate that was machined off following insertion. This left the roots of the pins exposed and flush with the surface of the CFRP laminate. It is believed that machining back the metallic substrate in this way may have altered the delamination distribution compared to a specimen that had a metallic substrate/component beneath the impact side (due to a reduction in stiffness). This would not be representative of a real application but this methodology had previously been used for a set of filled-hole compression (FHC) tests [8]. These FHC specimens had the same CFRP layup, pin geometry and array size so a direct comparison could have been made if the CAI tests had been undertaken. Prior to the impact, a "window" was fixed over each specimen to provide a fixed boundary condition; in a similar manner to that reported by Rhead [75]. The unpinned panel and one of the pinned panels were hit centrally and the second pinned panel was impacted at the edge of the array; as indicated by the black dots in Figure 3.26. Note that that all three panels were struck with an impact of 30J and that the panels with reinforcement were impacted from the opposite side to which the pins were inserted.

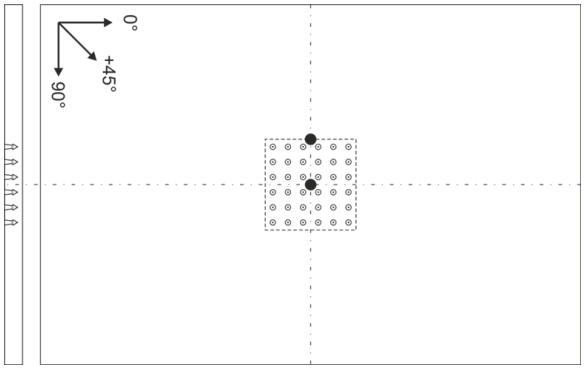

Figure 3.26: Specimen used for impact tests and subsequent NDT. All three panels were 150×100×5 mm. Two were reinforced with 36 HYPER pins, inserted centrally. Black circles show the two impact locations; one in the centre and one at the edge of the array.

Pulse-echo inspection was conducted from the impact side of the panels. This directed the incident waves towards the tips of the pins (rather than the roots) unlike the preferred method in the previous study. It was believed that damage would predominantly surround the pin array and any loss of signal/focus *within* the pin array would not be as significant for this particular study. This orientation was also more representative of an in-service damage/inspection event on an aircraft as impact damage would be more likely to occur on an external surface and the HYPER joined component be attached internally. For example, it would also be more straightforward to inspect the cover of a wing from the outside. The scan area was 100 mm square which covered the entire width of a panel. A 25 mm strip was excluded from the top and bottom of the coupons as it was not anticipated that any damage would have propagated to these boundaries. Otherwise, the setup procedure was identical to the other ultrasonic inspections already reported; e.g. 35 MHz probe, scan speed of 10 mm/s and transverse step of 0.1 mm. As detailed in Section 3.3.2, CT scanning was conducted using a Nikon X-Tek XT-H-225-ST, reconstruction with Nikon CT Pro 3D and post-processing with Avizo Fire.

3.7.2 Results

All three panels were CT scanned and also ultrasonically scanned. Unfortunately, porosity within the unpinned laminate reduced C-Scan quality. Figure 3.27 shows a cross-sectional CT scan in which the extent of the porosity can be observed. This panel was manufactured by Airbus Group and it is believed that the panel was not consolidated adequately and/or frequently enough during the layup procedure. These resin rich features may have "blunted" crack tips and reduced propagation of delaminations. Hence, it is likely that this made comparison of the samples somewhat conservative as damage would have been more extensive in the reference panel; if it had been pristine like the two reinforced panels.

Figures 3.28 to 3.30 each show an ultrasonic C-Scan and an enhanced CT rendering for each of the specimens; left and right respectively. The unpinned panel initially appeared to be less severely damaged, however, the CT image shows additional delamination at ≈4.5mm from the upper surface of the laminate. This is shown in red/orange in Figure 3.28. The thickness has been scaled in this isometric view to separate delaminations and improve visual clarity. It is believed that the deepest delamination could not have been observed with ultrasound unless the specimen had also been scanned from the second side. This is was due to the incident wavefront being reflected from the more shallow delaminations and thus, there was insufficient energy in the signal to transmit any deeper into the panel. This could potentially have been avoided by using a lower frequency probe but spacial resolution would then have been reduced.

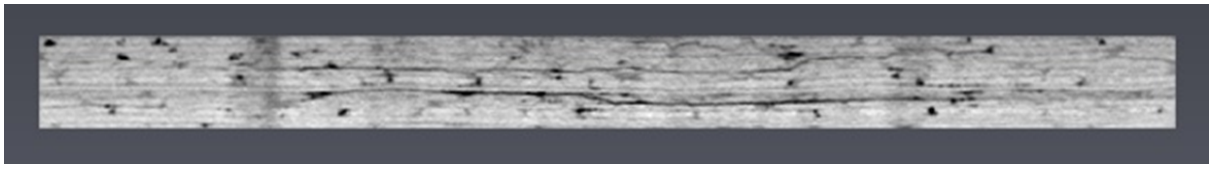

Figure 3.27: CT image of reference panel showing damage and significant porosity.

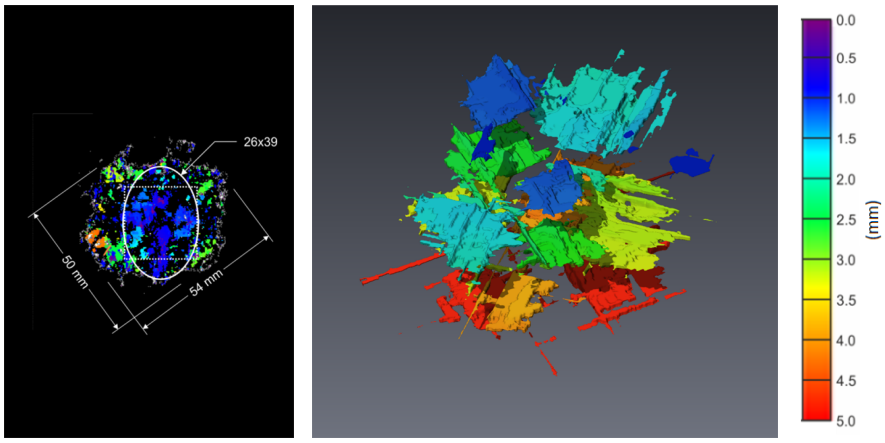

Figure 3.28: Unpinned specimen with central impact of 30J. C-Scan (left) and CT Scan (right). Porosity reduced the quality of the C-Scan. The deepest impact is hidden in the C-Scan but visible in the CT scan. Thickness scaled to improve visual clarity in isometric view.

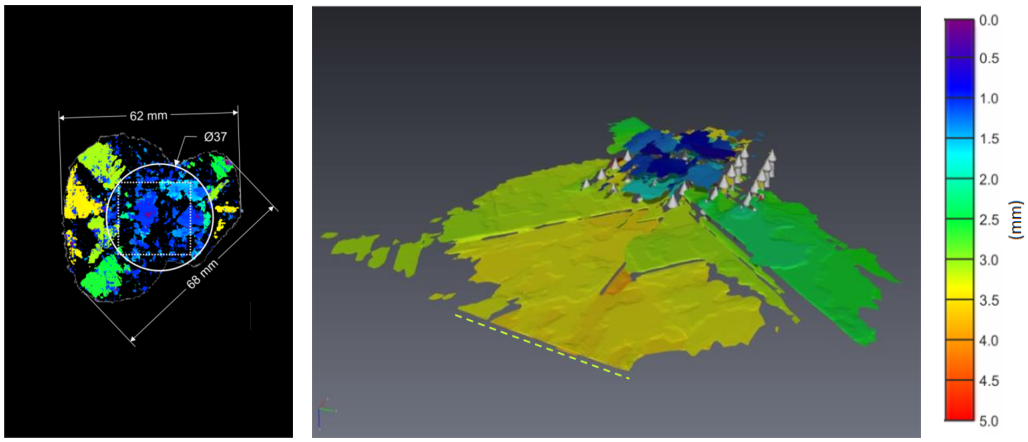

Figure 3.29: HYPER Panel 1; 30J impact at the centre of the array. C-Scan (left) and CT Scan (right). Dashed line shows where the delamination exceeded the sampled volume.

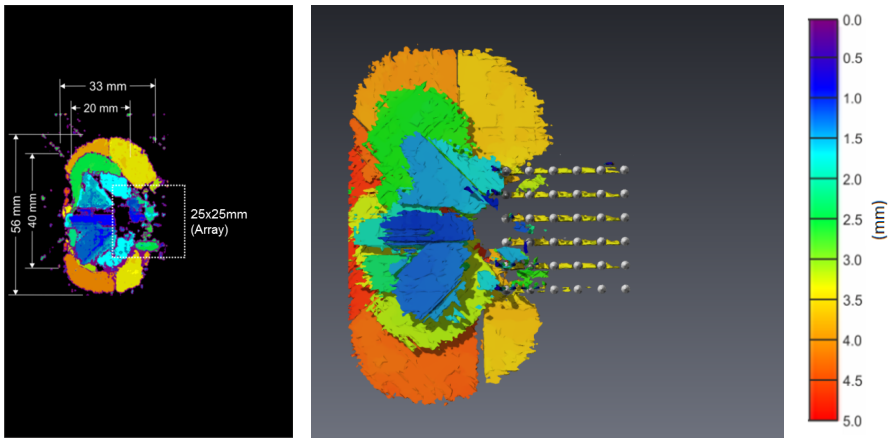

Figure 3.30: HYPER Panel 2; 30J impact at the edge of the array. There was an excellent correlation between the ultrasonic C-Scan (left) and CT Scan (right).

However, damage was still significantly more severe in the reference panel than the two HYPER panels that were also impacted with 30J. Summation of the delamination areas was approximately 5050mm^2 for the reference, 3600mm^2 for HYPER Panel 1 (central impact) and 3475mm^2 for HYPER Panel 2 (impact at array edge). Therefore, it is proposed that HYPER pins restrict the growth of delaminations. This is emphasised by the asymmetric growth observed in Panel 2; see Figure 3.30. Although there are some delaminations between pins, it is believed that the array has limited the extent of lateral propagation. The clamped boundary condition did then influence direction of growth (given the straight edge of the left side of the delamination). Assuming a mode shape with double curvature, upon approaching the point of inflection, the delamination would have slowed laterally but continued to grown up and down the panel prior to arrest. Delaminations were primarily in the central third of the laminate (through-thickness) at the pin tips and widest point of the pin head. It is proposed that this was due to some initial imperfections during manufacture; fibre misalignment, etc. It is also observed that delaminations are generated deeper within laminate in Panel 2 and are at comparable level to the panel without reinforcement (red/orange, ≈4.5mm). It is hypothesised that this is the result of inducing higher curvature and membrane strain in the reference and Panel 2. In the reference, this is due to increased compliance (without reinforcement) and thus increased central deflection, as shown in Figure 3.31. However, in Panel 2, curvature is high (on one side) due to a combination of the offset impact site and requirement to maintain an appropriate mode shape with the clamped boundary condition. It is recommended that compression testing of these panels and further analysis of this problem is completed as part of a future work programme in order to "close the loop".

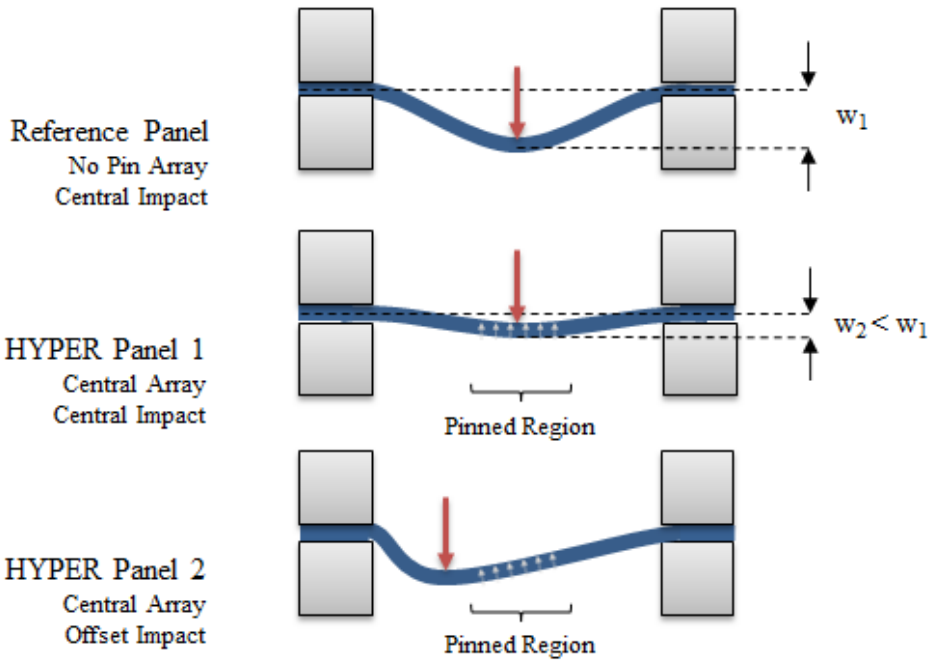

Figure 3.31: Mode shapes induced during impact due to clamped boundary conditions. Illustrative only, not to scale.

From an NDT perspective, it can be seen that there is excellent correlation between the ultrasonic and CT scans for both HYPER panels. Given that the capital expenditure and process time required to generate the CT scans were an order of magnitude higher, the advantage of ultrasonics is clear. Maintenance is also more routine and can be conducted by internal technicians rather than having to have a maintenance contract. The working envelope of CT systems is also an order of magnitude lower than ultrasonic systems and, although less of a problem for research and coupon testing, this restriction would rule out CT for many industrial applications.

3.8 Concluding Remarks

The HYPER joint manufacturing methodology and pin profiles are unique and they are inherently challenging to inspect. As a result, little application specific information was found in the public domain and no details of NDT research programmes were reported in the literature for similar hybrid joining technologies (such as Comeld and CMT).

X-ray computed tomography was found to be very effective for assessment of flaws within the CFRP laminate *and* the pins. Advanced post-processing utilities were exploited to extract and visualise both defects and damage. This capability enabled a number of test cases to be generated as benchmarks for the other methodologies subsequently investigated. Artefacts were generated due to the large difference in material density and X-ray absorption but these were not prohibitive to evaluation. Overal, despite impressive results, CT scanning was found to be a time consuming and expensive process that would not suitable for a production environment with larger components or increased throughput of parts.

Thermography was found to be effective for detection of surface breaking flaws (cracks at the edge of the joint interface) but this only provided *limited* information. This may be suitable as initial inspection but a secondary method would still be required for a comprehensive and quantitative evaluation of damage magnitude. Internal defects could not be identified with the methods investigated. A numerical thermal model showed that even by using the structure of the joint advantageously (transmission through the highly conductive of the metallic part), adequate contrast and resolution could not be achieved.

Pulse-echo immersion ultrasound was the third method of non-destructive inspection trialled during this project. Initially, application of this technique to HYPER joints was not promising as C-scans lacked clarity. It was believed that this was the result of the conical heads of the HYPER pins scattering the incident signal. Modelling was subsequently used to analyse this problem and this revealed that the scattering effect could potentially be reduced with the use of a smaller diameter probe, although this was not proven experimentally. However, inspection capability was significantly improved by rotating the specimens so that evaluation was conducted through the metallic substrate. Although resolution was not as good as that achieved with CT, this strategy was still capable of detecting disbonding of the joint interface, delaminations within the composite *and* defects within the pins. This was a crucial finding.

Inspecting through the metallic substrate did still present challenges. This included the potential for "repeat" signals to mask damage at certain depths within the laminate, however, a strategy to assess these zones was also proposed.

Although pulse-echo immersion ultrasound has been demonstrated to be a successful method for non-destructive inspection of coupon-sized HYPER joints (further validated is provided in later chapters), the method is not without its limitations. In a real application it may not be possible to access the metallic side of the joint and, even if it is, there may not be a planar face behind the pin array. For example, there could be geometric features on the metallic component that would obstruct the path of incident ultrasonic waves. It is hoped that this risk can be mitigated by improving inspection capability from the composite-side of the joint.

It was proposed (following the analytical modelling herein) that the use of a smaller probes and phased-array techniques should offer increased resolution. It is strongly recommended that, as part of a future HYPER joint research programme, experimental trials are completed to test this hypothesis. Furthermore, although immersion ultrasound can be simulated in a production environment with a water-jet system, the use of a "dry" probe (coupled with a thin film of gel) would be desirable and, thus, should also be trialled. The development of a bespoke inspection utility was begun but this should be evolved further as it is believed to offer the best method for an integrated inspection system that could combine HYPER specific techniques within a single, user-friendly interface.

Finally, it is also recommended that compression testing is conducted with the panels that were impacted during this investigation. Furthermore, additional damage tolerance analysis should be conducted with the insertion of a more representative HYPER-joined metallic component. A larger composite panel would also reduce the influence of the test boundary conditions and, again, make the test more representative of a real application.

Chapter 4

Static Performance

4.1 Summary

Single-lap HYPER joint coupons are subjected to quasi-static mechanical testing. Different pin geometries and surface treatments are evaluated and compared. An ultrasonic, non-destructive inspection method is also used to determine failure modes. It is shown that the pins delay the initiation of failure, slow the propagation of damage and increase the ultimate tensile strength by 6.5 times compared to an unpinned co-bonded reference joint. The mean elongation at failure is also increased by 407% and energy absorption by 83-fold. Surface "nano-structuring" is found to improve titanium-composite adhesion strength and consistency; the range was reduced by over 50%. Subsequently, an approximately 25% higher load is required to initiate failure as damage occurs within the laminate rather than that the interface beween substrates.

4.2 Motivation and Objectives

Pilot studies by collaborators at Airbus Group Innovations suggested that HYPER joining provided a large increase in ultimate strength and toughness compared to an unpinned co-bonded reference. However, a comprehensive assessment of pin geometry and/or joint configurations had not been undertaken. Furthermore, investigation of non-destructive testing methodologies by the author (Chapter 3) revealed that manufacturing quality and, in particular, bonding of the metal-composite interface, could still be inconsistent. Thus, the objectives of this chapter were to quantify the upper and lower bounds of HYPER joint performance for multiple pin geometries. For example, a conservative measure of strength could be gained by artificially disbonding the interface. Secondly, if possible, improve the bond strength and consistency through investigation of surface treatments and increase the joint strength beyond that of standard co-bonding. For each case, utilise the NDT knowledge gained to date to monitor the associated failure modes and further improve characterisation of this technology. This would allow more informed decisions to be made on future design perturbations. This would also serve to validate the ultrasonic NDT methodology, albeit still in a research environment.

4.3 Background

As described previously in Chapter 2, through thickness reinforcement with stitches, rods or pins can significantly improve mechanical performance (both strength and toughness) of adhesively bonded joints [54]. Crucially, unlike mechanically fastened joints, the substrates does not have to be drilled and fibres cut/damaged. Stitches are typically 0.5-1.0mm in diameter and can provide a 40% increase in UTS. Fatigue life can be increased by two orders of magnitude. Chang et al. [16] present a thorough experimental investigation of Z-pinned single lap joints using two pin diameters (0.28 and 0.51mm) and three pin densites (0.5-4.0%). The UTS is again increased by up to 40%, the elongation to failiure by 55% and fatigue strength by 40% at 10^6 cycles.

Stitching and Z-pinning are now comparatively mature concepts having been first proposed in the early 1980's [45] and studied extensively since. More recent advances in manufacturing technologies for metals have enabled integration of hybrid metal-composite structures using similar pinning techniques. Smith reported preliminary experimental results of the Comeld joining system which utilised the "Surfi-Sculpt" surface texturing method [80]. Steel-composite double-lap joints achieved a 31% increase in UTS compared to a co-bonded benchmark. Elongation at maximum load was approximately twice that of the reference joint. The pins do not have a head feature which is a distinct disadvantage as they would be suceptible to pullout. Thus, it is proposed that performace gains would be less significant if a single-lap coupon had been used. This is because of the inherent rotation of this type of joint and the increase in peeling at the edges of the overlap (Mode I). Furthermore, unlike other pinning methods found in the literature, inclusion of the pins could exhibit a brittle failure response. Catastrophic seperation of the adherends resulted from interlaminar shearing of the laminate at the tips of the pins. This was due to the low aspect ratio and high density of pins so the layer into which the pins penetrate would have have a high equivalent modulus. Hence, there would have been minimal deformation of this "protrusion" layer and the plane of load transfer was translated to the boundary with the unpenetrated laminate, see Figure 4.1.

This failure mechanism is in contrast to the ductile response of joints reinforced with slender welded pins, fabricated by cold metal transfer (CMT). Experimental performance of the CMT technique was presented by Ucsnik et al. [90]. Again, double-lap metal-composite joints were compared to an adhesively bonded benchmark. This pin welding approach allowed freedom to vary the pin design and two style were evaluated; straight cylindrical and ball headed. An 11% increase was achived with the straight pins and a 52% increase with the ball headed pins. Elongation at maximum load was increased by 470% and 1000% respectively which resulted in up to 30 times the energy absorption. Whilst the stright pins eventually failed by pullout, the ball head features prevented this mechanism, causing ultimate failure to be shearing and fracture of the pins close to their roots; as shown in Figure 4.2. These vast increases in allowable strain clearly show the advantage of plastic pin deformation. The increased pin penetration and inclusion of $\pm 45^\circ$ plies in the laminate would also have been of benefit compared to the Comeld joints which used a $0/90^\circ$ layup.

Figure 4.1: Double-lap Comeld joint fabricated from glass fibre and steel. Plane of failure can be seen above/below the protrusion layer [80].

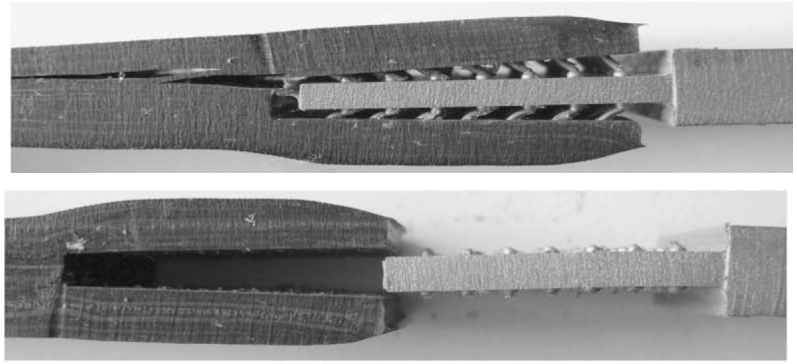

Figure 4.2: Comparison of CMT failure mechanisms. Straight-cylindrical pins were prone to pulling out of the composite. The inclusion of a ball shaped head feature prevents pullout of the pins and they fail by shear close to their base [90].

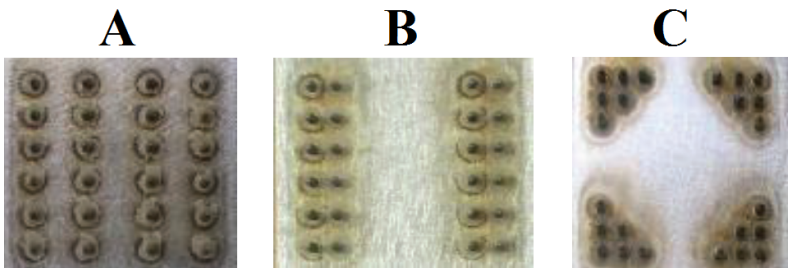

Figure 4.3: Array designs tested by Stelzer et al. [82]. Design A achieved the greatest ultimate load due to dispersion of pins across the length of the overlap. Design B required a greater load to initiate damage because of the higher pin density at the edges of the overlap. Design C was the weakest of the three.

Stelzer et al. developed this work further in a later paper focusing on single-lap, composite-composite joints reinforced with interleaved plates that had pins welded onto both sides using CMT [82]. The notable feature of this work was that design perturbations were made at the array level rather than varying the pin geometry; the designs A, B and C are identified in Figure 4.3. All three designs achieved a large increases in UTS compared to an unpinned reference joint: 97, 87, 69% respectively. Design A had the greatest UTS due to even dispersion of pins across the length of the overlap. Once the damage has accumulated at the edges of the overlap and the outer rows yielded, the load can be picked up by the inner rows. These central pins provide a crack arrest mechanism once damage propagates inwards. By increasing the density of pins close to the edge of the overlap (Design B), peeling and shear stress concentrations were reduced and a greater load was required to trigger damage initiation (the first failure event, F1). Compared to the unpinned reference, increases in F1 of 70, 79 and 56% were reported for Designs A, B and C respectively.

Nogueira and colleagues at Airbus Group Germany tested the "RHEA" concept which, like the work of Stelzer et al. [82], used interleaved plates with double-sided pins to join composite-composite substrates [68]. The pins were, however, not welded but pressed from the interleaved sheet. Although the increase in performance, compared to a bonded benchmark is still impressive (19% increase in UTS and 69% in elongation at maximum load), the gains were not as impressive as those presented by Stelzer et al. in their 2013 paper [82]. Due to the lack of bulbous head feature, constraining pullout of the inserts, the pins act more like Z-pins and bridge delaminations rather than carrying a large shear load and failing by fracture at the base.

4.4 Test Coupon Specifications

The objective of this work was to investigate several HYPER design variables with coupon-scale tests. Single lap shear specimens were used. The Airbus Baseline pin design and joint geometry was tested with three different interface conditions (no bonding, standard bonding and enhanced bonding). An alternative pin design (the "Bath Baseline") was also tested with the same three interface conditions and an unpinned, co-bonded metal-composite joint was tested as a benchmark. Specimens were labelled SLS-XX-YY in order to differentiate manufacturing batches (XX) as well as the individual coupons (YY); as previously described in Section 3.6. A test matrix is shown below in Table 4.1 and a full index of specimens/results in Section 4.6.5.

	Disbonded (PTFE)	Standard Bonding	Laser Treated (LT)
Unpinned Reference	-	6	-
Airbus Baseline	3	6	3
Bath Baseline	3	3	3

Table 4.1: Test matrix for quasi-static investigation.

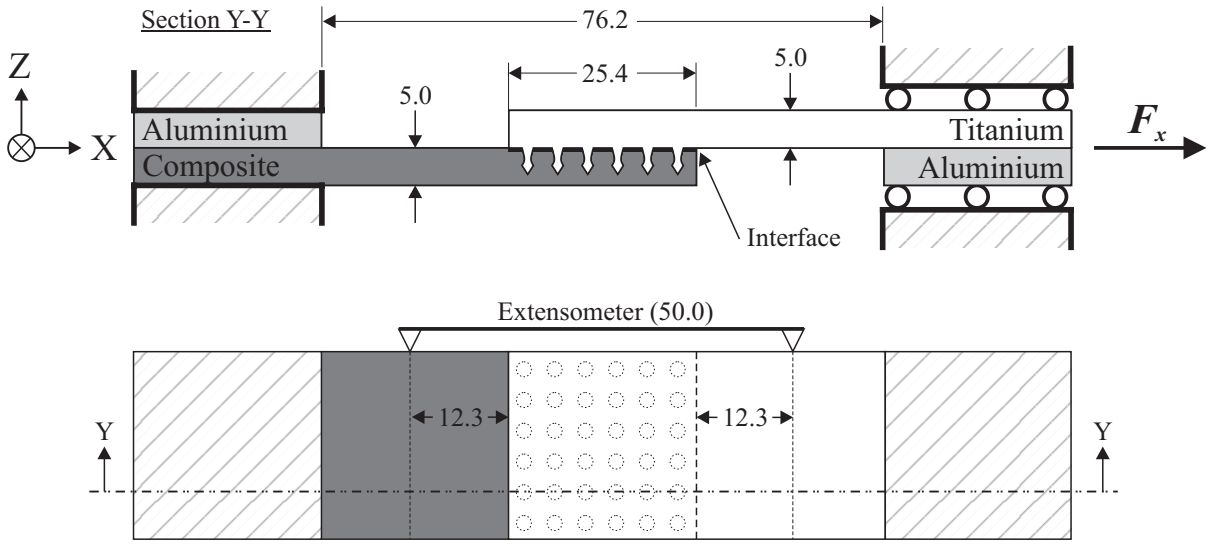

Figure 4.4: Section and plan view of the test specimens showing pins, boundary conditions and instrumentation. All dimensions in millimeters, geometry illustrative, not to scale.

4.4.1 Adherend Geometry

The metallic substrate was titanium alloy (Ti-6Al-4V) and the composite adherend was constructed using Hexcel M21-T800S. Both titanium and composite adherends were 101.6mm long, 25.4mm wide and had a nominal thickness of 5.0mm. Twenty 0.25mm plies were required and a 20/60/20 (0, 45 and 90° respectively) ply percentage used: $[\pm 45/0/90/\pm 45/0/90/\pm 45]_S$. The gauge length (76.2mm), overlap length (25.4mm) and number/pitch of pins was fixed for all tests. The overlap contained a uniformly distributed, 6×6 array of additively manufactured HYPER pins. Aluminium tabs were adhered to the ends of the substrates to maintain the adherend offset, allowing the coupon to be clamped in a standard set of tension jaws and the load applied through the centreline of the specimen (see Figure 4.4).

4.4.2 Pin Geometry

The key dimensions of the two pin designs tested are listed in Table 4.2. Both designs had a conical head feature to aid embedding and then "grip" the fibres providing a mechanical interlock following consolidation. The pin height and head angles were identical for both types and all pins penetrated 72% through the laminate. The root or base diameter of the pins (D_b) was the difference between the two designs and the alternative geometry was 17% larger than the Airbus design. This revised design was known as the "Bath Baseline" as it became the standard geometry tested by the author at the University, it was not a design investigated by Airbus Group Innovations prior to the research collaboration.

Description	D_b	D_n	D_h	Z	θ_1	θ_2
Airbus Baseline	1.2	0.9	1.5	3.6	90	60
Bath Baseline	1.4	0.9	1.5	3.6	90	60

Table 4.2: Pin geometries used during the static testing. Dimensions in millimetres and degrees; as per Equation 2.1.

4.4.3 Interfacial Treatments

The standard interface condition was resin bonding between the CFRP and titanium adherends due to redistribution of matrix during consolidation and co-bonding. This planar interface is identified in Figure 4.4. Polytetrafluorethylene (PTFE) film was used for some coupons to artificially generate a disbond at the flat interface between adherends. This isolated the contribution of the pins and provided a conservative measure of strength. This was designed to be analogous to a weak/contaminated bond. The PTFE was placed onto the laminate prior to the embedding of the pins - which subsequently penetrated this additional layer as they were pressed into the laminate. Laser induced, surface "nano-structuring" was also trialled for a select number of coupons in an attempt to enhance adhesion of the epoxy matrix to the titanium [53]. This was applied to the metallic substrate prior to integration with the CFRP. Unless specified as laser treated, the default surface preparation for the metallic part (following additive manufacture) was gritblasting.

4.5 Experimental Methodologies

4.5.1 Overview

Two different loading strategies were employed. Primary tests were loaded in one continuous action to identify the likely point(s) of damage initiation and rate(s) of propagation. These were determined as load discontinuities, changes in compliance or audibly if there was cracking. Based on these results, subsequent tests were then selectively halted in order to conduct ultrasonic NDT (described in Section 4.5.3) and determine the nature and magnitude of the damage. The coupon was then loaded again, typically to a higher load, to generate further failure events. This process was repeated until ultimate failure was achieved; commonly five to eight loadings. This two phase approach also determined whether or not the interrupted NDT method had an impact on the UTS.

4.5.2 Tensile Testing

The HYPER joint coupons were loaded in an Instron 5585 using displacement control at a rate of 0.05mm/min. This velocity was much lower than specified by the most applicable standard for testing of fibrous lap-shear specimens (ASTM D5868, 13.0mm/min [11]) but this reduced rate allowed small discontinuities and subtle changes in compliance to be observed. The coupon compliance was monitored with an extensometer; as shown in Figure 4.4. Data acquisition (load, displacement and extension) was accomplished using Instron Bluehill software and a CSV file exported for post-processing. Data must be exported with resolution specified to the maximum number of significant figures not decimal places or else the accuracy is inadequate for analysis; there were discrete steps in the data. Additional instrumentation was also utilised for two preliminary tests to assess the quality of the machine setup and test procedure. This included: dial gauges for out of plane deflection, digital image correlation (DIC) and strain gauges. The strain gauges used were Vishay Micro Measurements 350Ω quarter bridges (N2A-06-T004R-350).

Data acquisition from the strain gauges required use of an additional computer with Spider8 and Catman hardware/software. Load data from the analog output of the Instron was transfered to the secondary system through a BNC connection. It must be ensured that voltage scaling in Bluehill and Catman is identical (e.g. 0.1V/kN). The DIC equipment employed was a stereo (dual camera) Limess system and post-processing was realised using VIC-3D. Imaging was conducted across the width of the coupon during one test (x-y plane) and on the side face for a second (x-z plane). In order to correlate the applied load and data from the DIC system, a LCD was connected to the Instron digital output to provide readout of force and positioned in camera shot.

It was paramount to ensure the test setup procedure was extremely consistent as some coupons had to be repeatedly removed from the machine for non-destructive evaluation. The configuration of the test machine is shown in Figure 4.5.

1. The lower jaw assembly was pinned into the mounting boss on the bed of the Instron 5585. The jaws required for the lap-shear testing were one inch wide and had a "thin" set of inserts attached in order to provide the range required (0.25-0.50inch). With reference to Figure 4.5, lock ring A was tightened clockwise (right-hand thread). All rotational directions, described below, are as though the machine is viewed from above.

2. A piece of metallic bar was clamped into the lower jaw by rotating handle 1 anti-clockwise. This dummy specimen was used to ensure that the upper and lower jaws were concentric and co-planar.

3. It was found to be essential that the rotary backlash from the lower jaw assembly was now removed by rotating the outer casing of jaws clockwise. This prevented excessive twisting of the specimen as the second jaw was fastened. The same procedure was followed for the initial setup of the machine and clamping of the test coupons.

4. With the upper jaw and mounting bosses assembled in the Instron crosshead, the crosshead was lowered to set the gauge length and the upper jaw clamped onto the coupon (clockwise rotation of handle 2).

5. Lock ring B was now tightened against the mounting boss (righthand thread, anti-clockwise) and, crucially, the applied force reacted against the upper jaw casing to minimise twisting of the bar/test coupon. Finally, locking collar C was tightened against the Instron crosshead (left hand thread, rotated clockwise).

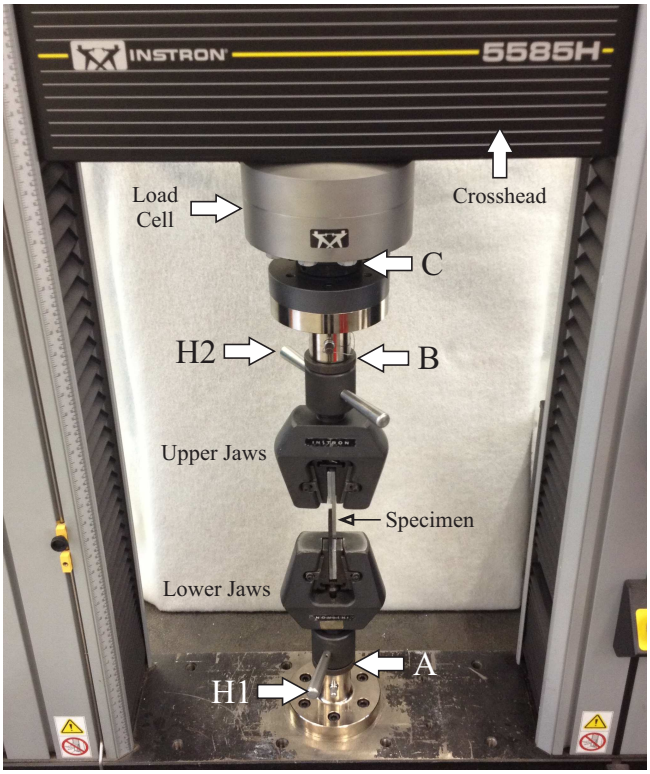

Figure 4.5: Test setup, with locking rings (A-C) and handles (H1-2) identified. Extensometer and digital image correlation system removed for clarity.

The metallic bar/dummy specimen was removed by reversal of the fitting procedure (excluding steps 1 and 5) and the machine was now prepared for testing. The procedure varies slightly for clamping of the actual test coupons because they were fastened into the top jaw (connected to the load cell). By balancing the cell before clamping the lower jaw, the weight of the coupon could then be discounted. Hence, after tightening, the casing of the upper jaw must be rotated anti-clockwise to remove the rotary backlash. Despite carefully following this protocol, it was found that twist could still be induced in the coupons. The consequences of this imperfection are discussed in the Results (Section 4.6.4).

4.5.3 Non-destructive Evaluation

As shown in the previous chapter, it was found that the success of ultrasonic inspection of HYPER joints is dependent on the orientation of the specimen [71]. Assessment of damage through the carbon side proved difficult as C-Scans were distorted by undesirable signal noise. It is believed that this was caused by the laminated structure and the pins scattering the incident signal due to the angle and surface irregularity of the head feature. However, it was found that inspection of the interface can be achieved from the metallic side, due to the comparably undistorted response of titanium. This technique will be used extensively throughout the remainder of the experimental programme.

As HYPER pins are an integral part of the metallic adherend, when the ultrasonic probe passes over an unbroken pin, there is no discontinuity and the wave front travels into the pin; see Figure 4.6. This is subsequently scattered so there is no (or a very weak) signal reflected and the pins can be observed. Furthermore, signals reflected from a disbond are much stronger than those from a good bond. By selectively excluding weaker signals bondline quality can be determined [41]. Similarly, if the stronger signals are excluded, weak echoes returned by fractured pins can be observed [70]. All coupons were inspected before testing to ensure bond/pin quality and generate a reference image for those subjected to the interrupted approach (see Chapter 3).

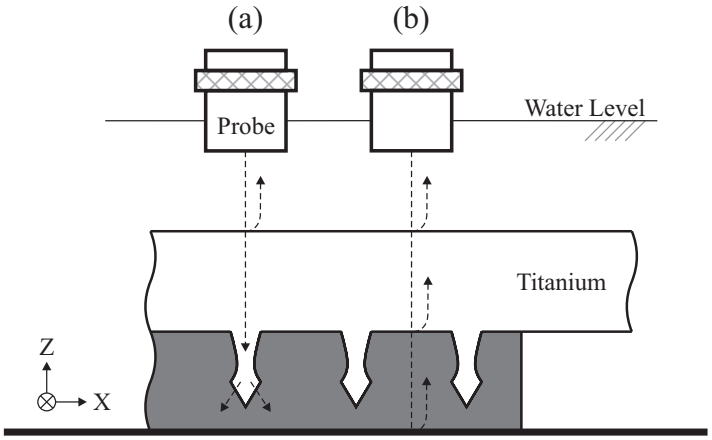

Figure 4.6: Orientation of the coupon for non-destructive inspection. Ideallised wavepaths also shown for two probe positions. (a) Over a pin no signial is returned due to scattering of the incident signal. (b) Between pins an echo is generated at the interface between substrates.

Unfortunately, NDT could not be conducted in-situ so coupons had to be removed from the testing machine for inspection. However, using a bespoke jig (see Chapter 3), consecutive scans could be conducted with ease. A spherically focused, 35MHz probe was again used with a focal length of 1.5 inches (38.1mm). To focus the probe on the interface the theoretical probe offset (water path) was 18.1mm however this was manually adjusted (typically ≈1-2mm) to maximise the strength of the reflected signal. The scanning speed was 10mm/s and the transverse step size was 0.1mm. The scanning window (region of interest) was 35mm square. This was centered on the overlap region and allowed an additional 5mm boundary on each side. The gain was set at 20dB to ensure a strong signal was reflected from the interface.

4.6 Results and Discussion

Firstly, the ultimate tensile strength of each pin design and interface condition is compared. Secondly, stiffness variations and discontinuities in applied load and extension are identified to determine the onset of damage. Finally, results from the non-destructive testing are analysed in order to characterise these failure events/sequences. In addition, the influence of coupon manufacturing quality and the setup procedure are also discussed.

4.6.1 Ultimate Tensile Strength

4.6.1.1 Airbus Baseline Design

Figure 4.7 shows a comparison of the ultimate tensile strength of the coupons tested. The Airbus Baseline design with a standard resin co-bond is more than five times stronger than the unpinned reference joint. The use of PTFE and subsequent lack of interfacial bonding between substrates reduces the ultimate tensile strength of this joint by 8% showing that matrix co-bonding does influence performance. There was also less scatter when the coupons were artificially disbonded with PTFE and, hence, it is assumed that the variation found with the standard co-bonding resulted from inconsistent adhesion. The laser treatment had a less significant effect joint strength as, on average, the UTS was only 2% higher than the standard interface condition. However, this treatment did improved the consistency of the co-bonding as the range was reduced significantly (from 3751N to 2152N).

4.6.1.2 Alternative Design (Bath Baseline)

Changing the root diameter of the pins further increased the strength of the HYPER joints. Coupons with standard bonding were 25% stronger than the Airbus geometry and 6.5 times higher than the average reference joint. There was a similar knockdown in UTS when the interface was artificially disbonded and also a minor increase with the laser treatment (9% and 1% respectively). Again, the major difference resulting from the laser treatment was a reduction in scatter and the range was far lower compared to the standard bond for this pin geometry (from 2152N to 1197N).

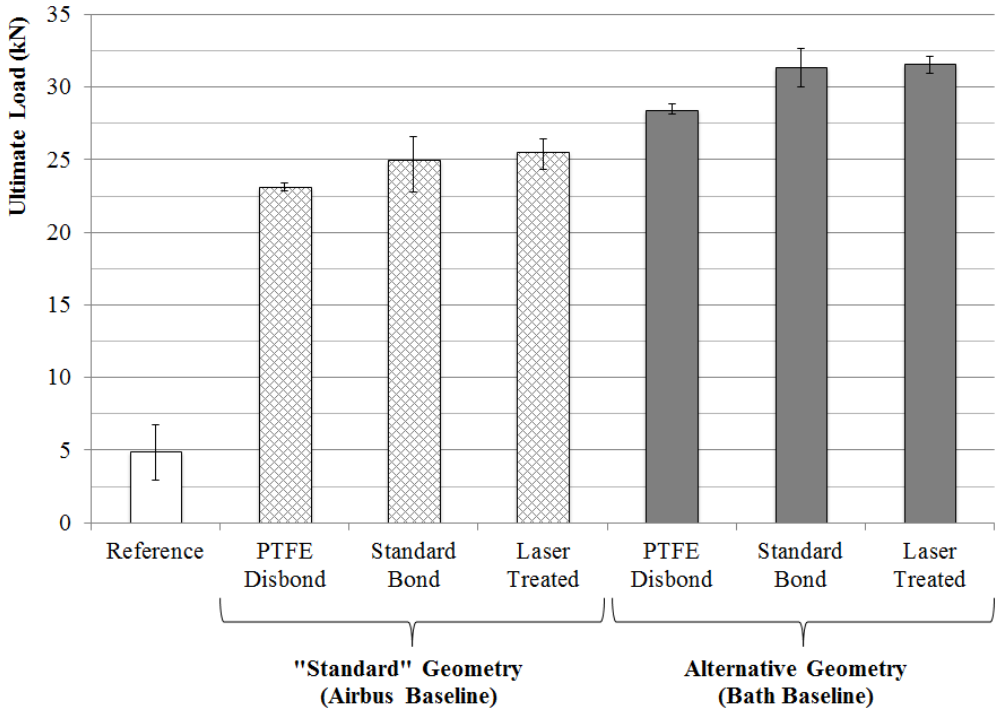

Figure 4.7: Comparison of ultimate static strength; unpinned reference (white), Airbus Baseline (hatched) and Bath Baseline (grey). Whiskers show range of each data set.

This alternative design with laser treatment is not only the strongest configuration but also achieved the highest elongation at the point of failure. The mean extension was 407% greater than the benchmark joint which equates to a 83-fold increase in energy absorption (16.7J compared to 0.2J). Force-extension data is shown in Figure 4.8.

Although these results show significant improvement, a 36% increase was anticipated given the difference in pin shear area. It is thought that, although the pins carry some load whilst the bondline is intact (unlike a bonded-bolted joint [46]), the magnitude is much more significant once the bondline is damaged. As the interface disbonds, the load redistributes to the outer pin rows which, it is assumed, subsequently yield. Some of the load is then transferred to those pins positioned more centrally in the overlap. However, this second redistribution is inadequate to uniformly share the applied stress across the overlap and the pins closest to the edges remain more highly loaded. This leads to failure before the idealised prediction which was based on the total load being averaged evenly across all pins.

Despite the different pin profiles, coupons were all from the same AM batch so any heterogeneity would be similar for all coupons and it is not thought that the process would be sensitive to geometric change of this magnitude. Furthermore, all PTFE coupons were tested in the continuous manner so the interrupted technique is not thought to be a factor given that the difference is consistent for both PTFE and coupons with standard bonding. Misalignment of fibres during embedding of the pins would increase with pin diameter but, again, it is not thought that a change of this magnitude would contribute significantly. The influence of fibre misalignment is explored with finite element analysis in Chapter 6.

4.6.2 Initiation of Damage

Figure 4.8 compares force-extension data for three joint configurations. The Airbus (PTFE) and Bath (laser treated) baseline results are included to show the performance envelope of the HYPER configurations tested. It was thought that these two designs would have been the most and least compliant configurations respectively but it can be seen that any difference in stiffness is minimal given the experimental variation.

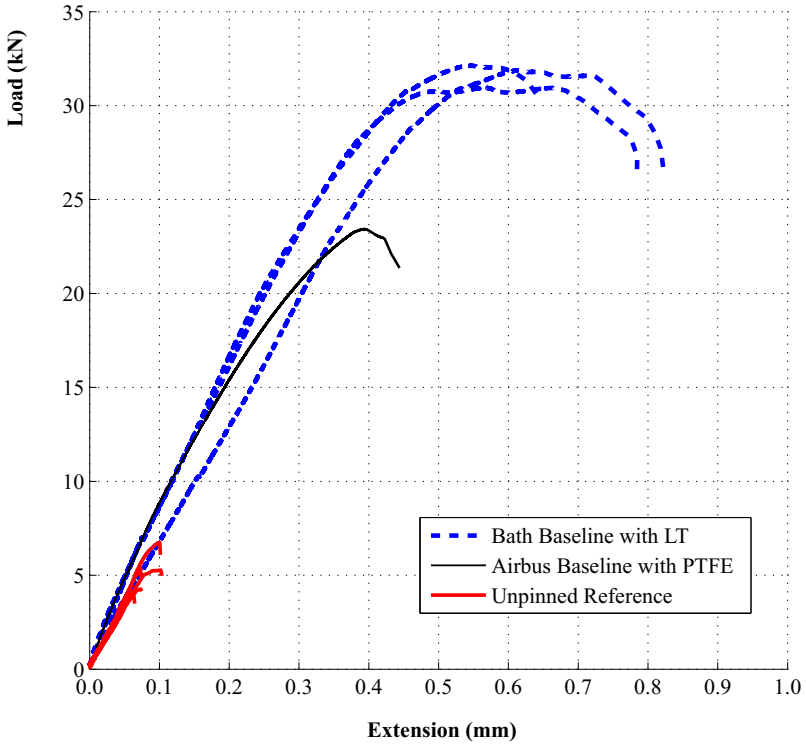

Figure 4.8: Comparison of load and specimen elongation (extensometer) for three joint configurations. The mean strength and energy absorption of even the weakest HYPER joint configuration (Airbus-PTFE) is far superior to the unpinned benchmark.

However, there were still detectable changes in compliance for all tests at low loads. For example, the Bath Baseline coupons (regardless of interface treatment), showed a small reduction in stiffness at about 2-3kN. This was then followed by more discrete event (discontinuity) but the load at which this occurred *was* dependent on the interface treatment. For the alternative geometry with standard interface bond, the discontinuity was observed, on average, at 5.5kN whereas the comparable laser treated coupons did not show a significant discontinuity until around 6.9kN. These primary events, at 2-3kN, were thought to be experimentally induced (e.g. the coupon slipping in the jaws and subsequently a small change in gauge length). The secondary events (discontinuities) are thought to be the initiation of matrix cracking at the edges of the joint and hence, define the "limit load" or first failure event (F1). Therefore, laser treatment increased the limit load of the HYPER joints by 25% compared to coupons with standard bonding. The limit load of the laser treated coupons even exceeds the ultimate load of the unpinned benchmark joints.

Although laser treatment provides the highest initiation load, the average F1 load with standard co-bonding is still higher than the (average) ultimate strength of the reference joint. This is further evidence that HYPER delays the onset of matrix cracking which is contrary to other hybrid joining schemes. For example, bolts have little influence on adhesive stresses at the edges of joints because of the minimum edge distances specified by established design rules [67, 62].

The responses shown in Figure 4.8 were all from tests that were completed in one continuously loading cycle. Figure 4.9 shows examples of force-extension data from two coupons that were subjected to the interrupted loading regime. The maximum load achieved for each stage of the test, and the point at which it was stopped for inspection, is highlighted with a circular marker. In general, it can be seen that the stiffness reduces with subsequent loading. This hysteresis would have be expected due to an accumulation of damage and/or yielding of the pins. However, this softening response does not occur for the penultimate/final loading and the coupons stiffen before finally failing. NB: It is believed that if coupon SLS-02-08 had not been stopped on the eighth loading and had run until failure, the response would have been identical to coupon SLS-02-09 (Figure 4.9). This effect was unlikely to have been experimental error (e.g. variation in setup procedure) as the response was consistent for both the coupons presented. Furthermore, the discrete nature of the response makes work hardening of the pins unlikely as it is anticipated that this would have been a more progressive change. It is thought to have occurred due to the sudden growth of the delamination in the composite at 20kN; see Figure 4.11. Although damage growth is more typically associated with a *decrease* in stiffness, it is proposed that because (for the laser treated coupons) the delamination is within the laminate, not the interface between substrates, extension-bend coupling is created. This induces bending in the opposite sense to the natural rotation of the joint and hence additional force is required to generate the same extension. It is recommended that, in a future work package, this hypothesis is tested by artificially seeding delaminations at different interfaces.

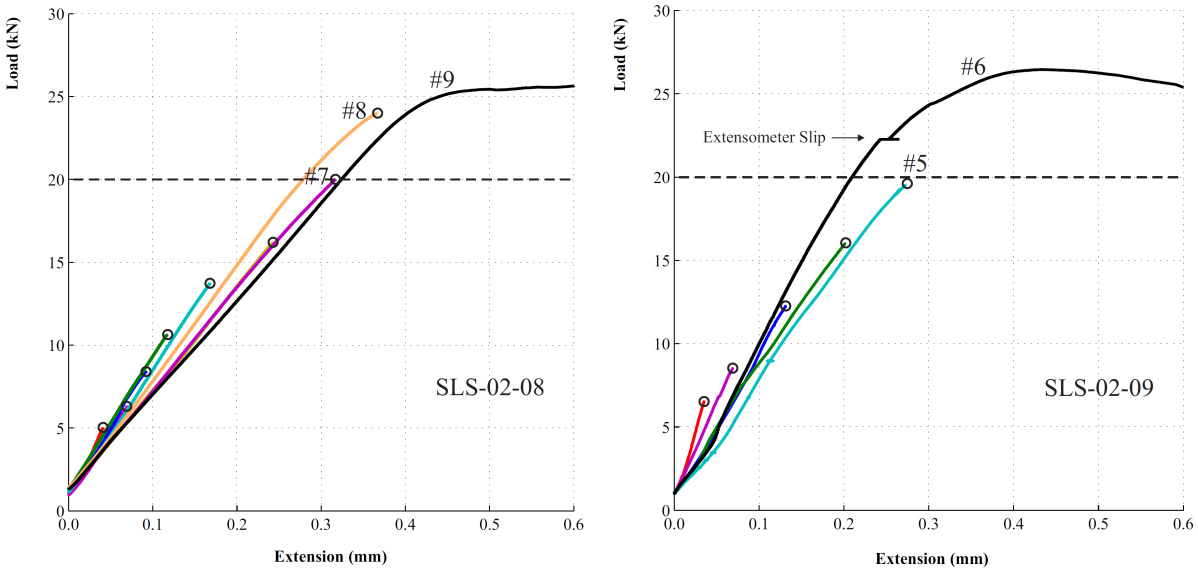

Figure 4.9: Compliance of coupons SLS-02-08 and SLS-02-09. Both specimens were subjected to the interrupted loading regime (load/unload/inspect). The peak force per cycle is shown with a circular marker. After loading to 20kN, both coupons exhibited a stiffer response.

4.6.3 Failure Analysis

4.6.3.1 Interface Disbonding

Through the use of ultrasonic non-destructive inspection, the propagation of damage at the adherend interface has been captured. Figure 4.10 compares the damage growth for two different coupons with the Bath pin design and standard bonding. Coupons 8 and 13 from Batch 1 were chosen for the interrupted regime as they appeared to have the most complete interfacial bond following manufacture. Although it is believed that F1 occurred at an average of 5.5kN (for the coupons with configuration), this was only determined following the completion of testing and the first ultrasonic inspection was not completed until the coupons had been loaded to 7kN.

This inspection revealed that a small amount of damage had indeed occurred and was observable adjacent to Side A. However, it should be noted that due to the loss of transducer focus at this edge of the coupon, it was not possible to observe the entire region between the outer row of pins and the edge of the overlap (see Chapter 3). Therefore, the damage on Side A of both coupon SLS-01-08 and SLS-01-13 may have been slightly larger than is shown in Figure 4.10. A second loading to 9kN was adequate to propagate the existing damage to the second row of pins and well inside the observable area. In the case of SLS-01-13, this second loading also initiated a disbond on the opposite edge (Side B).

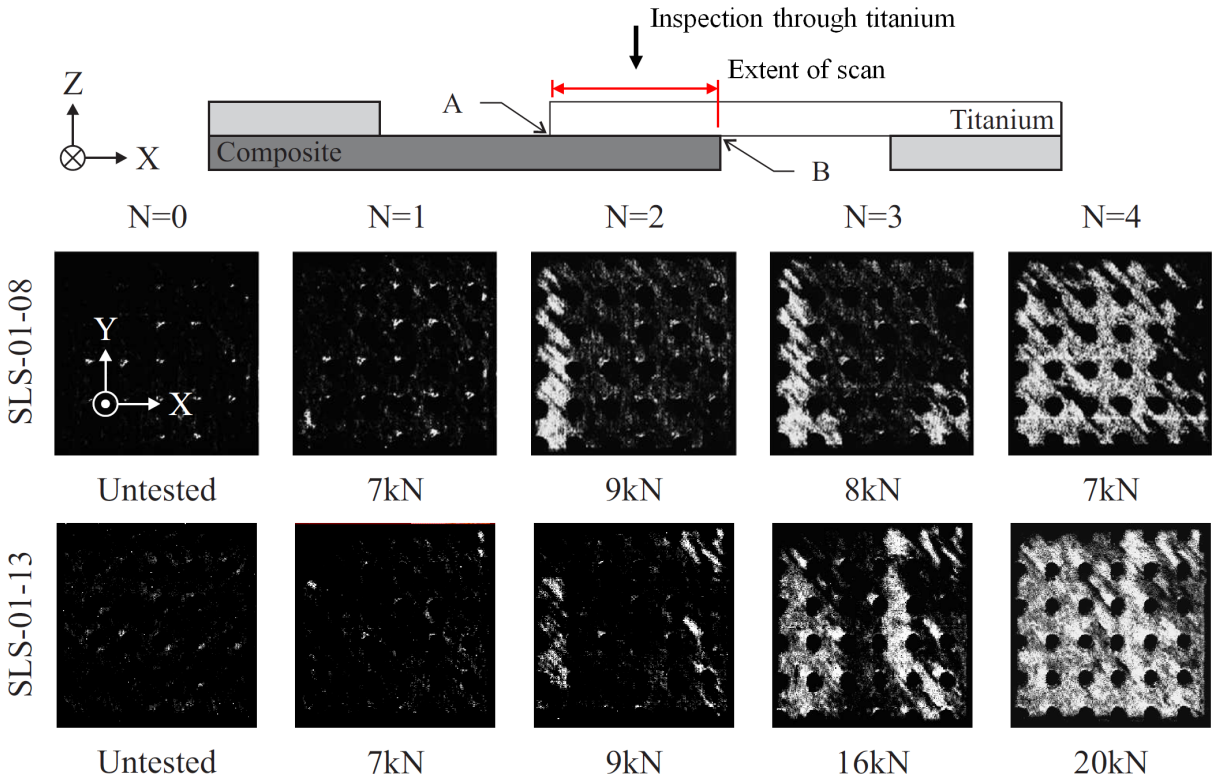

Figure 4.10: C-Scans of titanium-CFRP interface showing typical disbond growth with increased load for two coupons with standard bonding (Bath Baseline pin geometry). Intensity of white proportional to strength of reflected signal and severity of damage. Peak shear stress, and hence initiation, occurred first at Edge A (left-side of C-Scans).

The difference in adherend stiffness results the shear stress being higher at edge A of the overlap [1]. It would have been expected that damage would not only initiate at this side but would then continue to propagate from the same side as this boundary should remain more highly stressed regardless of disbond propagation. It is believed that a disbond also initiated at the Side B due to the outer pins on Side A sharing a higher proportion of the load following F1. This minimised peel/shear stress locally and *temporarily* prevented additional growth from the first edge. Although a third loading cycle was required to disbond both edges of coupon SLS-01-08, propagation of these disbonds was subsequently achieved at a lower loads than for SLS-01-13. Thus, there may have been a reduction in the bond strength within the central part of the overlap. Despite these differences in magnitude, the trend is the same for both specimens and propagation is restricted by discrete amounts due to the pins. For coupon SLS-01-13, a load of 20kN was required to grow the regions of damage adequately for them to connect and fully disbond the interface. Coupons with the laser treatment performed considerably better and disbonding is not only delayed but, subsequently, does not then propagate as severely as the standard bonded coupons when subjected to the interrupted loading regime. For all three examples shown in Figure 4.11, the extent and the rate of disbonding was very consistent. An additional inspection was included at 12kN compared to the coupons with the standard bonding. It can be seen that to induce a disbond on both sides of the overlap, at least an 80% higher load was required (16kN compared to 9kN for the standard, untreated coupons).

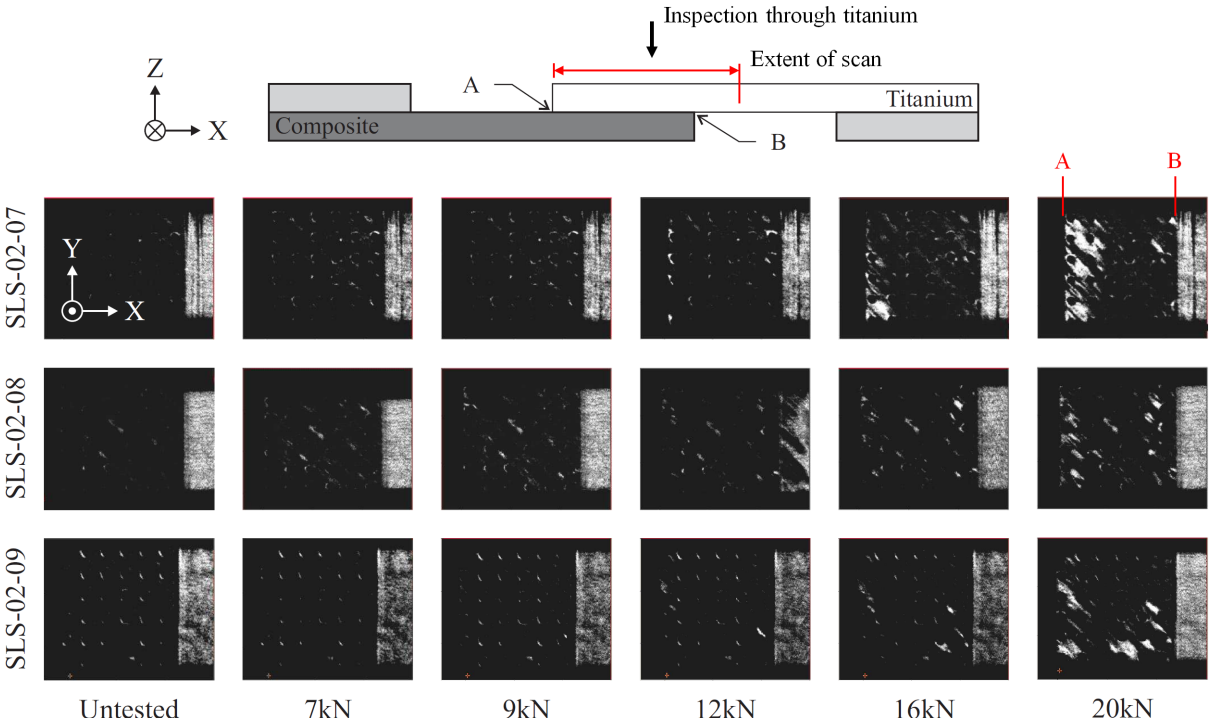

Figure 4.11: C-Scans of titanium-CFRP interface showing typical disbond growth with increased load for three laser treated coupons with the Airbus Baseline pin geometry. Adhesive failure at this interface was less significant compared to specimens without surface treatment. NB: These C-Scans show a larger proportion of each coupon than those in Figure 4.10 and, as a result, the titanium/water interface can also be seen to the right of Edge B.

It should be noted, "time of flight" C-Scans actually revealed a change in failure mode and that the disbond was not at the titanium-CFRP interface but within the laminate (cohesive failure not adhesive). Following completion of the tests, visual inspection confirmed that delaminations had occurred at the first and second interfaces of the laminate; examples are shown in Figure 4.12. This result was consistent for all three laser treated tests and, therefore, it is concluded that laser treatment does increase the toughness of the titanium-CFRP interface.

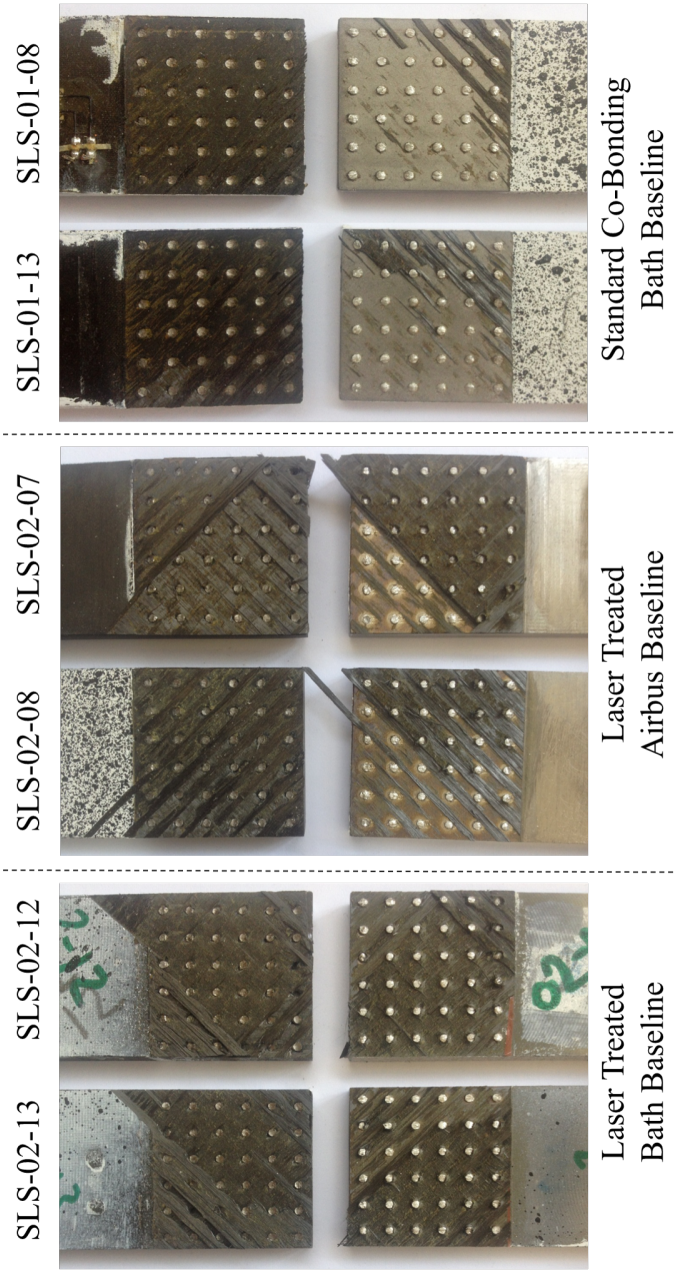

Figure 4.12: Failed coupons showing overlap region and roots of fractured pins. Without laser treatment, CFRP adherend mostly disbonded cleanly from the titanium substrate. Laser treatment resulted in excellent bonding of CFRP and titanium and significant delamination occurred within the laminate (interfaces 1 and 2).

4.6.3.2 Pin Fracture

Although the ultrasonic inspection technique is capable of detecting pin fracture, this was not observed at any of the inspection points; even when the interface had fully disbonded. Hence, as previously suggested, it is proposed that pin rows yield gradually in order to redistribute the load across the array as disbonds propagate. HYPER joints have high structural redundancy and following total disbonding of the adherend interface, the pins provide significant residual strength. The load can be increased at least half as much again (for the alternative Bath geometry) and withstand considerably higher elongation than the unpinned benchmark even with a complete disbond; see Figure 4.8. For example, coupon SLS-01-13 was fully disbonded at 20kN yet did not fail catastrophically until an ultimate load of 30.0kN. Coupon SLS-01-08 withstood four loadings not exceeding 9kN but achieved a UTS of 32.7kN. Once the ultimate load was reached, failure resulted from complete fracture of all pins just above the root, approximately 0.25mm from the substrate. In all cases, this occurred almost instantaneously rather than progressively, row-by-row. Following the tests, visual inspection of the adherends found that the pins remained inside the laminate suggesting that they had not fractured at the neck, see Figure 4.12. Therefore, even with a single lap configuration and the subsequent rotation of the coupon, Mode I opening of the joint remains less dominant than the shear load (Mode II). Furthermore, post-test inspection revealed that only small levels of damage had been generated in the laminate, again shown in Figure 4.12. Hence, despite the performance increase achieved with the alternative pin design, the base pin diameter could be increased further, to reduce the stress at the pin root and increase the membrane stress within the laminate. This would make HYPER joints more structurally efficient and would be likely to increase the ultimate strength further. This trend would continue until net-section failure was generated in the laminate *prior* to shearing of the pins. As the design was believed to be sub-optimal, it would have been desirable to conduct a parametric investigation of the pin design but, unfortunately, this was beyond the scope of the project. However, as a pre-cursor to the realisation of this objective, finite element modelling strategies for HYPER joints were evaluated and this work is presented in Chapter 6.

4.6.4 Manufacturing and Experimental Imperfections

4.6.4.1 Coupon Bending

Following curing of the laminate, in addition to the ultrasonic evaluation, the coupons were also measured for geometric accuracy. This was completed using a surface plate and digital height gauge and revealed that it was found that the two substrates were not always parallel. Figure 4.13 shows the orientation of the coupons for inspection, the measurements made and the relative direction of the distortion. The average deflection was 0.43mm which is equivalent to 0.24 degrees over the length of the metallic part. The worst distortion was 0.52mm (0.30 degrees). It is believed that these defects were the result of more significant consolidation of the CFRP outside of the overlap. The titanium was 5.0mm thick and the average laminate thickness was 5.1mm yet $\bar{z}_1$=10.8mm.

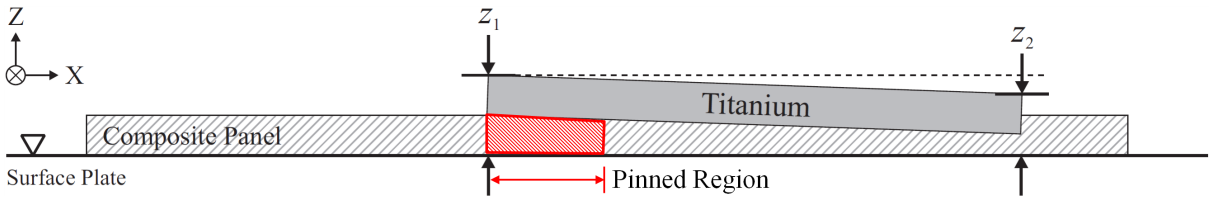

Figure 4.13: Orientation of the coupons for metrology, position of measurements (z_1 and z_2) and the direction of distortion. It is believed that the CFRP consolidated more significantly outside of the pinned region. Not to scale.

As a result of this distortion, a slight bend was induced in the coupon during tightening of the Instron jaws. With the coupon clamped in the upper jaw, as the lower jaw was closed, it was visually observed that contact was made on one side before the other (the jaws close self-similarly, see Figure 4.14). As the lower jaws were tightened further, the coupon was bent like a cantilever beam with a point load. Once contact was made with the opposing jaw, the final stage of clamping would have induced a moment on the free end and constrained rotation of the free end. This was response was captured with the strain gauges and an example is also shown in Figure 4.14.

Despite the flexural modulus of the titanium being more than twice that of the laminate, the final strains recorded on gauges 1 and 2 were higher. It is assumed that if the titanium had deflected less, the CFRP substrate would have been forced into a double, rather than single, curvature mode. Therefore, it is thought that this single curvature mode is the lowest energy state for the coupon. Although pre-straining of coupons was undesirable, it is not thought to have been a significant influence on coupon performance because the strains achieved during the test would have been an order of magnitude higher (i.e. several thousand micro-strain in both the titanium and CFRP).

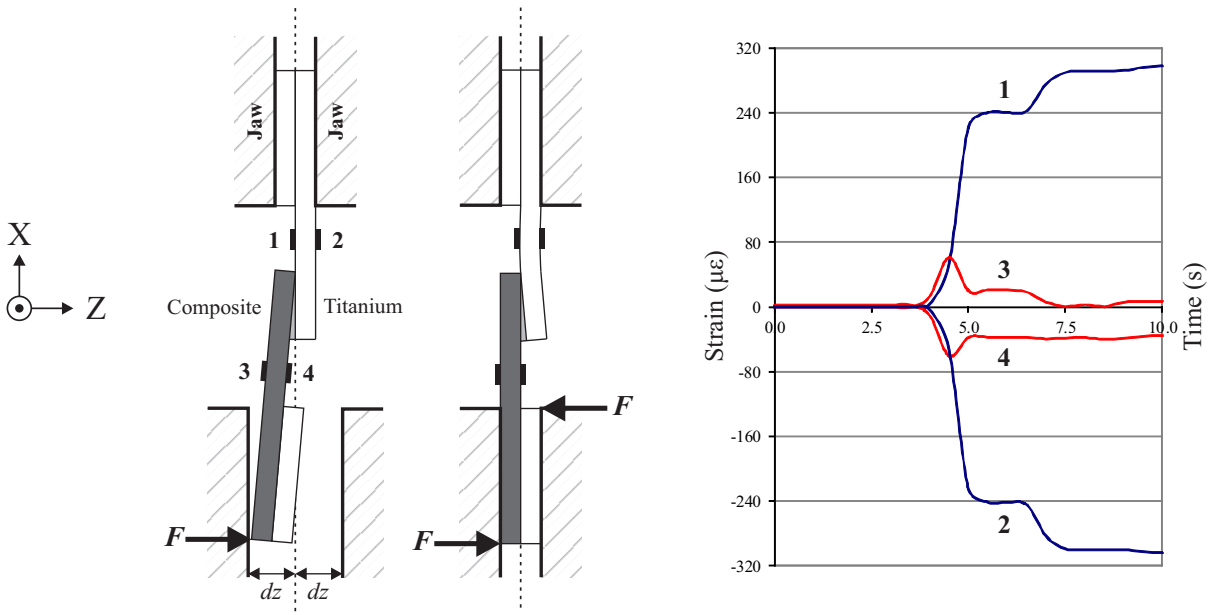

Figure 4.14: During the clamping process, test specimens with distortion were bent as the jaws were tightened. Strain gauges 1-4 are identified and typical response also shown. Not to scale.

4.6.4.2 Coupon Twist

Despite the thorough clamping process (see Section 4.5.2), it was found that tightening of the jaws could induce a rotation of up to 2.8° (about the loading axis). Even if this rotation was identified using the dial gauges and the coupon then straightened, it is likely that stressing the coupon in this manner could have damaged the interfacial bond and lead to premature initiation of damage. Unfortunately, evidence attained from the DIC system suggests that some tests were still conducted with coupons initially twisted.

Figure 4.15 shows the longitudinal surface strain of coupon SLS-01-13 at two load increments generated from DIC imaging. Due to the initial twist, the load transfer and strain is greatest on the left hand side of the coupon. As the applied load is increased, the strain energy in the coupon becomes adequate to overcome the friction in the test assembly and, to some extent, reduce the initial twist. This results in the compressive strain distribution across the width of the coupon becoming more uniformly distributed. However, the strain remains greatest on the left side of the overlap and, subsequently, the interface had not disbonded at the bottom right corner (A) by the 9kN ultrasonic inspection. Corner A is transposed to the top left corner of the overlap in Figure 4.11.

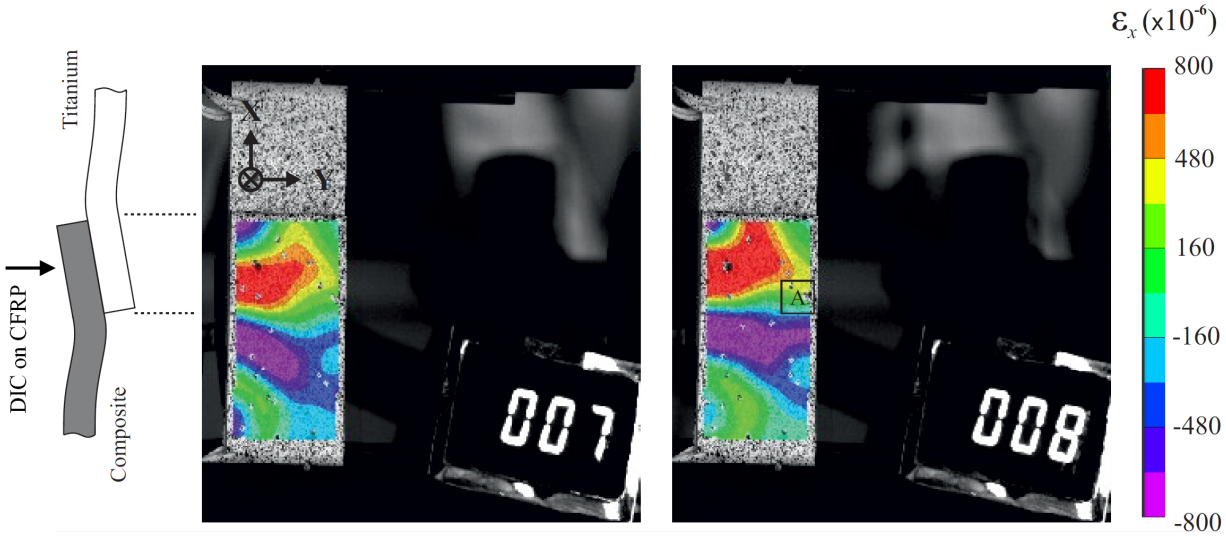

Figure 4.15: CFRP strain in the loading axis (ϵ_x, vertical) in coupon SLS-01-13 at two load increments(7 and 8 kN) captured with digital image correlation. Twist of the coupon induces at proportionally high load on the left side of the coupon. The twist reduces at 8kN and the compressive strain distribution becomes more uniformly distributed but the load transfer remains asymmetric. Consequently, corner A had not disbonded by the 9kN inspection interval.

4.6.4.3 Coupon Slip and Rotation

It was also found that there was rotation of the jaws in the axis perpendicular to the loading direction. Figure 4.16 shows the side profile of an exemplary coupon at a load of 20kN. It was calculated that the ends of the coupon had rotated within the Instron jaws by (on average) -0.6 degrees. This rotation was clockwise and in the opposite sense to that of the overlap.

Consequently, although the magnitude of the the rotation is comparatively small (with respect to the overlap region), the boundary conditions are imperfect as coupon curvature was subsequently reduced. The theoretical coupon shape would have double curvature in each substrate to conform to the zero rotation constraint at the clamped boundaries yet allow rotation of the overlap; analogous to a buckled strut with one end pinned and the other fixed. The observed single curvature mode is clearly the lowest energy state despite the friction that must have been present in the jaw assemblies. Consequently, the load regime will be more dominated by shear and the peeling force (Mode I) would have been slightly reduced at the edges of the overlap.

Results from the DIC data also revealed that slip of the coupon in the jaws was considerable. Although this was expected to some extent, it was anticipated that this would be a second order error. Figure 4.16 shows that, at a load of 20kN, the coupon has displaced by around 0.3mm vertically from the lower jaw (the upper jaw was actuated). It is thought that the jaws were potentially not tightened as much as they could have been in order to prevent excessive twisting of the test specimens. This could be overcome if hydraulically actuated jaws were used.

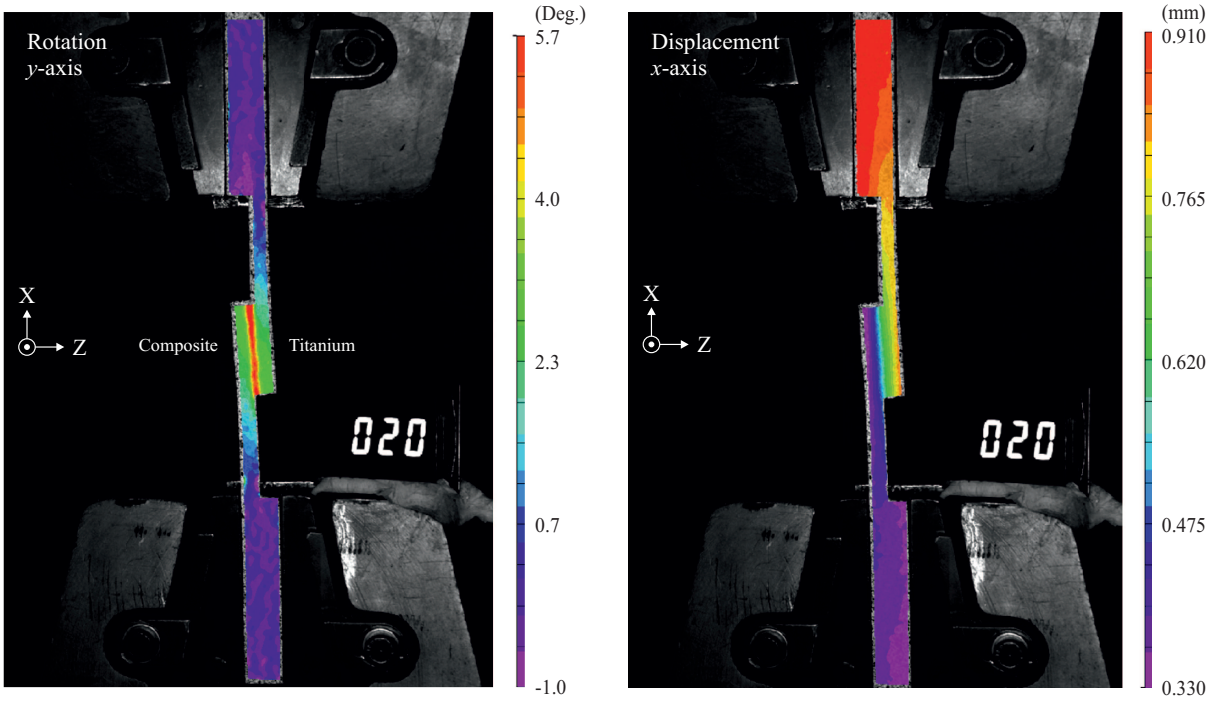

Figure 4.16: Examples of rotation and displacement fields of a typical coupon captured with digital image correlation. Rotation of the jaws creates a compliant boundary condition that allows a single curvature mode shape within the substrates. Positive rotation is anti-clockwise. The right-hand plot shows the vertical translation of the coupon. Slip of the coupon in the jaws is considerable, possibly due to them not being tightened as fully as possible.

4.6.5 Tabulated Results

Abbreviations: STD = standard co-bonding, PTFE = artificially disbonded, LT = laser treated.

Specimens with the prefix AGI were manufactured by Airbus Group and were not labelled with the same convention as those manufactured at the University of Bath.

Coupon Id.	D_b (mm)	Spec.	F_{max} (kN)	Notes
AGI-01-03	N/A	STD	4265	Unpinned
AGI-02-03	N/A	STD	4095	Unpinned
AGI-03-03	N/A	STD	2942	Unpinned
AGI-04-03	N/A	STD	6748	Unpinned
AGI-05-03	N/A	STD	5388	Unpinned
AGI-06-03	N/A	STD	5274	Unpinned
AGI-07-03	1.2	STD	22797	
AGI-08-03	1.2	STD	23555	
AGI-09-03	1.2	STD	26119	
AGI-10-03	1.2	STD	24533	
AGI-11-03	1.2	STD	26548	
AGI-12-03	1.2	STD	26544	
SLS-01-01	1.4	STD	23879	Outlier, discounted
SLS-01-02	1.4	STD	-	Defective, untested
SLS-01-08	1.4	STD	32690	Interrupted regime
SLS-01-13	1.4	STD	29990	Interrupted regime
SLS-02-01	1.4	PTFE	28175	
SLS-02-02	1.4	PTFE	28820	
SLS-02-03	1.4	PTFE	28312	
SLS-02-04	1.2	PTFE	22814	
SLS-02-05	1.2	PTFE	23427	
SLS-02-06	1.2	PTFE	23066	
SLS-02-07	1.2	LT	24298	Interrupted regime
SLS-02-08	1.2	LT	25774	Interrupted regime
SLS-02-09	1.2	LT	26450	Interrupted regime
SLS-02-10	1.4	LT	-	Untested
SLS-02-11	1.4	LT	-	Untested
SLS-02-12	1.4	LT	31674	
SLS-02-13	1.4	LT	32131	
SLS-02-14	1.4	LT	30944	

Table 4.3: Results from the static testing programme.

4.7 Concluding Remarks

Two HYPER pin geometries and three different interface conditions were mechanically tested and the performance of each compared to an unpinned co-bonded reference. The strongest joint configuration was the alternative Bath design with a laser treated interface. The UTS was increased by 6.5 times and the elongation at failure by 407% compared to the reference joint. This geometry/interface combination also had the least scatter and the range was reduced by over 50% compared to the coupons with standard bonding. When interface bonding was artificially prohibited with PTFE, the ultimate strength was reduced by 8-9% (depending on pin geometry) compared to standard resin bonding.

Although the laser surface treatment only improved the UTS by 1-2% compared to the standard co-bond, the limit load was increased by 25% which even exceeded the ultimate load of the reference joint. Following damage initiation, laser treatment also resulted in a reduced and, crucially, consistent rate of damage propagation. This switched the failure mode from adhesive to cohesive and at least 80% higher load was required to grow an equivalently sized disbond.

The NDT methodology was successfully used to observe and characterise the associated failure modes. Pins do carry load before disbonding as F1 could be increased beyond the ultimate strength of the reference joint; unlike a bonded-bolted joint. The epoxy matrix was still the dominant load path and interface failed first. Load share on pins then became more significant and they temporarily prevent additional growth from the initially damaged edge. A disbond consequently initiated on opposite side of the overlap and they then both grew in discrete steps, arrested each time by the pins. The NDT technique confirmed that pin fracture did not occur until after the interface was fully disbonded. The number and magnitude of loads required for a full disbond did vary due to the mixed bond quality found in specimens.

Although some flaws were found the manufacturing and testing procedure, it is not thought that any defects significantly influenced the results and suitable recommendations have been proposed. These include: bespoke tooling to ensure more thorough consolidation of the laminate, flatter coupons and, subsequently, no bending of the coupons when clamped. Hydraulically actuated jaws could prevent twisting and slip of the coupons and loads would then be more uniformly distributed across the joint.

HYPER joining is a very promising technology for the future integration of hybrid structures. This investigation has shown the impressive strength and toughness of HYPER but it is believed that, with additional work, pin/array designs could be better optimised for static performance. For example, by increasing the pin diameter even more, the root stress would decrease whilst the load on the laminate would be increased. At present, the laminate was largely undamaged following failure of the joints. This could not only improve the joint strength but make the HYPER joint design more structurally efficient.

Chapter 5

Fatigue Performance

5.1 Summary

Single lap HYPER joint coupons were subjected to high-cycle fatigue testing. A backface strain technique was used to identify damage initiation/growth and an ultrasonic inspection method was also used to characterise damage initiation and growth. It was found that fatigue life was governed by one of two failure modes. At severities greater than 32% of UTS, the pins failed just above the pin root as was observed in the static test programme. However, at severities less than 32% of UTS, fatigue life was governed by fracture of the pin at the neck and tearing of the pins from the metallic adherend (the fracture surface propagated into the substrate). Failure was controlled and repeatable and there was minimal damage to the composite due to the sacrificial role of the pins. Based on this experimental evidence, it was proposed that the neck diameter should be increased in order to increase the fatigue life. A design perturbation was completed but it was found that manufacturing quality was a more significant influence on mechanical performance.

5.2 Motivation and Objectives

In addition to the static lap shear tests conducted by the author (presented in the previous chapter), pilot studies with lap-shear and ARCAN specimens [10] had been undertaken in completed by collaborators at Airbus Group Innovations [8, 27]. However, no fatigue testing had been conducted on any HYPER joint configuration. It was essential to gather this data for the continued development of the technology. As stated in Chapters 1 and 2, it is believed that future applications will utilise HYPER to increase the structural redundancy and provide energy absorption capability in hybrid structures. Hence, ultimate strength is important but residual strength after prolonged durations in service (at lower loads) was equally fundamental. Thus, the primary objective of this part of the project was to establish baseline high-cycle performance data for a baseline HYPER joint lap-shear coupon. Secondly, it was desirable to identify the point of damage initiation and rate of propagation. If the failure sequence and mode(s) could also be characterised with NDT, this would provide valuable insight for subsequent design perturbations.

5.3 Background

Unlike HYPER joining, mechanical fastening of joints is a mature concept and thus, extensive experimental evidence was found in the literature. It is not unreasonable to consider a bolted or riveted joint analogous to a (disbonded) HYPER joint and thus, an appreciation of potential failure modes/sequences could be gained through investigation of this joining methodology. As with quasi-static testing of mechanically fastened joints, there are four classical failure modes: bearing/hole elongation, net section, shear out and failure of the fastener (the first three resulting from failure of the substrate). As has been discussed in previous chapters, the failure mode is dependent on a large number of design parameters but two driving factors are the ratio of fastener diameter and edge distance and the number of fasteners in an array [81]. However, in the context of a fatigue test, it is possible for the failure mode of a single joint design to vary with the severity of peak load.

At high loads, the failure mode may be similar to the quasi-static mode but, as the load is reduced, the mode can change and in the low load/high cycle regime, bolt failure is the more common [77]. This results from the fatigue life curve of a metallic component being steeper than that of a comparable composite part. Hence, at low load levels there would be a more significant difference in the fatigue life. This would lead to a two phase or bilinear response as shown in Figure 5.1. Additional considerations are that thicker adherends tend to promote fastener failure and fatigue life is further reduced if the fasteners have countersunk heads. Pretensioning the fasteners can increases fatigue life as a greater proportion of the load is transfered by friction between substrates and the shear load on the bolts is decreased.

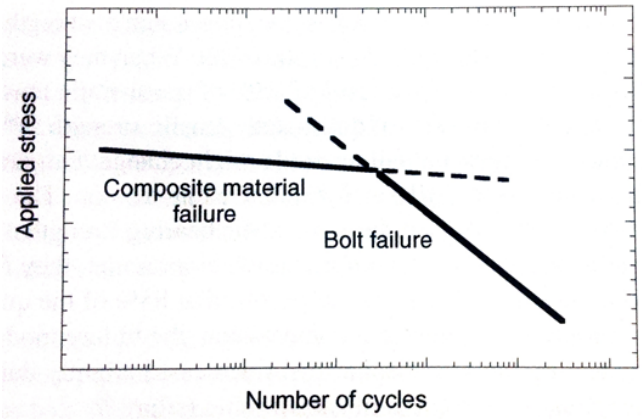

Figure 5.1: Generalised transition between fatigue failure modes, from [77].

When the failure mode results from degradation of the composite substrate, it is most commonly due to localised wearing of fibres in the vicinity of the hole and accumulation of matrix cracking globally. After a period of steady growth, this will increase rapidly approaching failure. Another difference between a metallic and fibre-reinforced composite materials is the sensitivity to overloads. It is possible for a metallic joint/fastener to yield under a sudden severe load and then offer increased fatigue life as a result of load redistribution. Composites are more sensitive to overloads as a high load may break fibres and generate intra-laminar cracks. Fatigue life would then be reduced as the (weaker) matrix would have to transfer more load due to the discontinuity in the fibre.

The literature also includes a number of papers detailing hybrid adaptations of traditional techniques. Hybrid assemblies are considered to be joints constructed of dissimilar substrates or utilising multiple fixing methodologies; e.g. metal-composite and bonded-bolted respectively. It is believed that a combination of these two configurations (metal-composite bonded-bolted) forms a close parallel to HYPER joining. However, Schön and Starikov state that there is "no fundamental difference" between the fatigue response of metal-composite and composite-composite joints and can be treated alike [77]. There may be a difference in the rate of wear in the vicinity of the hole but this would not significantly change the failure characteristics. Therefore, bonded-bolted composite-composite joints were also of prime interest.

Kelly [48] conducted a series of bonded-bolted fatigue tests using fibre reinforced composites and also compared two adhesives and different adherent geometries. A notable finding was the existence of a three phase failure sequence. Initiation of damage was found following fatigue of the adhesive at the edge of the joint. This was followed by propagation of damage through the adhesive layer which increased the compliance of the joint and transfered load onto the bolt. Finally, due to delamination of the interface and the increased load on the bolt array, catastrophic failure of the joint resulted from fracture of the bolt.

Comparison of the number of cycles to initiation revealed that there was good correlation between a benchmark (purely) bonded joint and the hybrid scheme. Hence, proof that bolts do not initially carry a significant proportion of an applied load. At approximately 60% UTS, initiation was found to occur at approximately 1% of the fatigue life. Initiation can be delayed, and the fatigue life increased, by using a more flexible adhesive as the bolts carry more load and reduce the adhesive stress.

The most comparable work in the field of hybrid joining has been undertaken by Graham et al. [38] and Nogueira et al. [68]. Graham's work also utilised AM as the enabling technology but the pin designs were more simplistic and the double-lap joints were constructed from steel and glass reinforced plastic. Contrary to Kelly's findings [48], Graham stated that damage in the hybrid joints was found to initiate at a lower number of cycles that the benchmark joints. This may have been due to pre-stress in the interface due to thermal mismatch of the substrates. It was found that the rate of damage growth reduced considerably as the crack front reached each row of reinforcing pins. This supports the experimental findings presented in Chapter 4.

Graham et al. stated that the fatigue life of the hybrid joints was "at least" as long as a control joint for a severity of 50% UTS and thus, has comparabale performance to Z-pinning [16]. Testing was completed with a R-ratio of 0.1 and a cyclic frequency of 3Hz. This was a promising result given that the UTS of the hybrid specimens was twice that of the control. It was proposed that if subjected to similar loads, the hybrid concept would be able to tolerate "significantly more cycles" before catastrophic failure. Additional testing would be required to ensure that a change in failure mode did not adversely influence fatigue life at lower load severities; as already discussed. This hypothesis was confirmed by Nogueria et al. [68] using the hybrid "RHEA" technique (bonded-pinned composite-composite). Experimental evidence shows that fatigue life with RHEA reinforcement can be *one order of magnitude* higher than a co-bonded reference, making it comparable to Z-pinning.

Reinforcement enhanced the damage tolerance of the joint and delayed the propagation of delaminations and cracks. It was found that cracks (adhesive and cohesive) grew from just one end in the control joints because, once started, propagation was unstable. However, damage in the RHEA joints grew from both ends as the pins arrested the cracks from the first edge. Damage in the hybrid joints had to propagate all the way through the pinned area before catastrophic failure occurred. This is identical to the behavior found by the author [71] and by Schön and Starikov [77].

Nogueira et al. also commented on finding a high degree of scatter in the test data and, although to some extent this is inherent with fatigue testing, it was thought to have been made worse by manufacturing irregularities. Manufacturing defects may also have been an influence on the results of Graham et al. and have been a further reason for the number of cycles to damage initiation being less than expected. It is known, from first hand experience, that ensuring consistent manufacturing quality can be challenging at low TRL levels.

As stated in Chapter 4, the cold metal transfer (CMT) and Comeld joining techniques are two further hybrid joining technologies that have similarities to the HYPER technique. Although experimental quasi-static data has been published for both CMT and Comeld [90, 82, 87], no published work could be found reporting their fatigue performance.

5.4 Experimental Methodology

5.4.1 Overview

The test coupons were geometrically similar to those used for the static test programme (Chapter 4) which conformed to ASTM D5868 [11]. As for the quasi-static tests, each adherend was 101.2mm long, 25.4mm wide and nominally 5.0mm thick. The metallic adherend was titanium alloy (Ti-6Al-4V) and the composite adherend was constructed using Hexcel M21-T800S and, again, a 20 ply layup: $[\pm 45/0/90/\pm 45/0/90/\pm 45]_S$. The gauge length was 76.2mm and the overlap was 25.4mm which included a 6×6 array of additively manufactured HYPER pins, see Figure 5.2. The "Bath Baseline" pin geometry (with standard co-bonding) was used as it offered the best static performance and would allow comparisons to be draw between the monotonic and cyclic failure modes. The dimensions are provided again in Table 5.1, below. Aluminium tabs were adhered to the ends of the substrates to maintain the adherend offset whilst allowing the coupon to be clamped in a standard set of tension jaws. Testing was undertaken using a servo-hydraulic Instron 1332. Load control was used with a sinusoidal waveform, a load ratio of 0.1 (tension-tension) and a cyclic frequency of 2Hz. Four load severities were used: 5, 10, 15 and 20kN (peak). These equate to 16, 32, 48 and 64% of the ultimate (monotonic) strength respectively. A full list of specimens (and results) is included in Section 5.6.4.

Description	D_b	D_n	D_h	Z	θ_1	θ_2
"Bath Baseline"	1.4	0.9	1.5	3.6	90	60

Table 5.1: Pin geometry used for fatigue testing. Dimensions in millimeters and degrees.

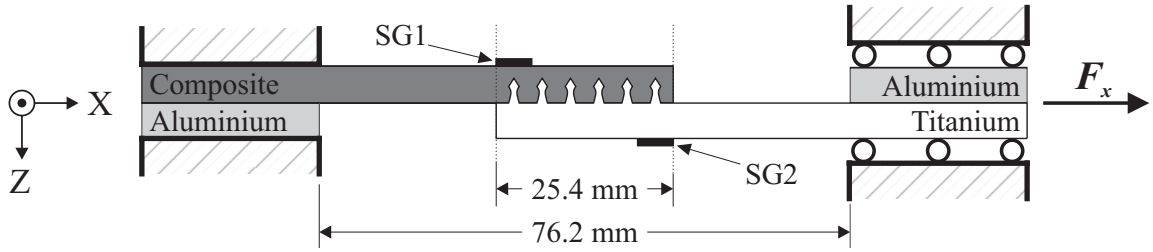

Figure 5.2: Section of a test coupon showing pins. Strain gauges (SG1-2) are positioned on the mid-line of the specimen, aligned with (and perpendicular to) the edges of overlap. All dimensions in mm, not to scale.

Two strain gauges (SG1 and SG2) were used to help identify the initiation of damage and subsequent growth using the backface strain technique (BST) [94, 21]. Initiation events in lap shear tests can be captured using the BST as the first failure is typically adhesive/matrix cracking at the free edges of the joint. This causes an effective reduction in overlap length and joint stiffness and hence, there is a change in curvature. The gauges are optimally positioned to record the resulting alteration in surface strain. They were adhered to the midline of the coupon and the edge of their active length was aligned with the edge of the joint.

The effectiveness of the BST technique for thick, stiff adherends with a comparatively large overlap and short gauge length was unknown. For example, Zhang and Shang [94] used 1.3mm thick, steel adherends and Crocombe et al. [21] used 2.0mm thick, aluminium adherends. Therefore, the number of cycles required to initiate damage, and the subsequent rate of propagation, were also determined by monitoring variations in the displacement amplitude; an approach also adopted by Kelly [48].

Furthermore, ultrasonic inspection was conducted for the coupons tested at 5 and 10kN peak load (every 50,000 cycles). The technique was identical to that used in the static test programme and is described in Chapters 3 and 4. The interrupted approach may have had an influence on performance at the higher severities due to the short duration of these tests but it was assumed that there would be a near instantaneous initiation and disbonding anyway so little would have been gained with NDT. The edge of the coupon was also painted white to aid observation of crack initiation and growth in situ. The success of each of method is compared in Section 5.5.

5.4.2 Setup Procedure

The test coupon was firstly clamped into the upper jaw as these were attached to the load cell. It was ensured it the specimen was central in the jaws and perpendicular to the loading direction with a set square and a metal bar rested across the jaws. This reduced the likelihood of a moment being applied and altering the loading regime. However, it was found that the piston actuating the lower jaw was not completely constrained transverse to the loading direction. As a result, the jaws could rotate by 1-2° about the y-axis if the lower jaw was raised by 50mm to the nominal zero position; positive displacement was downwards as shown in Figure 5.3. This would have resulted in a non-idealised boundary condition that was neither fixed or pinned and would have been comparable to a stiff rotational spring.

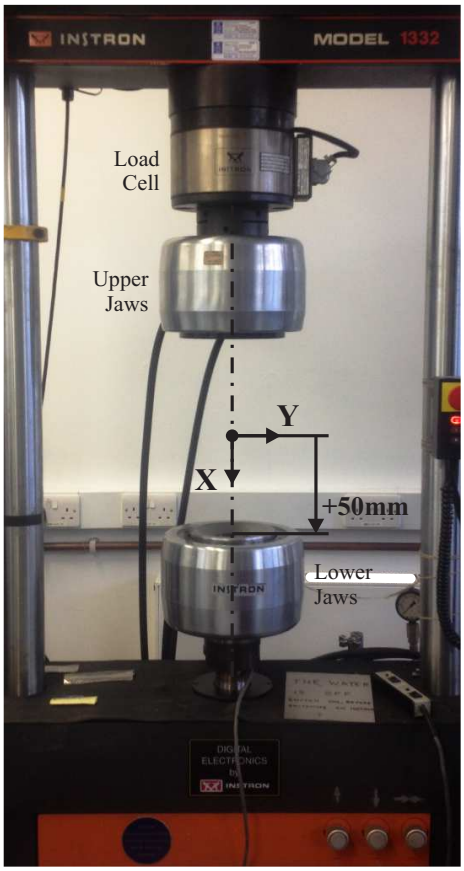

Figure 5.3: Instron 1332 used to conduct the fatigue testing programme. Positive displacement was vertically downwards, the lower jaw is shown at the limit of its range ($x \approx 50$mm).

To minimise deflection of the lower jaw, it was left close to the fully retracted position and the upper jaws were lowered accordingly. With the machine in displacement control, the lower jaw was then raised to set the correct gauge length and allow adequate travel for the test ($x = 48$mm, $\Delta x = \pm 2$mm). The load was now balanced, the machine switched to load control and the lower jaw closed as quickly as possible. If the machine was left in displacement control as the lower jaw was closed, it was found that a load could be induced. In load control, the lower jaw is free to displace and maintain the (negligible) load that would have been present after the cell was balanced; protecting the coupon. The gauge length could now also be reset to zero. Both the load and displacement limits were then applied in order to protect the machine following failure of the coupon (typically $\pm 10\%$). This was essential as, due to the length of the tests, the machine was often left running outside of typical working hours. The "loop tuning tool" was also used to automatically adjust the feedback response of the machine for the coupon. The Fastrack live display was intially set to "track" the load and displacement in order to setup the test. However, once the test has begun, due to the cyclic frequency of the tests, tracked displays would not refresh quickly enough to display current data. Thus, to monitor the test in-situ, the mean and amplitude displacements are also displayed along with the maximum and minimum loads, all of which are specified to update every three cycles (which allowed time for them to be updated).

The machine was now configured for testing. The next stage of the procedure was to setup the data acquisition systems. Hardware limitations meant that strain gauge data could not be recorded on the computer controlling the Instron. Although load and displacement data could be transferred to a secondary system in real-time, acquisition could not be synchronised with the loading cycle and therefore peak strains could not be captured on a cycle-by-cycle basis. As a result, a post-processing algorithm was written in MATLAB. BNC leads were used to establish a connection between two analog channels of the Instron 8800 module and the secondary computer which ran Spider8 and Catman software. The Instron channels were set to output (track) load and displacement in the Fastrack software. The voltage scaling set in Fastrack had to match the values defined in the Catman software; e.g. 0.1V/kN and 1V/mm. Given the load and displacement amplitude used, it must be ensured that the maximum voltages did not exceed the range specified in Spider8.

The strain gauges used were 350Ω quarter bridges, manufactured by Vishay Micro Measurements (N2A-06-T004R-350). These could now be connected and tared, ensuring the load was still zero. By closing the jaws with load control activated and taring the strain gauges afterwards, any coupon distortion (resulting from manufacture) that led to bending of the adherends, would not be captured. This would have resulted in a small discrepancy between the true coupon strain and that recorded from the gauges although this was believed to still be negligible. This effect was described in Section 4.6.4. A input/output channel definitions file was created/loaded in Catman and it was ensured that the database was clear. The sampling rate, period and interval were all configured in the logging module and the graphical output set to display the active channels so that the progress of the test could be monitored in real time.

Finally, the Fastrack Waveform Generator was used to apply the mean load, amplitude and frequency. "Amplitude control" was selected to ensure that the maximum and minimum loads would remain constrained at the expense of frequency, if one could not be maintained. It was believed that a small fluctuation in frequency would be less serious than the load being exceeded and ensure a fair test.

5.4.3 Post-Processing

As peak strains could not be captured on a cycle-by-cycle basis on the secondary computer system, a three cycle "snapshot" was recorded at predefined intervals (sampling rate 100Hz). Hence, at a frequency of 2Hz, 150 points are recorded on each acquisition channel (load, displacement, strain, time, etc.) per sampling period. The Catman acquisition software only allowed 20,000 data sets to be captured in total and thus, at the designated sampling rate, this equated to 133 sampling periods. Therefore, the duration between sampling periods had to be adjusted depending on the anticipated length of the test.

The peak values for each dataset were then extracted with the Peaks Analysis function in Catman. This provided maxima/minima (and associated times) which were then averaged with an algorithm written in MATLAB. Although, three cycles were recorded for each sampling period, it was possible for the Catman analysis to record an additional erroneous maximum or

minimum for each cycle. For example, an additional maximum could be found at the final data point of the set if the following sampling period began at a different phase of the loading cycle and the differential between these consecutive points was negative - as shown in Figure 5.4.

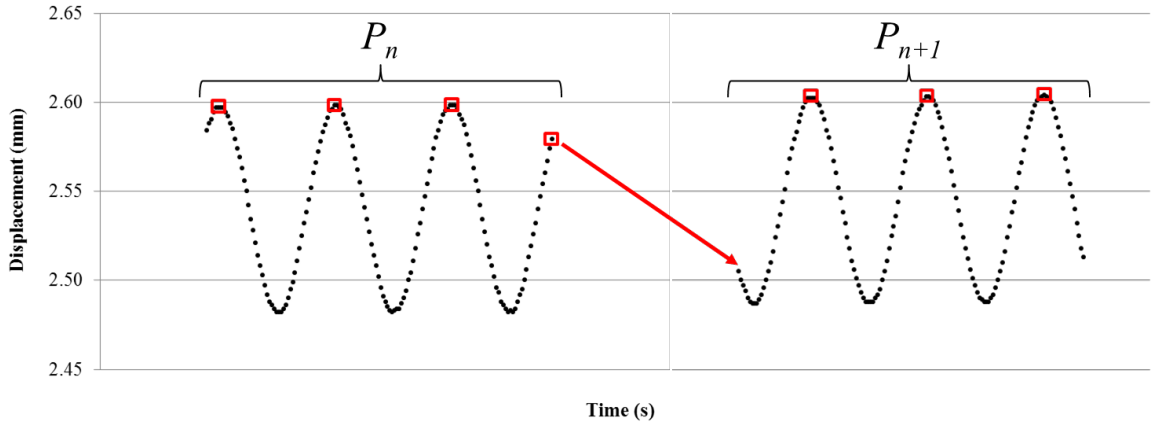

Figure 5.4: Example of crosshead displacement for two consecutive sampling periods, P_n and P_{n+1}. Maximas identified with Catman Peaks Analysis shown by square markers. As data acquisition was not perfectly synchronised with the loading cycle, an erroneous fourth maximum was found in sampling period P_n as the first point of the following sample was significantly lower.

Hence, if these erroneous data points existed, they had to be identified and removed as their inclusion would reduce the average value. Firstly, the times were discretised into sampling periods and the data from each segregated into a group (array). Group by group, the data (strains, displacements, etc.) were then sorted into ascending order. The first three were then averaged to find the maximum and last three for the minimum. Whether or not the array contained any invalid points, the method was unaffected. It should be noted that the strains were always negative. The values were sorted in descending order for displacement sets as these were always positive. Finally, the cycle number of each sampling group was calculated and output with the averaged strain/displacement values.

5.5 Results

5.5.1 Assessment of Fatigue Life

Figure 5.5 shows fatigue life plots for the Bath Baseline HYPER joint design with standard co-bonding. A detailed table of results is included in Section 5.6.4. It can be seen that there was good correlation in both the number of cycles to failure and cycles to damage initiation, which occurred at approximately 10% of the total fatigue life. The latter was determined using a combination of the three techniques described in Section 5.4 (BST, amplitude and ultrasound). Given the loads that were required to disbond the interface (in the static tests, reported in Chapter 4), it is assumed that the interface fully disbonded within the first few cycles. Thus, the initiation event presented in Figure 5.5 is assumed to be damage occuring within the pins.

Although a comparable co-bonded joint (without reinforcement) was not tested, based on the observations of Kelly [48] and Nogueira et al. [68], it is proposed that catastrophic failure of a benchmark joint would occur almost instantaneously once damage had initiated (i.e. there would be no stable crack growth). Therefore, it is believed that HYPER provides an increase in fatigue life of several orders of magnitude. This is believed to be a conservative estimate as the static test programme revealed HYPER pins can delay the initiation of damage so an unpinned benchmark could have initiated at an even lower number of cycles. Furthermore, it should be noted that most coupons had a some degree of interface disbonding following manufacture (see Section 3.6) and, given that fatigue performance is largely influenced by nucleation of damage at defects, this again suggests that Figure 5.5 presents a conservative measure of HYPER joint performance.

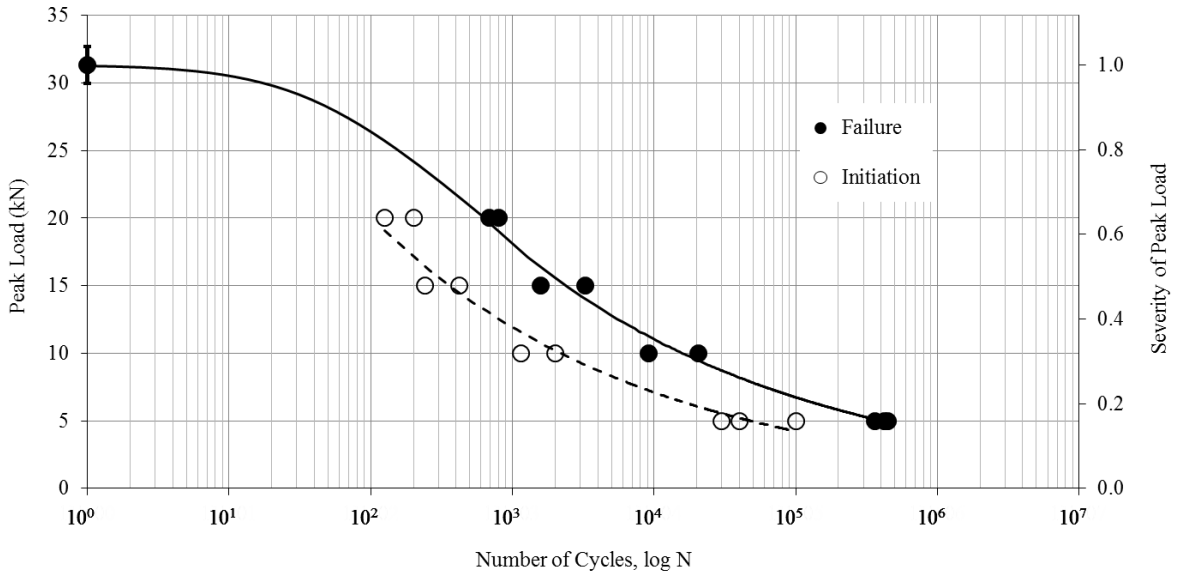

Figure 5.5: Fatigue life plots for lap-shear HYPER joint coupons with the Bath Baseline pin geometry.

5.5.2 Identification of Damage Initiation

Variation in the displacement amplitude of the machine crosshead was found to be a simple and effective measure of damage initiation within the pins as well as the subsequent rate of propagation. Figure 5.6 shows the change in amplitude with increased cycles, normalised for comparison as amplitude was proportional to peak load. The point of first amplitude change was assumed to be the time of initiation. Slippage of the coupons in the machine's jaws could have been an influencing factor on amplitude change as an increase in gauge length would increase compliance and require greater displacement to maintain a constant peak load. However, this was not thought to be the case as there was negligible variation in the minimum crosshead position. With an increased gauge length, if the original minimum position was maintained, the resulting minimum load would have become too low. The relative change in compliance between initiation and failure can be seen to be inversely proportional to peak load. This suggests that

there was a change in the failure characteristic, from brittle to ductile, as the load was reduced. In general, at a high peak load, failure is driven by the rate of damage propagation as it can be assumed that initiation would have occurred very quickly. The growth of damage (second phase of Paris' Law) would have been comparably brief. Conversely, at low load, the rate of propagation would have been much lower and accumulation of damage more progressive.

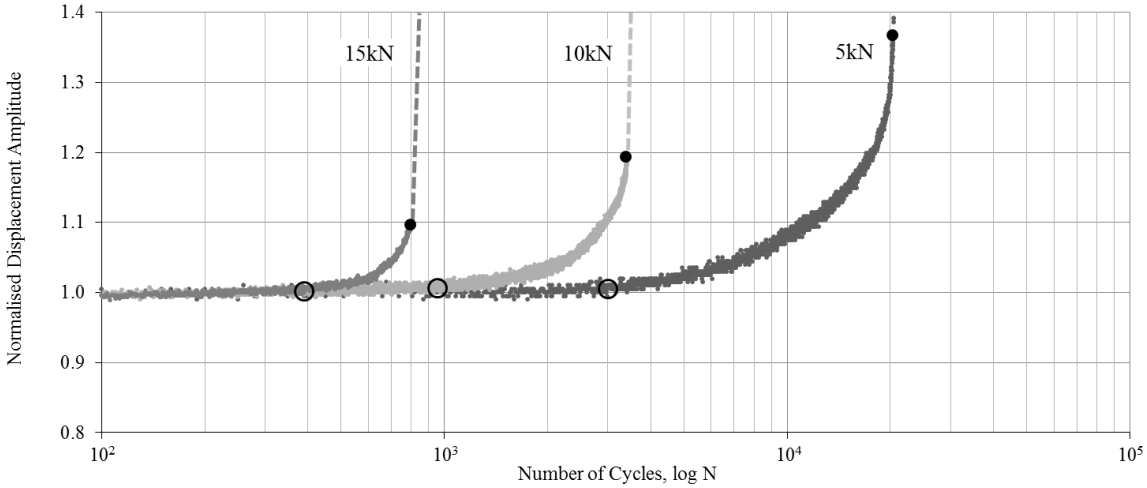

Figure 5.6: Change in normalised displacement amplitude for three typical coupons, each at a different peak load. The point of initiation is identified with a hollow marker and joint separation with a solid marker. Failure resulted in a sudden, significant increase in amplitude as shown with dashed lines.

5.5.3 Analysis of Strain Gauge Data

It has been shown that the BST is capable of detecting both damage initiation and evolution in comparably thick, stiff adherends. Figure 5.7 shows a typical response from one of the coupons subjected to a low load severity. It is thought that, for this particular coupon, the initiation of damage was between 20,000 and 30,000 cycles as there was negligible variation in strain prior to this. Beyond 30,000 cycles, the magnitude of SG1 reduces and SG2 increases. It is believed that this was because damage developed primarily in the pins at the end of the overlap adjacent to the CFRP adherend. It is well established that this side of the overlap would be more highly loaded in both shear and peel due to the imbalance in adherend stiffness. Considering the undamaged joint shown in Figure 5.7, the points of maximum curvature are A and B; the location of SG1 and SG2 respectively. Firstly, it is believed that a substantial disbond initiated and the load on the first row of pins increased. These pins then became damaged and the joint opened further, causing an increase in the free length (l_1) and the overlap length (c) to decrease. Maximum curvature in the CFRP shifted to A$'$ and consequently, there was a reduction in strain at A (SG1). As a result of the reduced overlap length, joint rotation increased and thus, strain at B (SG2) increased. There was negligible change in l_2 and thus, no detectable translation of maximum curvature in the titanium adherend.

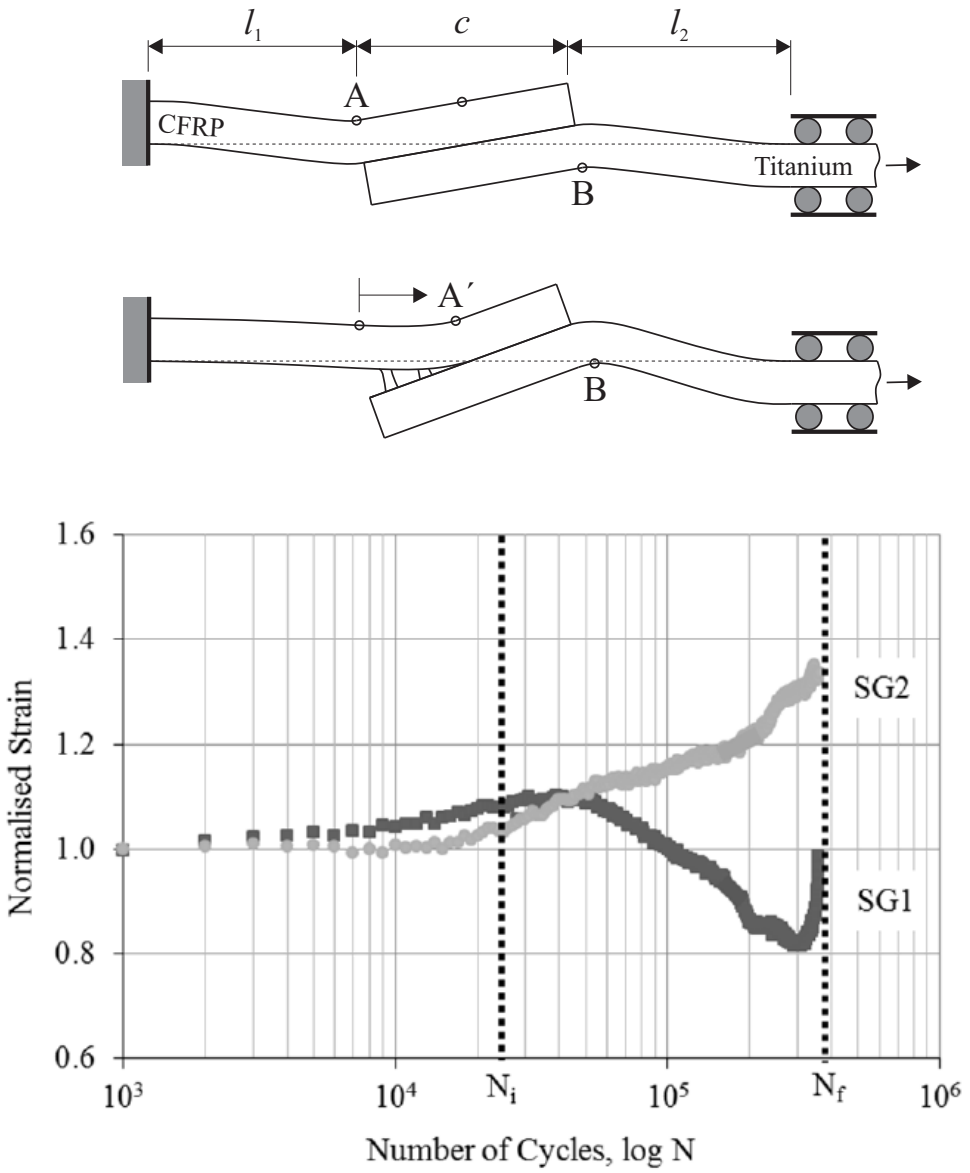

Figure 5.7: Normalised peak strains for coupon SLS-01-06 at a maximum load of 5kN (16% UTS). Shift in maximum curvature from A (SG1) to A′ following interface disbonding and onset of pin damage. Not to scale.

5.5.4 Ultrasonic Non-Destructive Evaluation

It has already been shown that the growth of a disbond at the adherend interface could be observed using pulse-echo immersion ultrasound (Chapters 3 and 4). It was proposed that pin damage/fracture could also be identified with this method but, given the instantaneous and catastrophic nature of the pin failure observed during the static tests, it was impossible to validate this hypothesis. In short, the pins can be observed through the metallic adherend with this technique as they are an integral part of the adherend and the incident ultrasonic wave is not reflected. However, if damage was present, the resulting discontinuity would cause a detectable echo.

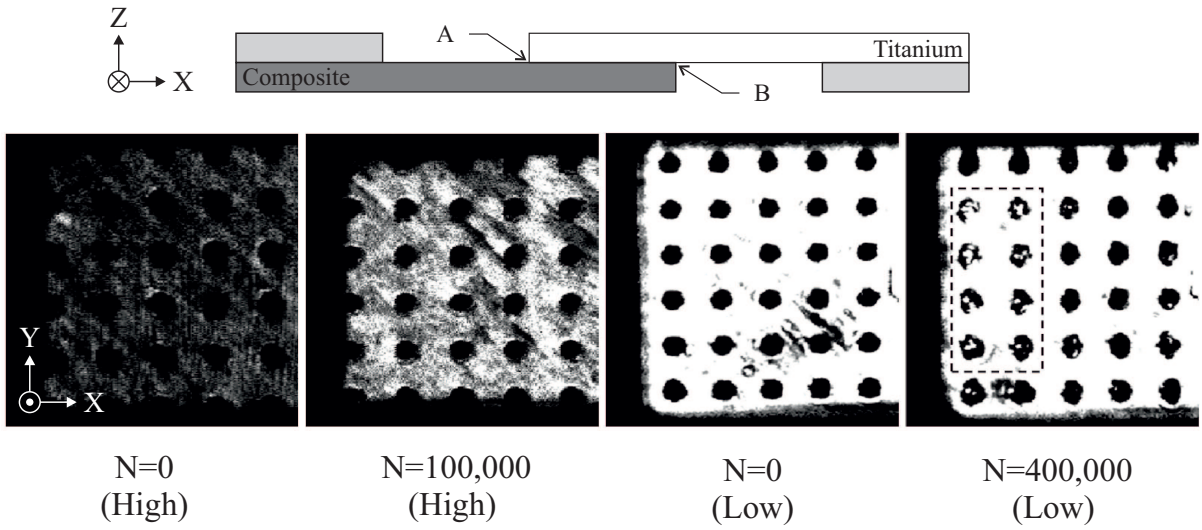

Figure 5.8: C-Scans of adherend interface, from left: as manufactured (high threshold), after 100,000 cycles (high signal threshold), as manufactured (low signal threshold) and after 400,000 cycles (low threshold). Pin damage highlighted with a dashed box.

Figure 5.8 shows four C-Scans of a representative coupon in three different conditions using two different signal thresholds. Images were constructed using signal amplitude and the intensity of white is proportional to signal strength. In order to identify interface damage, a comparison must be made at a high threshold. In this configuration, only the strongest signals are visible so it is possible to differentiate between disbonded regions and areas of good adhesion as the latter returns a comparatively weak echo. It can be seen that by 100,000 cycles, the interface had completely disbonded. Secondly, the signal threshold (limit) was set at a low level so that the weaker signals from within the pins were not excluded (edges of joint also more visible). In the manufactured condition, the pins are seen as sharp, discrete features however, by 400,000 cycles, damage could be seen within their perimeter. The best examples have been identified within a dashed box but it should be noted that the positioning of the strain gauges distorted the right side of these images. Hence, they have been cropped for clarity and only 30 of the 36 pins are visible.

5.6 Discussion

5.6.1 Global Failure Mechanisms

The sequence of failure events is similar for both static and fatigue tests (the initial failure is disbonding of the resin interface), but as expected, fracture of the pins was more progressive with reduced load severity. Visual inspection of the coupons after testing revealed that there was a significant difference in the nature of the fracture. After high severity loadings, it can be seen that the fracture surface was circular and above the root fillet radius of the pins. In this case, the pins were cleanly sheared at a near constant height from the substrate. Contrary to this, a high-cycle low load regime, resulted in a much wider fracture surface that was below the pin base (within the substrate).

It appeared that these pins had been torn from the substrate. It is believed that the variation of failure mode with peak load is the result of the non-linear geometric effects of a single lap joint and a change in the pin load mixity. At low peak loads, there is minimal rotation of the joint so the pins are exposed to a large moment at their base compared to the axial and shear loads. It is assumed that the pins remained below their elastic limit. Slender pins would be able to form a mode shape with double curvature to compensate but the pins are short compared to their diameter. As a consequence, pin fracture must initiate to redistribute the load to the inner rows and the pins tear from the substrate to relieve the moment (Figure 5.9). It is this mechanism that allows the interfacial disbond to propagate. The pin heads also have to react a moment and thus, it is proposed that they are torn in the same manner but more quickly due to the reduced cross-sectional area. This exacerbates tearing at the pin root as the pins can pull out, effectively increasing the lever arm. This process allows the pins to rotate and they act like rigid links with pinned ends.

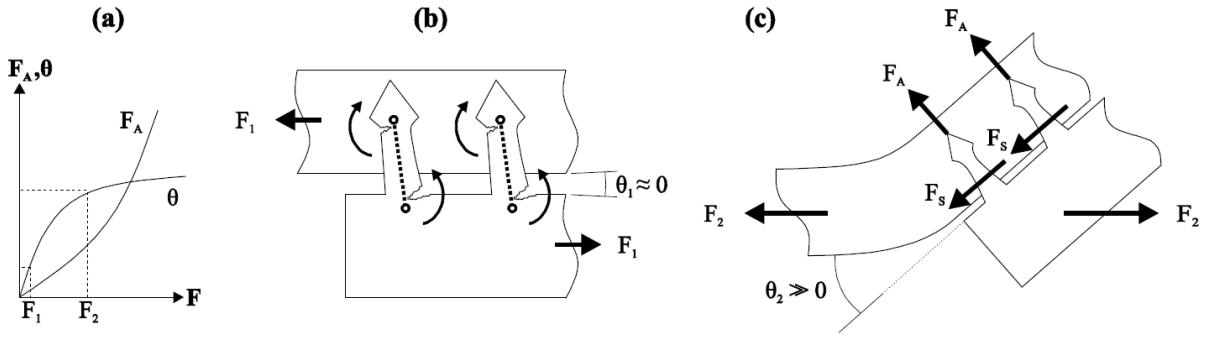

Figure 5.9: Failure sequences for the two load cases, F_1 and F_2. (a) Comparison of axial pin force, F_a and joint rotation θ with applied load F. (b) At low loads, joint rotation is minimal and pins tear to relieve root/head moments. (c) At high loads, axial and shear forces are dominant on the pins. Not to scale.

At higher loads, the pins exceed their elastic limit so load redistribution and interface disbonding occurs within the first few cycles, prior to the initiation of pin fracture. With increased joint rotation, root bending moment is also less significant compared to axial pin load (F_a) and shear load (F_s). It is thought that the pin head does not fail in tension, despite the reduced cross-section, as shear force at the base is more dominant. Once pin fracture has initiated, because the pins have already yielded and the load is shared more evenly amongst the whole array, cracks grow rapidly and failure is catastrophic.

5.6.2 Local Failure Mechanisms

The tearing of the pins from the substrate at low loads was indisputable as, post-failure, it was found that some pins were still partially attached to the adherend. In addition, these semi-attached pins all had their upper section (head) removed; see Figure 5.10. It was initially thought there was a plane of weakness between the micro-structure of the AM pin and stock material. It is known that the high temperature gradients during AM change the equiax grain structure of the stock material and that the AM material is formed from thin columnar

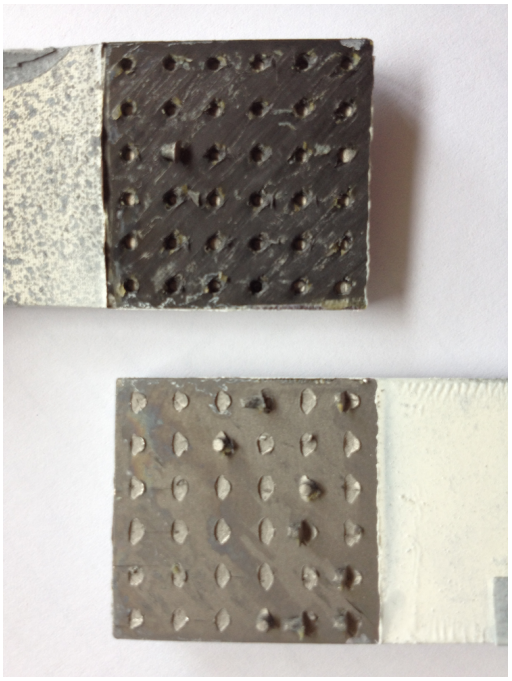

Figure 5.10: Visual inspection of the adherend after testing revealed tearing of the pins at neck and base for load severities of approximately 32% UTS or less. Example shows coupon SLS-01-06 which was subjected to 5kN peak load (16% UTS).

grains [9]. Thus, analysis of the pin microstructure and fracture surfaces was made using optical microscopy. Measurement of the fracture "craters" was undertaken using a Leica M205 camera/microscope and Leica Analysis Suite. Figure 5.11 shows two examples and compares the average crater aspect ratio with row position and peak load. Error bars show 5% deviation, deemed to be the maximum possible discrepancy during measurement of craters. There was little variation in aspect ratio across the width of the coupon yet, there was some change with row position in the loading direction for coupons subjected to a 10kN peak load (32% UTS). Given that there is little variation for the other load severities (consistent aspect ratio with row), it is believed that a 10kN peak load was a transition point between modes. In addition, the 5kN load case appears to exhibit a mixed growth rate within individual craters. It is proposed that at initiation, there was rapid growth (for distance u) which resulted in a circular crater but propagation was then more gradual in the elliptical area. It is possible to see some evidence of "tide marks" in the elliptical region of the craters which is evidence of a progressive high-cycle ductile failure, as suggested following by the displacement data.

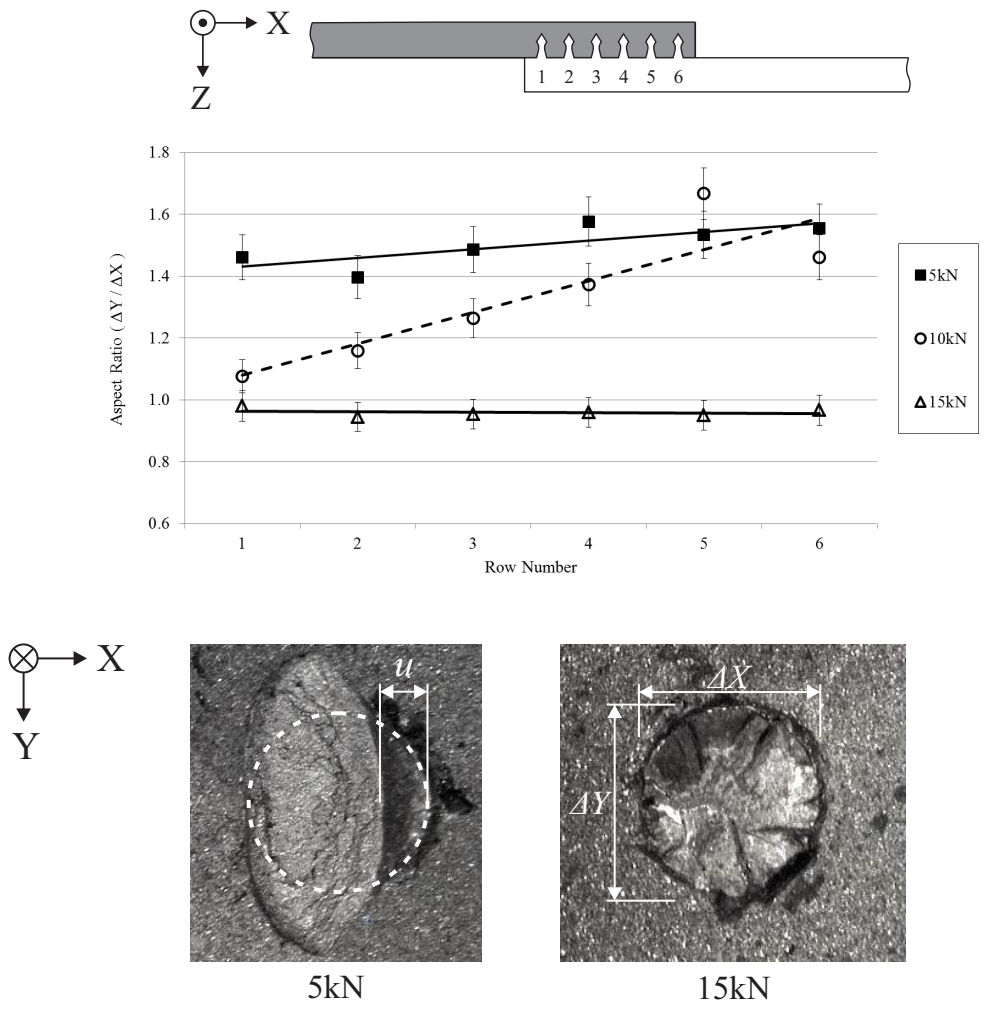

Figure 5.11: Averaged aspect ratio of pin fracture surface with respect to row position for coupons subjected to three different peak loads; 5, 10 and 15kN. Coupon orientation and two plan view photos of pin fracture surfaces also shown. The crater of the 5kN load case exhibits two types of crater growth, firstly, circular (for distance u) and then elliptical.

Figure 5.12 shows the polished section of a pin that had been sheared above the base but had also developed a sub-surface crack. This example was subjected a peak load of 10kN and almost resulted in the tearing failure mode. It can be seen that the crack has propagated through the stock material, below the boundary with the AM material. The boundary of the melt pool was around 0.06mm deep whilst the crack propagated to 0.13mm and then 0.22mm below the surface of the substrate. A shallow melt pool would be expected given that the AM is conducted with a low power laser for accuracy of build rather than a higher powered electron beam process which would typically be used for larger parts [9].

It is thought that, although cracks did not propagate through this interface (between materials of different grain structure), it is likely that this local difference in micro-structure and the anisotropy of the AM material influenced initiation. Despite a fillet radius at the pin root, the discrete change in stiffness between the AM and stock material would have caused a stress concentration. Following initiation, there would have been a significant energy release as the load was redistributed to the inner rows of pins and the crack propagated rapidly down into the

stock material (distance u, Figures 5.11 and 5.12). As the crack reached the finer, quasi-isotropic grain structure of the stock material, less energy would have been required for additional growth and the crater widened. The crack(s) would have grown more slowly during this secondary phase as the applied load was shared more evenly across the pin array.

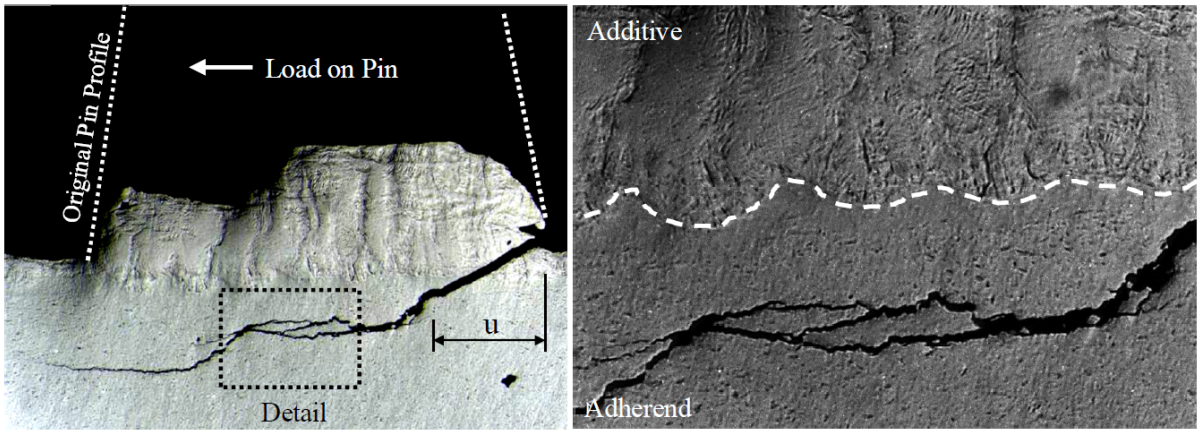

Figure 5.12: Optical microscopy of sectioned coupon showing a fractured pin with sub-surface crack. Initiation resulted in rapid growth for distance u. Boundary of columnar grains shown with dashed line (right).

Despite this variation in the fracture surface, it can be seen that the metallic adherend is largely undamaged and the same is true of the composite adherend. The pins essentially act as sacrificial elements and as a result, the failure mode is controlled and repeatable (for a given load severity). Generally, this is not the case for conventional, mechanically fastened composite joints as the failure mode varies with the peak load, resulting in more significant (and often severe) adherend damage. At high loads, adherends will fail catastrophically (either in net-section or shear out) whilst at lower intensities there will be extensive bearing damage and hole elongation [48, 77]. Therefore, it is believed that HYPER joining not only provides excellent ultimate strength and fatigue life (compared to a benchmark joint) but also great potential for in-service repair as damage has not penetrated the outer surface of the CFRP.

5.6.3 Design Perturbation

Following the completion of this first fatigue trial, and based on the failure mechanisms identified, a design change was implemented in order to try and increase the high cycle fatigue performance. in an effort to prevent rotation of the pin and, subsequently, fracture of the neck and tearing of the pin head, the neck diameter was increased to reduce the stress concentration. A comparison of the baseline and revised geometry is shown in Table 5.2, D_n was increased by one third. It was initially thought that the ratio of D_n:D_h would be maintained (1.67) however, this would have increased the surface area of the central frustum and could have resulted in a larger load being applied to neck. To ensure a fair comparison, the surface area of the frustum and head angles were contrained (1.13mm^2, 90° and 60° respectively) so the free variables were pin height (Z) and head diameter, D_h.

Description	D_b	D_n	D_h	Z	θ_1	θ_2
Loop 1: "Bath Baseline"	1.40	0.90	1.50	3.60	90	60
Loop 2: "Large Neck"	1.40	1.20	1.70	3.77	90	60

Table 5.2: Pin geometry used for second batch of fatigue tests. Dimensions in millimetres and degrees.

As a precursor to fatigue testing, three quasi-static tests were conducted to establish the single cycle failure load ($N = 1$). It is believed that static performance is largely influenced by the base diameter of the pin so a comparison was made with the Bath Baseline results; see Figure 4.7. Surprisingly, it was found that there was a 23% reduction in coupon ultimate tensile strength. It is know that if the interface is disbonded, the UTS would be expected to decrease by 8-9% but the strength of the new coupons was 15% lower than even the artificially disbonded specimens. As a result, it was believed that the quality of the pin manfacture may have been sub-standard so computerised tomography (CT) imaging was used to examine the new coupons for porosity. Figure 5.13 shows sectional views of four representative pins from a Loop 2 coupon and reveals that considerable porosity was present.

As the additive manufacturing was conducted by Airbus Group, it was not known if the correct manufacturing protocol had been followed for the construction of this batch of coupons. Assuming these defects were not a result of impurities in the (raw) metallic powder, it is known that porosity/voiding can occur if the laser is not appropriately focused/calibrated [8]. Figure 5.14 shows two examples of similar porosity defects in two different pin geometries. Through the refinement of processing parameters (by collaborative partners), at the time of manufacture, it would have been expected that porosity levels would be as low as 0.02-0.04% for HYPER pins manufactured with selective laser sintering [8]. Given that the porosity observed in the new fatigue coupons appears to be well in excess of 0.4%, it is less surprising that such poor static strength was found considering the potential reduction in cross-sectional area and subsequent increase in stress. However, due to the prohibitive leadtime required to manufacture a new batch of coupons, a set of these defective coupons were still subjected to fatigue testing.

Figure 5.15 shows three new data points plotted against the original fatigue life curve from the baseline pin geometry. It can be seen that, despite the porosity, the old and new designs correlate very well. Therefore, although a conclusive assessment could not be made, it is believed that the revised pin design *would* have resulted in an improvement in fatigue performance had it not been for the manufacturing defects. Although it could not be accomplished within the scope of this doctoral project, it is proposed that as part of a future work package, the Loop 2 fatigue trial is repeated to confirm this hypothesis and validate the design change.

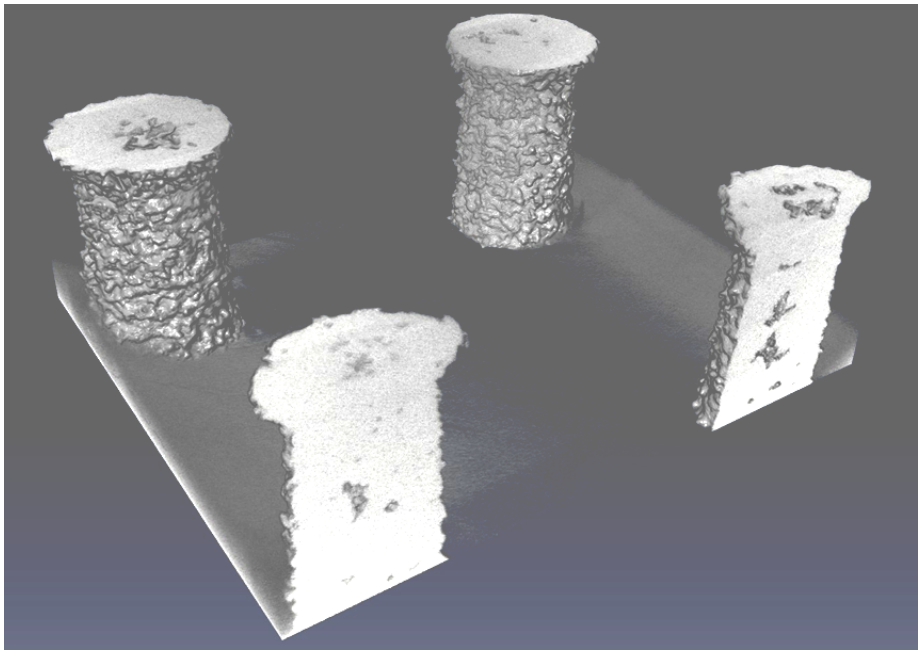

Figure 5.13: Example of computerised tomography showing internal porosity. Four pins with the Loop 2 design perturbation are sectioned in two planes. Images generated by author at University of Bath.

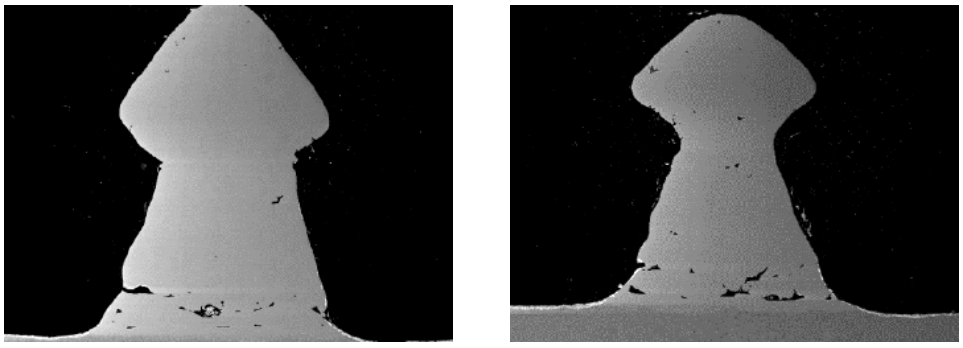

Figure 5.14: Microscopy of polished pin sections showing porosity due to lack of fusion. Two different pin geometries are shown, both have 0.4% porosity. Images courtesy of University of Manchester/Airbus Group Innovations.

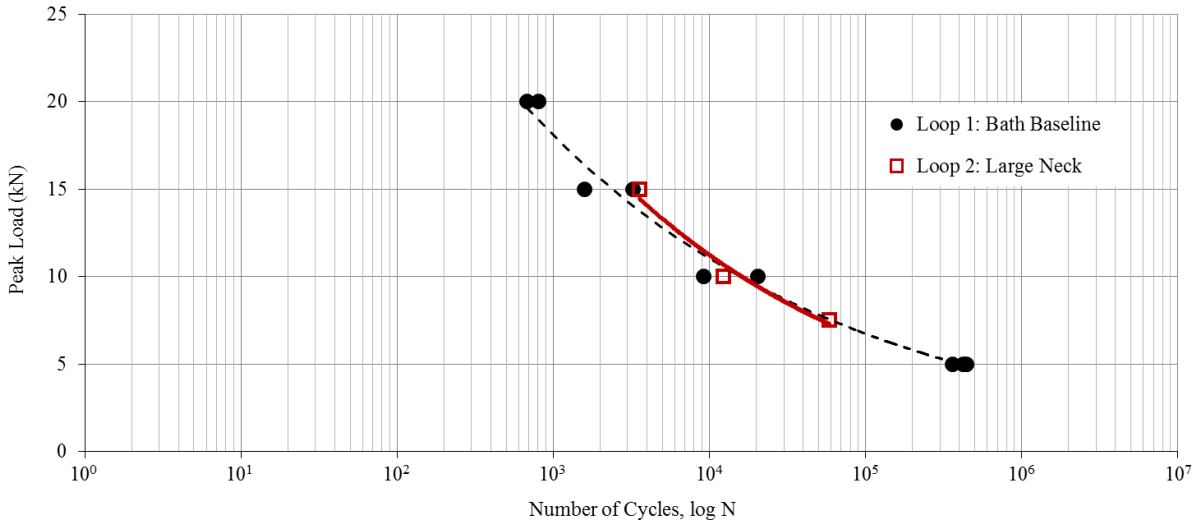

Figure 5.15: Comparison of the fatigue life for the Bath Baseline pin geometry (Loop 1) and the Loop 2 revised design with the increased pin neck diameter.

5.6.4 Tabulated Results

Coupon Id.	D_b (mm)	Spec.	F_{peak} (kN)	N_f	Notes
SLS-01-03	1.4	STD	5	445,807	
SLS-01-04	1.4	STD	5	422,805	
SLS-01-05	1.4	STD	10	20,495	
SLS-01-06	1.4	STD	5	361,159	
SLS-01-07	1.4	STD	15	3251	
SLS-01-09	1.4	STD	20	803	
SLS-01-10	1.4	STD	15	1585	
SLS-01-11	1.4	STD	10	9163	
SLS-01-12	1.4	STD	20	682	
SLS-03-01	1.4	STD	27,674	1	
SLS-03-02	1.4	STD	24,631	1	
SLS-03-03	1.4	STD	19,869	1	Loop 2, D_n=1.2, D_h=1.7
SLS-03-04	1.4	STD	15.0	3567	
SLS-03-05	1.4	STD	10.0	12284	
SLS-03-06	1.4	STD	7.5	58982	

Table 5.3: Results from the fatigue testing campaign.

5.7 Concluding Remarks

Fatigue life of single lap-shear HYPER joint coupons was investigated. It is proposed that metal-composite HYPER joints offer an increase in fatigue life of several orders of magnitude compared to an unpinned and co-bonded benchmark. Damage initiation at the joint interface almost certainly occurred within the first few cycles given the magnitude of the peak loads used for testing. It is believed that damage did not initiate within the pins until at approximately 10% of the total number of cycles required for failure of the test specimens.

The BST has been shown to identify and characterise damage initiation and growth despite the coupon geometry and high adherend stiffness. The ultrasonic NDT method, used for the quasi-static test campaign, has been further validated and it has been shown that both interfacial disbonding and pin damage are observable with this technique. However, conducting an interrupted inspection regime is more suited to static testing and variation in displacement amplitude was the most efficient method for determining initiation of damage and rate of propagation.

It was found that there was a change in failure mode with reduced load severity. At low peak loads ($\leq$32% UTS), failure was governed by the strength of the material directly beneath the pins. Fracture was within the surface of the metallic adherend, not above the pin root as observed in previous quasi-static tests. This mode change, which has not been reported for similar hybrid joining technologies, resulted from a tearing action as joint rotation was low and there was a proportionally large moment at the pin root. At high peak loads, fracture was above the pin root as the shear load on the pins was dominant. With increased joint rotation, the axial pin load was also much larger and resulted in the radial pin stress variation becoming less significant. At low loads, interfacial disbonding was driven by initiation of pin fracture whereas, at high loads, propagation was the result of the pins yielding. At peak loads around 10kN (32% UTS), it was possible to generate both types of failure within a single coupon.

Localised modification to the adherend microstructure during AM was not thought to create a plane of weakness but the boundary between AM and stock material may have initiated cracking due to the difference in compliance and a high stress gradient. It is also proposed that the high surface roughness of the pins would have been likely to have initiated fracture. Alternative and/or more thorough surface preparation of the metallic parts (e.g. shot peening) could have led to a substantial increase in fatigue life. Although it is believed that the joints performed well against an unpinned benchmark, it is anticipated that the fatigue life would have been comparatively low versus a mechanically fastened joint.

Supplementary high-cycle fatigue tests are required with the revised joint design due to the presence of porosity during the Loop 2 perturbation. Testing specimens with a higher quality surface finish would also be desirable. This would allow a more quantitative assessment of performance and better comparison with the Bath Baseline data.

Chapter 6

Detailed Finite Element Modelling

6.1 Summary

A refined method for analysing load transfer in HYPER joints is presented. Conventional finite element approaches for modelling CFRP are considered to have inadequate detail as individual plies are homogenised and are unrepresentative if fibres do not remain straight. A detailed finite element model of a HYPER pin within a CFRP unit cell is developed. Manufacturing characteristics (found during previous experimentation) such as fibre misalignment, variation in volume fraction and resin rich zones are included.

It was found that, for a $[0/90]_S$ laminate, a conventional model (with minimal detail) would transmit the greatest bearing load through the 0° plies. However, when accounting for manufacturing effects, the load transmitted through the 90° plies can actually be higher than that transferred by the 0° plies. Thus, due to the reduced bearing stiffness of the 0° plies, the equivalent bearing stiffness of the laminate can be significantly lower when $d/w \leq 0.3$ (where d is the pin diameter and w the unit cell width). Peak axial stresses are also reduced by up to 70% when the unit cell is modelled in high detail.

The bearing stiffness of the model is also determined to be highly dependent on the relative size of the pin. For larger pin diameters ($d/w > 0.3$), a detailed model can result in the bearing stiffness actually being higher than the conventional benchmark model. This can result from fibre misalignment alone but is even more severe if the volume fraction is allowed to vary proportionally with fibre misalignment.

Hence, this augmented (detailed) modelling approach is recommended for accurate simulation of load transfer in HYPER joints. It is believed that existing design rules, for mechanically fastened joints, do not apply to HYPER joints as subtractive machining (drilling) is not required and the absolute fibre content is maintained. It is proposed that a future work package should incorporate a failure criterion into the detailed model and failure modes should be explored in order to revise existing design rules, specifically for HYPER joints.

6.2 Nomenclature

d	Generalised pin diameter
D_b, D_n, D_h	Diameters of HYPER pin base, neck and head
$E_{1,2,3}$	Elastic modulus of the laminate principal directions
E_f, E_r	Isotropic elastic modulus of fibre and resin
F_x	Force applied to test specimen (in x-axis)
f_x	Force applied to the model (in x-axis)
G	Shear Modulus
L, H	Half-length/height of the unit cell
h	Fibre path offset in y-axis
R	Radius of HYPER pin
x, y, z	Cartesian position within unit cell
x', y'	Position on unrotated unit cell
δx, δy, δz,	Displacement in the three principal axes
Δx, Δy, Δz	Finite strip within the model
V_f	Local fibre volume fraction
V_f^0, $\bar{V}_f$, $\widehat{V}_f$	Nominal, mean and maximum volume fraction
w	Unit cell width (and height, as square)
α	Polar coordinate on unrotated unit cell
ν	Poisson's Ratio
θ	Local fibre orientation
ϕ	Undistorted fibre angle of each ply

6.3 Motivation

The goal of this work was to determine whether a conventional finite element approach (homogenisation of individual plies) was accurate for modelling HYPER joints or if a more accurate representation of the pin-fibre interaction was required. To date, collaborators at Airbus Group have constructed finite element models of HYPER joints with individual plies represented by homogenised layers [8]. This conventional straight fibre model would be representative of a bolted or riveted joint as the fastener is inserted into a drilled hole. However, it is known that, due to the HYPER joint manufacturing process, embedding of the pins results in fibre distortion (both in and out of plane) and resin rich zones in proximity to the pins; see Figure 6.1. Thus, a conventional approach would be overly simplistic.

Accounting for the interaction between the pins and the laminate is critical for the load transfer within these joints and, subsequently, to ensure accurate simulation of bearing stiffness, strength and failure modes. Thus, the conventional straight fibre approach (SF) is compared to a new detailed model that includes locally distorted fibres (DF) and resin rich zones. These differences are shown in Figure 6.2.

Analysis of the accuracy and efficiency of these two finite element approaches was required as a precursor to the development of a HYPER joint optimisation tool (although the latter could not be conducted during the course of the project). The experimental results presented in Chapters 4 and 5 have shown promising performance but, these coupon tests used baseline pin/array designs that are thought to be structurally sub-optimal. As already stated, additive manufacturing provides huge potential for optimisation of this joining technology (e.g. pin radii, height and spacing) but to date, limited work has been conducted (either by the author or externally at Airbus Group) in this area. In order to improve the joint design, without the need for further extensive test programmes, an accurate yet efficient method was required, so the analysis conducted herein was essential, for development of the HYPER joining concept.

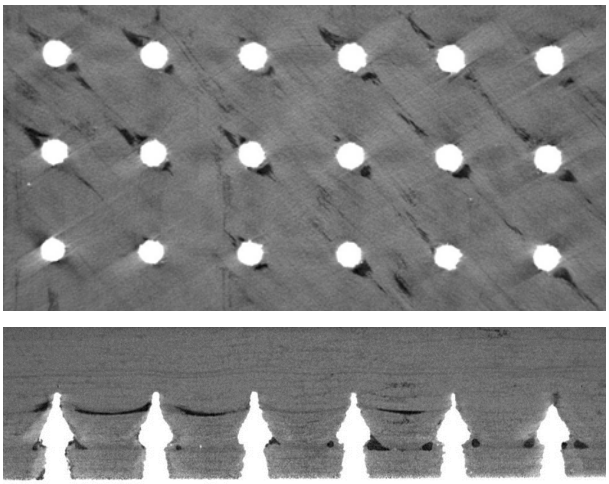

Figure 6.1: Computerised tomography showing a plan view of a -45° ply and a through thickness section of embedded HYPER pins. Resin rich zones are shown in black.

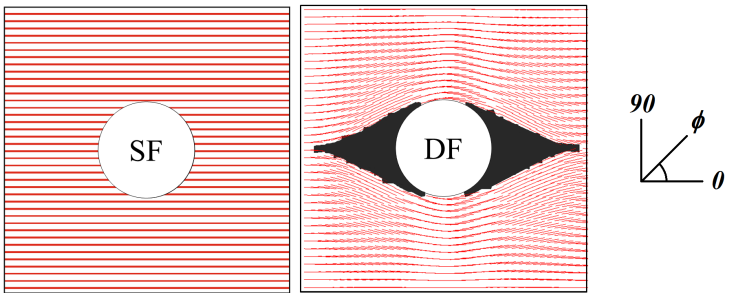

Figure 6.2: Examples of straight and distorted fibres in the two models, SF and DF respectively. Resin shown in black, nominal (undistorted) fibre angle $\phi = 0°$.

6.4 Background

HYPER joining has similarities to both mechanically fastened and Z-pinned joints. As these approaches are more mature, a large body of work has been completed in both areas. Camanho and Matthews provide a comprehensive review of methods of stress analysis and strength prediction of mechanically fastened joints specifically in fibre reinforced plastics [14]. Mechanically fastened joints can failure in a range of modes depending on the specimen geometry. The number of dependent variables increases significantly when fastening CFRP as the layup largely influences both stiffness and strength. There has been a significant focus on failure modelling and bearing stiffness is often overlooked [19]. Although two different stacking sequences may generate variation in ultimate strength and result in difference failure modes, their initial bearing stiffness can be very similar [92, 93]. However, it has been found that the inclusion of fibre waviness can lead to unexpected results.

Fibre waviness is also a factor for Z-pinned joints due to their manufacturing process. Just like HYPER joints, embedding Z-pins creates in-plane distortion of fibres and resin rich zones in reinforced areas. A review of the literature revealed that comparable approaches had been utilised by several authors to characterise Z-pinned CFRP laminates [28, 39, 51]. Unfortunately, due to the shape of these pinned regions, when multiple plies are stacked together, a very fine mesh is required in order to avoid geometric discontinuities. To avoid any discontinuities, Gunnion et al. [39] used voxels (three dimensional pixels) to model a Z-pinned representative volume element (RVE). By using a mesh of regularly structured, quadrahedral elements, multiple plies could be stacked together and geometric discontinuities avoided even with a large element size. Geometric and numerical accuracy was still largely dependent on the refinement of the mesh but it was shown that acceptable homogenisation of the RVE could be achieved with large computational savings. This method was suitable for this homogenisation task as the pins were small compared to the unit cell. Loads transmitted through the pin were neglected and boundary conditions were applied to the external edges of the RVE; comparable to a filled hole tension/compression test.

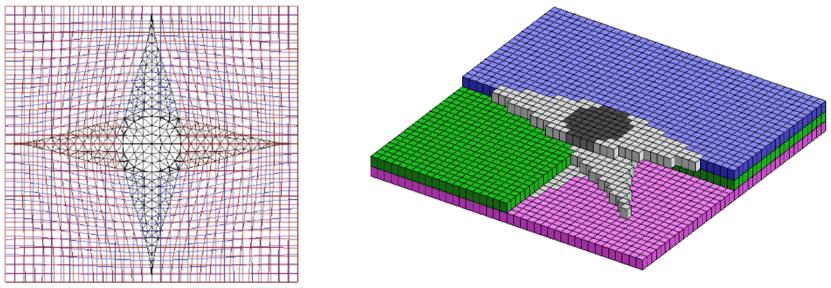

Figure 6.3: (a) Two overlapping meshes showing the potential for discontinuities at the tips of the resin rich zones. (b) The voxel approach of Gunnion et al. [39].

A voxel approach could not be used for HYPER as the pin aspect ratio and pin material results in them being stiffer than Z-pins and transferring a significant proportion of applied loads. Examples of pin and array geometry are listed in Chapter 2. Upscaling in the same way as Gunnion et al. would not accurately model any bearing load transferred through the HYPER

pin to the surrounding material. The bearing load induced on the CFRP by a cylindrical pin/fastener should be maximal at the centre of the contact face and decrease to zero at the edges due to the reduction in contact angle [19]. In Gunnion's model, because the mesh is formed of regularly spaced quadrahedral elements, for loads in the primary axes (x or y), the pin elements always contact the surrounding material perpendicularly. As a result, assuming that the pin is very stiff compared to the composite, the load would be uniformly distributed across the diameter of the pin and the contact pressure at the edges of the pin artificially high. Therefore, it is essential to model the pin/hole with greater geometric accuracy, even if the rest of the RVE is less refined. This is an approach adopted by several other authors [28, 51]. By using a common star shaped mesh design for each layer, resin rich zones can be included and mesh discontinuities still avoided.

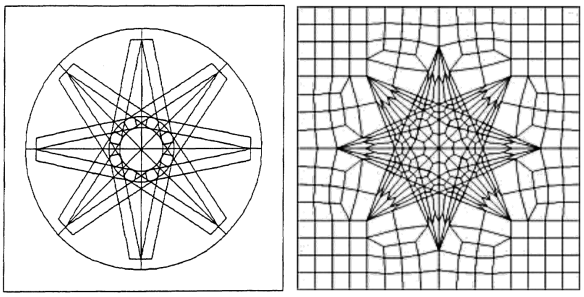

Figure 6.4: Star shaped mesh designs used to ensure mesh compatibility through thickness. The symmetry of these designs is application specific and would only be suitable for 0, 90 and $\pm 45^{\circ}$ plies [28, 51].

As previously stated, Comeld is a comparative hybrid (metal-composite) joining technique. Tu et al. completed a preliminary optimisation study of Comeld joints [89] using a mesh-free method [88]. This was completed with a two dimensional (through thickness) model and it is believed that no account was made for in-plane fibre distortion or resin rich zones. Although the Comeld pins are much smaller in diameter than HYPER pins, these manufacturing defects would almost certainly still occur during embedding of the pins due to the high density of Comeld pins.

6.5 Overview of Modelling

As already stated, the goal of this chapter was to investigate pin-fibre interaction with both a conventional straight fibre model and a detailed modelling technique accounting for distorted fibres. To achieve this aim it was not necessary to model an entire coupon/array and a new unit cell model was proposed. Although baseline coupon designs typically use a 6×6 array of pins, for the purposes of this study it is assumed that only a single row of pins exist in the loading direction. This configuration is more severe for the laminate as the entire load is transmitted through bearing and stress concentrations at the edges of the fastener are higher. Additional unit cells would had to have been modelled in series to account for the load bypass around the pin.

It was also assumed that longitudinal loads are predominantly transferred below the pin head thus, only the lower section of the pin was modelled; see Figure 6.5. Although HYPER pins have a complex tapered profile, it was assumed that they are cylindrical and that there is no variation in diameter through the thickness of the laminate. For simplicity, the non-linear geometric (rotational) effects of a single-lap joint were ignored. The metallic adherend was not modelled and it was assumed that the pin receives an in-plane load; Figure 6.5c. The inclusion of coupled, multi-axis loads/moments was beyond the scope of the project. Figure 6.5d shows a plan view of the unit cell. Although only a single row of pins was modelled in the loading direction, periodic boundaries are enforced to maintain continuity with adjacent cells across width of the coupon. Application of the boundary conditions is described in more detail in Section 6.6.5.

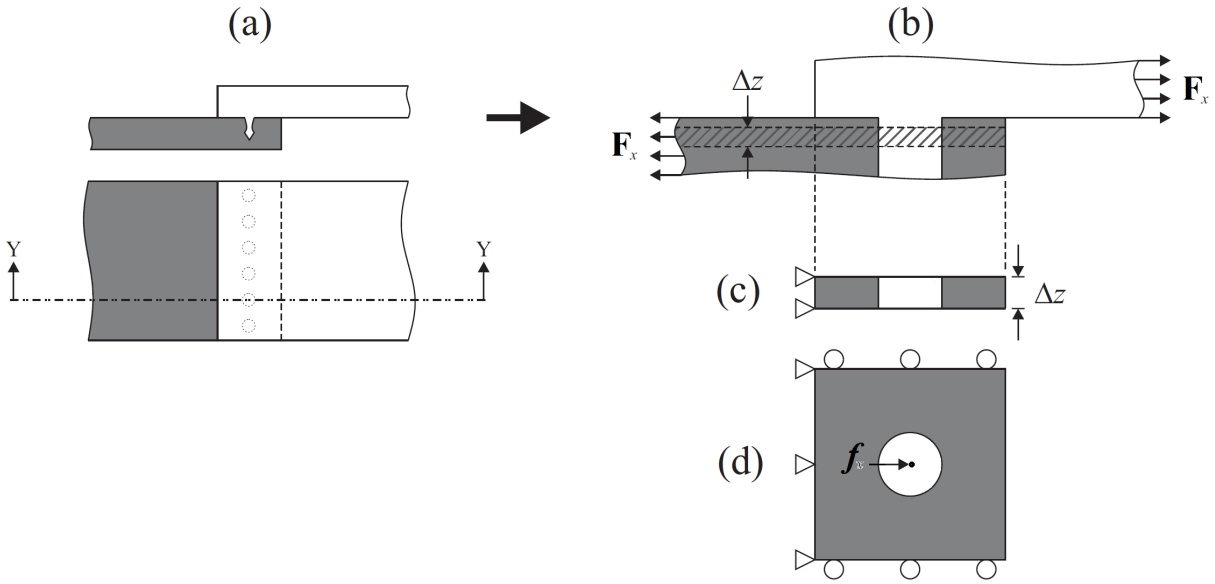

Figure 6.5: (a) Partial section of single-lap HYPER joint coupon showing a single row of pins. (b) A cylindrical pin is modelled without a head feature. (c) In-plane loading applied to pin within a finite strip of laminate, Δz. (d) Plan view of the unit cell model showing boundary conditions; transverse displacement constrained. Load f_x applied to central reference point and transfered to pin via a kinematic coupling.

Firstly, the pin-fibre interaction was assessed based on the in-plane stress distributions and compliance of two individual ply orientations: fibres aligned with the load direction (0 degrees) and fibres perpendicular to the load (90 degrees). These test cases were chosen as they should have the greatest and least membrane stiffness respectively (in the loading direction). Both fibre orientations were modelled using the new detailed model with distorted fibres (DF) and resin rich zones. A conventional straight fibre (SF) model was used as a benchmark, see Table 6.1 and Figure 6.2.

These four tests could be considered artificial as, typically, a laminate would not be constructed with these plies in isolation. However, these simulations emphasise the comparative differences between orthogonal fibre orientations. As through-thickness effects initially neglected, for these test cases, the unit cell modelled in two dimensions and plane stress assumed (as the thickness is small compared to the in-plane dimensions).

	Fibre Distortion and Resin Rich Zones	Variation in Fibre Volume Fraction (V_f)
Model SF Benchmark	No (Straight)	No
Model DF New Approach	Yes	Yes

Table 6.1: Configurations of the numerical model.

The pin diameter was initially fixed at one-third of the width of the unit cell ($d/w = 0.3$). This ratio is known to be an optimal compromise between bearing and net-section stress for a wide range of layups [67]. This ratio is comparable to the baseline (6×6) HYPER joint design as shown in Table 6.2.

Shape of Pin Array	**4×4**	**6×6**	**8×8**
Unit Cell Width (w)	6.350mm	4.233mm	3.175mm
0.9mm (D_n)	0.142	0.213	0.283
1.2mm (D_b)	0.189	0.283	0.378
1.5mm (D_h)	0.236	0.354	0.472
1.7mm ($D_h{}'$)	0.268	0.402	0.535

Table 6.2: Ratio of pin diameter to unit cell width (d/w) for four diameters and a three array sizes. The baseline neck, base and head diameters are provided (D_n, D_b and D_h respectively) as well as the revised head diameter from the fatigue investigation ($D_h{}'$). All values based on a 25.4×25.4mm overlap with uniformly distributed square arrays. For example, an array of 16 pins (4×4) would result in each individual unit cell being 6.35×6.35mm in plan view.

After these generalised test cases had been completed, a three-dimensional analysis was then conducted to examine whether any differences between the DF and SF models (seen in the idealised cases), would also be present when plies were combined in a more realistic ply combination; $[0/90]_S$. In addition, unlike the two dimensional models, the three dimensional DF and SF models were compared for a range of pin diamaters. These were in the range $0.1 \leq d/w \leq 0.5$ as these ratios would be of interest if different array sizes/spacings were trialled in future; again see Table 6.2. Mesh refinement studies were conducted for both the two and three dimensional models. All models were constructed and solved with the commercial finite element package ABAQUS [24]. Bespoke pre-processing routines were written by the author in Python.

6.6 Methodology

6.6.1 Mesh Generation

The height and width of both the 2D and 3D unit cell models (w) were 4.233mm which is equivalent to a 6×6 array within a one inch square overlap. The thickness of a ply was 0.25mm (5.9% of the in-plane dimensions). Two parts were created in ABAQUS, shell based geometry was used (for the two-dimensional model) to generate the pin and the laminate. Different element size, type and meshing algorithms were tested to ensure suitable convergence. The seed size was set as a percentage of the cell size. Plane stress elements were chosen as the laminate was considered to be very thin in comparison to the in-plane dimensions. Section thickness was specified as 0.25mm (a single ply).

The in-plane definition of the three dimensional mesh was identical to the two dimensional design. A swept mesh was used to project this design through thickness and maintain compatibility. Local edge seeds were specified to ensure that the number of elements/layers through thickness was maintained for all models. To improve the accuracy of the through thickness stress distribution and reduce the aspect ratio of the elements, two elements were used per ply. It is known that other authors have used only a single element per ply but it is believed that increasing the number of elements through thickness would increase accuracy. Unfortunately, due to time constraints, it was not possible to make a comparative analysis; with more or less elements per ply. The element thickness remains fixed for all tests so by refining the in-plane (x, y) dimensions the aspect ratio is increased. Having two elements through thickness ensures that this aspect ratio remains within the recommended limit of 1:10 [26]. For example, with in-plane element size refined to 0.75% of the unit cell width, the aspect ration was typically 1:4 rather than 1:8.

By modelling the hole within the laminate and then projecting the mesh design through the thickness of the part, a new hybrid variant of the voxel approach has been generated. Once the parts and mesh had been produced, the fibre orientations, material properties, boundary conditions, etc. could be applied.

6.6.2 Calculation of Fibre Angle

It was assumed that in-plane fibre waviness could be represented with the sinusoidal function:

$$y = R\Big(1 - \frac{h}{H}\Big)\cos^2\Big(\frac{\pi x}{2L}\Big) \tag{6.1}$$

where R is a given pin radius and h is an offset in y that also governs the decay of the amplitude. It is also assumed that the fibre distortion has fully minimised at $x = \pm L$ and $y = \pm H$, the full height and width of the unit cell although a more rapid decay in either axis could easily be implemented. The local fibre angle, θ can be found at any cell position (x, y) by rearranging Equation 6.1, solving for h and then substituting this value into the differential of Equation 6.1. This formulation is only valid for $h \geq 0$. Between this limit and $y = 0$, θ is not calculated as

the element is assumed to be 100% resin if it is not within the radius of the pin. These are the grey regions in Figure 6.6a. Below the centreline of the cell, a symmetry condition was applied ($y = -y$) so that θ could be determined in an identical manner to the upper half of the cell. This formulation is not mesh dependent and could be completed for any mesh as long as the nodal positions can be extracted, the local fibre angle can then be calculated at the centroid of each element.

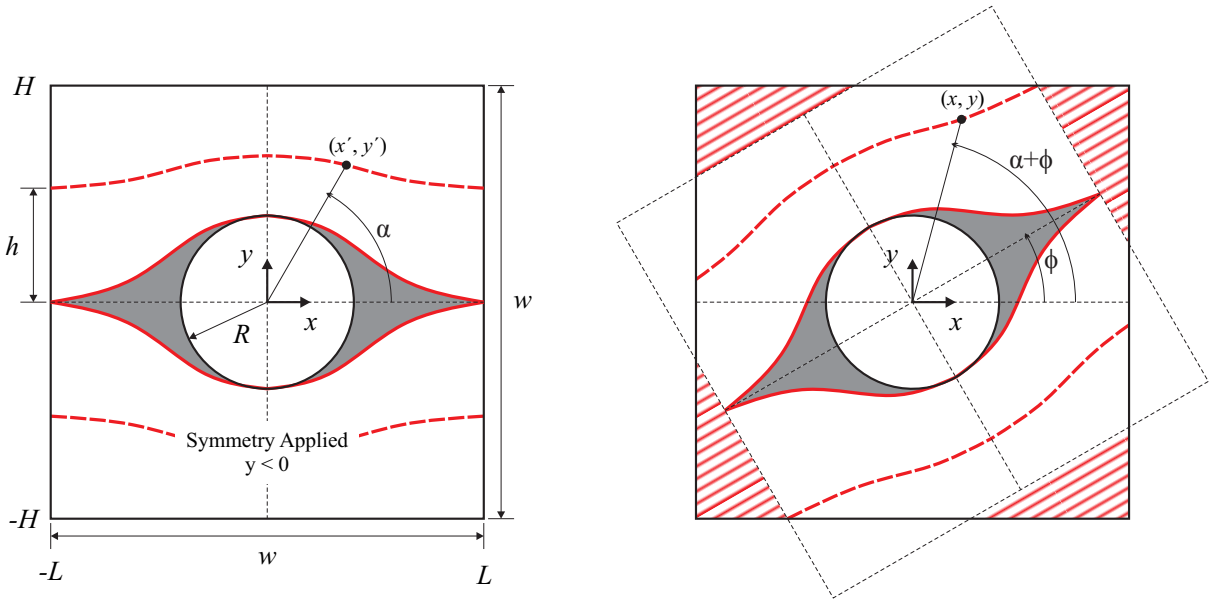

Figure 6.6: (a) Diagram of RVE showing a single, unrotated ply ($\phi = 0$) with four arbitrary fibre paths. Resin rich zones shown in grey. (b) Decay length/height remain constant regardless of ply angle (ϕ) thus, in hatched regions, there is no fibre distortion ($\theta = \phi$).

For non-zero ply angles ($\phi \neq 0$), a polar transformation was used to rotate the system $\pm 90°$. If $y \geq x \tan \phi$, the polar position on an unrotated system was found by:

$$\alpha = \begin{cases} \tan^{-1} \frac{y}{x} - \phi & x \geq 0 \\ \tan^{-1} \frac{y}{x} - \phi + 90 & x < 0 \end{cases} \tag{6.2}$$

The polar coordinates on the unrotated system are then reverted back to a Cartesian position (x, y) and θ calculated as previously described. On the original (rotated) system, the true local fibre angle is found with the addition of ϕ, as shown in Figure 6.6b. If the unrotated local position $y < x \tan \phi$, i.e. $y' < 0$, a symmetry condition can again be used to calculate the fibre orientation but, for this case, two conditions must be applied; $y = -y$ and $x = -x$.

6.6.3 Change in Fibre Volume Fraction

Unlike Gunnion et al. [39], a micro-scale materials model was also incorporated to account for the local changes in fibre volume fraction and the resultant modification to mechanical properties due to fibre distortion. The analytical fibre-resin model of Luciano and Barbero was used [57]. It is assumed that the volume of fibre in a strip of Δx is maintained when distortion is

induced (see Figure 6.7) and thus, the mean volume fraction in the new strip ($\bar{V}_f$), compressed by Δy, was given by Equation 6.3. It is assumed that the volume of resin displaced, fills the region adjacent to the pin.

$$\bar{V}_f(x) = \frac{V_f^0}{1 - \frac{\Delta y}{H}} \tag{6.3}$$

$$\Delta y = R\cos^2\left(\frac{\pi x}{2L}\right) \tag{6.4}$$

$$V_f(x, y) = A(y - H) + V_f^0 \tag{6.5}$$

$$A = \frac{2(V_f^0 - \bar{V}_f)}{H - \Delta y} \tag{6.6}$$

The fibre waviness minimises by $y = H$ (Equation 6.1) so the local fibre volume fraction, V_f would also have returned to the nominal value, V_f^0 at this limit. Furthermore, it is assumed that there is a linear variation in V_f between the nominal and maximum values, as given by Equation 6.5 and shown in Figure 6.7.

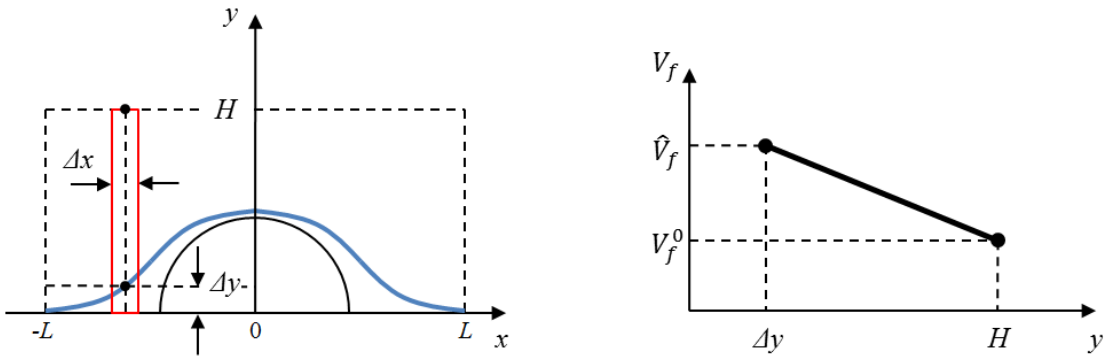

Figure 6.7: Plan view of half a unit cell with a linear distribution of local fibre volume fraction assumed with respect to y-axis position.

It should be noted it is possible for Equation 6.5 to yield $V_f > 1.0$. This would indicate that the ply requires a thickness change to maintain the constant volume condition. However, to simplify the model geometry and, subsequently generation of the mesh, it was desirable for the thickness of all plies to remain constant. In addition, Luciano and Barbero's model [57] assumes that the fibres are square packed and it is shown that, for this configuration:

$$\widehat{V}_f = \frac{A_{fibre}}{A_{total}} = \frac{\frac{1}{4}\pi r^2}{r^2} = 0.7854 \tag{6.7}$$

whereas, for a triangular/hexagonally packed RVE:

$$\widehat{V}_f = \frac{\frac{1}{2}\pi r^2}{4r^2\sin(30)\cos(30)} = \frac{\pi}{4\cos(30)} = 0.9069 \tag{6.8}$$

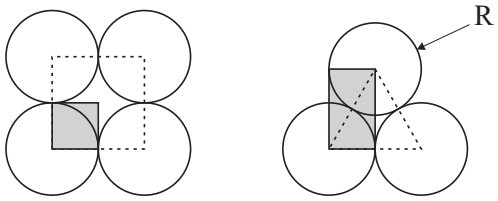

Figure 6.8: Square and triangular spaced fibre-resin RVEs. It is assumed that all the fibres are the same size (R).

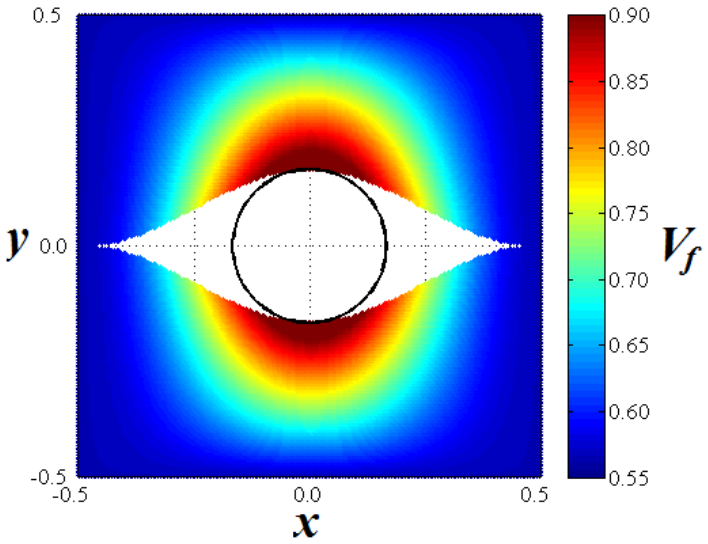

Figure 6.9: Plot of volume fraction variation within a unit cell, showing regions that exceed the volume fraction upper bound ($d/w = 0.3$, $\phi = 0$).

Thus, an upper bound was set such that $\widehat{V}_f = 0.785$ for all strips of Δx. Figure 6.9 shows the regions of a unit cell that would exceed this volume fraction upper bound if it were not enforced. For a pin diameter one-third of the unit cell width, 11.3% of elements assigned a revised volume fraction ($\theta \neq \phi$) would exceed the upper bound of 78.5%. Although it was not possible to fully evaluate the significance of this effect, it is thought that this results in the model being conservative. If the additional fibre was not discounted, the stress concentrations at the edges of the hole would actually be lower that seen in the model.

6.6.4 Materials and Orientations

The CFRP properties reported by Airbus Group for M21-T800S are listed in Table 6.3 [79]. This is contrary to other values found in the literature for the same material; also listed in Table 6.3 [36]. In order to allow for comparative analysis with existing modelling by Airbus Group, it was desirable to use the same properties as Sirna and Lanzi. However, the materials model [57] assumes linearly elastic and isotropic fibres and matrix and thus, the inputs required were only the modulus and Poission's Ratio of each. Values found in the literature were $E_f = 302$GPa, $\nu_f = 0.35$, $E_r = 1.5$GPa and $\nu_r = 0.4$, for fibre and resin respectively [36, 44]. However, these values resulted in apparently erroneous laminate properties when input to the materials model, as shown below (Set C). Luciano and Barbero's model was validated against experimental

data so it is believed to be accurate. Therefore, the individual fibre and resin moduli were adjusted to bring their combined properties inline with the values of Sirna and Lanzi ($E'_f = 276$, $E'_r = 2.04$GPa, Set D). As can be seen from Table 6.3, there is still variation between these sets (B and D). No failure criterion was incorporated as the applied stress remained low for all tests (see Section 6.6.5), although it would be desirable for this to be investigated in a future work package.

Data Set	E_1	E_2	E_3	G_{12}	G_{13}	G_{23}	ν_{12}	ν_{13}	ν_{23}
A. Giddings [36]	172	8.9	8.9	4.2	4.2	0.225	0.35	0.35	0.01
B. Sirna and Lanzi [79]	157	8.5	8.5	4.2	4.2	4.2	0.35	0.35	0.35
C. Erroneous Output	172	6.3	6.3	1.9	1.9	2.1	0.37	0.37	0.53
D. Parkes (Adjusted)	157	8.5	8.5	2.6	2.6	2.8	0.37	0.37	0.53

Table 6.3: Properties of the CFRP laminate within the model. Data used herein (Set D) generated by iterative adjustment of the inputs to the materials model [57]. Moduli listed in GPa.

As it was decided to fix the material parameters for all simulations, it was not necessary to repeatedly run micro-mechanics model for every model. Hence, the model was run for an evenly distributed set of volume fractions between the upper and lower bounds (0.566 to 0.785) in order to to generate data set for fitting of response curves. Figure 6.10 shows these results and it was possible to achieve adequate correlation ($R^2 \geq 0.9995$) using either linear or quadratic functions. This approach subsequently allowed greater computational speed during pre-processing.

For the 2D model, the local properties were applied to the unit cell, element by element. These properties did not vary within each element and were calculated based on the x-y position of the element centroid. Once the local fibre angle and volume fraction of an element were known, the material properties could be found from the six response curves (Figure 6.10) and a new material generated. This subsequently required a corresponding material section to be produced in ABAQUS and this could then be applied to that element. Consequently, this approach created a huge number of materials, sections and orientations and also led to the generation of duplicates. E.g. due to symmetry of the unit cell, an element at (a, b) would be identical to one at $(-a, -b)$. This approach performed adequately for the 2D models as total element count in the CFRP part was low, compared to a 3D equivalent, and as only a single ply was simulated, through thickness position of the element and stacking sequence did not have to be considered. However, for the 3D models, this initial method made pre-processing and manipulation of the ABAQUS GUI prohibitively slow; even on a high powered workstation. Thus, following preliminary investigations with the 2D model, the pre-processor was redesigned and additional constraints implemented.

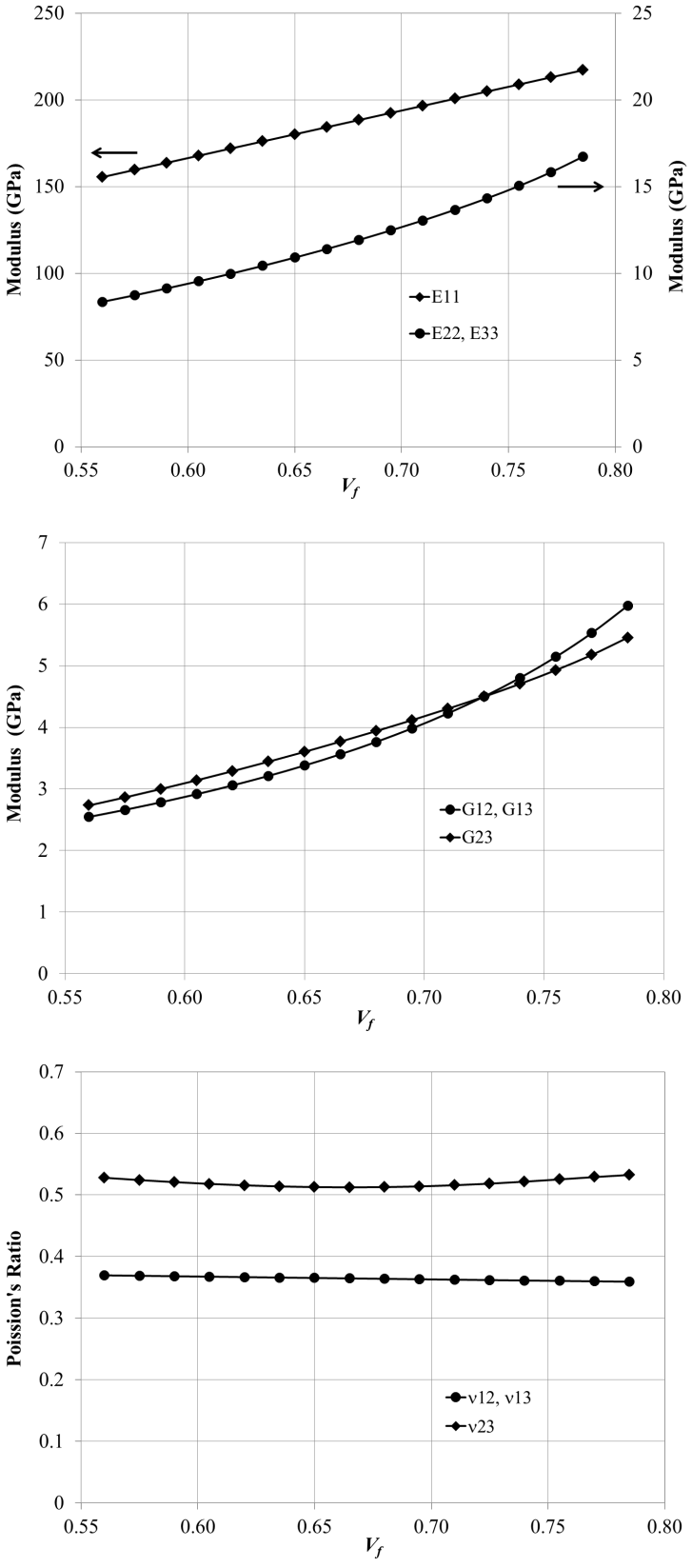

Figure 6.10: Variation in material properties with changing volume fraction. Generated using the model of Luciano and Barbero [57].

The refined approach grouped elements with similar properties into sets for application of materials and orientations. Once the local fibre angle, θ, was calculated it was rounded to the nearest integer value. This resulted in only 180 possible values (0-179 inclusive) because a ply with a nominal angle of -45° (315°) could be defined as 135°. The calculated fibre volume fraction was also rounded to three decimal places so that there were only 220 available perturbations ($0.566 \leq V_f \leq 0.785$).

It is believed that these restrictions would not significantly compromise accuracy but a comparison with an unconstrained model was not made. By restricting θ and V_f to a discrete set of values, elements with the same properties could be grouped into nested tuples. As before the Python script looped through all elements and, following calculation of angle and volume fraction, the appropriate tuples were appended with the element's label. Materials and associated material sections were only generated for populated tuples. Finally, when all of the elements' labels had been added to the material and angle tuples, the script looped through each list and assigned materials and angles in groups. This resulted in far superior pre-processing times as, previously, over 100,000 "materials" had to be created and individually applied.

6.6.5 Boundary and Contact Conditions

As the unit cell model was constructed using geometry based parts (rather than an independent orphan mesh), the boundary conditions could be applied to surfaces and edges rather than node/element sets. This meant that changes could be made to the mesh without having to re-apply the boundary conditions for each run. As shown in Figure 6.5, the left-hand face of the unit cell is effectively clamped by ensuring that $\delta x = \delta y = \delta z = 0$ at each node on the face (rotation prevented by adjacent nodes). The top and bottom faces were only permitted to slide in the loading direction to prevent transverse contraction due to Poisson's Ratio and maintain a periodic boundary ($\delta y = \delta z = 0$). This would have artificially stiffened the model but negated the use of multi-point constraints to retain equal nodal displacements along the top and bottom edges. For a $[0/90]_S$ case, due to the orientation of the symmetry planes, this was adequate to ensure that displacement and curvature along the free edge were equal and opposite respectively. Therefore, if cells were to be replicated in the transverse direction, continuity would be maintained (Figure 6.11). However, this would not have been true if a $[\pm 45]_S$ case had been used because of extension-shear coupling.

A multi-point constraint would have had to have been used to tie the active degrees of freedom of opposing nodes on the "free" edge, essentially creating a rigid link between them. This would have meant that displacement in the loading direction (δx) would remain equal at the boundaries and continuity would be maintained.

As different pin diameters were tested, and the bearing stiffness of each was anticipated to be different, a fixed load was applied (rather than displacement) for all simulations in order to make fair comparison between stress distributions. A small arbitrary load was applied to all models so that the material response would remain linear and the failure not induced. Based on the experimental quasi-static data (Chapter 4), it is believed that failure was not initiated

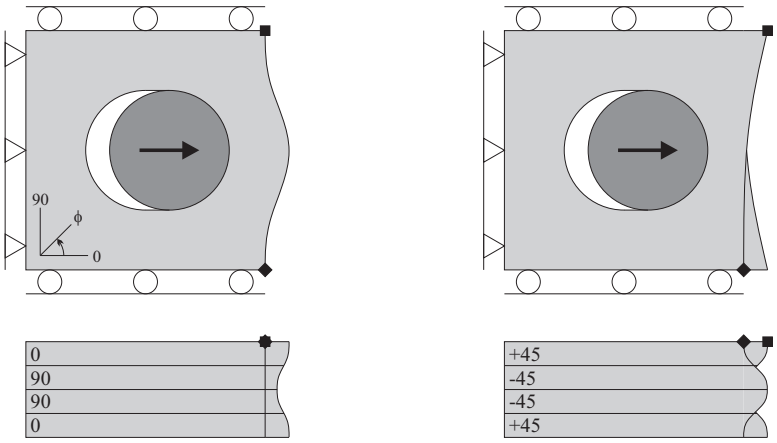

Figure 6.11: A periodic mode shape would not be maintained in a $[\pm 45]_S$ models without an additional boundary condition due to extension-shear coupling. For this case, a multi-point constraint would have been required to ensure translation of nodes on the free edge (e.g. nodes ◆ and ■) remained equal.

until the applied load (F_x) was in excess of ≈4.5kN; for the standard Bath lap-shear coupon. Thus, 125N was considered to be a safe load for a single pin, assuming all pins were uniformly loaded. A proportion of this load (f_x) was applied to a reference point (RP) at the centre of the pin (proportional to the number of plies in the unit cell). The RP was tied to the nodes of the pin's cylindrical surface with a kinematic coupling. This ensured that all of the degrees of freedom of the outer nodes matched those of the RP; effectively creating a rigid body. It is believed that (for this model) the deformation of the pin would be negligible compared to that of the laminate. All translational and rotary degrees of freedom of the RP were constrained except for δx so that it was free to displace as the laminate deformed. The bearing stiffness could be calculated from measurement of the pin translation. Finally, a contact condition was applied to integrate the pin and laminate. A single contact pair was established between the two cylindrical surfaces and the surface-to-surface algorithm used the "small-sliding" condition [25]. It was believed that small-sliding would be a suitable method for this problem as the loads and displacements remained low and there would be little relative translation between master and slave nodes. Therefore, these associations could be established once, at the beginning of the analysis, and would remain true for the whole simulation.

6.6.6 Integration of Pre-Processing

Automated pre-processing within ABAQUS can be realised using several different strategies. It is possible to directly write an input file for the solver module using a basic text editor. This process can therefore be automated in any programming language with simple input/output commands. This approach would totally bypass the "CAE" module and graphical user interface (GUI) and would be extremely efficient for geometrically simplistic models (e.g. if nodal positions and element connectivity could be easily formulated). For the models used herein, due to the complex geometry and highly detailed meshes, it was essential to take advantage of the ABAQUS' advanced built-in CAD and meshing capabilities. This was achieved by manipu-

lating these features/functions from the Python Development Environment. Upon submitting a model to the solver, the input file still needed to be written so this approach incurs an additional step for each perturbation of the model; see Figure 6.12. To avoid compromising the speed of the pre-processor further, unnecessary visualisation in the GUI was avoided by running Python scripts from the Windows command line interface. The command `abaqus cae noGUI=example.py` would "check out" the license file, run the script and then close ABAQUS. However, if multiple scripts were to be run, rather than repeatedly having to request the license file from the license server, it was more efficient to firstly enter the ABAQUS Python interface within the Windows shell by calling: `abaqus cae noGUI`. Scripts could then be run with the Python command `execfile('example.py')`. After a batch of models had been solved, the results were evaluated in the GUI.

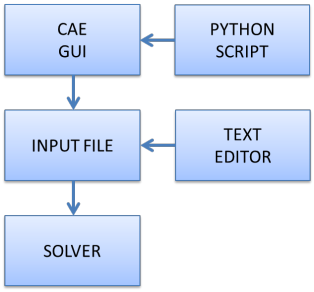

Figure 6.12: Information transfer within ABAQUS.

6.7 Results and Discussion

6.7.1 Two Dimensional Single Ply Models

6.7.1.1 Mesh Refinement

The mesh density determined the geometric accuracy with which the resin zone was be modelled as shown by the two examples in Figure 6.13. Hence, a mesh sensitivity study was completed for the DF model before stress distributions and model compliance were evaluated. This study determined the number/size of elements that would be used for each of the two test cases to ensure an efficient compromise between computational speed and accuracy.

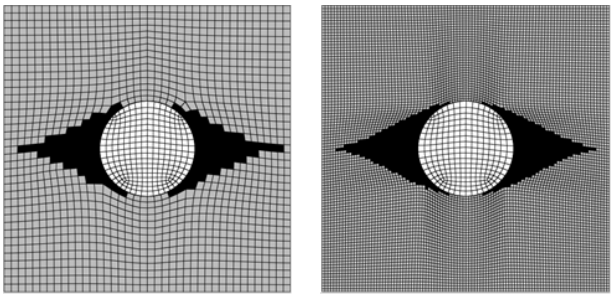

Figure 6.13: Two dimensional unit cell model with two different element sizes: 2.5% and 1.0% of the unit cell width, left and right respectively. Pin shown in white and resin zones in black. $d/w = 0.3$ and $\phi = 0$.

Five in-plane mesh refinements were made and element seed size was set as a percentage of the unit cell width (0.5-2.5%). Varying the mesh density resulted in a change to the stiffness of the model so, in order to fairly compare resulting stress distributions, a constant axial force was applied for all models; as previosuly described in Section 6.6.5.The models were run on an Intel-i7 (2.80GHz) desktop computer with 8Gb of RAM and computation times are shown in Table 6.4. As would be expected, the time required to solve the model increases exponentially as the element size is reduced. However, it was found that the total solution time is dominated by the duration of pre-processing and generation of the input file because of the methodology used (as described previously).

Element Size (%)	Total Elements	Solution Time
2.50	1416	0:00:49
1.25	5704	0:07:04
1.00	8978	0:13:28
0.75	15597	0:38:53
0.50	35352	3:06:20

Table 6.4: Comparison of computation times for five mesh densities using CPS4R plane stress elements. Element sizes are a percentage of unit cell width. Solution times are shown in hours, minutes and seconds.

The peak net-section stress (σ_x) at the edges of the hole ($x = 0$, $\alpha = \pm 90°$) were compared in order to select an appropriate mesh density. Variation in peak stress was found to reduce with increased mesh density as the solution converged. With an element size of 0.75%, there was a difference of only 3.5% in peak stress compared to a mesh size of 0.5% yet the computation time was reduced by 79.9%. Therefore, it was decided that a mesh size of 0.75% provided a good compromise between speed and accuracy and was used for all subsequent analyses. In addition, it was found that there was good correlation between linear and quadratic elements (CPS4R and CPS8R) as the model was well convergered. As a result, linear elements were used as they offered a comparative reduction in computation time. A more extensive convergence study is undertaken with the 3D model in the following section.

6.7.1.2 Comparison of SF and DF Models

The objective was to investigate the location and magnitude of the peak stresses in both the detailed and benchmark models. The displacement of the pin was also used to calculate and evaluate an equivalent bearing stiffness for each model. Figures 6.14-6.16 compare stress contours of SF and DF models for each of the two test cases ($\phi = 0$ and $\phi = 90$). The scaling varies between each figure but is identical for each pair of sub-plots so the two models could be directly compared. In both test cases, the SF benchmark generated peak stresses that were overly high and incorrectly located compared to the distorted fibre model (DF). As a result, a conventional modelling approach is overly conservative and the model would predict early failure of the laminate if a failure criterion were applied.

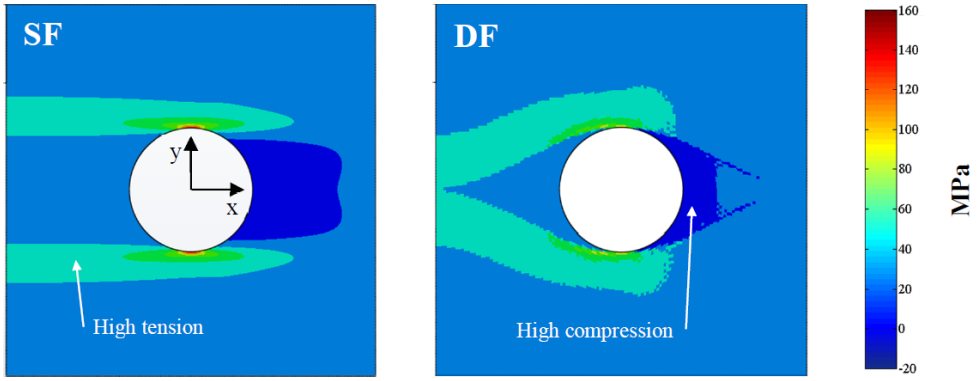

Figure 6.14: Axial stress (σ_x) for the 0 degree ply. Peak tensile stresses in the SF model are located at the top and bottom of the pin. The maxima in the DF model are located in similar positions but are 67% lower in magnitude. The influence of the fibre orientation on the load path can also be seen.

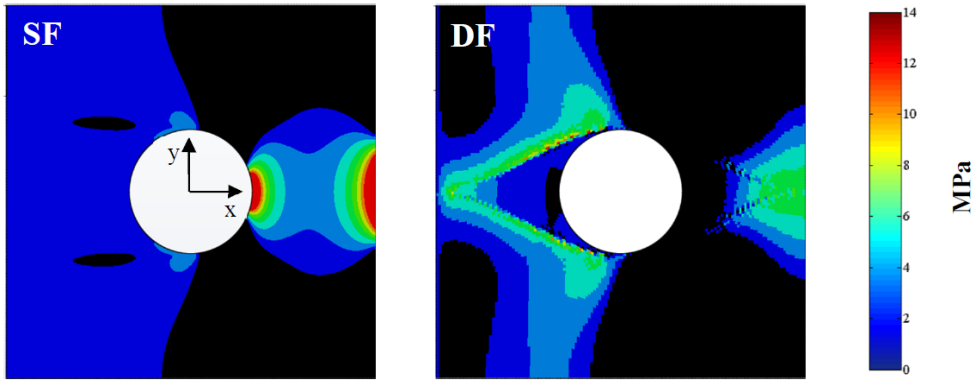

Figure 6.15: Transverse tensile stress (σ_y) for the 0 degree ply, compressive stresses excluded for clarity (black regions). SF model shows two regions of artificially high stress to the right of the pin. High stress at the tip of the resin zone (DF) was due to the fibres being forced apart.

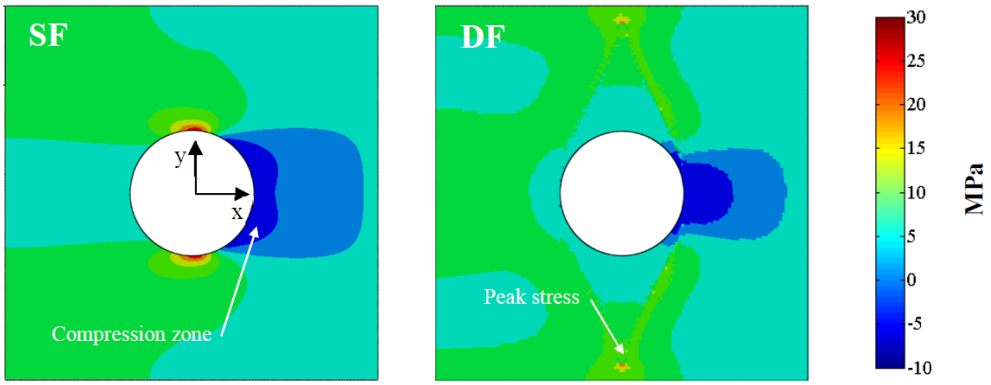

Figure 6.16: Axial stress (σ_x) for the 90 degree ply. The SF model again exhibits artificially high stresses. The maxima in the DF model can be seen at the tips of the resin zone. The compression zone is also more narrow due to the finite contact region between pin and fibres.

The displacement of the pin (δx) was also recorded for each of the models and test cases so that an equivalent bearing stiffness (K_x) could be calculated. Physically, this displacement would be the product of the "bearing strain" (local compression of the laminate/resin) and elongation of the hole due to tensile strain of the net-section (transverse cross-sectional area). Table 6.5 shows these bearing stiffnesses, normalised with respect to the 0 degree ply (SF model).

Ply Angle ϕ (Degrees)	SF Model (Benchmark)	DF Model (Detailed)
0	1.000	0.516
90	0.506	0.524

Table 6.5: Comparison of normalised equivalent bearing stiffnesses for the two models and two test cases.

It can be seen that modelling the fibre distortion of a 0 degree ply in high fidelity reduces the stiffness by almost a half. Conversely, the detailed model of the 90 degree ply actually showed a small increase (3.6%) in bearing stiffness compared to the SF model. More significantly, the DF model was actually slightly stiffer when the fibres were aligned perpendicularly to the load rather than parallel to it. It is thought that this was because the pin transferred load directly to the fibres rather than compressing into the soft resin rich zone. Therefore, it is proposed that both the 0 and 90 degree plies transmit an almost equal percentage of bearing loads in HYPER joints. These joints would also be considerably more compliant in a physical test than would be predicted using a conventional finite element approach.

6.7.2 Three Dimensional Four Ply Models

6.7.2.1 Mesh Convergence

The straight fibre $[0/90]_S$ model was chosen for this preliminary investigation ($d/w = 0.3$). Two element types and five mesh densities were chosen. Both were elements were eight node solid bricks, one was fully integrated and the second had reduced integration (C3D8I and C3D8R respectively). As with the 2D study, the element size was varied from 0.5-2.5% of the unit cell size which resulted in a mesh of between 12,000 and 133,000 elements. A concentrated load was applied to a central reference point and transfered to the pin with a kinematic coupling. The boundary and contact conditions were the same as the 2D model; see Figure 6.5. Again, contraction of the transvere edges was prevented but this negated the use of multi-point constraints. The bearing stiffness of the laminate calculated by extracted of the pin displacement.

It was assumed that the model had converged with C3D8I and an element size of 0.75% as there was only 0.2% variation in stiffness betweem consecutive data points. The asymptote is plotted with a dashed line at 4.51MN/m. It can be seen that the reduced integration element (C3D8R) had not converged for the same element size. Given the curvature of this dataset, it is believed that this element would achieve the same stiffness with continued refinement but it is thought that the computation time would quickly become prohibitive. These responses are typical for these elements types, as shown by Figure 6.18. This convergence response was generated as part

of a benchmarking excerise using a model of a cantilever beam. Sun [83] showed that, unlike the ABAQUS' fully integrated 8-node element (C3D8), using reduced integration (C3D8R) or the incompatible modes formulation (C3D8I) shear locking could be avoided. A widely reported numerical error which results in "parasitic" shear strains and overly stiff models [83].

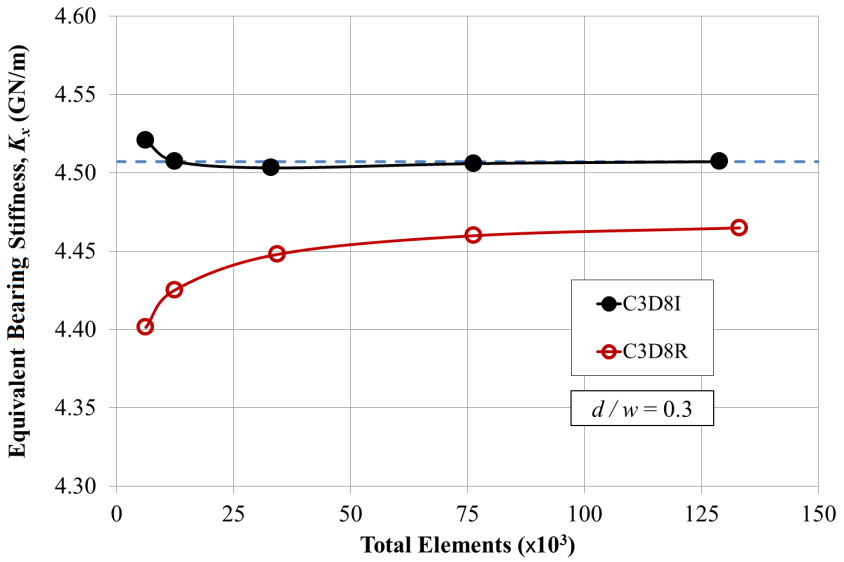

Figure 6.17: Stiffness convergence of the four ply SF model, $[0/90]_S$, with increased mesh refinement and two element types.

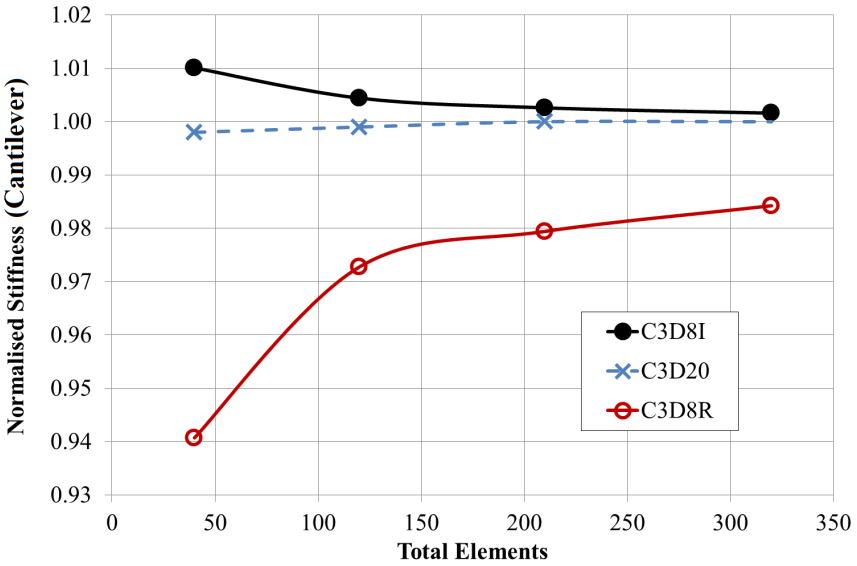

Figure 6.18: Stiffness convergence of benchmarking test on a cantilever beam. Produced from data set generate by Sun [83]. Normalised to most refined quadratic result (C3D20) which was fully converged with a mesh of more than 200 elements.

The 3D cell model used a circular partition to ensure consistent element geometry/shape in the highly stressed contact region surrounding the pin; a common approach [93]. This division was arbitrarily chosen to be midway between the pin edge and the edge of the unit cell. The medial axis meshing algorithm was chosen for the inner region of the cell to maintain radial and circumferential symmetry. The advancing front was used for the outer region generate a smoother transition between the circular and square boundaries, as shown in Figure 6.19. The concentric mesh in the center of the cell results in element size increasing with distance from the center of the cell. This is contrary to the shape of the resin zones which are assumed to taper with distance from the center. Hence, using a selection of a small element size will ensure that the geometry of the resin regions is more accurate and discontinuities between laminate and resin zone minimised.

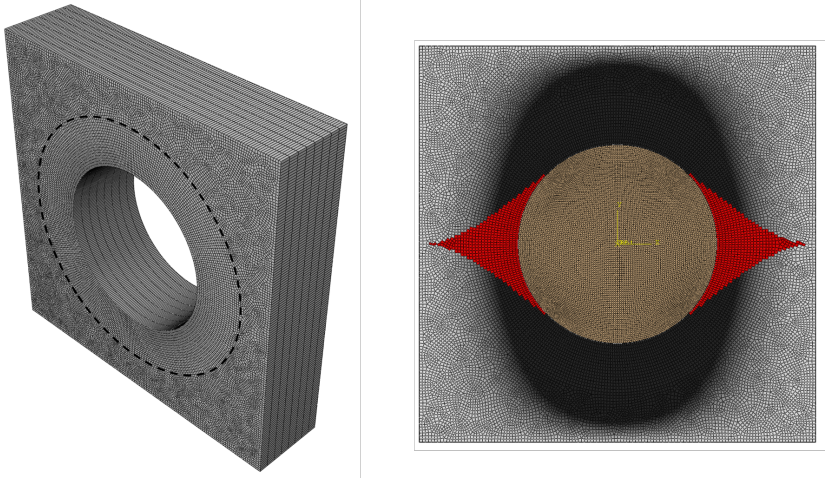

Figure 6.19: Mesh used for the three dimensional model ($d/w = 0.5$). (a) Isometric view with the boundary between partitioned regions (medial and advancing front meshes) emphasised with a dashed line. (b) DF model with variation in volume fraction and material properties. Darker regions of laminate generated with bespoke colour mapping by the author to show increased fibre content; resin regions shown in red and pin in brown.

It should be noted that if the medial axis algorithm was used, without creating the circular partition, results were unstable and convergence was not achieved, see Figure 6.20. It is believed that this was due to four regions of poor refinement close to the pin at ($\alpha \approx \pm 45, \alpha \approx \pm 135$) which subsequently let to excessive distortion for some simulations. It was found that this oscillatory behavior could be overcome, without partitioning, by using the advancing front algorithm but this made the model stiffer and converge more slowly. This was likely to have been as a result of the random nature of the mesh and the continued inclusion of some regions of poorly refined elements. Stress plots for the two best results (C3D8I and C3D8R, with medial axis and partitioned mesh) are show in Figure 6.17. These results are less well converged than the stiffness responses as the latter were a function of the displacement. It is well known that displacement errors are inversely proportional to the square of the mesh size whereas errors in stress reduce more slowly with mesh refinement.

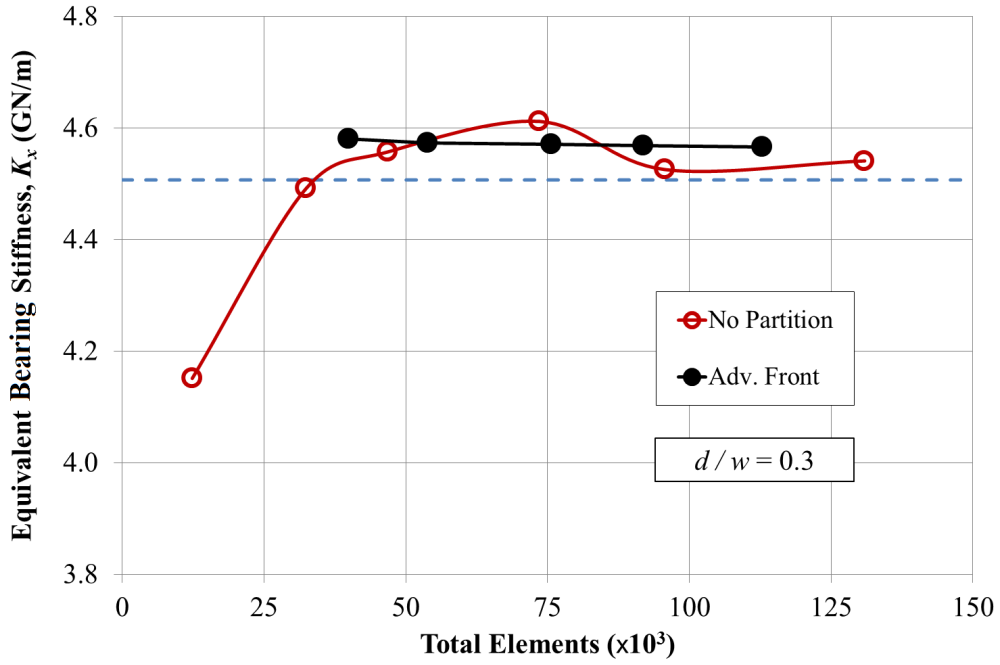

Figure 6.20: Comparison of stiffness of four ply SF model using two different meshing strategies. Both use $[0/90]_S$ and C3D8I elements.

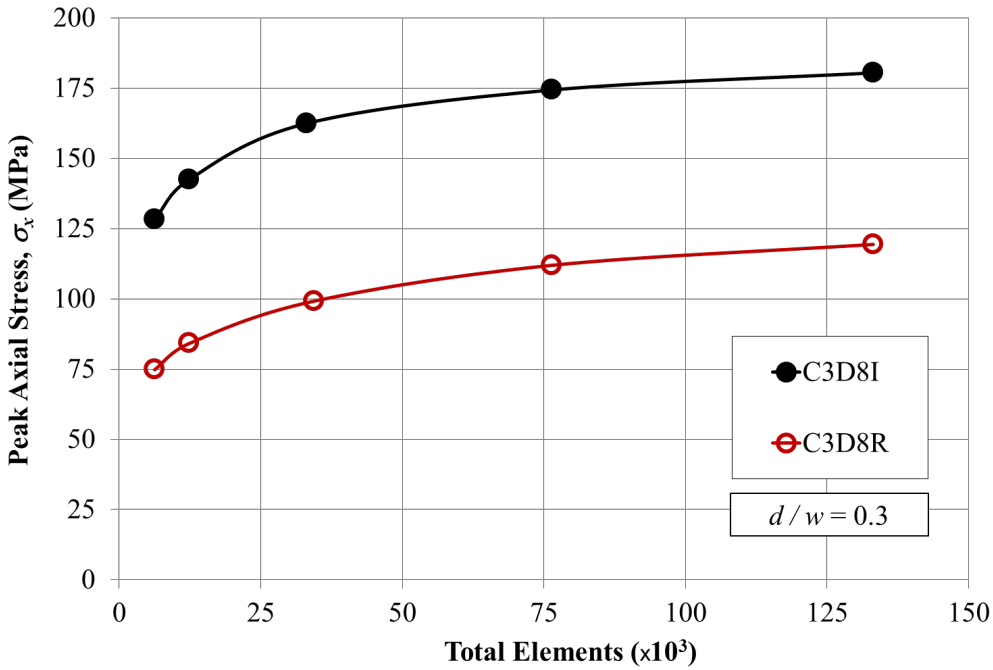

Figure 6.21: Comparison of peak axial stresses in the four ply SF model using two different element types. Both use $[0/90]_S$. Peak stresses occurred at approximately $\alpha = 90$.

Based on this convergence study, the element size chosen for the remainder of the four ply investigation was 0.75% of the cell width; resulting in a final mesh size of approximately 133,000 elements. This mesh density consequently led to a total solution time of around 2 hours 20 mins on a typical desktop PC (with an Intel-i7 processor) or 25 minutes on a high perfomance workstation (with dual Xeon-E5 processors). Pre-processing time accounted for only around 5 minutes in each case due to the revisions made since the 2D investigation.

As stated previously, the convergence tests were completed for a pin ratio of $d/w = 0.3$. It was assumed that the chosen element size, type and meshing strategy would also converge to the same extent for other pin diameters and model variations investigated in the following section. Given that the in-plane area of the laminate will reduce non-linearly as the pin diameter is increased, for the same element size, the number of elements (and degrees of freedom) will also decrease. Thus, in order to maintained the same mesh density, a constant number of degrees of freedom and allow a fair comparison between tests, the mesh seed size was iteratively adjusted. For example, at $d/w = 0.5$, the seed size was reduced to 0.70% to generate a mesh of 132,904 elements. As the mesh was prismatic, this difference was only 29 elements per layer which was considered to be negligible; a decrease of only 0.2%. However, to maintain the element count in the range $0.1 \leq d/w < 0.3$, the seed size actually had to be increased.

6.7.2.2 Analysis of Bearing Stiffness with Diameter Variation

Figure 6.22 shows two variations of the straight fibre model (SF), each one using a different set of material properties. For both cases, it can be seen that the equivalent bearing stiffness is inversely proportional to the diameter of the pin. This is intuitive as the edge distances and cross-sectional areas (of both the transverse and bearing planes) reduce if the pin diameter is increased [19, 92]. The absolute volume of fibre is effectively reduced for increased pin diameters which is analogous to a fastener located in a drilled hole.

The two sets of materials parameters trialled are quoted in Table 6.3. The baseline Airbus properties used in previous work by Sirna and Lanzi [79] were compared to the adjusted properties generated by the micro-mechanics material model [57]. When the materials model was used for the SF unit cell, the volume fraction was fixed at the nominal value ($V_f = 0.566$) for all elements of the laminate. It can be seen that use of the adjusted properties reduced the overall stiffness by approximately 20-25% for both stacking sequences. Given the magnitude of this difference, the SF model with adjusted properties was used for comparison with the DF model in order to make a fair test; see Figure 6.23.

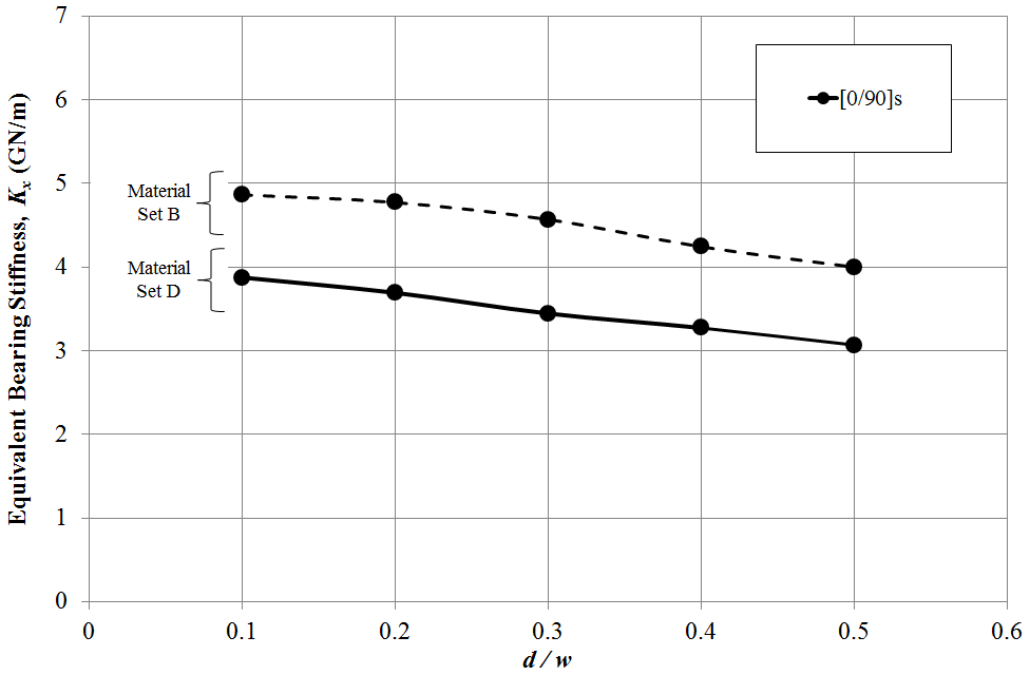

Figure 6.22: Two results from the straight fibre model with $[0/90]_S$ layup. Material properties for Sets B and D are listed in Table 6.3.

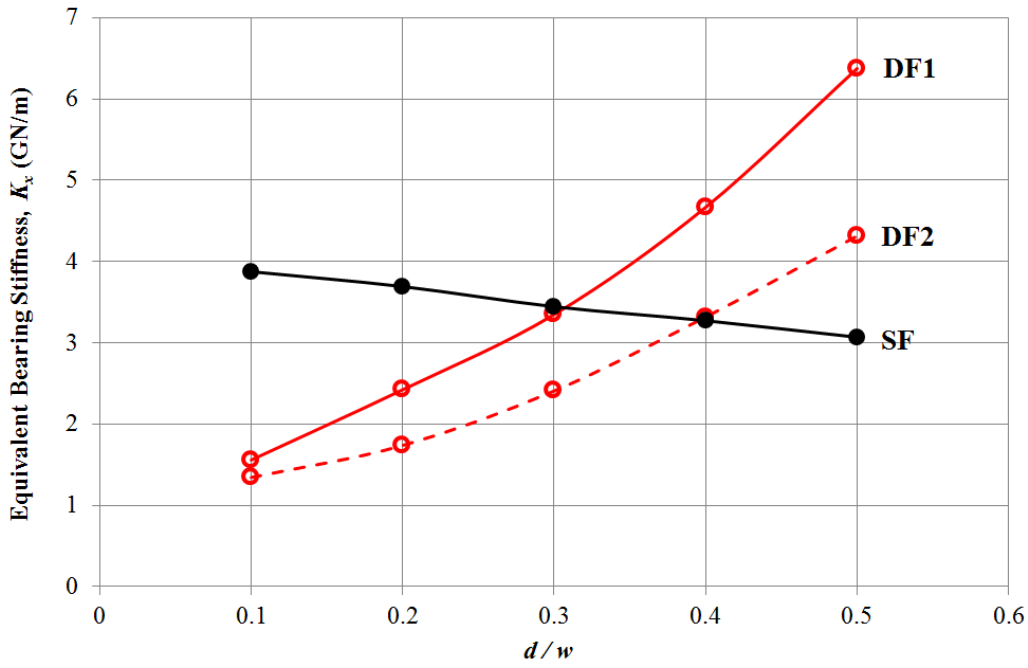

Figure 6.23: Equivalent stiffness of the conventional straight fibre model (SF) and two variations of the distorted fibre model (DF) for a range of diameters. DF1 accounted for variation in volume fraction and subsequent increase in material stiffness. The absolute fibre content was essentially maintained. Volume fraction in DF2 was fixed regardless of fibre distortion and all composite regions had nominal material properties; although fibres were distorted, total fibre content was not maintained. All three curves used the $[0/90]_S$ layup.

Figure 6.23 shows the equivalent bearing stiffness of the conventional straight fibre model (SF) and two variants of the distorted fibre model (DF1 and DF2) for a range of pin diameters. DF1 accounted for variation in volume fraction, maintaining fibre content and the subsequent increase in material stiffness. Volume fraction in DF2 was fixed regardless of the fibre distortion and all composite regions had nominal material properties ($V_f = 0.566$). This second configuration isolated the effect of the fibre distortion and the resin rich zones.

Unlike the SF models, the stiffness of the DF unit cell models with the resin zones and fibre distortion is proportional to pin diameter. Furthermore, the difference between the two models is significant at $d/w = 0.1$ where bearing stiffness of the DF model is much lower. The two responses converge and then diverge so that by $d/w = 0.5$, the DF models are up to 100% stiffer. Consequently, due to the convergent nature of the models, the large stiffness reduction seen in the 2D preliminary tests ($d/w = 0.3$) is not present. It is believed that this is because compatibility has to be maintained between adjacent plies and this through thickness interaction prevents such large displacements making the three-dimensional DF models stiffer.

As would be expected, the DF1 configuration, with locally increased fibre volume fraction and moduli is stiffer than the DF2 model for all pin diameters. However, because the DF2 model also exhibited a stiffening response, it can be assumed that this is generated from a combination of fibre distortion alone. Analysis of the reaction loads at the transverse boundaries revealed a significant difference between the SF and DF models. A compressive reaction load had to be applied to the SF unit cell model to prevent dilation and maintain the periodic boundary condition. However, the opposite was true for the DF models which required a tensile load to prevent contraction of the unit cell.

The orientation of these transverse reaction loads would subsequently influence the translation of the pin and the bearing stiffness of the laminate due to the secondary load induced. Evaluation of the average fibre angle in the unit cell for increased pin diameters shows that the deviation from the nominal angle can be significant at large pin diameters, see Figure 6.25. Two quadrants of the cell increase by this deviation and the other two decrease by the same amount, again shown in Figure 6.25.

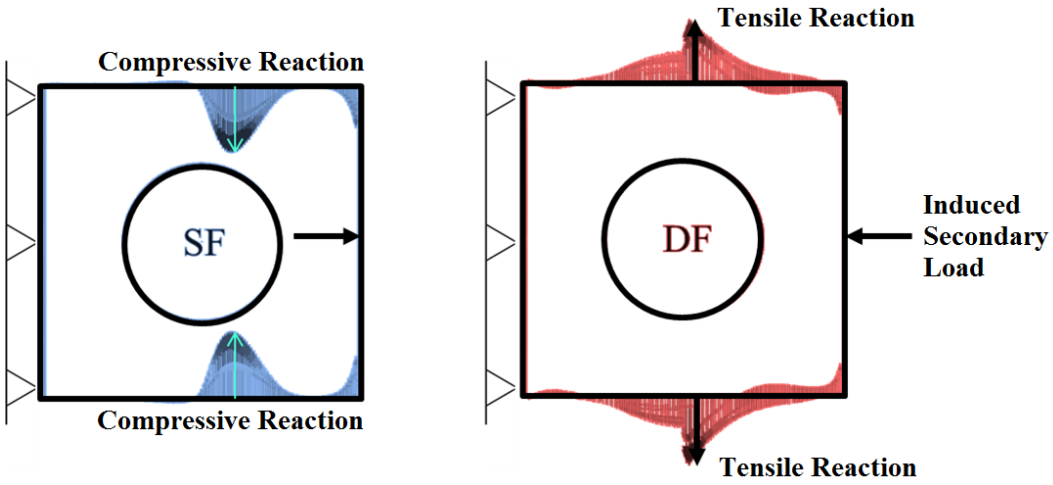

Figure 6.24: Reaction force distributions at transverse boundaries (f_y at $y = \pm 0.5$) for both SF and DF models; $d/w = 0.5$. The unit cell must be compressed for SF cases to prevent dilation. For the DF cases, due to the Poisson's Ratio increase, the cell would contract without a tensile reaction. This reaction induces a secondary load that acts against pin translation.

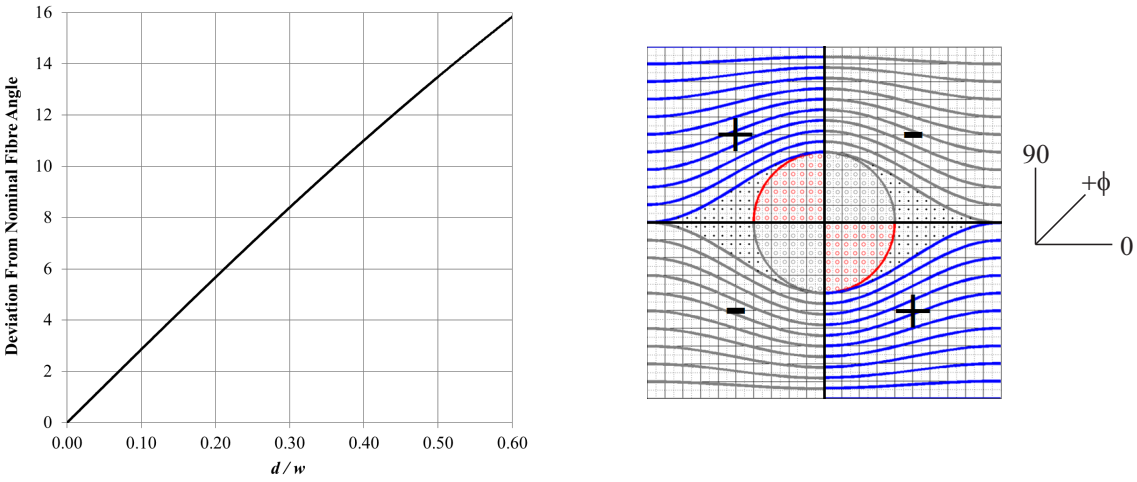

Figure 6.25: Deviation from the nominal ply angle with increased pin diameter. The average fibre angle in two quadrants of the unit cell will increase and two decrease, as shown. Zero degree plies would tend to $\pm 13.5°$ and ninety degree plies to $\pm 76.5°$ for $d/w = 0.5$.

6.8 Concluding Remarks

A conventional finite element modelling approach, with individually homogenised CFRP plies, was found to be inadequate for accurate simulation a HYPER joint unit cell. A detailed finite element model of a HYPER joint unit cell was developed as an alternative method for investigation of manufacturing effects such as local fibre distortion and resin rich zones.

The two dimensional model revealed that, for laminate dominated by 0 and 90° plies, a homogenised model would transmit the greatest loads from HYPER pins into the 0° plies due to the higher bearing stiffness of these layers. However, when accounting for the fibre distortion and resin rich zones, the load transmitted through the 0° plies was much lower (due to the reduced bearing stiffness) and was almost equal to that carried by the 90° plies (for $d/w = 0.3$). Therefore, a laminate with a high percentage of [0/90] plies, modelled with a conventional approach, would be stiffer that the response of a real coupon and, subsequently, peak stresses could be as much as 70% higher.

A detailed three-dimensional model exhibited a stiffening (bearing) response when the pin diameter was varied; which was contrary to the softening response of the conventional approach. For small pin diameters ($d/w \leq 0.3$), the detailed model was still much more compliant than the benchmark due to the presence of the resin zones and generation of high contact pressures. However, for larger pin diameters ($d/w > 0.3$), the detailed model could be more than 100% *stiffer* than the benchmark model.

This was found to be largely influenced by the increase in local fibre volume fraction and resulting increase in moduli. Even if the absolute fibre content was not maintained (analogous to a fastener in a drilled hole), the model still had a higher bearing stiffness than the benchmark. Thus, the stiffening trend could be generated by fibre misalignment alone. It was found that the fibre distortion in the DF models produced a tensile reaction at the transverse boundaries. This subsequently induced a secondary load in the opposite sense to the applied force so the net load on the pin was reduced. Hence, translation of the pin was decreased and the model exhibited a stiffer bearing response.

It is proposed that, contrary to established design rules for mechanical fasteners, it could be advantageous to increase the ratio of the pin diameter with respect to the the unit cell width (pin pitch) beyond 30%. Net-section and bearing stresses are lower (for a given applied stress) within a HYPER joint as integration of the assembly does not require subtractive machining (drilling) and total fibre content is maintained. It is recommended that, as part of future work package, a failure criterion is incorporated within the high fidelity model. This would allow design rules to be parametrically revised, specifically for HYPER, without extensive experimental testing. Subsequently, a more optimal pin geometry could be selected for future applications.

Chapter 7

Discussion and Conclusions

This final chapter serves two purposes: Firstly, several issues, that have not been addressed in previous chapters, are discussed. It has been shown throughout this thesis, that pin quality and joint integration is absolutely critical to performance yet, thus far, recommendations for the manufacturing strategy have not been made. Thus, underlying challenges that remain within powder-bed additive fabrication are covered and a manufacturing case study is presented. Secondly, conclusions from this final discussion, and all the preceding chapters, are combined to form a closing précis.

7.1 Discussion

Despite having a good appreciation of power-bed additive manufacturing (AM) and the fabrication of HYPER pins and joints, having only observed the process on a limit number of occasions, a comprehensive understanding of the intricacies of the technique was not held. For almost the entire duration of this doctoral project, the research herein was undertaken at the University of Bath. Although testing and analysis was conducted at the University, manufacturing of test specimens was (for the most part) conducted externally by Airbus Group. However, during the final stages of the project, the author was based in the company's offices in Filton, Bristol. This provided far greater insight into the complexities involved in the industrialisation of additive manufacturing processes and to observe, first-hand, the difficulties in repeatably achieving successful AM builds. As already described in Chapter 2, additive manufacturing is often perceived to be a shortcut to achieve a physical, near-net shape part from a digital model with negligible lead time and minimal user intervention (just "send to printer"). Although this can be possible with polymer AM, this is not necessarily the case for metallic sintering. Build success/quality is currently dependent on the individual part and the experience of the engineer. Following the design of a part, there are still many factors that must be considered. This includes the orientation of the part to minimise the requirement for sacrificial supporting structure, the dosing level to ensure no regions are staved of powder and avoiding feature convergence during the build. The latter is key factor as this can cause line defects due to translation of centroids and increased shrinkage.

It had (incorrectly) been assumed, during the early stages of the project, that the metallic parts provided by Airbus Group would essentially be defect free. Although, the joint technology as a whole was at a low technology readiness level (TRL), it was thought that pin manufacture was mature. Inclusion of HYPER pins on the surface of an additively manufactured component (as part of an integrated build) was relatively straightforward and did not add any real difficulties as long as the parameters (described above) were adequately addressed. However, building pins onto a pre-existing stock substrate, as per the coupons tested throughout this work, was found to be significantly more challenging. Given that future applications may require this "retro-fit" approach, it was not satisfactory to solely rely on use of the integrated method; even if this remained the most likely candidate for further development. As reported in Chapters 4, 5 *and* 6, high pin quality and robust insertion/consolidation was absolutely critical for predictable and repeatable mechanical performance. Complete fusion of the first few powder layers and minimal internal porosity were particularly important. It is possible that these types of defect may have had a negligible effect on the mechanical performance of a large component, but, given the potential scale of these flaws compared to the HYPER pins, a considerable knockdown in strength has been found. Being able to provide consistent, high-quality pin manufacture for even the most challenging build configuration (on a non-AM substrate) would be a significant milestone and also provide a strong business case for the technology. Thus, at the end of the project, and with full access to the additive manufacturing facility in Filton, it was possible to investigate this most critical aspect of HYPER joints in more depth; this is reported below.

7.1.1 Refinement of Pin Manufacture

A key requirement for the building of HYPER pins, onto an existing component/substrate, was that the build surface was flat and level (to around 10-20 micron) and remained so for the duration of the build, otherwise, the pins would not fuse to the substrate. As described in Chapter 2, securing the pre-machined ARCAN and (5 mm thick) lap shear specimens to the bed of the machine prior to a build could be achieved fairly easily given their geometry. They are adequately stiff and there is sufficient surface area to clamp them tightly on the build plate or within the build fixture, as shown in Figure 2.8. However, it was believed that this would not be the case if pins were to be built onto thinner substrates (circa 2 mm). Hence, this study was undertaken to develop an alternative methodology for coupons of reduced thickness. This was considered to be an extreme test case as, not only were the pins being built onto a substrate, but one which was thin, compliance and unlikely to be flat. A secondary requirement of this task was, if possible, to improve the in-plane accuracy with which the pins were located on the substrate. Ideally, this would remove the need to manually expose the first layer and then reposition the machine bed to correct the edge distances. This investigation was an excellent test case as it not only allowed more thorough process control to be established but highlighted many of the challenges described in the previous section. It should again be noted that the EOS machines were not designed for this specific task and were usually used to build parts directly onto the build plate (≈30mm thick), from which they would then be cut. Thus, complete fusion of the first layer was not as critical.

The lap shear specimen configuration was adopted for this trial following interest from an Airbus Group business unit. The substrate material was selected to be 1.7mm thick titanium plate (Ti-6Al-4V) and the build was to be conducted on the EOSINT M270 platform. Following consultation with collaborators at Airbus Group, it was decided that if the plate was pre-machined to the finished size of the coupons prior to the build (100 x 25 mm), it would be likely to induce distortion in the parts and subsequently clamping them onto the baseplate could induce a buckle. This would generate an unacceptable level of inconsistency across the build surface. Therefore, in contrast to the "standard" build methodology, where 14 pre-machined (SLS) substrates could be built upon simultaneously, it was it was decided that five pins arrays would be built onto a single piece of plate. This would then be cut into (five) individual coupons following completion of the build. Although machining of the plate into coupons (post-build) was a higher risk strategy, due to the value added by AM, it was felt that this would ensure a greater chance of the build successfully completing and the parts being fabricated accurately.

An additively manufactured "reference fixture" was also utilised to locate the titanium substrate on a standard build plate rather than the "universal" base plate that had been used previously. This ensured a direct correlation between the electronic model and physical part if both the fixture and pins were positioned in relative to the same coordinate system in CATIA. Any variation of the in-plane position between the digital model and physical parts would be identical for fixture and pins and thus, not influence the build. It was anticipated that this approach would result in excellent in-plane positional accuracy of the array on the substrate. This would remove the need for exposure of the first pin layer and manual perturbations of the machine bed to adjust the location of the pins.

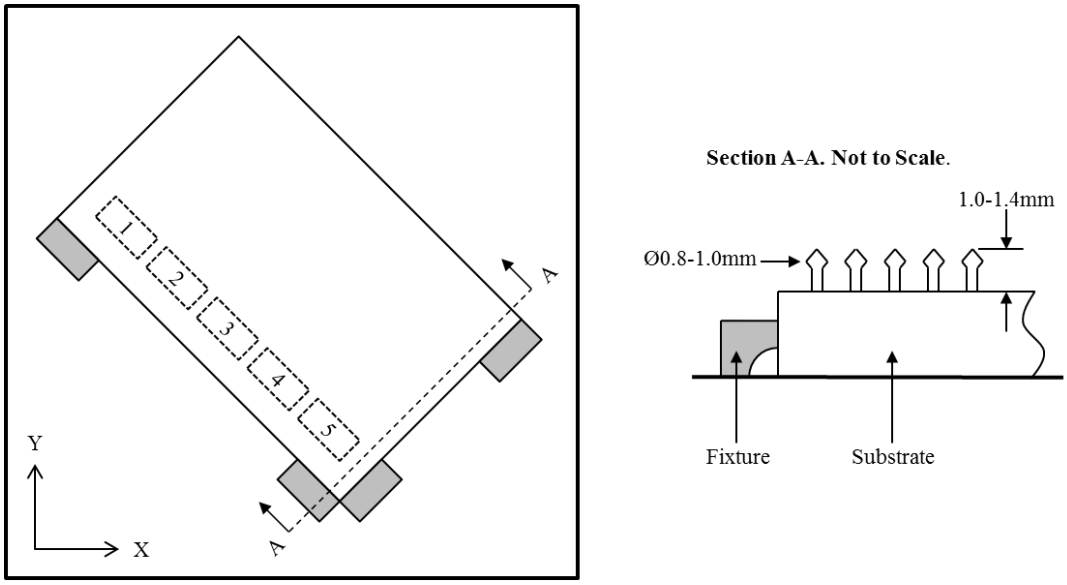

Figure 7.1: Build setup for manufacturing trials with thin substrates; showing the build fixture, substrate orientation, location of five pin arrays and pin design. The fixture had an undercut to ensure firm contact with the substrate.

On completion of building the fixture, the bed of the machine was lowered by the thickness of the plate and the powder was removed from its surface using a vacuum system. This now allowed the (grit-blasted) plate to be inserted into the machine. It was secured into the fixture using cyanoacrylate adhesive around the outer edges and centrally. It was ensured that the quantity of adhesive used was consistent to ensure flatness with respect to build plate. The height of the upper surface of the substrate from build plate was measured at each corner and centre with a dial gauge. A mass was placed onto the substrate to hold it in position whilst the adhesive cured. Once this was achieved, a second build was run to etch the outline of each coupon. This was possible by irradiating the surface without the addition of extra powder; the aim was to aid post-process machining of the plate into individual specimens. Powder was then re-coated across the top surface to fill in the gaps around the substrate and provide a new datum surface across the sheet material. Feeler gauges were used check the offset of the re-coater relative to the substrate. The HYPER pin arrays were then built on top of the substrate material. The design and positioning of the fixture, titanium plate and arrays within the build chamber is shown in Figure 7.1.

It should be noted that the pin diameters and heights were also somewhat smaller than had been used previously, again due to the specification set by the business unit. Three different pin heights and three different pin pitches were trialled although the penetration was comparable to the standard, thicker specimens. The plate was not set square to the build chamber in order to improve the distribution of powder across the plate, as described in Section 2.3. Once the build had completed, the part was removed from the build plate with a knife, all arrays were then grit-blasted and visually inspected with optical microscopy. Excess adhesive was also removed from the rear of the substrate to ensure subsequent metrology was accurate. In total three plates were built to provide fifteen coupons.

7.1.2 Results From First Trial

Given that the flatness of the plate was of primary interest, the heights of the pins were evaluated with a micrometer so that the shape of the plate (during the build) could then be inferred. This was possible as curvature in the plate would have varied the thickness of the first powder layer and, hence, the cumulative height of the built layers. A thick powder layer is generated by a depression in the substrate, an effect shown in Figure 7.2. The height of each pin array was measured at three points along the length (left, centre and right) and two points across the width (front and back) relative to the back of the plate. The thickness of the plate was measured at each corner, averaged and subtracted from the combined measurements to isolate the pin height. Given that three different pin designs were built, in order to make a fair comparison, the measured pin height was subtracted from the nominal height to find any deviation.

Figure 7.3 shows the results for each of three plates manufactured. The front and back data points for each measurement location along the length of the plate were averaged so each array is represented by three markers. The abscissa shows the lateral position of the measurement with respect to the centre of the plate. Again, it is noted that the deviate in pin height shown is actually the inverse of the substrate shape.

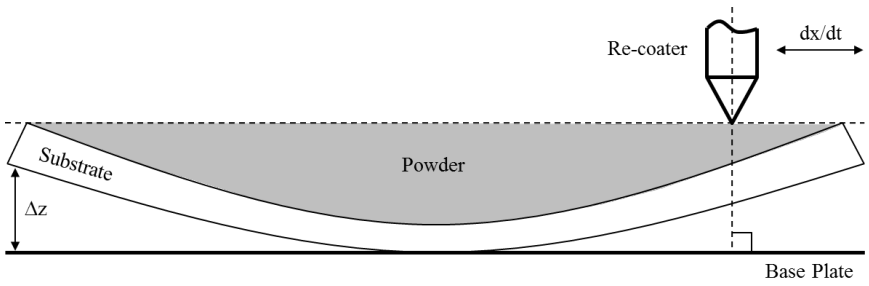

Figure 7.2: Creation of a powder layer with variable thickness due to distortion of metallic substrate. Illustrative only, not to scale.

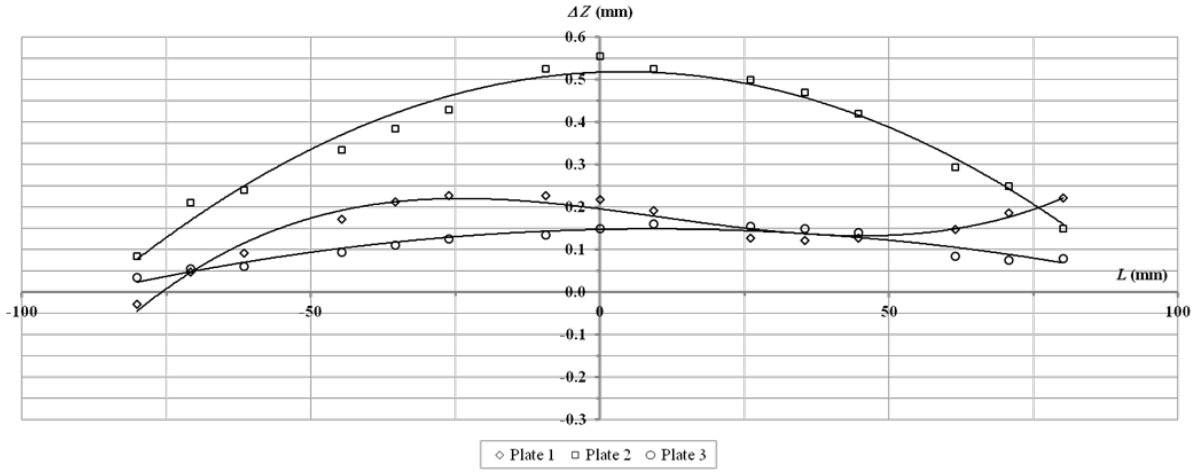

Figure 7.3: Averaged deviation in pin height from the nominal dimension on Plates 1-3, manufactured during the first trial. Three data points for each of the five pin arrays.

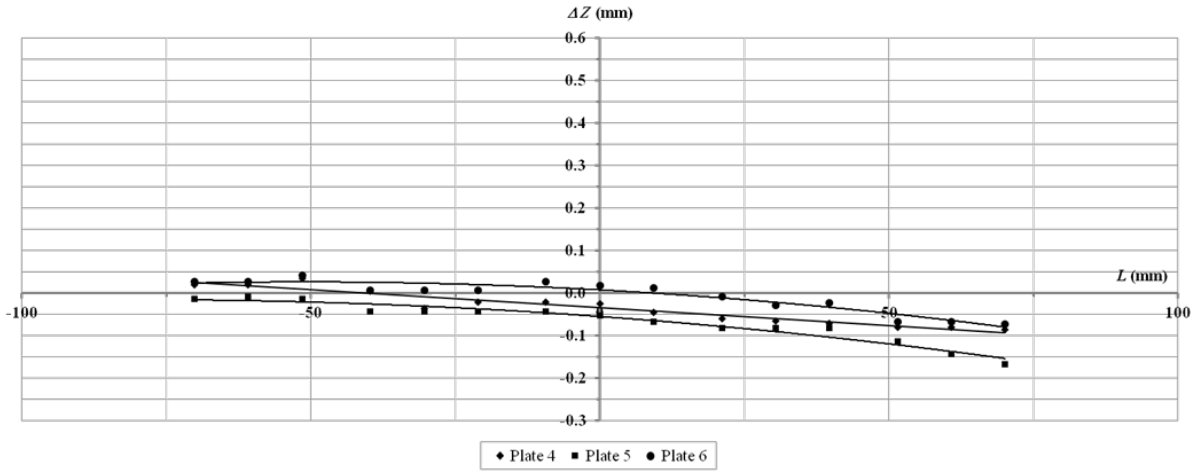

Figure 7.4: Averaged deviation in pin height from the nominal dimension on Plates 4-6, manufactured during the second trial. Three data points for each of the five pin arrays.

It can be seen that the average deviation in height is in excess of 200 micron and, at worst, over 500 micron (Plate 2). A second or third order polynomial was found to offer good correlation to the data implying that the plates had either single or double curvature; as can be observed in the plot. Unsurprisingly, such an excess of powder resulted in a lack of fusion at the pin base as the laser did not have adequate powder to fully penetrate and melt this layer. Several of the pins were removed due to the pressure generated during grit-blasting; see Figure 7.5. Furthermore, many of the pins that did remain attached to the substrate had severe voids. Clearly, there would have been a substantial reduction in performance if these pins had been tested as part of an integrated joint.

Some distortion had been observed prior to the build however it was felt that this had been reduced to an acceptable level by adhesion to the base plate. However, there may have been some "spring back" during curing of the adhesive and/or after removal of the retaining mass. Given the severity of these results, the methodology was refined again and the builds were repeated.

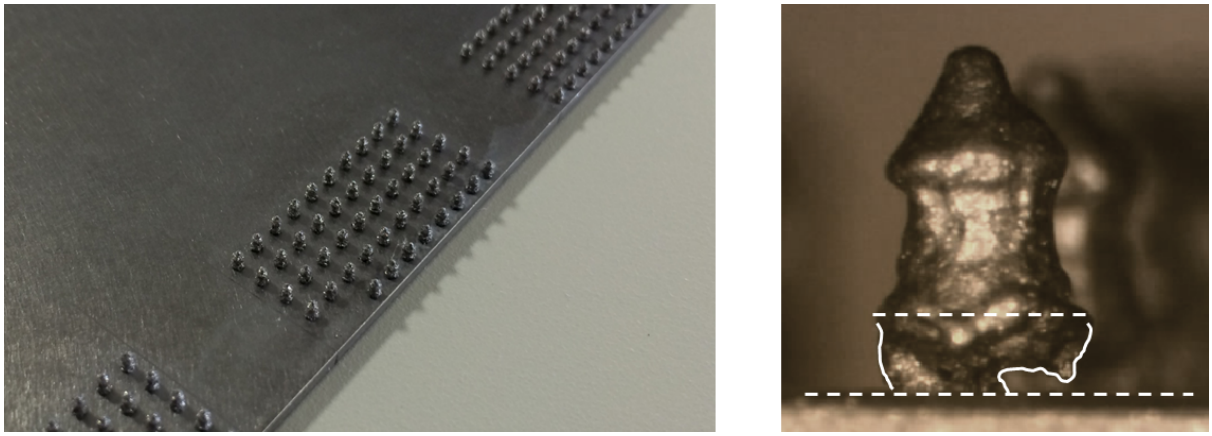

Figure 7.5: Left: Missing pins due to lack of fusion on Plate 2 (central array, L=±12.5mm). Right: Grit-blasting removed loose, poorly fused material from the base of other pins.

7.1.3 Results From Second Trial

It is believed that the curvature seen in the first set of plates was generated when they were cut to size as this operation was undertaken with a guillotine. The lead time required to having a second batch cut on a mill or by water-jet was prohibitive so it was proposed that a stress-relieving heat treatment would be used on a set of existing plates that were already correctly sized. Three new specimens were clamped between two titanium plates (each 25mm thick) and placed inside an argon filled container (to prevent oxidisation). This was then placed in a furnace for a 7 hour heat treatment cycle: 2 hour ramp up to 680 degrees Centigrade, held for 3 hours and 2 hour ramp down. They were then degreased and grit-blasted to roughen the build surface. Any remaining blast media was removed with compressed air. The three stage build process was identical to the first iteration and the same measurements taken following grit-blasting of the pins (to remove any partially sintered powder).

Results from this trial are shown in Figure 7.4. Although the pins built during the second trial were spread over a slightly different length, it can be seen that (even if compared over the same distance from the plate centre) there is a large reduction in the variation from the nominal pin height. This implies that the heat treatment was successful in relieving stress induced during the cutting process and resulted in flattening of the plates.

The average deviation in pin height was -35 micron and the greatest difference was -140 micron. A decrease from the nominal height may have resulted from a conservative setup and inadequate powder being spread onto the plate (to ensure that there was definitely fusion at the pin base). This may have also been influenced by the bed of the machine not being perfectly flat with respect to the re-coater arm and not distortion of the plate. This conservative approach would certainly be preferential for mechanical performance compared to achieving the correct pin height as the base of the pin would be considerably more stressed than the tip (considering the pin as a uniformly distributed cantilever). These deviation values equate to a 49% and 67% reduction in plate distortion respectively, if the results are scaled by 140 micron to remove influence of the operator/machine bed. However, as stated above, the difference in joint strength between specimens, from the first and second trials, would have been far more significant so these percentages offer a conservative assessment in process refinement.

It should also be noted that, in both the first and second manufacturing trials, the pins were located within 50 microns of the nominal in-plane position; as a result of the new, additively-built fixture method. This is a significant improvement compared to the previous (manual iteration) technique which could only achieve a tolerance of around 250 micron.

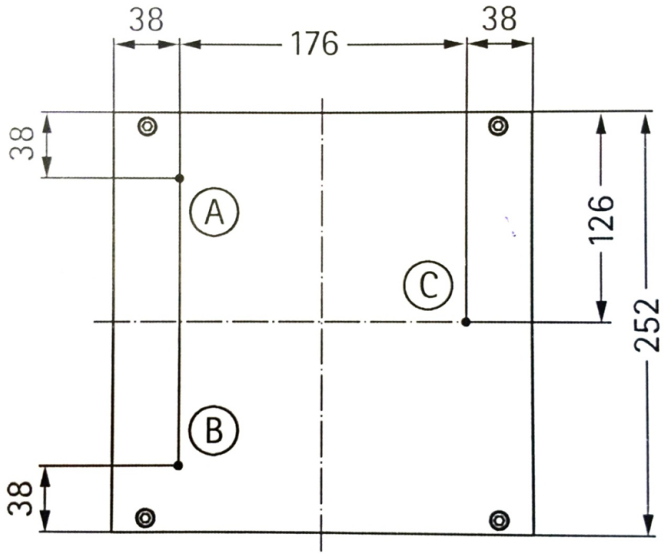

Figure 7.6: Location of the fulcrum (A) and two actuation points (B and C) used for leveling the build plate on an EOSINT M270. All dimensions in millimetres.

Heat treatment was successfully utilised to reduce the curvature of thin titanium plates and resulted in far more accurate building of pin geometry. This was helped by a conservative setup strategy and it is recommended that this is adopted for future builds. Furthermore, use of an additive fixture adds minimal process time and vastly improves the accuracy of array location (in-plane). However, adhesion of the substrate to the build plate should be completed using an accelerator to reduce the cure time.

As there remains some difference between the built and nominal pin sizes, it is proposed that further modifications should be made to the methodology and an additional trial conducted. Even if the substrate was perfectly flat, by not orientating the substrate square to the build plate (as shown in Figure 7.1), the machine bed must be manipulated in two axes to rotate the plate relative to its own principle axes. The positions of the fulcrum and two actuation points (A, B and C respectively) are shown in Figure 7.6. If one of the edges of the plate was collinear with the line A-B, it would be easier for the operator to shim the substrate relative to the re-coater arm and hence spread an even layer of powder over the entire plate. The "dosing" should then be increased to ensure that powder will be spread to a consistent thickness across the entire width of the build platform.

7.2 Concluding Remarks

This final section draws together the conclusions and recommendations from each of the individual chapters. This includes topics that were identified as being beyond the scope of project yet of potential interest should the project foreground allow.

7.2.1 Project Context

The first two chapters provided contextual information on the current state of the aerospace industry, additive manufacturing techniques, comparable hybrid joining methodologies and HYPER technology itself. In short, the current aircraft fleet must become more "green" and emissions must be significantly reduced (in real terms) during the next two decades. This is even more challenging given forecasts predict that the number of aircraft in service will almost double by the year 2030. Achieving this goal will only be possible with innovative solutions and this is driving a substantial research effort for weight minimisation and propulsion efficiency.

Over the last 40 years, development of fibre reinforced plastics has provided new opportunities for mass reduction due to their high specific strength. Yet, despite these advances, a significant proportion of metallic components are still used in aerospace structures as CFRP has a low fracture toughness and is inherently weak through-thickness. Therefore, there is a need to join these two dissimilar materials.

HYPER joining is a novel method for the integration of metallic and carbon fibre structures. This technology was conceived approximately three years prior to the start of this doctorate and thus, was still at a low technology readiness level. The author was tasked with the evaluation of inspection methodologies for HYPER joints, identifying the influence of defects and damage on the mechanical performance of HYPER joints and also determining potential designs/configurations that could increase the mechanical performance.

A literature review revealed that some similar hybrid joining technologies were under development by third parties. Like HYPER, these used features on the surface of the metallic part to reinforce bonding with a CFRP laminate. However, these features/pins were either welded on or created by melting and translation of material from the stock component; cold metal transfer and Comeld respectively. HYPER joint fabrication was, and remains, unique. Additive manufacturing provides unrivaled capability for optimisation of the pin geometry, angle and position.

7.2.2 Non-Destructive Inspection

The HYPER joint manufacturing methodology and pin profiles are unique and they are inherently challenging to inspect. As a result, little application specific information was found in the public domain and authors of similar hybrid joining technologies have not reported any detail information of non-destructive testing research and development.

X-ray computed tomography was found to be very effective for assessment of flaws within the CFRP laminate *and* the pins. Artefacts were generated due to the large difference in material density and X-ray absorption but these were not prohibitive to evaluation. However, despite impressive results, CT scanning was found to be a time consuming and expensive process that would not suitable for a production environment with large components or large throughput of parts.

Thermography was found to only be effective for detection of cracks at the edge of the joint interface. This may be suitable for an initial inspection but a secondary method would still be required for a comprehensive and quantitative evaluation of damage magnitude. Internal defects could not be identified with the methods investigated.

Pulse-echo immersion ultrasound initially achieved limited success as C-scans lacked clarity when inspected through the CFRP side of the joint. Analytical modelling revealed that the pins may have been scattering the incident signal but that this could potentially be reduced with the use of a smaller diameter probe. Fortunately, inspection capability was significantly improved simply by rotating the specimens so that evaluation was conducted through the metallic substrate. Although, resolution was not as good as that achieved with CT, this strategy was still capable of detecting disbonding of the joint interface, delaminations within the composite *and* defects within the pins.

Although pulse-echo immersion ultrasound was demonstrated to be a successful method for non-destructive inspection of coupons, the method employed required access to the metallic side of the joint. This is somewhat of a limitation as this may not be possible in future applications. Hence, it is strongly recommended that, as part of a future HYPER joint research, experimental trials are completed with smaller diameter immersion and/or "dry" phased-array ultrasonic probes which will hopefully improve inspection through the CFRP side of the joint.

Furthermore, given pin defects such as porosity and lack of fusion were found (in later chapters) to have such a significant influence on performance, inspection capability for *unembeded* pins should be established. Ultrasonic thermography is believed to be a suitable candidate based on the work conducted. In addition, it is also recommended that compression testing is conducted with the panels that were impacted during the NDT investigation.

7.2.3 Joint Performance

Once the NDT feasibility studies had been completed, these techniques were implemented during two mechanical testing programmes to aid the characterisation of the failure modes. In Chapter 4, two HYPER pin geometries and three different interface conditions were statically tested and each compared to an unpinned benchmark.

The strongest joint configuration was 6.5 times stronger than the benchmark joint and the elongation at failure was 407% higher. The same geometry/interface combination also had the least scatter and the range was reduced by over 50% compared to the coupons with standard bonding. When interface bonding was artificially prohibited with PTFE, the ultimate strength was reduced by 8-9% (depending on pin geometry) compared to the standard resin bond.

Although a laser surface treatment only improved the UTS by 1-2% compared to the standard co-bond, the limit load could be increased by up to 26% which even exceeded the ultimate load of some of the reference joints. Following damage initiation, laser treatment also resulted in a reduced and more consistent rate of damage propagation. This switched the failure mode from adhesive to cohesive and an ≈80% higher load was required to grow an equivlently sized disbond. It was found that HYPER pins *do* carry load before the initiation of failure, however, the epoxy matrix was still the dominant load path and interface failed first.

Load share on pins then became more significant and they temporarily prevent additional growth from the initially damaged edge. A disbond consequently initiated on opposite side of the overlap and they then both grew in discrete steps, arrested each time by the pins. Ultrasonic NDT through the metallic substrate confirmed that pin fracture did not occur until after the interface was fully disbonded.

Some flaws were found the manufacturing and testing procedure but it was not thought that these influenced the results significantly. However, in future, bespoke metallic tooling is recommended to ensure more thorough consolidation of the laminate to prevent bending of the adherends. Hydraulically actuated jaws could prevent twisting and slip of the coupons and loads would then be more uniformly distributed across the joint.

With the static performance and failure modes of HYPER joints identified, joint endurance was then investigated with series of fatigue tests. The fatigue life of single lap-shear HYPER joint coupons was investigated. It is proposed that metal-composite joints with HYPER pins offer an increase in fatigue life of several orders of magnitude compared to an unpinned, co-bonded benchmark. However, it is believed that performance would not have matched that of comparative, mechanically fastened specimens.

It was found that there was a change in failure mode with reduced load severity and this mode had not been reported for similar hybrid joining technologies. At low peak loads ($\leq$32% UTS), failure was governed by the strength of the material directly beneath the pins. Fracture was within the surface of the metallic adherend, not above the pin root as observed in previous quasi-static tests. This resulted from a tearing action as joint rotation was low and there was a proportionally large moment at the pin root. At high peak loads, fracture was above the pin root as the shear load on the pins was dominant. With increased joint rotation, the axial pin load was also much larger and resulted in the radial pin stress variation becoming less significant. At peak loads around 10kN (32% UTS), it was possible to generate both tyres of failure within a single coupon. Localised modification to the adherend microstructure during AM was not thought to create a plane of weakness but the boundary between AM and stock material may have initiated cracking due to the difference in compliance and a high stress gradient.

Supplementary high-cycle fatigue tests are required with the revised joint design as testing of this alternate geometry was begun but not completed. This was due to the presence of pin porosity and what was believed to be an unrepresentative reduction in strength and endurance. Sensitivity to pin surface roughness should also be considered. Completion of these tests with pristine coupons would allow a fair comparison.

7.2.4 Detailed Finite Element Modelling

With both the static and fatigue performance of baseline HYPER joint configurations quantified, it was desirable to optimise the pin/joint design for increased strength and endurance. As a *precursor* to this, it was necessary to investigate the interaction of the HYPER pins and the surrounding laminate, give the unique fabrication/integration approach. This was undertaken in Chapter 6.

A conventional finite element modelling technique, with individually homogenised CFRP plies, was found to be inadequate for accurate simulation of a HYPER joint unit cell. A detailed finite element model of a single HYPER joint pin was developed as an alternative method for investigation of manufacturing effects such as local fibre distortion and resin rich zones.

The two dimensional model revealed that, for laminate dominated by 0 and 90° plies, a homogenised model would transmit the greatest load (from the pins) through the 0° plies due the high bearing stiffness. However, when accounting for the fibre distortion and resin rich zones, the load transmitted into the 0° plies was much lower and almost equal to that carried by the 90° plies (for $d/w = 0.3$). Therefore, a laminate with a high percentage of [0/90] plies, modelled with a conventional approach, would be stiffer that the response of a real coupon and, subsequently, peak stresses could be as much as 70% higher.

A three dimensional, detailed model was then developed and this exhibited a stiffening (bearing) response when the pin diameter was varied. This was contrary to the softening response of the conventional approach. For small pin diameters ($d/w \leq 0.3$), the detailed model was still much more compliant than the benchmark due to the presence of the resin zones and generation of high contact pressures. However, for larger pin diameters ($d/w > 0.3$), the high fidelity model could be more than 100% *stiffer* than the benchmark model.

This was found to be largely influenced by the increase in local fibre volume fraction and resulting increase in moduli. Even if the absolute fibre content was not maintained (analogous to a fastener in a drilled hole), the model was still stiffer than the benchmark. Thus, the stiffening trend could be generated by fibre misalignment alone.

It was found that fibre distortion produced a tensile reaction at the transverse boundaries. This induced a secondary load in the opposite sense to the applied force so the net load on the pin was reduced. Hence, translation of the pin was decreased and the model exhibited a greater bearing stiffness. It is proposed that, contrary to established design rules for mechanical fasteners, it could be advantageous to increase the ratio the pin diameter with respect to the the unit cell width (pin pitch) beyond 30%. Net-section and bearing stresses are lower (for a given applied stress) within a HYPER joint as integration of the assembly does not require subtractive machining (drilling) and total fibre content is maintained.

It is recommended that, as part of future work package, a failure criterion should be incorporated into the high fidelity model. Design curves could then be parametrically identified for HYPER joints, without extensive experimental testing. This would subsequently allow more optimal pin geometries to then be selected for future applications.

7.2.5 Pin Refinement

Even if the high fidelity model was utilised to find the optimum pin geometry for a given laminate specification, this would be redundant if the quality of the manufactured product could not be guaranteed. During the latter stages of the project, the author was able to make full use of Airbus Group's additive manufacturing facility so could examine the pin manufacturing process first-hand and in far greater detail. Hence, with the resources now available, the critical path was determined to be refinement of the fabrication methodology rather than optimisation of the joint design.

The findings of this manufacturing study were discussed in the first half of Chapter 7. In summary, although additive manufacturing is becoming increasingly mature, there are still numerous challenges and the application of EOS machines for HYPER pins fabrication (on stock substrates) remains difficult. This is particularly true for thin substrates due to the risk of surface irregularity.

Heat treatment was successfully utilised to reduce the curvature of thin titanium plates and resulted in far more accurate building of pin geometry. This was helped by a conservative setup strategy and it is recommended that this is adopted for future builds. Furthermore, use of an additively manufactured fixture added minimal process time and vastly improved the accuracy of array location (in-plane). However, adhesion of the substrate to the build plate should be completed using an accelerator to reduce the cure time.

Despite the limited time available by this point in the project, an investigation into the refinement of HYPER joint manufacturing was achieved but, as a result, an optimisation study was not. Hence, the modelling work in Chapter 6 should be combined within an optimisation strategy and utilised as part of a future research programme.

7.2.6 Outlook and Opportunities

HYPER joining is a very promising technology for the integration of hybrid structures. This doctoral project has shown the impressive strength and toughness of HYPER but it is still believed that, with additional work, pin/array designs could be better optimised for both static and dynamic performance.

For example, by increasing the pin diameter, the root stress would decrease whilst the load on the laminate would be increased. At present, the laminate was largely undamaged following failure of the joints. This could not only improve the joint strength but make the HYPER joint design more structurally efficient.

Nevertheless, the work reported within this thesis has played a key role in the advancement of HYPER joining technology. The NDT feasibility studies, results from the mechanical test campaigns and analysis methods developed by the author have, in part, enabled the progression to a new Technology Readiness Level. Within the next two years it is anticipated that HYPER joints will be included on a large scale structural demonstrator and the manufacturing processes be highly industrialised.

References

[1] R.D. Adams and N.A. Peppiat. Effect of poisson's ratio strains in adherends on stresses of anidealized lap joint. *Journal of Strain Analysis*, 8(2):134, 1973.

[2] Advisory Council for Aviation Research and Innovation in Europe (ACARE). ACARE Homepage. http://www.acare4europe.com. Accessed: 02-11-2014.

[3] Air Transport Action Group (ATAG). *Beginners guide to aviation efficiency.* ATAG, 33 Route de l'Aéroport, P.O. Box 49, 1215 Geneva 15, Switzerland, 2010.

[4] Air Transport Action Group (ATAG). Global briefing issue 1. http://www.atag.org/, October 2011. Accessed: 02-11-2014.

[5] Air Transport Action Group (ATAG). Global briefing issue 2. http://www.atag.org/, February 2012. Accessed: 02-11-2014.

[6] Airbus. The Future by Airbus: The Concept Plane. http://www.airbus.com/innovation/future-by-airbus/concept-planes/. Accessed: 02-11-2014.

[7] Airbus. Determination of compression strength after impact - fibre reinforced plastics - Airbus test method (AITM1-0010), October 2005.

[8] Airbus Group Innovations. Private communications. 2010-2014.

[9] A.A. Antonysamy. *Microstructure, texture and mechanical property evolution during additive manufacturing of Ti-6Al-4V alloy for aerospace applications.* Ph.D. Thesis, University of Manchester, England, 2012.

[10] M. Arcan, Z. Hashin, and A. Voloshin. Method to produce uniform plane-stress states with applications to fiber-reinforced materials. *Experimental Mechanics*, 18(4):141–146, 1978.

[11] ASTM. Standard test method for lap shear adhesion for fiber reinforced plastic (FRP) bonding (ASTM D5868-1), 2008.

[12] B. Baufeld, E. Brandl, and O. van der Biest. Wire based additive layer manufacturing: Comparison of microstructure and mechanical properties of Ti-6Al-4V components fabricated by laser-beam deposition and shaped metal deposition. *Journal of Materials Processing Technology*, 211(6):1146–1158, 2011.

[13] T. Blomberg. *Heat Conduction in Two and Three Dimensions*. Ph.D. Thesis, Lund University, Sweden, 1996.

[14] P.P. Camanho and F.L Matthews. Stress analysis and strength prediction of mechanically fastened joints in frp: a review. *Composites Part A: Applied Science and Manufacturing*, 28:529–547, 1997.

[15] P. Cawley and R.D. Adams. Defect types and non-destructive testing techniques for composites and bonded joints. *Materials Science and Technology*, 5:413–425, 1989.

[16] P. Chang, A.P. Mouritz, and B.N Cox. Properties and failure mechanisms of pinned composite lap joints in monotonic and cyclic tension. *Composites Science and Technology*, 66:2163–2176, 2006.

[17] C.H.E. Cheung, P.M. Gray, G.E. Mabson, and K.Y. Lin. Analysis of fasteners as disbond arrest mechanism for laminated composite structures. In *51st AIAA Structures, Structural Dynamics and Material Conference*, Orlando, Florida, USA, April 2010.

[18] P.A. Colegrove, H.E. Coules, J. Fairman, F. Martina, T. Kashoob, H. Mamash, and L.D. Cozzolino. Microstructure and residual stress improvement in wire and arc additively manufactured parts through high-pressure rolling. *Journal of Materials Processing Technology*, 213(10):1782–1791, 2013.

[19] T.A. Collings and M.J. Beauchamp. Bearing deflection behaviour of a loaded hole in CFRP. *Composites*, 15(1):33–38, January 1984.

[20] M.W. Commander, D.H. Woolstencroft, and J.C. Hendry. Advanced composite tooling and manufacturing methods. In D.H. Middleton, editor, *Composite Materials in Aircraft Structures*, chapter 10, page 162. Longman Scientific and Technical, 1990.

[21] A.D. Crocombe, C.Y. Ong, C.M. Chan, and M.M. Abdel Wahab. Investigating fatigue damage evolution in adhesively bonded structures using backface strain measurement. *Journal of Adhesion*, 78:745–776, 2002.

[22] Lucas FM da Silva, Paulo JC das Neves, RD Adams, and JK Spelt. Analytical models of adhesively bonded jointspart i: Literature survey. *International Journal of Adhesion and Adhesives*, 29(3):319–330, 2009.

[23] Lucas FM da Silva, Paulo JC das Neves, RD Adams, A Wang, and JK Spelt. Analytical models of adhesively bonded jointspart ii: Comparative study. *International Journal of Adhesion and Adhesives*, 29(3):331–341, 2009.

[24] Dassualt Systemes Simulia Corp. Abaqus v6.11-1. Computer Program, 2011. Providence, Rhode Island, USA.

[25] Dassualt Systemes Simulia Corp. Abaqus v6.11-1 analysis manual, 2011. Providence, Rhode Island, USA.

[26] Dassualt Systemes Simulia Corp. Abaqus v6.11-1 user's manual, 2011. Providence, Rhode Island, USA.

[27] A. de Oliveria. Hyper joint pre-sizing methods - AGI reports RP1015456 and IW200647. Technical report, Airbus Group Innovations, 2010.

[28] L. C. Dickinson, G. L. Farley, and M. K. Hinders. Prediction of effective three-dimensional elastic constants of translaminar reinforced composites. *Journal of Composite Materials*, 33(11):1002–1029, 1999.

[29] M.J. Donachie. *Titanium a technical guide*. ASM International, Materials Park, OH, USA, 2000.

[30] Electro Optical System (EOS) GmbH. EOSINT M270 Technical Data. http://www.eos.info/en, 2014. Accessed: 02-11-2014.

[31] S. Erland, T. Dodwell, and R. Butler. Inter and intra-ply shear of uncured carbon fibre laminates. In *16th European Conference on Composite Materials*, Seville, Spain, June 2014.

[32] European Union. Clean Sky: Innovation takes off. http://www.cleansky.eu. Accessed: 02-11-2014.

[33] E.O. Ezugwu and Z.M. Wang. Titanium alloys and their machinability - a review. *Journal of Material Proccessing Technology*, 68(3):262–274, 1997.

[34] L.A. Feldkamp, L.C. Davis, and J.W. Kress. Practical cone-beam algorithm. *Journal of Optical Society of America*, 1(6):612–619, June 1984.

[35] M. Genest, M. Martinez, N. Mrad, G. Renaud, and A. Fahr. Pulsed thermography for non-destructive evaluation and damage growth monitoring of bonded repairs. *Composite Structures*, 88(1):112–120, 2009.

[36] P.F. Giddings. *Piezoelectrically actuated bistable composite laminates for structural morphing*. Ph.D. Thesis, University of Bath, 2010.

[37] Ma Goland and E Reissner. The stresses in cemented joints. *Journal of applied mechanics*, 11(1):A17–A27, 1944.

[38] D.P. Graham, A. Rezai, D. Baker, P.A. Smith, and J.F. Watts. A hybrid joining scheme for high strength multimaterial joints. In *18th International Conference on Composite Materials*, Jeju Island, South Korea, August 2011.

[39] A.J. Gunnion, M.L. Scott, R.S. Thomson, and D. Hachenberg. A linear 3-d finite element unit cell model for fibre waviness in composite materials. In *23rd International Congress of Aeronautical Sciences*, Toronto, Canada, September 2002.

[40] R. Halmshaw. Electrical methods. In *Non-Destructive Testing*, chapter 6, pages 230–233. Edward Arnold, 1991.

[41] R. Halmshaw. Ultrasonic testing of materials. In *Non-Destructive Testing*, chapter 4, pages 101–200. Edward Arnold, 1991.

[42] L. J. Hart-Smith. Adhesive bonded single lap joints. *NASA Report CR112236*, 1973.

[43] L. J. Hart-Smith. Bonded-bolted composite joints. *Journal of Aircraft*, 22(11):993–1000, 1985.

[44] Hexcel Corporation. M21 product data sheet. http://www.hexcel.com/Resources/DataSheets/Prepreg-Data-Sheets/M21_global.pdf, 2010. Accessed: 02-11-2014.

[45] D.J. Holt. Future composite aircraft structures may be sewn together. *Journal of Automotive Engineering*, 90(7), 1982.

[46] V. A. Imperiale, E. Cosentino, P. M. Weaver, and I. P. Bond. Compound joint: A novel design principle to improve strain allowables of FRP composite stringer run-outs. *Composites Part A: Applied Science and Manufacturing*, 41(4):521–531, Apr 2010.

[47] G. Kelly. Load transfer in hybrid (bonded/bolted) composite single-lap joints. *Composite Structures*, 69(1):35–43, Jun 2005.

[48] G. Kelly. Quasi-static strength and fatigue life of hybrid (bonded/bolted) composite single-lap joints. *Composite Structures*, 72(1):119–129, Jan 2006.

[49] D. King, O. Inderwildi, and C. Carey. Advanced aerospace materials: past, present and future. *Aviation and the Environment*, pages 22–27, 2009.

[50] P.A. Kobryn and S.L. Semiatin. The laser additive manufacture of Ti-6Al-4V. *JOM*, September 2001.

[51] V. Koissin, J. Kustermans, S. V. Lomov, I. Verpoest, H. Nakai, T. Kurashiki, K. Hamada, Y. Momoji, and M. Zako. Structurally stitched woven preforms: experimental characterisation, geometrical modelling, and fe analysis. *Plastics, Rubber and Composites*, 38(2-4):98–105, May 2009.

[52] J.P. Kruth, M.C. Leu, and T. Nakagawa. Progress in additive manufacturing and rapid prototyping. *Annals of the CIRP*, 47(2):525–540, 1998.

[53] A. Kurtovic, E. Brandl, T. Mertens, and H.J. Maier. Laser induced surface nano-structuring of Ti-6Al-4V for adhesive bonding. *International Journal of Adhesion and Adhesives*, 45:112–117, 2013.

[54] F. Lenzi, A. Riccio, A. Clarke, and R. Creemers. Coupon tests on z-pinned and unpinned composite samples for damage resistant applications. *Macromolecular Symposia*, 247(1):230–237, 2007.

[55] G. N. Levy, R. Schindel, and J.P. Kruth. Rapid manufacturing and rapid tooling with layer manufacturing (LM) technologies, state of the art and future perspectives. *CIRP Annals - Manufacturing Technology*, 52(2):589–609, 2003.

[56] K. Lu. The future of metals. *Science*, 328(5976):319–320, April 2010.

[57] R. Luciano and E.J. Barbero. Formulas for the stiffness of composites with periodic microstructure. *International Journal of Solid Structures*, 31(21):2933–2944, 1995.

[58] X. Maldague and S. Marinetti. Pulse phase infrared thermography. *Journal of Applied Physics*, 79(5):2694–2698, Mar 1996.

[59] MATLAB. *Version 7.6*. The MathWorks Inc., Natick, Massachusets, 2008.

[60] F.L. Matthews. Load-carrying joints. In D.H. Middleton, editor, *Composite Materials in Aircraft Structures*, chapter 9, pages 142–155. Longman Scientific and Technical, 1990.

[61] J. Meyer and D. Johns. Hybrid component, 2010. International patent number WO2010/112904A1.

[62] D.H. Middleton. Composite materials in the airbus. In D.H. Middleton, editor, *Composite Materials in Aircraft Structures*, chapter 14, pages 228–229. Longman Scientific and Technical, 1990.

[63] A. P. Mouritz. Review of z-pinned composite laminates. *Composites Part A: Applied Science and Manufacturing*, 38(12):2383–2397, 2007.

[64] M. Muir, J. Meyer, and A. Diskin. Multi-disciplinary optimisation of a business jet MED hinge for production by additive manufacturing. In *6th ALTAIR European Technology Conference*, Turin, Italy, 2013.

[65] L.E. Murr, S.M. Gayton, D.A. Ramirez, E. Martinez, J. Hernandez, and K.N Amato. Metal fabrication by additive manufacturing using laser and electron beam melting technologies. *journal of Materials Science Technology*, 28(1):1–14, 2012.

[66] Nikon. *XT H Series*. Nikon Metrology NV, Geldenaaksebaan 329, B-3001 Leuven, Belgium, 2014.

[67] M.C.J. Niu. Joining. In *Composoite Airframe Structures*, pages 285–356. Hong Kong Conmilit Press Limited, 2nd edition, 1996.

[68] A.C. Nogueira, K. Drechsler, and E. Hombergsmeier. Analysis od the static and fatigue strength of a damage tolerant 3d-reinforced joining technology on composite on composite single lap joints. In *53rd AIAA Structures, Structural Dynamics and Material Conference*, Haweii, USA, 2012.

[69] Olympus Corporation. Inspection and Measurement Systems. http://www.olympus-ims.com/, November 2014. Accessed: 02-11-2014.

[70] P. Parkes and R. Butler. Fatigue of metal-composite joints using hybrid penerative reinforcement. In *54th AIAA Structures, Structural Dynamics and Material Conference*, Boston, Massachusetts, USA, 2013.

[71] P.N. Parkes, R. Butler, and D.P. Almond. Growth of damage in additively manufactured metal-composite joints. In *15th European Conference on Composite Materials*, Venice, Itlay, 2012.

[72] E. Paroissien, M. Sartor, and J. Huet. *Hybrid (bolted/bonded) joints applied to aeronautic parts: Analytical one-dimensional models of a single-lap joint.* Advances in Integrated Design and Manufacturing in Mechanical Engineering II. Springer, Dordrecht, 2007.

[73] Arnaldo Manuel Guedes Pinto, AG Magalhães, Raul Duarte Salgueiral Gomes Campilho, MFSF de Moura, and APM Baptista. Single-lap joints of similar and dissimilar adherends bonded with an acrylic adhesive. *The Journal of Adhesion*, 85(6):351–376, 2009.

[74] J.G. Ratcliffe and T.K. O'Brien. Discrete spring model for predicting delamination growth in Z-fibre reinforced dcb specimens. Technical report, NASA, 2004.

[75] A.T. Rhead. *Analysis and optimisation of post-buckled damage tolerant composite laminates.* Ph.D. Thesis, University of Bath, 2009.

[76] A. Schierl. The CMT process - a revolution in welding technology. In *Welding in the World*, volume 49, page 38. Institut International de la Soudure, 2005.

[77] J. Schön and R. Starikov. Fatigue of joints in composite structures. In B. Harris, editor, *Fatigue of composites: science and technology of the fatigue response of fibre-reinforced plastics*, chapter 23, pages 633–640. Woodhead Publishing, England, 2003.

[78] M. Shellabear and O. Nyrhilä. DMLS - delevopment history and state of the art. In *4th International Conference on Laser Assisted Net Shape Engineering*, Erlangen, Germany, September 2004.

[79] M. Sirna and L. Lanzi. Hyper joint detailed fe modelling. Technical report, Airbus Group Innovations, 2010. Report No. IW101279-02-i2.

[80] F. Smith. Comeld : An innovation in composite to metal joining. *Materials Technology*, 20(2):91–96, June 2005.

[81] R. Starikov. *Quasi-static and fatigue behaviour of composite bolted joints.* Ph.D. Thesis, Department of Aeronautics, RIT, Stockholm, Sweden, 2001.

[82] S. Stelzer, S. Ucsnik, J. Tauchner, T. Unger, and G. Pinter. Novel composite-composite joining technology with through thickness reinforcement for enhanced damage tolerance. In *19th International Conference on Composite Materials*, Montréal, Canada, 2013.

[83] E.Q. Sun. Shear locking and hourglassing in MSC Nastran, Abaqus and Ansys. In *Americas Virtual Product Development Conference*, Huntingdon Beach, California, July 2006. MSC Software Corporation.

[84] L. H. Tenek and E. G. Henneke. Flaw dynamics and vibrothermographic-thermoelastic nde of advanced composite-materials. *Thermosense XIII*, 1467:252–262, 1991.

[85] The Economist. 3d printing: The printed world. http://www.economist.com/node/18114221, February 2011.

[86] L. Thijs, F. Verhaeghe, T. Craeghs, J. Van Humbeeck, and J. P. Kruth. A study of the micro structural evolution during selective laser melting of Ti-6Al-4V. *Acta Materialia*, 58(9):3303–3312, May 2010.

[87] W. Tu, F. J. Guild, and P. J. Hogg. Comeld joints: A novel technique for bonding composites and metal. *Rare Metal Materials and Engineering*, 38:134–141, 2009.

[88] W. Tu, P. H. Wen, and F. J. Guild. Multi-region mesh free method for Comeld joints. *Computational Materials Science*, 48(3):481–489, 2010.

[89] W. Tu, P. H. Wen, P. J. Hogg, and F. J. Guild. Optimisation of the protrusion geometry in Comeld joints. *Composites Science and Technology*, 71(6):868–876, Apr 12 2011.

[90] S. Ucsnik, M. Scheerer, S. Zaremba, and D. H. Pahr. Experimental investigation of a novel hybrid metal-composite joining technology. *Composites Part A: Applied Science and Manufacturing*, 41(3):369–374, 2010.

[91] United Nations. Kyoto protocol to the united nations framework convention on climate change. http://www.unfccc.int/essential_background/kyoto_protocol. Accessed: 02-11-2014.

[92] B. Vangrimde and R. Boukhili. Measuring bolted joint bearing deformation and stiffness. In *12th International Conference on Composite Materials*, Paris, France, 1999.

[93] B. Vangrimde and R. Boukhili. Analysis of the bearing response test for polymer matrix composite laminates: bearing stiffness measurement and simulation. *Composite Structures*, 56:359–374, 2002.

[94] Z. Zhang, J.K. Shang, and F.V. Lawrence. A backface strain technique for detecting fatique crack initiation in adhesive joints. *Journal of Adhesion*, 49(1):23–36, 1995.